OPTIMIZATION OF PROSTATE PLAN IN A PELVIC PROSTHESIS PHANTOM

by

Khombo Eunice Dumela

2095338

A thesis

Submitted in fulfilment of the requirements for the degree

Doctor of Philosophy

in

Physics

in the Faculty of Science, University of the Witwatersrand, Johannesburg, South Africa

Johannesburg, September 2024

Supervisor: **Prof I.T. Usman**

Co-supervisor: **Prof O.M. Oderinde**

DECLARATION

I, the undersigned, hereby declare that this thesis titled “Optimization of Prostate Plan in a Pelvic Prosthesis Phantom” is my own unaided work. It is being submitted for the Degree of Doctor of Philosophy at the University of the Witwatersrand, Johannesburg. It has not been submitted previously for any degree or examination at any other University.

(Signature of candidate)

5th day of September 2024 at Northgate

ABSTRACT

Background: An increasing number of elderly prostate cancer patients with high-density material hip prosthesis are referred for external beam Radiotherapy (EBRT). Radiation treatment of pelvis cancer patients with high-density hip prosthesis needs special attention because of the artifacts created in the computed tomography (CT) field of view and the radiotherapy dosimetry challenges. The accuracy of the treatment planning dose calculation algorithms determines the accuracy of the dose delivered to the patient during radiation therapy. However, the most available algorithms do not accurately model the absorption of high-density metals' scattering properties and underestimate the resulting dose perturbations.

Aim: This study aims to optimize the dose distribution of prostate 3D conformal treatment, intensity-modulated radiotherapy (IMRT) and volumetric-modulated arc therapy (VMAT) in an in-house metallic hip prosthesis phantom.

Methods and materials: In this study, an ionization chamber and Gafchromic (EBT3) films were used to physically measure the prostate point dose in an in-house pelvic phantom. The pelvic phantom was irradiated on the Linac with four static fields, namely, (1) anterior field, (2) posterior field, (3) right lateral field passing through the bone of the normal hip and (4) left lateral passing through the hip prosthesis. IMRT and VMATs plans were also generated on the phantom. The phantom was also irradiated with IMRT and VMATs plan. The use of single arc versus two arcs with avoidance sector were also evaluated. The phantom consists of different materials; Nylon-12 (a solid water-equivalent material) to simulate the prostate with a central cavity to accommodate an ionization chamber and film, superflab gel bolus to simulate human soft tissue, dental wax to simulate human soft tissue, bone anatomy for the right hip and a titanium implant to replace the bony structure of the left hip.

For the static fields, an in-house pelvic phantom was simulated using the EGSnrc Monte Carlo code, and 6 and 15 MV photon energies were employed as in an experimental setting. The prostate point doses computed by the Treatment Planning

System (TPS), measured using ionisation chamber, and Gafchromic EBT3 film were compared with the prostate point doses simulated by Monte Carlo code.

Results and discussion: The novel phantom was constructed using superflab gel bolus, Nylon-12, dental wax, pig bone insert and a titanium alloy hip replacement. The radiological equivalence of the superflab gel bolus and dental wax was determined employing linear attenuation coefficients and then compared to an RW3 Solid water phantom.

EGSnrc Monte Carlo (MC) code was used in this study. Before using Monte Carlo codes, they need to be validated by comparing the Linear accelerator Monte Carlo simulated dose distribution with the experimental data measured in a Linear accelerator using water and ionization chamber for 6 MV and 15 MV photon beams of different field sizes. The EGSnrc dose distributions were compared with the experimental measurements using a gamma analysis, employing a 2 %/2 mm distance-to-agreement criterion. The EGSnrc Monte Carlo calculated dose distribution agreed well with experimental measurements within 2 %. The MC beam model was then used to compute the dose distribution in an in-house pelvic phantom.

The comparison of the measurements between the TPS calculated prostate point dose and ionization chamber for the 6 MV and 15 MV photon beams was: anterior (gantry 0°) 1.8 % and -0.5 %; posterior (gantry 180°) 1.7 % and -0.2 %; left lateral (gantry 90°) 6.3% and 4.2 %; right lateral (gantry 270°) -2.2 % and -2.1 % respectively. Results obtained for Gafchromic EBT3 film measured doses were: anterior 2.3 % and 1.3 %; posterior -0.9 % and 0.2 %, left lateral 4.5 % and 3.5 %; right lateral -2.1 % and -2.5%, for the 6 MV and 15 MV photon beams, respectively. Consequently, results obtained for comparison of TPS, ion chamber and Film with MC simulated doses were: anterior 3.9 %, -2.1 and -1.6% %; posterior 1.8 %, -0.1% and -2.7 %; left lateral -0.2 %, 6.5 % and 4.7 %; right lateral 0.4 %, -2.6% and -2.5 %, for the 6 MV photon beam. And for 15 MV photon beam the results were: anterior 1.9 %, -3.8 and -0.6% %; posterior 2.0 %, -2.3 % and -2.2 %; left lateral 0.5 %, 3.7 % and 2.9 %; right lateral 0.4 %, -2.4 % and -2.9 %. Monte Carlo simulations and film measurements have a statistically significant difference of $p<0.001$, with the film measurements having a higher value than MC simulations except on the left lateral field. Monte Carlo

simulations and ionization chamber measurements also show a significant difference of $p<0.001$, with the ionization chamber having a higher value than the MC simulation, except for the left lateral field passing through the hip prosthesis.

The comparison of the measurements between the TPS calculated prostate point dose with ionization chamber and Gafchromic EBT3 film for the 6 MV IMRT plan of the beam passing through the prosthesis was 2.2 % and 3.3%, respectively. While the IMRT plan with avoided beam was 1.9 % and 3.1% for ionization chamber and Gafchromic EBT3 film, respectively. The comparison of the measurements between the TPS calculated prostate point dose for the 6 MV VMAT plan without avoiding for the beam passing through the prosthesis was 1.1 % and 2.2 % for ionization chamber and Gafchromic EBT3 film, respectively. While for VMAT plan with avoided sector was 3.0 % and 4.0% for ionization chamber and Gafchromic EBT3 film, respectively. The test suggested a significant difference of $p=0.0001$ between the distribution of film measurements and TPS calculated dose. Meanwhile, for ionization chamber measurements and TPS calculated dose; the test indicated a significant difference between ion chamber measurements and TPS calculated dose with a significant level of less than 0.001. in addition, MC simulated dose and TPS calculated dose; the test shows a percentage difference of -0.2 % and 0.5 % for 6 MV and 15 MV photon beams in the lateral field that passes through the prosthesis. The test indicated the significant difference of $p=0.001$ which is slightly lower compared to the other comparisons.

Conclusion: The dual dosimetric pelvic prosthesis phantom is easy to assembly and is more convenient for second dose check for patients with hip prostheses. Through the use of the pelvic phantom, it was possible to measure the prostate point dose using ionization chamber and films. The TPS overestimated the prostate point dose because the treatment planning algorithm could not accurately determine the CT number and the electron density of the prosthesis due to the limitation on the CT scanner. The maximum deviation calculated in this study for TPS, ionization chamber Gafchromic EBT3 films when compared to Monte Carlo simulated dose comes from the lateral fields passing through the prosthesis for both 6 MV and 15 MV photon beams.

ACKNOWLEDGEMENTS

I wish to express my sincere gratitude to the following people and organisations that made the completion of this study possible:

- The Almighty Father from whom all things come, including this research.
- Professor IT Usman, my supervisor, for her guidance, patience, and encouragement during this research. Her devotion made it possible for me to complete this thesis.
- Professor OM Oderinde, my co-supervisor, for his guidance, patience, and encouragement during this research, and for introducing me to Monte Carlo simulation. His devotion made it possible for me to complete this thesis.
- Mr Hassen from Red Apple 3D printing company for designing the intended original phantom design and making the Nylon-12 prostate piece.
- Azimed for supplying superflab gel bolus and dental wax.
- Dr RH van der Plank, an orthopaedic surgeon, for donating a titanium alloy hip replacement.
- Ms Aviwe Makenzi, Mrs Lethabo Khosa and Ms Mamiki Marhanele for their support throughout the study.
- Ms Rose Molatedi and Ms Thendo Alidzulwi for their assistance throughout the study.
- Mr Itumeleng Setilo, for his assistance throughout the study.
- Mrs Hilary and Mr John Harrison for their continuous support during the study.
- Ms Tatjana Ivanoff for her continuous support during the study
- The Radiotherapy department at the Netcare Olivedale Hospital for the use of the linear accelerator and the radiotherapists who helped during data collection.
- My mom Anicky Vulani Helani, sister, two brothers and friends for their prayers and unwavering faith in my abilities.

DEDICATION

Dedicated to my son Vukosi Jay Mabasa; my mom, Anicky Vulani Helani; my late father, James Dumela; my sister, Talent and my brothers: Akani, Mukondleteri, Ponani; my nieces: Vukona, Vutshila, Vuleteri, Vunene and Mahlahle; My nephews: Malwandla and Makungu

TABLE OF CONTENTS

LIST OF FIGURES

LIST OF TABLES

ABBREVIATION

2D	Two-Dimensional
3D	Three-Dimensional
3DCRT	Three-Dimensional Conformal Radiation Therapy
AAA	Anisotropic Analytical algorithm
AAPM	American Association of Physicists in Medicine
BEV	Beam's Eye View
BSDF	Backscatter Dose Perturbation Factor
CT	Computed Tomography
CTV	Clinical Tumour Volume
DD	Dose Difference
DTA	Distance-to-Agreement
EBRT	External Beam Radiotherapy Treatment
EGSnrc	Electron-Gamma-Shower
EPID	Electronic Portal Imaging Device
FBP	Filtered Back Projection
GTV	Gross Tumour Volume
HU	Hounsfield Units
ICRU	International Commission on Radiation Units and Measurements
IMRT	Intensity-Modulated Radiotherapy
keV	KiloElectron Volts
kVP	KiloVoltage Peak
LINAC	Linear Accelerator
MAR	Metal Artifact Reduction
MARIS	Metal Artifact Reduction in Image space
MC	Monte Carlo
MCNP	Monte Carlo N-particle Transport
MeV	Mega electron Voltage
MHz	MegaHertz
MLC	Multileaf Collimators

MU	Monitor Units
MV	Megavoltage
NCR	National Cancer Registry
OAR	Organs at Risk
OD	Optical Density
O-MAR	Metal Artifact Reduction for Orthopedic Implants
PDD	Percentage Depth Dose
PENELOPE	Penetration and Energy Loss of Positron and Electrons
PHSP	Phase space
PTV	Planning Target Volume
QA	Quality Assurance
RED	Relative Electron Density
RF	Radiofrequency
SEMAR	Single Energy Metal Artifact Reduction
TLD	Thermoluminescent Dosimeter
TPS	Treatment Planning System
VMAT	Volumetric Modulated Arc Therapy

CHAPTER 1: INTRODUCTION

According to the National Cancer Registry (NCR) (2013), the lifetime risk for prostate cancer in men in South Africa is one-in-eighteen. It develops mostly in older men who may have osteoarthritis (Rama, 2014). Advances in orthopedic surgery have resulted in a significant number of patients with osteoarthritis receiving hip replacements (Giantsound *et al*., 2017).

The benefit of hip replacement surgery for the patient is the ability to move and walk without pain. An increasing number of elderly prostate cancer patients with high density material hip prostheses are referred for External Beam Radiation Therapy (EBRT) (Ng *et al.,* 2015). Hip replacement prostheses are manufactured from high atomic number (Z) material such as titanium or steel. Radiation treatment of prostate cancer patients who have high density hip prostheses poses the following challenges:

Firstly, there could be an inaccurate radiotherapy dose distribution because of radiation transport through a high-density material. The high Z prosthetic material causes increased beam attenuation. This creates perturbation of the absorbed dose distribution. The increased beam attenuation leads to reduced target dose and dosimetry uncertainty at the soft tissue interface. The soft tissue interface uncertainty is caused by electron backscatter from the prosthesis. (Ade *et al*., 2017 and Prabhakar *et al*., 2013).

Secondly, when a patient with a high-density prosthesis is scanned in a computed tomography scanner (CT-SCAN) image artifacts are produced. These artifacts are due to four main factors, namely: beam hardening, scattering, noise (Giantsound *et al*., 2017) and photon starvation (Ali, 2018). These factors will be discussed in detail in Chapter 3 section 3.3.2.

The radiation particle interaction of the bone-metal interface and secondary photons will increase electron scattering, resulting in high doses at the beam entrance and exit surface of the prosthesis. Dose absorption in the prosthesis itself will also cause shadowing in the regions beyond it (Reft *et al*., 2003). The increased dose at a bone-metal interface depends on factors such as the thickness and width of the interface,

the design and atomic composition of the interface, the thickness of the medium overlying the interface, field size of the beam, the differences in multiple scattering of the secondary electrons and scattering of the incident beam (Ade *et al*., 2017).

Kling *et al*. (2013), Giantsound *et al*. (2017) and Reft *et al*. (2003) further postulate that the main challenge encountered in patients with hip prostheses during radiotherapy treatment planning is the inability to delineate the target volume accurately. The lack of accuracy is due to streak artifacts created by the prostheses on the CT images used for planning. These artefacts may conceal the true anatomy of an organ and make organ borders indistinct.

The accuracy of the treatment planning dose calculation algorithms determines the accuracy of the dose delivered to the patient during radiation therapy (ICRU report 91, 2014). Kernel-based algorithms such as pencil beam kernel, cone convolution, and superposition work well with slight differences in tissue density to calculate a dose distribution (Reft *et al*., 2003). However, these algorithms do not accurately model the absorption of high-density metals' scattering properties (Prabhakar *et al*., 2013) and underestimate the resulting dose perturbations (Lloyd, 2011).

The CT number and the electron density of the prosthesis cannot be determined accurately by treatment planning algorithms because of image artifacts produced during CT scanning in the presence of a prosthesis in the field of view (Reft *et al*., 2003). Due to errors in electron density or stopping power estimates (Giantsound *et al*., 2017) the treatment planning system (TPS) may not accurately predict doses at the bone-metallic interface and may result in significant dose calculation uncertainties (Ng *et al*., 2015). This may compromise tumour local control.

It has become a common practice in radiotherapy treatment planning to avoid direct irradiation through a high-density hip prosthesis (Prabhakar *et al*., 2013) because of the higher energy absorption of the prosthesis compared to normal tissue and thus the poor penetration of the beam through the prosthesis. Reft *et al*. (2003) stated that although this method avoids the dosimetric complications of the high-density metallic inhomogeneity, it becomes challenging to achieve an acceptable dose distribution coverage of the target (PTV/Prostate) whilst attempting to minimize the dose to the critical organs (e.g., bladder and rectum). Some treatment beams may exit through the prosthesis to obtain a homogenous dose distribution.

Garth (2005) attempted an alternative method to overcome uncertainties in contouring soft tissue densities by overriding the artifacts in the CT images. This method delivers an apparently acceptable dose distribution. However, the resulting distribution is not accurate for the following reason:

Quality assurance (QA) or patient-specific dosimetric verification of IMRT and VMAT plans is an important part of the clinical implementation of IMRT/VMAT into any clinic (Agazaryan *et al.*, 2003). Dose verification is an essential part of IMRT and VMAT clinical practice. A QA system should be able to detect any planning and machine errors before the actual treatment (Liang *et al*., 2016). IMRT/VMAT treatment plan in the TPS, the patient's plan can be mapped onto a phantom and the dosimetry can be viewed and delivered on the treatment machine for treatment quality assurance (QA) or patient-specific dosimetric verification.

To measure patient specific quality assurance, a choice of software such as Verisoft (PTW-Freiburg, Germany), COMPASS (IBA Dosimetry, GmbH, Germany), ArcCHECK (Sun Nuclear Corporation, Melbourne, FL, USA) is used. These software programs use the gamma evaluation method which helps locate hot and cold spots in the dose distribution. They determine maximum and average deviation between a TPS calculated and Linac measured plan (Nalbant *et al*., 2014). However, the influence of artefact will not be noticed, and the QA test will pass if a patient-specific verification plan has been created from the same plan with overriding artefacts and measured using homogenous phantom. Therefore, Garth's method will lead to inaccuracies. In our study a phantom that has a femoral bone and titanium alloy was used to verify the TPS calculated dose.

The Monte Carlo (MC) simulation technique is another QA tool used in radiotherapy for modelling of electron, photon, and proton beam dose distributions. MC is the most accurate method for dose calculation because all particle interactions (protons, photons, and electrons) are considered and accounted for in the dose calculations. Monte Carlo codes are known to model high-density scatter very accurately (Cecen, 2013).

An example of an MC utilized in radiotherapy dosimetry is Electron Gamma Shower (EGSnrc), which was developed by the National Research Council of Canada (Oderinde *et al*., 2015 and Yani *et al*., 2016). EGSnrc MC Codes use the BEAMnrc

code system for simulation of the heads of linear accelerators (LINAC) and DOSXYZnrc code is used for dose calculation for patient treatment. The main output of this code is the phase space (phsp) file that contain the particle information released from the LINAC (Yani *et al*., 2016).

Bednarz *et al*. (2009) have identified a growing concern about radiation-induced second cancers associated with radiation treatment. It is thus essential to provide a means of determining doses specifically for the prostate tumour volume and reducing the dose to organs at risk, namely the rectum, bladder, and femoral heads. The International Commission on Radiological Protection (ICRP), the National Council on Radiation Protection and Measurement (NCRP) and the American Association of Physicists in Medicine (AAPM) have recognized the importance of secondary cancer risks as a result of radiation therapy (Cho *et al*., 2011).

1.1 Problem statement

Prostate cancer patients with hip prosthesis are becoming more common. As the prostheses are manufactured from high-density material, they perturb the absorbed dose distribution by attenuating the beam and by beam interactions at bone-metal interfaces. Commercially available planning calculation algorithms do not model the absorption of the scattering properties of the metal accurately and are more likely to overestimate the dose to the target volume of the prostate (Prabhakar *et al*., 2013). Some CT scanners have a threshold Hounsfield number that are lower than the high-density material implants and any high-density material will be assigned the threshold value even when its physical density is higher than this threshold.

To avoid a beam passing through a prosthesis in the planning process, Reft *et al*. (2003) and Prabhakar *et al.* (2013) designed a treatment plan with the beam avoidance structure around the prosthesis and used the planning optimizer to give 0 % of the prescribed dose to this structure. This enabled the treatment beam to pass through this avoidance structure without delivering any dose. This method may compromise the local tumour control resulting in the treatment plan that is inhomogeneous and increase the dose to the organs at risk.

The commercially available patient specific phantom used for verification of treatment plan is homogenous. Homogeneous phantoms do not account for high density material implants, and this is essential to accurately verify treatment plans with high density materials. The phantom with high density hip prosthesis is needed for the verification of treatment plans. An independent calculating system is needed to validate the TPS dose distribution for 3D, IMRT and VMAT treatment plans with prostheses in place. The dose distribution for 3D patients with prostheses is evaluated using a Monte Carlo code.

The novelty of the study is to develop a patient-specific verification phantom with all organs defined, a prostate tumour and high-density implants in place. Since the dose distribution is only predicted by TPS, there is no physical evaluation of the dose distribution for patients with implants, so this dual dosimetric phantom features a slot for an ionisation chamber and film for dose distribution estimation. Understanding the impact of the high-density material on the dose distribution requires the use of an independent dose calculation and a phantom with high density material, as certain centres do not have access to CT scanners with high density ranges.

The dose distribution of 3D conformal plans, IMRT, and VMATs with and without a hip prosthesis was measured using an in-house pelvis phantom. The 3D conformal, IMRT and VMATs measured dose distributions were compared with TPS calculated dose. The measured 3D dose distribution using ionization chamber and film in an in-house pelvic phantom was compared with Monte Carlo simulated dose.

1.2 Purpose of the study

1.2.1 Aim

This research study aims to optimize the dose distribution of prostate 3D conformal treatment, intensity-modulated radiotherapy (IMRT) and volumetric-modulated arc therapy (VMAT) in the metallic hip prosthesis phantom.

The aim of the study is achieved through the following steps:

- Develop a novel patient-specific verification phantom with all organs defined and a prostate tumour pressing on the urethra.
- Optimize treatment planning using an analytical anisotropic algorithm (AAA) TPS algorithm.
- Perform prostate point dose measurements of 3D conformal, IMRT and VMATs plans.
- Perform Monte Carlo calculation of 3D static field.

1.2.2 Objectives

- To develop a pelvic phantom with an ionization chamber, insert, a slot for Gafchromic film and include a hip prosthesis.
- To optimize the 3D conformal, IMRT and VMATs plans of the novel prosthesis phantom.
- To estimate the prostate point dose using an ionization chamber and Gafchromic films for 3D conformal plans.
- To estimate the prostate point dose using an ionization chamber and Gafchromic film for IMRT and VMAT plans.

- To validate the Monte Carlo code by comparing the dose distribution, the percentage depth dose curves and beam profiles of 6 MV and 15 MV photon beams in a water phantom with the EGSnrc Monte Carlo simulation results.

- To investigate the pelvic prostate dose distribution with and without a hip prosthesis using Gafchromic EBT3 films, ionization chamber and perform a comparison with the Monte Carlo simulated results.

1.3 Thesis Structure and Overview

The chapters are described below:

- Chapter 1 presents a brief introduction to the research problem, describes the major aims of this work, and details the structure of each section in this thesis.
- Chapter 2 provides the physics background information for this project.
- Chapter 3 provides a literature review, the radiation therapy prostate cancer treatment with metallic implants, photon beam radiation therapy prostate treatment technique, treatment planning system dose uncertainty due to high-density materials and the different phantom used in the literature to estimate dose in the presence of high-density material.
- Chapter 4 describes the materials and methods used for this study.
- Chapter 5 summarizes the results of the thesis, describes the outcomes, as well as the limitations and also provides a discussion of the results obtained in the study.
- Chapter 6 is the conclusion which describes the projects outcome and provides insight into future works.

CHAPTER 2: PHYSICS BACKGROUND

This chapter provides an overview of the interaction of radiation with matter and the coefficient of attenuation.

2.1 Interaction of radiation with matter

When ionizing radiation interacts with matter (tissue), it deposits energy into the cells of the tissues through which it passes (Baskar *et al*., 2012 and Tremthick, 2012). Radiation can be divided into two types: ionizing and non-ionizing. In radiotherapy, ionizing radiation is used to treat cancer. Ionizing radiation is further classified into two categories, direct and indirect ionizing radiation (Podgorsak, 2012). Both direct and indirect radiation may result in deoxyribonucleic acid (DNA) damage (Tsai *et al.*, 2015).

Direct ionizing radiation occurs when heavy charged particles such as alpha particles and protons, or light charged particles such as electrons and positrons having sufficient kinetic energy, interact with the atoms of DNA molecules directly resulting in immediate damage (Mohammed *et al*., 2018). Ionization is produced at a very short interval by these particles. The damage caused by direct interaction may result in the cell being unable to reproduce or cell death. Damaged cells which survived, may later induce carcinogenesis or other abnormalities (Desouky *et al.*, 2015).

The intermediate step of free radical formation is caused by indirect ionizing radiation and occurs when non-charged particles such as photons, X-rays, gamma rays, and neutrons, interact with water molecules contained in a cell. The energy absorbed by the water molecule forms ion pairs resulting in the formation of metabolites by reactive oxygen such as hydroxyl radicals ($^{\bullet}OH$) and ionized water (H_2O^+). These free radicals interact with cellular atoms and molecules resulting in damage to the DNA as the human body is composed mostly of water (Reisz *et al*., 2014).

In external beam radiation therapy, electron and photon beams interact differently with matter. When an electron beam interacts with matter (tissue), it loses energy.

However, its intensity or number of charged particles remains the same. The energy is continuously lost until the charged particle stops. For cancer treatment, the dose (energy) deposited by an electron in a first approximation is constant from the patient's skin to the maximum penetration depth (Bochorishvili, 2018). When photons are used, the initial photon is attenuated when the beam transverses the tissue and as a result, a new scattered photon is ejected. Photon beam intensity thus decreases with penetration depth. In photon interactions, very little energy is lost over distance (Podgorsak *et al*., 2009 and Bochorishvili, 2018).

2.1.1 Interaction of charged particles with matter

Charged particles (electrons and positrons) continuously interact with matter by Coulomb force where particles attract or repel each other. A charged particle interaction with matter involves interaction with the electrons surrounding the nucleus. An atom can be excited to a higher energy level or ionized by the ejection of valence electrons (Attix, 2019).

Excitation occurs when some of the particle's energy is transferred to the orbital electron of a target material, but not enough energy is transferred to free the electron, leaving the atom in an excited state. Ionization occurs when an incident charged particle removes an electron from an atom or molecule leaving the material with a net positive charge (Connolly, 2012). The charged particles impart a small portion of their kinetic energy to secondary electrons. In tissue, an electron loses about 30 electron volts in each interaction (Bochorishvili, 2018).

2.1.1.1 Elastic and Inelastic scattering

Elastic scattering occurs when the incident charged particle (electron) is scattered without any energy change. The electron can change direction but does not change the wavelength (Inkson, 2016). Inelastic scattering occurs when the energy of the incident particle is changed.

2.1.1.2 Bremsstrahlung radiation

Bremsstrahlung radiation occurs when an incident charged particle (electron) strikes the nucleus of a target and is attracted by the nuclear force field of an atom. The incident electron slows down near the nucleus and changes direction (Strurk, 2019). The energy lost as the electron slows down becomes an X-ray photon. This process is called Bremsstrahlung emission. Bremsstrahlung increases with increasing electron kinetic energy and atomic number, Z (Clarlsson *et al*., 1996).

2.1.1.3 Stopping power

Stopping Power (S) is defined by the International Commission on Radiation Units and Measurements (ICRU) as the average energy dissipated by the charged particle as it penetrates a medium (Mohammed *et al.*, 2018). The fraction of energy loss '*dE*' of an electron per unit of path length 'dx' provides the quantity linear stopping power (MeV cm^{-1}) (Tremethick, 2012).

The mass stopping power is defined as the linear stopping power divided by the density of the absorbing medium. Stopping powers are widely used in radiation dosimetry, but they are rarely measured and must be calculated from theory. Stopping power consists of two components: collision stopping power and radiative stopping power (El-Ghossain, 2017).

2.1.2 Interaction of photons with matter

The interaction of photons (X-rays) with matter can be categorized as reflected, deposited, and transmitted (Oderinde *et al*., 2015). Photons are inelastically scattered via four main mechanisms: Compton (incoherent) scattering with atomic electrons, Rayleigh scattering (Cecen, 2013), photoelectric effect and pair-production in the nuclei or electromagnetic field (Khan *et al.*, 2016). These mechanisms are dependent on photon energy.

2.1.2.1 Compton scattering

Compton (incoherent) scattering is a major mechanism for photon-produced electron excitation. An incident photon strikes a “free” electron in an atom producing an energetic electron and a scattered photon of lower energy. Compton scattering dominates other photon interactions in the 200 keV to 20 MeV energy range (Garth, 2005). This is the energy range used for radiation therapy. Compton scattering may occur either in the accelerator treatment head or patient (phantom) (Khan *et al.*, 2016).

2.1.2.2 Coherent scatter

Coherent scatter consists of interactions occurring between a photon and an atom (Hunter, 2011). There are two types of coherent scatter, namely Thomson and Rayleigh scattering. These scattering processes can take place either:

• From bound electrons (Rayleigh scattering) on condition that the electrons do not receive sufficient energy to eject them from the atom

• From free or loosely bound electrons (Thomson’s scattering) (Dowsette, 2006).

The scattered photon and the incident beam have the same wavelength and the photon does not lose energy in the medium (Benni *et al*., 2018). It is predominant at low incident X-ray energies, small scattering angles and high atomic number of the target (Sharma *et al.*, 2009).

2.1.3.3 Photoelectric effect

In the photoelectric process, the photon is absorbed by an inner shell electron of an atom and ejects a photoelectron. The relationship between the ejected photoelectron and the incident electron ($h\nu$) can be written as $E_{photon} = (h\nu + E_{electron})$ (Connolly, 2007). Depending on the inner shell involved, the electrons are called K-, L- and M-photoelectrons.

Characteristic radiation is created when the vacancy in the electron shell is filled by an electron falling from a higher energy shell. The K-shell photoelectric interaction varies with atomic number Z and photon energy. It is dominant in medium-to-high Z materials below 200 keV (Muhammad, 2017). The characteristic X-rays are absorbed in the medium by another photoelectric interaction or by ejected Auger electrons.

2.1.2.4 Pair production

X-ray photons with an energy greater than 1.02 MeV (Chaudhary, 2018 & Sprawls, 1995) interact with a nucleus to form an electron and a positively charged positron particle (Chaudhary, 2018). This process becomes increasingly important above 2 MeV and is the dominant interaction above 30 MeV. This is another mechanism by which photons produce electrons (Garth, 2005).

As the positron loses kinetic energy and slows, it will interact with a free electron in its vicinity to give rise to two annihilation photons emitted at 180 degrees from each other because momentum is conserved. Each photon has an energy of 0.51 MeV.

The photon interaction process that dominates depends on the mass absorption characteristic of the target and the energy of the photon as shown in Fig.2.1. below.

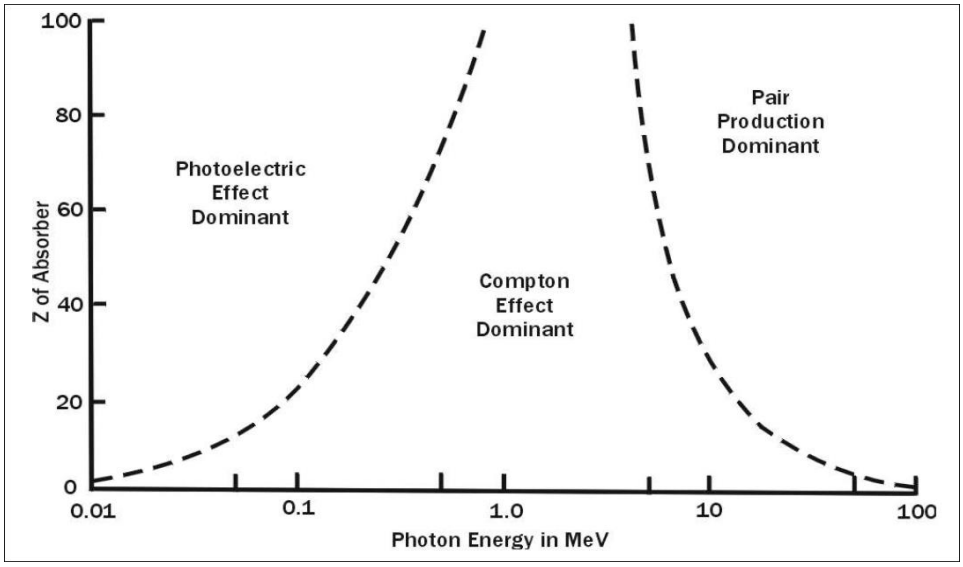

Figure 2. 1: Illustration of the importance of photoelectric absorption, Compton scattering and pair production (Connolly, 2007).

Figure 2.1 shows that the photoelectric effect increases with increasing atomic number of the absorber and dominates in heavy elements, at low photon energies. It increases abruptly at energies corresponding to the orbital electron binding energies of the absorber element. The Compton-scatter component decreases with increasing photon energy and with increasing absorber atomic number. The pair production component is zero for energies less than 1.02 MeV and it increases with increasing photon energy and the atomic number of the absorber. Pair production dominates at higher photon energies in absorbers of high atomic numbers (Cherry *et al*., 2003).

2.2 Principles of photon attenuation

Photons are attenuated as they pass through matter. Each interaction of a photon with an atom of an absorbing material removes a photon from the beam, reducing its intensity. For monoenergetic photons, the number of photons removed from the primary beam when it is incident on a thin layer of material is proportional to the number of incident photons (*N*) and the thickness of the layer (*dx*) (Carlsson *et al*., 1996) as shown in Fig.2.2 below is given by,

$$dN=-\mu N dx \quad \text{..... (2. 1)}$$

where μ is the total linear attenuation coefficient defined in section 2.3.1 of the medium for the photons of interest (Martin, 2006) given by

$$\mu=\frac{dp}{dx} \quad \text{..... (2. 2)}$$

where *p* is per unit length (Carlsson *et al.*, 1996).

The number of photons remaining after traversing a distance *X* through an absorbing medium is given by

$$N=N_o e^{-\mu x} \quad \text{..... (2. 3)}$$

Where N_o is the number of photons in the incident beam (Carlsson *et al.*, 1996 and Martin, 2006).

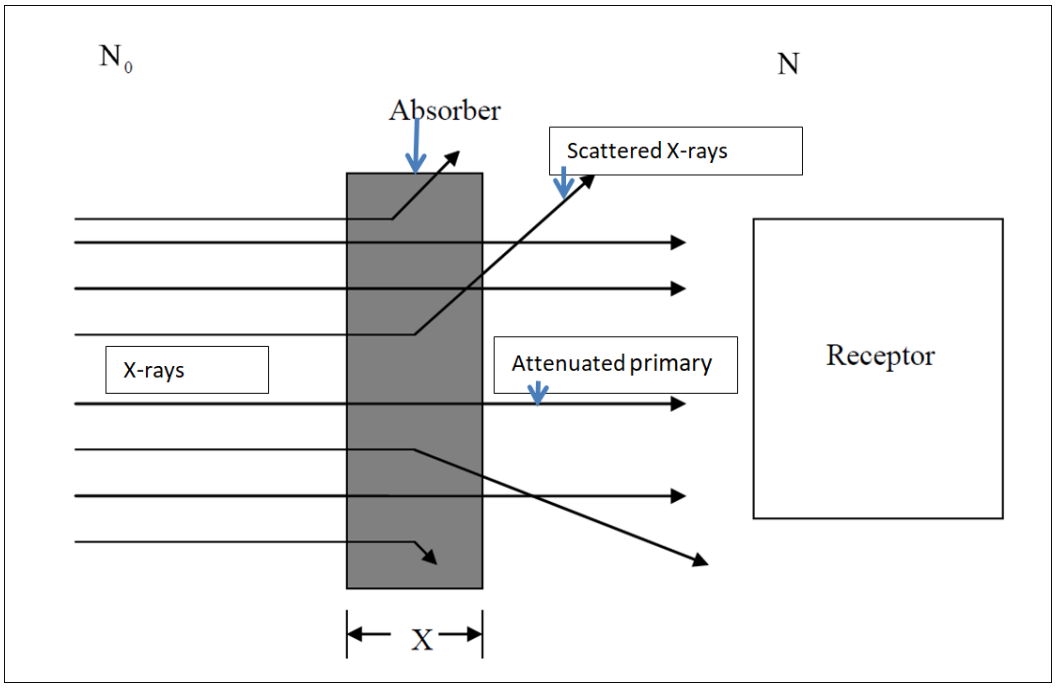

Figure 2. 2: Attenuation process of the photon beam (Martin,2006).

2.3 Attenuation coefficient

Attenuation is the reduction in intensity of a photon beam as it transverses matter. The reduction caused by absorption or by scattering of photons from the beam can be affected by different factors, such as beam energy and the atomic number of the absorber (Mousa *et al*., 2017). The attenuation coefficient μ of the material is defined as

$$\mu = \sigma N \quad \text{..... (2. 4)}$$

Where $\boldsymbol{\sigma}$ is the total cross-section of the material and N is the number of atoms per unit volume. The total cross-section of the material is the sum of the cross-section of all interactions including photo-electric interaction and Compton scattering interaction for the keV range of photons (Rhee *et al*., 2019).

2.3.1 Linear attenuation coefficient

The linear attenuation coefficient (μ) describes the fraction of a beam of photons that are absorbed or scattered per unit thickness of the absorber (Mousa *et al*., 2017). The different interaction processes add their contributions to the total linear attenuation coefficient μ given by

$$\mu = \boldsymbol{\sigma}_{coh} + \boldsymbol{\sigma}_{c} + \boldsymbol{\tau} + \boldsymbol{\kappa} \quad \text{..... (2. 5)}$$

Where $\boldsymbol{\tau}$ is the contribution from photoelectric absorption, $\boldsymbol{\kappa}$ from pair production, $\boldsymbol{\sigma_c}$ from Compton (incoherent) scattering and $\boldsymbol{\sigma_{coh}}$ from coherent scattering (Carlsson *et al*., 1996). The linear attenuation coefficient depends on the atomic number Z, the density of the material and the energy of the photon (Seibert, 2005).

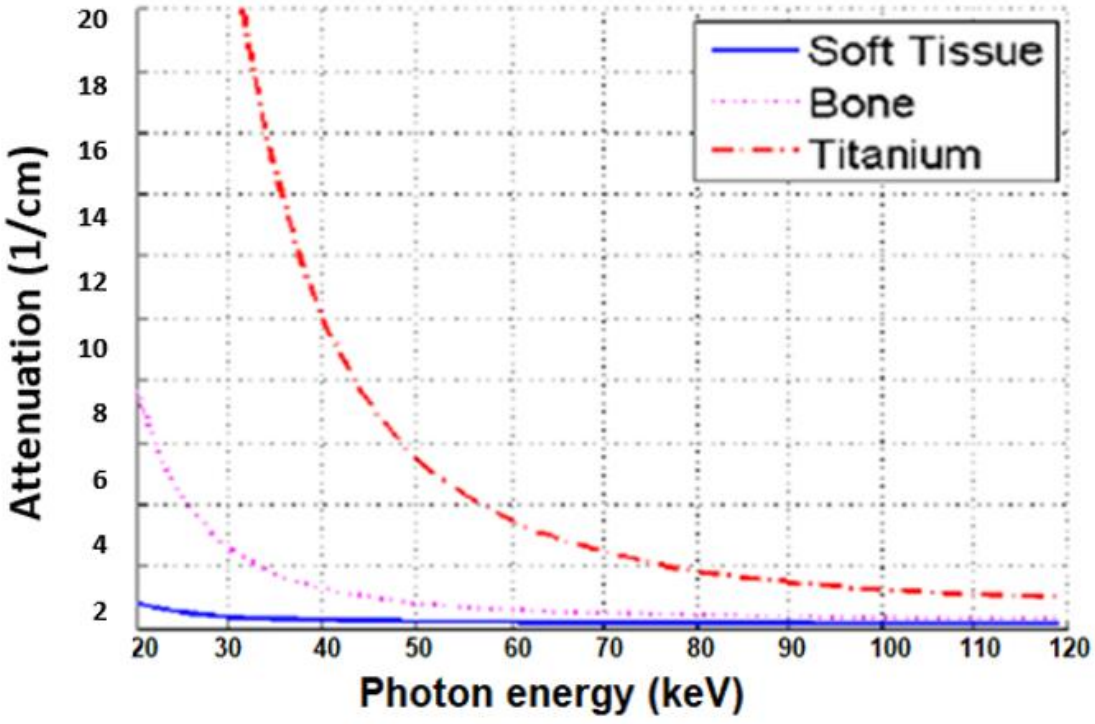

Figure 2. 3: The linear attenuation of cortical bone, soft tissue, and titanium as a function of photon energy (Yang *et al*., 2019).

Figure 2.3. shows that the dependence of soft tissue, cortical bone and titanium on the photon energy is non-linear and is different due to their different atomic numbers (Yang *et al*., 2019).

2.3.2 Mass attenuation coefficient

The mass attenuation coefficient is the measurement of the probability of an interaction occurring between incident photons and matter per unit mass per unit area (Akça *et al*., 2014). The area mass is the product of material thickness and density (Sprawls, 1995) given by

$$Area\ mass\ \left(\frac{g}{cm^2}\right) = Thickness\ (cm)\ X\ Density\ (\frac{g}{cm^3}) \quad \text{..... (2. 6)}$$

The relationship between the mass and linear attenuation coefficient is

$$Mass\ attenuation\ Coefficient\ \left(\frac{\mu}{\rho}\right) = \frac{Linear\ attenuation\ Coefficient\ (\mu)}{Density\ (\rho)} \quad \text{..... (2. 7)}$$

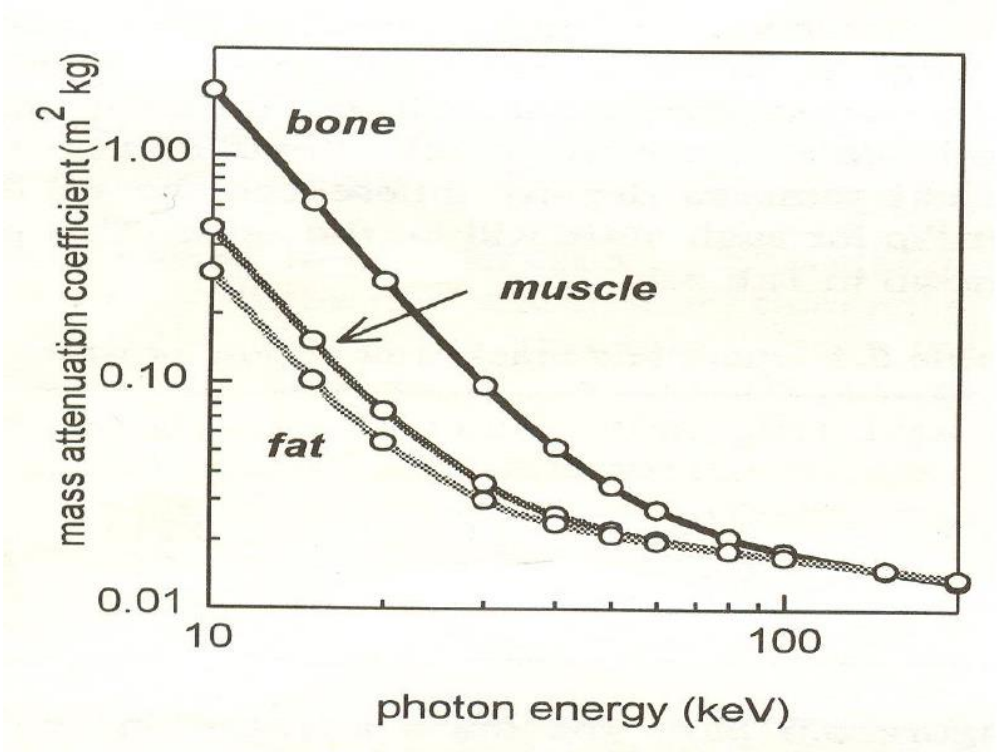

Figure 2. 4: The mass attenuation coefficients matching fat, muscle, and bone (Dowsett *et al.*, 1998).

The density of a material has an impact on the mass attenuation coefficient which is visualised above in Fig. 2.4. The mass attenuation coefficient for a specific material is a sum of the individual interaction probabilities given by (Seibert, 2005).

$$\frac{\mu}{\rho} = \frac{\tau}{\rho} + \frac{\sigma_{coh}}{\rho} + \frac{\sigma_c}{\rho} + \frac{\kappa}{\rho} \quad \text{..... (2. 8)}$$

2.3.3 Mass energy transfer coefficient

El-Jaby (2009) defined the mass-energy transfer coefficient μ_{tr}/ρ as the product of the mass attenuation coefficient μ/ρ and the mean energy transfer fraction $\underline{f_{tr}}$. The total mean energy transfer faction $\underline{f_{tr}}$ is defined as the total mean energy transferred $\underline{E_{tr}}$ normalized to the incident photon energy $h\nu$. The mass transfer coefficient is expressed in units of cm^2/g and is given by

$$\frac{\mu_{tr}}{\rho} = \frac{\mu}{\rho}\underline{f_{tr}} = \frac{\mu}{\rho}\frac{\underline{E_{tr}}}{h\nu} \quad \text{..... (2. 9)}$$

2.3.4 Mass energy absorption coefficient

When electrons resulting from photoelectric and Compton scattering events travel through an absorber (Dowsett *et al*., 2006) their energies transferred to the secondary charged particles are lost in the absorber, mainly through Bremsstrahlung. The mass-energy absorption coefficient is computed as:

$$\frac{\mu_{en}}{\rho} = (1-g)^{\frac{\mu_{tr}}{\rho}} \quad \text{..... (2. 10)}$$

Where *g* is the average fraction of kinetic energy of secondary electrons produced by the photoelectric effect and Compton scattering, later lost due to Bremsstrahlung taken as zero and equation 2.10 becomes (Dowsett *et al*., 2006 & Cunningham *et al*., 2019).

$$\frac{\mu_{en}}{\rho} = \frac{\mu_{tr}}{\rho} \quad \text{..... (2. 11)}$$

CHAPTER 3: LITERATURE REVIEW

This section provides a brief overview of the prostate radiation therapy treatment including (1) the basic physics of CT images with prosthesis present, (2) artifact reduction methods, (3) the treatment process of prostate cancer patients who have had hip prostheses inserted (4) external beam treatment techniques, (5) the Monte Carlo techniques used for electron and photon transport and (6) phantom design in the literature.

3.1 Radiation therapy prostate cancer treatment

Radiation therapy uses high-energy beams of ionizing radiation to treat cancer. Prostate cancer is the cancer of the prostate gland. Prostate cancer is usually rare before the age of 40 and develops mostly in older men who may have osteoarthritis (Rama, 2014). Advances in orthopaedic surgery have resulted in a significant number of patients receiving metal implants (Giantsound *et al*., 2017) or hip replacements. Hip replacement is a surgical procedure in which the hip joints are replaced by a prosthesis (Prabhakar *et al*., 2013). The benefit of the hip replacement to the patient is the ability to move and walk without pain. External beam radiation therapy (EBRT) is the main modality in treating prostate cancer, either alone or in combination with surgery, brachytherapy or chemotherapy (Al-Mohammed, 2011).

External radiotherapy treatment for prostate cancer treatment planning comprises an immobilization device to hold the patient still in a comfortable position, computed tomography planning scans, MRI scans for accurate volume rendering, CT/MRI image fusion, volume delineation (Tumour volume and organ at risks), 3DCRT and VMAT/IMRT treatment planning which includes optimization, patient-specific quality assurance, verification images and delivery of dose to the patient (Chandarana *et al*., 2018).

3.2 Patient immobilization and positioning

Pelvic immobilization for daily setup accuracy is a vital step in minimizing treatment set-up errors during prostate radiotherapy (Pang *et al*., 2017). Immobilization devices play a crucial role in maintaining a reproducible position for planning CT scans and treatment delivery sessions (Inui *et al*.,2018). Conformal radiotherapy, IMRT, VMAT and hypo fractionated prostate stereotactic body radiotherapy (SBRT) treatment requires treatment set-up errors to be minimized because of the small target margin added to the clinical tumour volume (CTV) (White *et al*., 2014).

Many studies have emphasised the importance of using immobilization devices to minimize set-up errors which may affect the clinical outcome. A prostate cancer patient is positioned supine or prone position. The supine position is commonly used by most elderly men (Li *et al*., 2021). Different immobilization devices are available worldwide. Immobilization devices like casts, knee and feet rests and vacuum are used for pelvic cancer treatment.

3.3 Computed tomography simulation

A computed tomography (CT) scanner uses computers and rotating X-ray machines to create cross-sectional images of the body. CT scans are used in radiation therapy treatment planning to determine clinical and physical information (Thomas, 1999). CT images are utilized as fundamental input data for most radiotherapy treatment planning systems (TPS) (Ogata *et al*., 2013). CT images are also used to calculate the absorbed dose to heterogeneous tissue during radiation treatment planning (Ogata *et al*., 2013 and Ziemann *et al*., 2018).

Accurate planning requires the correct reconstruction of Hounsfield units (HU) and the corresponding tissue electron or mass density values (Ziemann *et al*., 2018). In a TPS, a CT image data set is converted from Hounsfield units (HU) to the corresponding electron density values using a calibrated CT relative electron density (RED) curve. However, imaging prostate cancer patients with high-density hip prostheses is challenging due to image artifacts and distortions created on the CT

images. These artifacts lead to inaccurate reconstructed Hounsfield units in CT data sets (Ziemann *et al*., 2018) and hinder the ability to delineate the tumour and organ at risk.

3.3.1 Electron density and Hounsfield units

In radiotherapy, CT attenuation values are expressed according to a linear density scale as Hounsfield units (HU) and must be converted to electron density values for radiation dose calculation by a TPS for cancer treatment.

For accurate dose calculations, the correct relationship between HU and electron density is essential (Mohmoudi *et al*., 2016). The HU in each voxel of a CT image requires calibration in terms of mass density (ρ) and effective atomic number (Z_{eff}) to define the tissue type (Trujillo-Bastidas *et al*., 2016). The HU depends on many factors such as photon energy spectrum, detector sensitivity, the geometrical configuration of the phantom system and the reconstruction algorithm (Mohmoudi *et al*., 2016).

The data from the CT scan is used as input for the radiation therapy treatment planning system. The treatment planning system (TPS) takes into account the effect of inhomogeneity in dose calculations (Mahur *et al*., 2017). The CT software measures the attenuation coefficient of an object and converts the value assigned to each voxel into a CT number expressed in HU (Rhee *et al*., 2019). An HU from a CT image provides information on the attenuation characteristic of the X-ray beam in a particular volume element in a patient body relative to that of water at a specific kVp (Mahur *et al*., 2017). The absorbed dose to a patient in radiation therapy is calculated using the electron density of each voxel in the patient's CT data set (Rhee *et al*., 2019).

HU is defined as:

$$HU = 1000\left(\frac{\mu-\mu_w}{\mu_w}\right) \quad \text{..... (3.1)}$$

Where μ is the attenuation coefficient and μ_w is the attenuation coefficient of water (Rhee *et al*., 2019). The Hounsfield scale represents the relative density of body

tissues according to a calibrated grey-level scale, based on values for air (−1000 HU), water (0 HU), and bone density (+1000 HU) (Silva *et al*., 2012). It is recommended that the relationship between the electron density and HU be measured for each CT scanner used for treatment planning (Thomas, 1999).

However, the CT number to electron density conversion factor may not account for the high-Z inhomogeneity and the electron density of the prosthesis may not be determined accurately by the treatment planning algorithms (Reft *et al*., 2003).

3.3.2 Image artifacts

An artifact is an error or distortion in an image that is unrelated to the subject being imaged. The term artifact is also applied to any systematic discrepancy between the reconstructed image and the true attenuation coefficients of the object (Veikutis *et al*., 2015). Artifacts are a common phenomenon in X-ray CT (Boos *et al*., 2017). In CT, the attenuation coefficients of high-density materials are much higher than those of soft tissues. Because the X-ray beam is highly attenuated by metals an insufficient number of photons reaches the detector resulting in corrupted projection data (Yu *et al.*, 2007).

The image artifacts created by high-density metal implants or prostheses in the field of view of a CT scanner are due to four main factors, namely: beam hardening, scatter, noise (Giantsound *et al*., 2017) and photon starvation (Ali, 2018).

3.3.2.1 Beam hardening and scatter

Beam hardening occurs because low energy photons are attenuated to a greater degree than high energy photons when passing through high atomic number (Z) scanned objects (Ali, 2018 & Anderson *et al*., 2015). This leads to an increase in the mean energy of the photon spectrum overall and induces typical beam hardening artifacts (Boas *et al*., 2012). Two common artifacts resulting from these effects are: (1) Cupping artifacts originating when X-rays passing through the central thicker

portion of the scanned objects are "hardened" compared to those passing through the thinner edges. This physical effect results in a characteristic cupped shape (Veikutis *et al*., 2015).

Streak artifacts occur when the beam passes through a high Z object at a certain tube position and is “hardened less” than when it passes through two or more objects at another tube position (Veikutis *et al*., 2015). The combination of beam hardening and added scattered radiation creates streaks in the image along the axis of greatest attenuation, while the metal shows up as white (Giantsoundi *et al*., 2017).

Current CT scanners include a series of correction steps (discussed in section 3.3.3) for beam hardening, scattered radiation, and noisy measurements. However, these correction steps are usually based on simple physics models which do not account for cases of extreme density inhomogeneity (Giantsoundi *et al*., 2017).

3.3.2.2 Noise

Poisson noise is caused by statistical errors of low photon counts which result in random, thin, bright, and dark streaks that appear in the direction of greatest attenuation. Because of increased noise, notable contrast objects such as bone may still be visible but low contrast soft-tissue boundaries may be obscured. Poisson noise can be decreased by increasing the mAs (Boas *et al*., 2012).

3.3.2.3 Photon starvation

Photon starvation artifacts are caused when photons transverse a high-attenuation coefficient material (Giantsound *et al*., 2017 and Anderson *et al*., 2015). An insufficient number of photons reaches the detectors resulting in noisy projections (Anderson *et al*., 2015).

These factors degrade the capabilities of CT images to provide correct information about the HU and electron density of structures (Giantsound *et al*., 2017).

3.3.3 Artifact reduction

Several methods have been proposed for the reduction of metal artifacts in CT images: Filter back projection (FBP) is the standard reconstruction method for most scanners. The projection data are filtered to sharpen edges, and the filtered data are then back-projected (Boas *et al*., 2012).

(1) FBP is an analytic reconstruction algorithm (Rim *et al*., 2018) that assumes accurate projection data and ignores the fact that low photon counts result in a large Poisson error (Boas *et al*., 2012). The application of FBP in the presence of sharp gradients in sonogram data is one of the sources causing the metal artifact (Rim *et al*., 2018). FBP reduces radiation dose to the patient, but the noise and image quality become poorer (Boas *et al*., 2012).

(2) In some cases where projection through metals generates corrupted data (metal trace) (Liugang, 2016), the Sinogram correction can be applied. A sinogram is a collection of all line attenuation measurements acquired for an image (Gjesteby *et al*., 2016). The surrogate data is estimated by performing interpolation in the sinogram space or by forward projection (Liugang, 2016).

Interpolation-based methods are also used to correct the corrupted projection data by using the uncorrupted data on both sides of the metal trace. The surrogate data and the surrounding original uncorrupted data are not continuous. This results in the structure information of the metal trace being lost. However, reducing metal artifacts using this method introduces new artifacts and can increase the obscurity of normal tissue structures (Liugang, 2016).

Iterative reconstruction is also one of the artifact reduction methods used to lower image noise and ultimately to reduce exposure to radiation for patients. Metal artifacts reduction (MAR) algorithms compensate for photon starvation caused by attenuating material in the X-ray path. This cannot be achieved with filter back projection (Blum *et al*., 2016). However, most MAR algorithms require faster computer chips (Boas *et al*., 2012).

Ali, (2018) indicated that increasing the tube peak voltage can also be used to reduce metal artifacts but this solution is insufficient in terms of image quality for

diagnosis. Increasing the tube peak voltage reduces the metallic artifact to a minor degree but may not improve the scatter caused by imaging hip prostheses. Increasing the tube current also increases the radiation dose to the patient (Anderson *et al*., 2015).

Dual-energy CT reduces metal artifacts by making use of the different absorption spectra of metal and tissue in extrapolated monoenergetic images. This method has shown value in osteosynthetic material, such as spinal fusion implants. However, this is associated with artifacts less metallic in origin than a thick and dense metallic hip prosthesis (Morsbach *et al*., 2013).

One advantage of Dual-energy CT is the reduction in beam-hardening effects by scanning at different energies. However, this method does not correct scatter, which matters in many scans especially when the metal absorbs nearly all photons (Boas *et al*., 2012).

Several CT vendors use different terminology to explain the metal artifacts reduction (MAR) algorithms in their reconstruction software such as:

Metal Artifact Reduction in Image Space (MARIS^{TM}) (Siemens Healthcare GmbH, Erlangen, Germany) was introduced to improve image quality for radiation therapy planning (Boos, 2017). Single Energy Metal Artifact Reduction (SEMAR^{TM}) (Canon/Toshiba) is the raw data-based technique utilizing the gradient correction features of iterative reconstruction. The original raw projection data undergoes filtered back-projection to generate an image series. The metal is segmented from this image to generate a metal-only-image. The metal-only image is forward projected to identify the metal trace (Zhang *et al*., 2018).

Metal artifact reduction for orthopedic implants (O-MAR) (Philips Healthcare, Cleveland, Oh, USA) is an iterative projection modification method optimized for imaging orthopedic devices. The CT data set acquired with the scanner is used as an input into an iterative loop, where the output is a correction image that is subtracted from the input image. O-MAR uses segmentation and replaces data points identified as metal with interpolated values (Anderson *et al*., 2015).

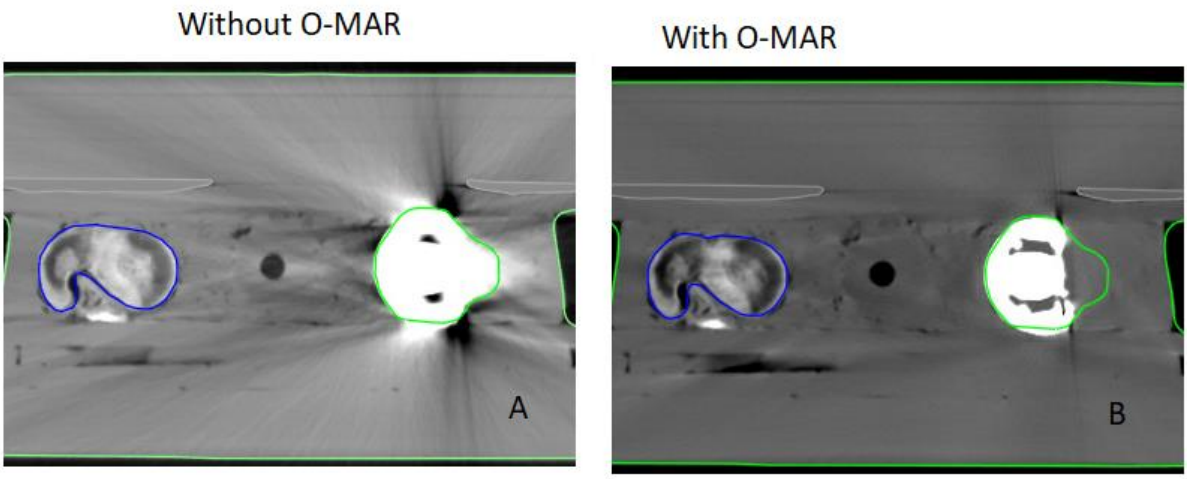

Figure 3. 1: Coronal images (A) without O-MAR applied showing bright and blackness artifact from prosthesis obscuring soft tissue detail and (B) with O-MAR applied (Eclipse treatment planning system (Varian Medical Systems, Palo Alto, CA)).

Figure 3.1 (A) shows a CT scan without artifact reduction with the dark and bright streaking artifact degrading the image quality. Because streak artifact alters the CT Hounsfield unit, it has an impact on the precision of dose calculation in a treatment planning system, (B) showing the CT scan reconstructed with O-MAR (Philips) with streaking artifact improvement. However, there is a concern that MAR may not provide accurate attenuation values near the high-density material and may hinder the ability to detect lesions by smoothing interfaces in an attempt to reduce noise as shown in Fig.3.1 (B). (Rim *et al*., 2018).

Metal implants that saturate the CT number scale may require dosimetrist and physicist involvement to correct. This can be done by contouring the high-density metal and scatter artifacts, and manually assigning a CT number to those regions corresponding to the desired relative electron density (RED) as shown in Fig 3.2 below.

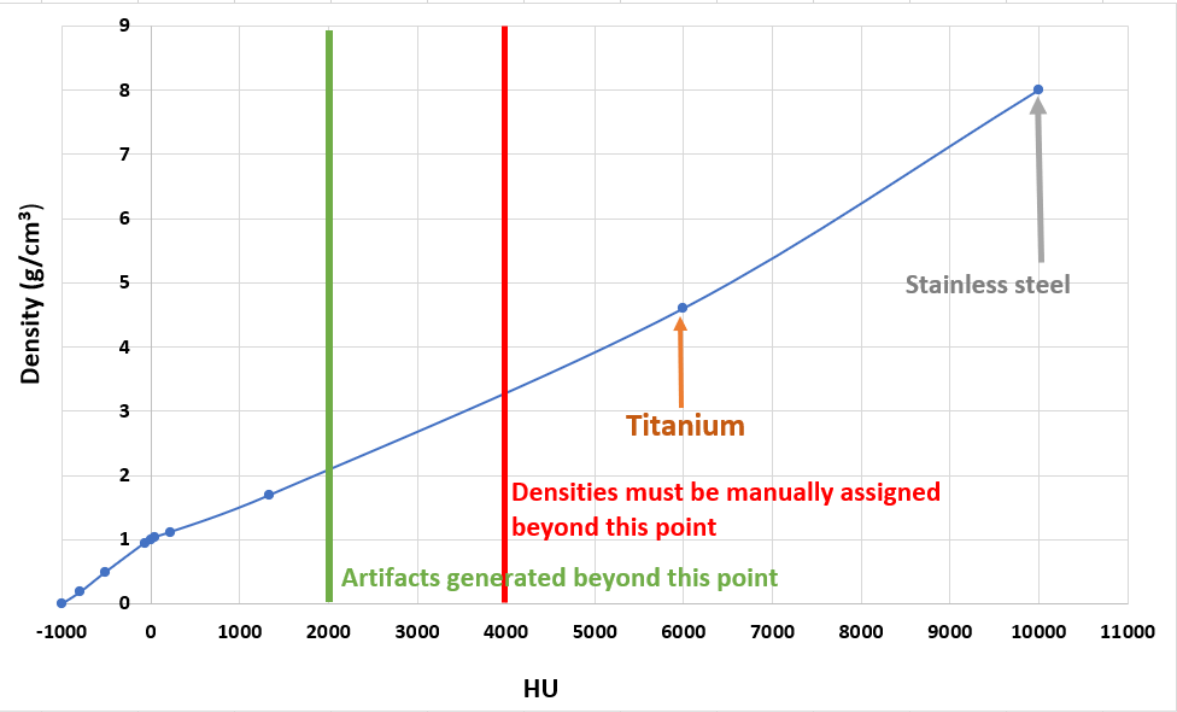

Figure 3. 2: CT number to electron density calibration curve (Sutherland, 2019).

3.4 Definitions of volumes and delineation

The volumes related to tumours and organs at risk have to be outlined for treatment planning and reporting processes. Delineation of these volumes is an essential step in the planning process (ICRU 83, 2010 & Hussain *et al*., 2017) because the absorbed dose cannot be prescribed, recorded, and reported without specification of these volumes (ICRU 83, 2010). According to ICRU 83 (2010), organs at risk are tissues that, if irradiated, could suffer significant toxicity. The bladder, rectum, femoral heads, and penile bulb are considered the organs at risk during prostate cancer treatment.

The volumes for treatment planning and dose reporting are defined as follows: The gross tumour volume (GTV) is the visible extent and location of the primary tumour. The clinical target volume (CTV) contains the GTV and any tissue with subclinical cancer involvement (Zaorsky *et al*., 2016). The internal target volume (ITV) is defined as the CTV plus a margin considering uncertainties in size, shape, and position of the CTV within the patient (ICRU 83, 2010).

The planning target volume (PTV) encompasses the CTV plus an additional margin to account for patient movement, setup error, and organ movement (Zaorsky *et al*., 2016 and Mostafaei *et al*., 2020). Set-up errors increase the chance of under dosing the tumour volume and unnecessary irradiation of organs at risk (White *et al*., 2014).

The entire prostate gland is regarded as GTV and CTV may include the entire prostate gland, seminal vesicles and the pelvic lymph nodes as shown in Fig.3.3 below.

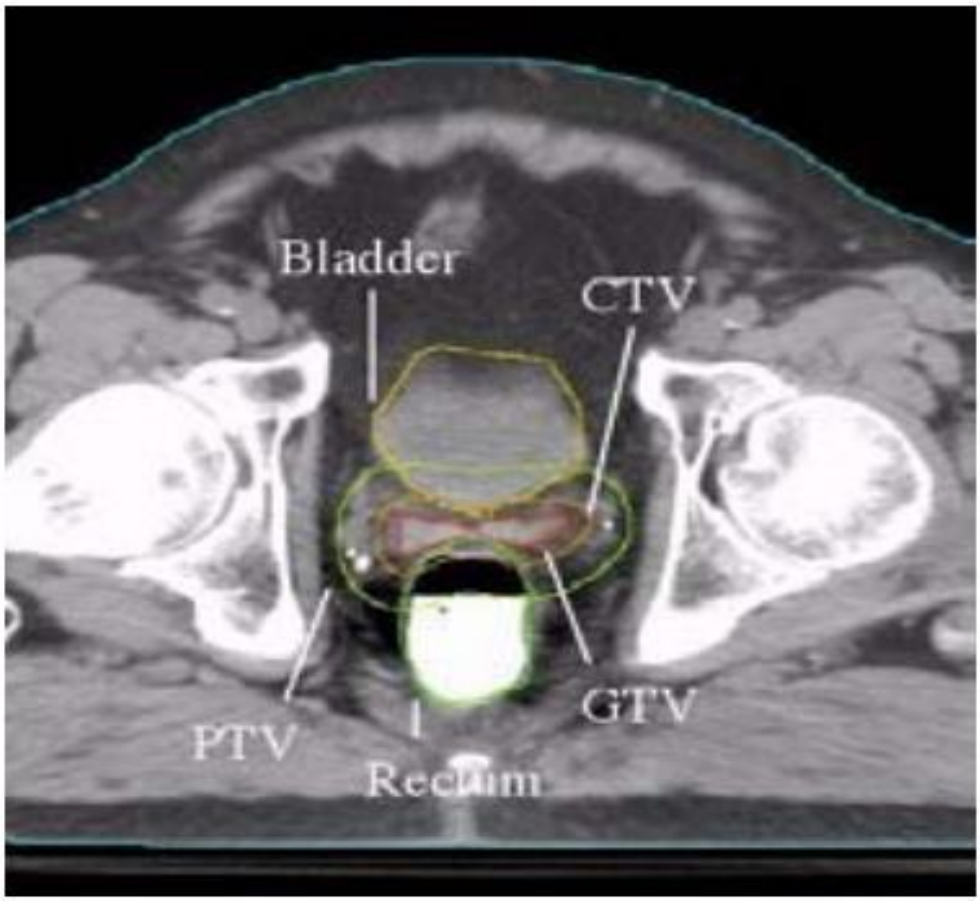

Figure 3. 3: GTV, CTV, PTV and organs at risk (bladder and rectum) contours for a prostate treatment plan (Parker *et al*., 2012).

3.4.1 CT-MRI image fusion

Delineation of prostate tumour volume and the organs at risk are challenging due to artifacts and distortion created in a CT image due to high density hip prosthesis. Magnetic resonance imaging (MRI) and CT are increasingly used for prostate cancer

diagnosis and accurate staging (Daryanani *et al*., 2021). MRI localized prostate cancer due to its advantage of excellent soft tissue contrast compared to CT scanning. MRI can also be used to determine whether the cancer has spread which aids in the delineation of both the tumour and OARs (Chandarana *et al*., 2020 and Schmidt *et al*., 2015).

To construct an image with MRI, radiofrequency pulses are used to detect proton orientation, density, and diffusion in the tissue and massive magnets to align hydrogen atoms (Daryanani *et al*., 2022). An axial MRI image is superimposed on a CT image utilising a registration feature on a treatment planning system's software to perform CT-MRI fusing. The CT-MRI image fusion is visually examined, and if an ideal superposition of anatomical landmarks is identified in every direction, it is approved. On top of each scan's axial CT and MRI slices, contours of the are drawn. MRI scans are employed for precise volume rendering, while CT images continue to serve as the reference scan.

3.5 Photon beam radiation therapy treatment techniques

External beam radiotherapy (EBRT) for prostate cancer with photon-based radiation techniques has advanced from 2-dimensional (2D) planning using X-ray fields based on landmarks (Fischer-Valuck *et al*., 2018) to 3-dimensional conformal radiation therapy (3DCRT), Intensity-Modulated Radiotherapy (IMRT) and Volumetric Modulated Arc Therapy (VMAT) (Duffy *et al*., 2018).

3.5.1 Three-dimensional conformal radiation therapy (3DCRT)

Three-dimensional conformal radiotherapy (3DCRT) consists of EBRT delivery using forward-planned static fields with customized treatment planning and aperture design (Zaorsky *et al*., 2017). It uses CT-based planning and sophisticated software to integrate volumetric data regarding the patient’s tumor and organs at risk (Fischer-Valuck *et al*., 2018). Identification of the target in 3-dimensions by CT technology

introduced two important improvements. Firstly, the ability to conform the beam shape to match that of the target volume whilst avoiding organs at risk. Secondly, the use of the beam's eye view (BEV) to assess the beam shape. However, obtaining an acceptable dose distribution often remains a challenge with part of the rectum and bladder receiving unacceptably high doses with prostate cancer treatment (Fischer-Valuck *et al*., 2018).

Prostate cancer radiotherapy prescription ranges from 45 to 74 Gy (1.8 to 2.0 Gy per fraction). 3D conformal radiotherapy treatment for localised disease and lymph nodes metastatic are treated as follows: (1) a four-field box is used to treat the entire pelvis including the prostate to 45-46 Gy in 1.8 -2 Gy per fraction. The four-field box shields the portion of the rectum and bladder in the lateral field sparing these organs at risk from high-radiation dose. (2) Six-field techniques which include oblique fields typically utilize parallel opposed anterior and posterior oblique fields angled 45° from the lateral fields. An addition of 25-28 Gy is given using these techniques to make the total dose of 70-74 to the prostate. Table 3.1 shows the fractionation schemes commonly used for external beam radiation for prostate cancer.

Table 3. 1: Prostate fractionation schemes (Radiation Therapy Oncology Group (RTOG-0938 and RTOG 0126))

Conventional fractionation	
2 Gy x 25 fractions (50 Gy)	Prostate plus seminal vesicles
1.8 Gy x 25 fractions (45 Gy)	Post brachytherapy
1.8 Gy x 40 fractions (72 Gy)	No brachytherapy
2G y x 37 fractions (74 Gy)	No brachytherapy
Hypofractionation	
10 Gy x 5 fractions (50 Gy) 7.25 Gy x 5 fractions (36.25 Gy) 10 Gy x 5 fractions (50 Gy) [a]	Stereotactic treatment

[a]Boike et al., 2020.

Table 3.2 shows the organ at risk constraint for a standard fractionation, and stereotactic prostate treatment. It is taken from the Quantitative Analyses of Normal

Tissue Effects in the Clinic (QUANTEC) group. The dose tolerance for organ at risk differs from stereotactic treatment because some organs cannot tolerate a single high dose.

Table 3. 2: Organ at risk dose constraint for standard fractionation from QUANTEC.

Organ at risk	**Dose limit (Gy)/volume parameter for standard fractionation**	**Dose limit (Gy)/volume parameter for stereotactic fractionation**
Rectum	V50 < 50%	V30<3.5%
	V60 < 35%	V23<20%
	V65 < 25%	
	V70 < 20%	
	V75 < 15%	
Bladder	V50 < 50%	V12<15%
	V65 ≤ 50%	
	V70 ≤ 35%	
	V75 ≤ 25%	
	V80 ≤ 15%	
Femoral heads	V50< 10%	V15<10%

3.5.2 Intensity-Modulated Radiotherapy (IMRT)

Intensity Modulated Radiotherapy (IMRT) involves dose delivery in which the fluence distribution in the plane perpendicular to the incident beam is modulated (Khan *et al*., 2016) by dividing each beam into segments. IMRT has two types of treatment delivery modes: step-and-shoot mode delivery and sliding window/dynamic mode delivery that delivers doses from a different beam angle (Herman *et al*., 2013).

In step-and-shoot IMRT, the fluence map is sequenced into a set of segments for each treatment angle. Each segment is irradiated individually, that is, the multileaf collimator (MLC) leaves move to the desired position (Khan *et al.*, 2016) and delivers the beam when the leaves are stationary (Herman *et al*., 2013). In the sliding window/dynamic mode of IMRT, beam delivery is maintained while the MLC leaves move across the treatment aperture.

The IMRT treatment planning method is inverse, performed by a treatment planning computer, resulting in radiation fields with numerous small field segments (Winkler *et al*., 2005). IMRT uses the dose deposition matrix concept. For dose calculation, the patient is discretized into small volume elements referred to as voxels. A dose calculation algorithm is used to calculate the dose distribution of every beamlet in the fluence map of the patient. Assuming the dose that beamlet *j* contributes to voxel *i* in the patient as D_{ij} and denote the intensity of beamlet *j* as x_i

The total dose d_i delivered to voxel *i* will be given by the superposition of all beamlet contributions:

$$d_i = \sum_i D_{ij} x_i \quad \text{..... (3.2)}$$

The matrix of dose contributions D_{ij} of beamlets *j* to voxel *i* is referred to as the dose-deposition matrix (Khan *et al*., 2016). The dose-deposition matrix concept is convenient since it allows the separation of the mathematical optimization of beamlet intensities x_i from the dose calculation algorithms.

The IMRT treatment planning process requires defining dose constraints during optimization for the PTV (prostate) and organ at risk (rectum, bladder, and femoral heads). The minimum and maximum dose to cover a PTV needs to be defined during the optimization process. IMRT prescription for prostate cancer is the same as the one mentioned in section 3.5.1.

3.5.3 Volumetric Modulated Arc Therapy (VMAT)

Volumetric Modulated Arc Therapy (VMAT) (sometimes called arc therapy) is an extension of IMRT static field therapy to a rotational therapy treatment mode, delivered using linear accelerators equipped with a multi-leaf collimator (MLC) (Khan *et al*., 2016). During VMAT delivery, field shapes, dose rate, and gantry rotation speed vary simultaneously. These additional degrees of freedom increase the capability for the beam's intensity-modulation (Macchia *et al*., 2017). VMAT treatment is delivered using fewer monitor units than traditional IMRT (Bailey *et al*., 2012). The complex features of its beam delivery system demand stricter quality

assurance (QA) than required for conventional fixed gantry IMRT (Rahman *et al*., 2019).

VMAT is the preferred treatment technique for prostate cancer and has shown better conformity, homogeneity, and more sparing of organs at risk (OAR) compared to the IMRT technique (D *et al*., 2021 and Quan *et al*., 2012). One or two full arcs are utilized for prostate cancer radiotherapy treatment planning. The collimator rotation of greater than 5 ° is recommended to minimize the leaf leakage, tongue, and groove effect (Sandrini *et al.*, 2018). The goal of radiotherapy planning is to achieve uniform dose distribution inside the PTV. However, it is challenging to achieve a uniform dose when the patient has hip prosthesis.

To overcome this challenge, Task Group 63 and Prabhakar *et al.,* (2013) recommend the beam arrangements that avoid dose going through the hip prosthesis. Many studies created VMATs plans with skip arcs or avoidance sectors or structures to block radiation from entering through the prosthesis during treatment. Prabhakar *et al*., (2013) created a structure around the prosthesis with 1 cm margin. During optimization, the planning objectives were set to 0 % of the structure volume should not receive more than 50 Gy to avoid the beam passing through to the prosthesis.

The Varian treatment planning system has an avoidance sector that can be utilized to avoid entrance or exit doses into the prosthesis. This allows the use of full arcs, and the beam switches off (zero radiation) when passing through the avoided structure.

D *et al*., (2021) investigate VMATs planning for bilateral hip prostheses prostate patients while avoiding the entrance dose to the prostheses. In their study, they used 3 different VMAT planning techniques: (1) two full arcs with the prosthesis maximum dose criteria set to 50 Gy, (2) two full arcs with 10 % of the prosthesis not receiving a maximum dose of 50 Gy, and (3) PA avoiding prostheses. The dose constraint was similar to that used by Prabhakar *et al*., (2013). They found that the PA technique that limits the entrance dose through each prosthesis to ensure that the AAPM TG-63 recommendations are met, displays the most unacceptable dosimetric and delivery results.

3.5.4 Image-guided Radiotherapy (IGRT)

Image-guided radiotherapy (IGRT) is a new form of radiation therapy using X-ray imaging equipment mounted on a linear accelerator for the determination of tumour location and proper focusing of the radiation beam to the tumour (Arabloo *et al.*, 2016). The process of imaging is performed daily during a course of highly conformal radiation therapy (Nabavizadeh *et al*., 2015). This allows the daily adjustment of patient setup and positional corrections during treatment delivery (Dang *et al.*, 2018) to improve the target treatment accuracy (Nabavizadeh *et al*., 2015). However, the frequency of IGRT depends on the anatomical site being treated. kV/kV orthogonal imaging system (integrated kV/kV system) and Cone-Beam-Computed tomography (CBCT) are commonly used for IGRT verification (IAEA Human Health Reports 16, 2019).

Wang *et al.,* (2023), has reported that the PTV margins of prostate cancer can be reduced from 15 mm to 7 mm with weekly IGRT and daily IGRT may further reduce the margins to 5 mm, which results in approximately 20 mm^3 PTV reduction. A tighter PTV provided an opportunity for high prescription dose escalation (75.6 Gy to 79.8 Gy). For a radiotherapy department with a heavy workload, IGRT might be a challenge because of increased treatment delivery time.

3.5.5 Stereotactic body radiation therapy

Stereotactic Body Radiation Therapy (SBRT) is a type of radiation therapy that uses a stereotactic equipment and narrow beams delivered through noncoplanar isocentric arcs to treat lesions to control early-stage primary and metastatic cancers (Khan, 2010). SBRT, unlike conventional radiation treatment, delivers large doses in a few fractions at locations throughout the abdominopelvic and thoracic cavities, and at spinal and paraspinal sites. This results in a high biologically effective dose (BED) (Benedict *et al*.,2010). SBRT radiotherapy techniques allow the prostate to receive higher doses in a few fractions using tighter margins. A typical prostate prescription is 5 Gy in 10 fractions (50 Gy).

3.6 Treatment planning system (TPS)

Computerized treatment planning systems (TPSs) are used in EBRT to generate beam shapes and dose distributions with the intent to maximize tumour control and minimize normal tissue complications (Podgosak, 2005). The entire process includes the following essential activities: structure contouring or delineation, the determination of the cancer volume, the amount of dose to be delivered (dose prescription), dose calculation and treatment delivery and evaluation. (Maulana *et al*., 2016 & Yani *et al*., 2016).

The human body consists of a variety of tissues with different physical and material properties (such as water and bones) and the density of each tissue is varied. Each tissue has different radiation dosimetry characteristics (Yani *et al*., 2016). An accurate dose calculation by the treatment planning system is only possible when accurate data are obtained from the patient via CT imaging. These data include the body contour, shape and density of the internal organs and the location and spread of the tumour volume. The dose calculation is performed on the CT image data set of the patient. Which is imported into the treatment planning system as the input data in the treatment process (Mohmoudi *et al*., 2016).

CT images which contain a hip prosthesis and are used in radiotherapy treatment planning introduce inaccuracies in dose calculation because of metal artifacts (Anderson *et al*., 2015). The dose distribution in the target volume depends upon the location of the prosthesis relative to the planning target volume (PTV), the size, shape and material of the prostheses and the beam energy (Reft *et al*., 2003). The TPS may not predict doses accurately at this tissue-metallic interface (Ng *et al*., 2015) and this may compromise tumour local control.

3.6.1 Hip prosthesis.

Hip prostheses have three parts: a femoral head or ball-like component, a hip stem component, and an acetabular component. Between the acetabular cup and the femoral head there is a polymer-based bearing insert made of high density or similar

material. The bearing is affixed between the cup and the femoral head for smooth articulation (Derar *et al*., 2015). Figure 3.4 shows the individual components of a titanium hip replacement, and how they merge and ultimately are implanted.

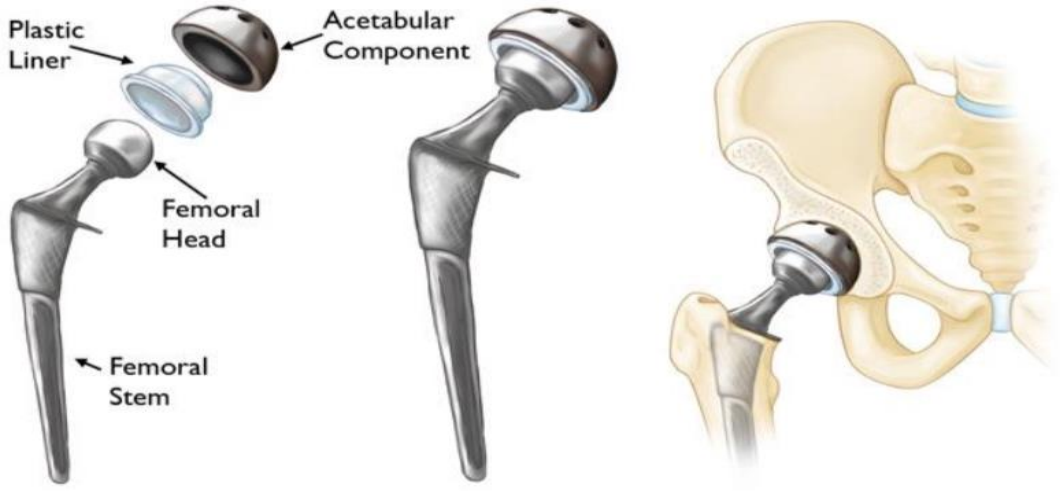

Figure 3. 4: Illustrates (Left) the individual components of a total hip replacement. (Center) The components merged into an implant. (Right) The implant as it fits into the hip (Faron *et al.*, 2015).

Hip prostheses are made from high atomic number (Z) materials such as cobalt-chrome-molybdenum (Co-Cr-Mo), stainless steel or titanium (Mohammadi *et al*., 2019 & Keall *et al*., 2003). Cobalt-chrome-molybdenum (Co-Cr-Mo), stainless steel has a higher density than titanium. Some patients have a femoral head and stem implant only whilst others have all three parts. The head consists of a polyethylene core with a metal shell of titanium alloy, steel, or cobalt-chromium-molybdenum (Co-Cr-Mo). The stem is also made from titanium alloy, steel, or Co-Cr-Mo (Reft *et al.*, 2003). Prostheses vary in size and may have solid or hollow femoral heads. Hollow prostheses tend to be larger (Keall *et al*., 2003).

3.6.2 Dose uncertainty due to high-density material

The presence of high-density implants in CT imaging causes image artifacts (Giantsoundi *et al*., 2016). Hip prostheses cause streak artifacts due to aliasing (Keall *et al*., 2003). CT data is lost in the region of the streak artifact.

Metal streak artifacts are extremely common in CT images and are caused by multiple mechanisms, some of which are related to the metal edges. Artifact intensity depends on the type of metal used (Blum *et al*., 2016). Metal artifacts are more pronounced with high atomic number metals, such as iron or platinum or chromium-cobalt and less pronounced with low atomic number metals such as titanium (Boas *et al*., 2012). Because of these artifacts and the loss of CT data within them, it is impossible to determine the exact CT number of the prosthesis through conventional CT. This adversely affects the calculated dose distributions created by the treatment planning system (Gao *et al*., 2018).

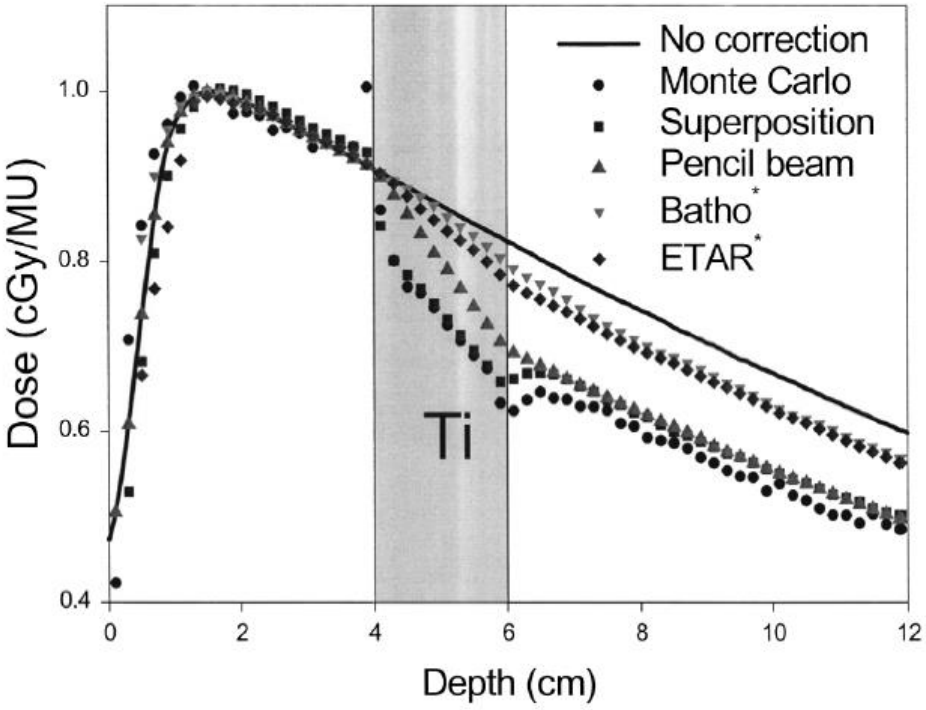

Figure 3. 5: Comparison of the percentage depth dose of Monte Carlo simulated with TPS calculated (Reft *et al*., 2003).

Figure 3.5 shows the percentage depth dose of Monte Carlo calculated compared with superposition, pencil beam, Batho, and ETAR calculation algorithms for a 6 MV photon beam. The calculations were performed on a water phantom containing a 2 x 2 x 2 cm^3 titanium implant. The Batho and the ETAR calculations were performed on a TPS which has an implant density upper limit of 3.0 g/cm^2 (Reft *et al*., 2003).

3.6.3 Dose attenuation effect of hip prostheses

The decrease in intensity of the beam of ionizing radiation at distances greater than the secondary electron range downstream from the inhomogeneity can be calculated with the knowledge of the density and the atomic number of the material and its linear (μ) or mass attenuation (μ/ρ) coefficients.

The primary fluence beyond the metallic implant is approximately given by

$$\psi = \psi_o e^{-\mu t} \quad \text{.....} \quad (3.3)$$

where ψ is the photon fluence after passing through the thickness t of high atomic material, ψ_o is the initial fluence and μ is the total composite linear attenuation coefficient including the interactions: photoelectric effect ($\boldsymbol{\tau}$), Compton ($\boldsymbol{\sigma}$) and pair production ($\boldsymbol{\kappa}$) averaged over the photon spectrum (Reft *et al*., 2003),

$$\mu = \boldsymbol{\tau} + \boldsymbol{\sigma} + \boldsymbol{\kappa} \quad \text{.....} \quad (3.4)$$

A higher atomic number material causes the photon spectrum to be attenuated more by photoelectric and pair production interactions and less by Compton interaction than an equivalent mass of water (Keall *et al*., 2003). Perturbations of absorbed dose distribution occur as a result of the increased attenuation of the radiation beam by the prosthetic device and the changes in electron scatter photon interactions (photoelectric effect and pair production) that occur at the bone-metal interface (Ade *et al*., 2017).

Reft *et al.*, (2003) published data as per Table 3.3 below on the transmission factor through hip prosthesis devices made of Co-Cr-Mo, Ti, and stainless steel for 4 MV and 10 MV photons. The transmission was measured in water with 0.1 cm^3 sealed ionization chambers and with the central axis of the beam passing through the approximate center of the solid stem of each prosthesis.

Table 3. 3: Transmission factors for 4 MV and 10 MV photon beams for stainless steel, Co-Cr-Mo and Ti prostheses (Reft *et al*., 2003).

Photon energy	**4 MV**				**10 MV**			
Field sizes (cm^2)	8 × 8		15 × 15		8 × 8		15 × 15	
Prosthesis/depth (cm)	10	15	10	15	10	15	10	15
Stainless steel	0.763	0.764	0.786	0.795	0.807	0.799	0.816	0.819
Co-Cr-Mo	0.657	0.672	0.708	0.714	0.735	0.736	0.748	0.749
Ti	0.861	0.855	0.869	0.876	0.887	0.879	0.891	0.894

The transmission increases with field size due to the increased photon scatter (which partially offsets the shielding effect of the prosthesis) and energy (Reft *et al*., 2003). Co-Cr-Mo alloy with a high relative electron density is likely to have a greater impact on the dose distribution than steel and titanium which have lower densities. The densities of prostheses are shown in Table 3.4 below (Sutherland, 2019). The attenuation effect of prostheses is density-dependent (Ade *et al*., 2017).

Table 3. 4: Showing the density, effective atomic number and electron density of different prosthesis materials (Sutherland, 2019).

Material	**Density (g/cm^3)**	**Effective atomic number**	**Electron density**
Stainless steel	8.10	26.70	6.80
Co-Cr-Mo	7.90	27.60	6.70
Titanium	4.50	21.40	3.60
Ceramic (Al_2O_3)	3.97	≈16.00	3.50
Muscle	≈1.00	≈7.40	3.30
Bone	≈1.60	≈12.50	3.00

Materials with a density greater than titanium saturate CT numbers and thus are indistinguishable from each other on the image (Rijken *et al*., 2017). The high atomic number and high density of metallic prostheses relative to water yield challenges in radiotherapy dose computation. When radiation passes through a prosthesis, the dose attenuation during pelvic irradiation could be of significance (Ade *et al*., 2017).

3.6.4 Dose calculation Algorithms

The limitation on the accuracy of the dose delivered to the patient in radiation therapy is determined by the accuracy of the treatment planning dose calculation algorithms (ICRU report 91, 2014). To meet the International Commission on Radiation Units (ICRU) criteria, dose calculation accuracy must be within 2–3% (Elcim *et al*., 2016).

Kernel-based algorithms such as pencil beam kernel, cone convolution, superposition and convolution-superposition algorithms used in clinics for daily treatment planning (Lloyd, 2011) can correct some inhomogeneity. However, these corrections are insufficient in the presence of very high-density materials such as steel or titanium alloy and underestimate the resulting dose perturbations. Dose calculations using these algorithms depend on the properties of the material contained in the planning image and the physical interactions that govern the transport of radiation through media (Lloyd, 2011).

3.6.4.1 Pencil beam kernel algorithms

The fastest Mega electron Voltage (MeV) dose calculation algorithm is the pencil beam algorithm in which a photon beam is divided into narrow pencil beams. The dose deposited under the patient's surface by a single pencil beam has a definite spatial distribution called a dose kernel. Pencil beam (PB) algorithms generate the dose distribution by integrating the pencil beam kernels to account for the changes in primary intensity and by modifying the shape of the pencil beam with depth and tissue density (Evans, 2012).

Inhomogeneity corrections in the pencil beam algorithm method take into account only the central axis along the beam path. This may result in unpredicted errors in dose calculation for tissues containing high or low-density heterogeneity (Elcim *et al*., 2016). The pencil beam algorithm uses only longitudinal scaling for the heterogeneities handled via effective path length (Knőős, 2008).

3.6.4.2 Cone convolution algorithms

Cone convolution algorithms reduce calculation time by using approximations in the physics of radiation transport (Kim *et al.*, 2020). In this algorithm, the description of primary photon interaction is separated from the transport of energy via scattered photons or charged particles produced through the process of the photoelectric effect, Compton scattering and pair production. Dose distribution is incorporated by the changes in scattering due to changes in the beam shape, beam intensity, patient geometry and tissue inhomogeneities (Evans, 2012).

A collapsed cone convolution algorithm is a volume-oriented algorithm involving a convolution technique among dose deposition kernels and the total energy released per unit mass as shown in Fig.3.6. It accounts for lateral energy transport and may deal with the effects of tissue heterogeneities in areas of perturbed electronic equilibrium such as tissue–air interfaces and tissue–bone interfaces (Elcim *et al*., 2016).

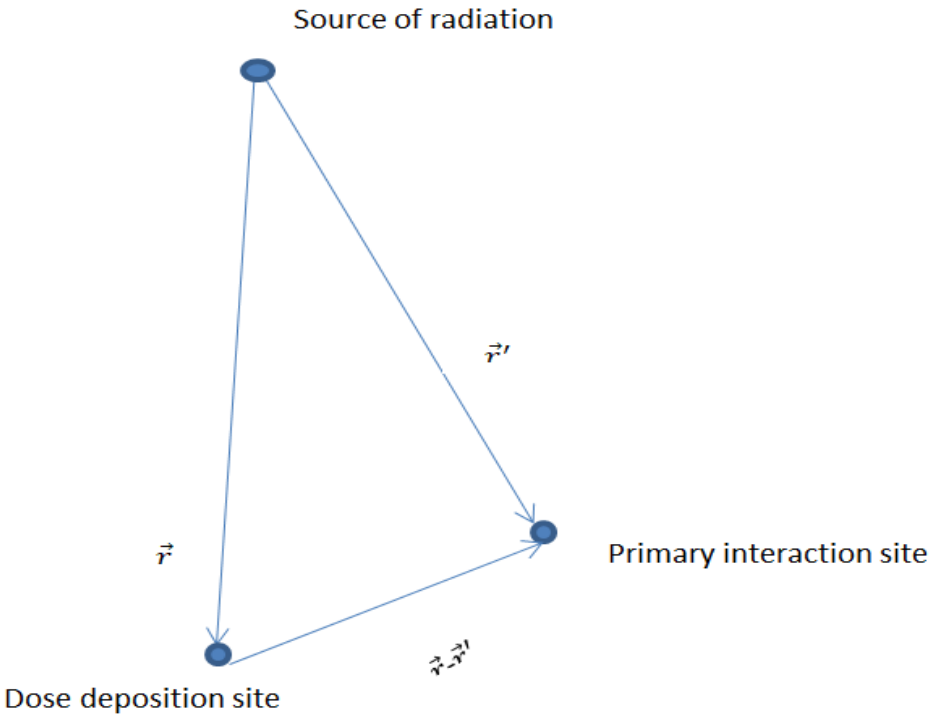

Figure 3. 6: Graphical representation of dose computation using convolution (Mackie, 2019).

The dose distribution is computed using the following convolution equation,

$$D\,(\vec{r}) = Z_{\rho}^{\mu}\,\psi\,(\vec{r}')\,A\,(\vec{r}-\vec{r}')dV \quad \text{..... (3.5)}$$

Where $Z_{\rho}^{\mu}\,\psi\,(\vec{r}')$ is the primary dose fluence and $A\,(\vec{r}-\vec{r}')dV$ is the kernel derived from Monte Carlo (Oelfke *et al*., 2019).

3.6.4.3 Convolution-superposition algorithms

When one considers a charged particle under equilibrium conditions, the total energy absorbed by the charged particle's position *r* is the same as the total energy which is scattered due to photon interactions at the same location. The primary dose D_p and the first scattered dose from a parallel beam of monoenergetic photons can be computed as:

$$D_P\,(r) = \big(K_C(r)\big)P \quad = \left(\frac{\mu_{en}}{\rho}\right)_p \psi_p(r)$$

$$= \left(\frac{\mu_{en}}{\rho}\right)_p \phi_p\,(r=0)\,hv\,p^{e^{-\mu r}} \quad \text{..... (3. 6)}$$

Where $\psi_p(r)$ and $\big(K_C(r)\big)P$ are the primary fluences and collision kerma respectively, at point *r* $\left(\frac{\mu_{en}}{\rho}\right)_p$ is the mass energy absorption coefficient, $\phi_p\,(r=0)$ is the primary photon fluence at the surface of the phantom, hv_{p} is the primary photon energy and μ is the attenuation coefficient of primary photons.

The total dose is the sum of the primary and scatter components.

$$D_{tot}\,(r) = D_p\,(r) + \int D_p\,(r')\frac{(\mu_{en})_{scat}}{(\mu_{en})_p}\frac{(hv)_{scat}}{(hv)_p}\frac{dP_{scat}\,(\theta,r')}{dV}\,e^{-\mu_{scat}\,(r'-r)}\,dV \quad \text{… (3. 7)}$$

Where $dP_{scat}\,(q, r')/dV$ is the probability per unit volume of a primary photon being scattered into a solid angle centered about angle *q* (Khan *et al*., 2016).

In heterogeneous media, the radiological path length is used in place of the actual length to account for the difference in electron density from that of water, and the convolution changes to convolution-superposition (Elcim *et al*., 2016). The two components, TERMA and dose kernels, are combined to achieve the accurate calculation of the absorbed dose. TERMA (T) is defined as the total energy per unit mass released by a radiation field interacting with a medium density *ρ* at a certain point $\vec{r}$

$$T\ (\vec{r}) = \frac{\mu}{\rho}\ (\vec{r})\ \psi(\vec{r}) \quad \text{..... (3. 8)}$$

Where ψ is the energy fluence of the primary photons determined by the absorption of the linear photon coefficient *μ(E)* at the interaction point of the primary photon $\vec{r}'$ given by

$$\psi(\vec{r}) = \Phi(\vec{r}, 0)\ E e^{-\mu E} \quad \text{..... (3. 9)}$$

where *Φ* is the initial fluence and *E* is the energy of the beam.

Convolution-superposition algorithms integrate the dose contributions at each point *r* by superimposing the dose distribution from all dose kernels *K (r, r, E)* of the defined energy spectrum originating from all primary interaction points $\vec{r}'$ as shown in Fig.2.18 and weighs their contribution concerning TERMA (Oelfke *et al*., 2019)

$$D(\vec{r}) = \int dE\ d^3\vec{r}'\ \ T\ (\vec{r}\ , E)\ K(\vec{r}, \vec{r}', E') \quad \text{..... (3.10)}$$

Most of these dose algorithms have been designed for lower densities and do not model accurately the absorption of the scattering properties of high-density metals or materials (Prabhakar *et al*., 2013). They have an upper limit for the electron density used for heterogeneity correction algorithms (Reft *et al*., 2003).

3.6.4.4 Monte Carlo Algorithms

The Monte Carlo (MC) methods are stochastic approaches to problem solving that involve the use of random numbers and probability statistics (Jabbari, 2011). A

longer discussion of it can be found below in section 3.9. It has long been predicted that clinical radiation treatment planning systems will incorporate Monte Carlo dose calculation methods. The amount of computation time needed for Monte Carlo Treatment Planning (MCTP) has prevented its early use in clinical settings (Spezi *et al*., 2008). Some commercial treatment planning systems have incorporated the Monte Carlo approach, which allows accurate dose calculation for radiotherapy treatment planning.

Traditional dose calculation techniques provide patient dose information in terms of dose to water with varying electron density; in contrast, the Monte Carlo approach computes the energy deposition in multiple media and expresses dose to medium (Ma, 2011).

3.7 Patient-specific dosimetry quality assurance

Pre-treatment patient-specific quality assurance in radiation therapy is used to verify patient dose (Pimthong *et al*., 2016) and also to check the mechanical issues of the treatment unit (linear accelerator) (Takahashi *et al*., 2014). The patient-specific pre-treatment quality assurance for complex treatments such as IMRT, VMAT, and SBRT is performed before the patient's treatment commences (Rahman *et al.*, 2019).

Radiation dose in IMRT and VMAT is modulated by MLCs. The patient's specific QA is required to ensure that the intensity map pattern matches with that created by the TPS and that the MUs specified by the TPS are delivered as intended (Utitsarn *et al*., 2011). Because of the large number of monitor units associated with the use of these modalities, attention needs to be focused on the risk to patients treated with these modalities (Teoh *et al*., 2011).

3.7.1 Dosimetric devices for patient-specific quality assurance

Several devices including diode or Ion chamber (2D/3D) array, portal dosimetry (EPID), film dosimetry and gel dosimetry for relative dose evaluation have been suggested for patient-specific dosimetry. An ionization chamber for absolute dose measurements can also be used (Elawady *et al*., 2014). However, the 2D array is inappropriate for pre-treatment verification of SBRT, which usually involves field sizes smaller than 5 × 5 cm^2. Its lower spatial resolution results in a coarse sample size insufficient for adequate gamma analysis (Min *et al*., 2015). Phantoms like Octavius 1600 SRS should be used for SBRT plan verification and quality control.

Most commercially available dosimetric phantoms have an almost homogeneous density throughout their volume, whilst a patient's body has variable and varying densities (Gurjar *et al*., 2014).

3.7.1.1 Diode or Ion chamber array

Many dosimetric devices have been developed for IMRT, VMAT and SBRT patient-specific QA such as the 2D/3D ion chamber array shown in Fig.3.7, 2D diode array (Maraghechi *et al*., 2017), ArcCHECK, MapCheck, EPIdose (Sun Nuclear Corporation, Melbourne, Florida, USA) (Maraghechi *et al*., 2017 and Nalbant *et al*., 2014), Mapcheck, Delta 4 (ScandiDos AB, Uppsala, Sweden), MatrixXX (IBA Dosimetry GmbH, Schwarzenbruck, Germany) (Maraghechi *et al*., 2017).

Figure 3. 7: PTW Octavius phantom used for IMRT/VMAT patient-specific QA.

The 2D/3D array is connected outside the treatment room to a laptop computer which runs the software. Portal dosimetry, Mapcheck and MatrixX cannot give three-dimensional information about a dose distribution because these methods do not use the patient CT image. However, they are used in the clinical situation as a QA tool (Rahman *et al*., 2019).

The software programs utilized by these devices for dose distribution analyses use the gamma evaluation method. This method locates hot and cold spots and determines the maximum and average deviation between a calculated and measured plan (Nalbant *et al*., 2014). Gamma index methods are one of the metrics which are widely used for patient-specific quality assurance (Park *et al*., 2017) for IMRT and VMAT.

3.7.1.2 The electronic portal imaging device (Portal dosimetry)

The electronic portal imaging device (EPID) is mounted on a medical linear accelerator as shown in Fig.3.8 below and is widely used not only for the verification of patients' daily/weekly setup before radiation therapy treatment (Singh *et al*., 2019 and Cho *et al*., 2011) but also for quality assurance (QA) of the treatment machine (Singh *et al*., 2019). High contrast, large detector density, large detecting surfaces, linear response to radiation dose and efficient online capabilities make EPID a good candidate for IMRT and VMAT QA. However, a high-Z component material makes EPIDs far from water-equivalent (Bailey *et al*., 2012).

Figure 3. 8: Patient-specific QA setup using EPID.

Many vendors have produced algorithms capable of predicting calibrated EPID response or which can convert calibrated EPID response into a simulated dose plane. The EPID images can then be used to verify the calculated plane dose in the delivery of IMRT fields and VMAT. EPIDose uses digital imaging and communication in medicine (DICOM) radiation therapy (RT) EPID response images and converts them into dose plans for comparison to similar treatment planning system calculated planes (Bailey *et al*., 2012).

The Portal Dosimetry (PD) system was developed for the pre-treatment verification of IMRT and VMAT plans (Cho *et al*., 2011). Portal dosimetry is an effective method for pre-treatment verification because of its prompt setup, easy data acquisition and high spatial resolution (Min *et al*., 2015). The operation of the EPID is based on the conversion of signals obtained from it into radiation-absorbed dose (Singh *et al*., 2019). A portal dose image (PDI) can be acquired by the EPID for each patient treatment IMRT field or arc and compared with the predicted PDI from the treatment planning system. The results are analyzed in the same way as when measuring data using a 2D/3D array.

3.7.1.3 Film dosimetry

A Gafchromic film is used for dosimetry in the volumetric region due to its flexible nature and high spatial resolution. The advantages of the film are a high degree of spatial resolution, self-developing and nearly tissue equivalent (for EBT3 Zeff = 6.84 and water Zeff = 7.3) and physical toughness. The films are energy independent at megavoltage energies (Ade *et al.*, 2018). This film can measure absorbed dose up to 10 Gy (Gafchromic EBT3 specifications, 2020), and it is unaffected by interior room light (Van Eeden, 2014). These films can be curled around an area of interest for dose assessment (Butson *et al*., 2001) as shown in the Fig.3.9 below.

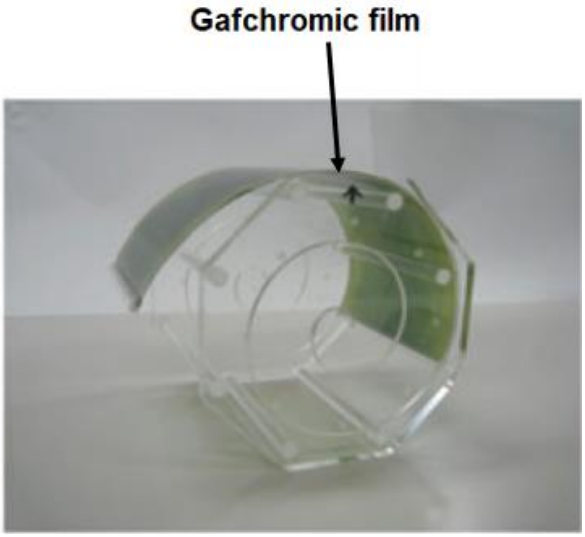

Figure 3. 9: Illustration of Gafchromic film curled around the spiral water phantom for film dosimetry (Tanooka *et al*., 2013).

A typical film dosimetry system requires the establishment of a calibration curve which converts the optical density (OD) to absolute dose. This dose-response is often non-linear, and the calibration curve is sensitive to changes in scanning conditions thus increasing error in dose measurements and limiting its use to relative dosimetry (Cai *et al*., 2017). Gafchromic films should be handled with soft gloves or tweezers to avoid fingerprints and other contaminants which affect the readout. The Gafchromic film is prone to scratching which can also affect the optical density readout and care should be taken not to slide the film on the surface with any force (Butson *et al*., 2001).

3.7.1.4 Gel dosimetry

Gel dosimetry systems are described as true 3D dosimeters because they can be moulded to any required shape and measure the 3D geometry absorbed dose distribution (Izewska *et al*., 2012). The gel dosimeters are divided into two:

1. Fricke gel dosimeters which contain aqueous ferrous sulfate solution and expressed in G value. G value is the radiation chemical yield, which is the number of moles of ferric ions produced per joule of the energy absorbed in the solution.

2. Polymer gel dosimeters are made from chemicals that are sensitive to radiation (Gallo *et al*., 2023). The functionality of the polymer gel dosimeters is based on the effect of radiation-induced polymerization (Fitilis *et al*., 2022) which is due to absorption of radiation directly or through intermediate water free radical (Izewska *et al*., 2012). The advantage of the polymer gel is that it can fill phantoms designed for a specific purpose because it is in a liquid form. Polymer gel is typically composed of 85-90 % water and 5-10 % gelatine (Fitilis *et al*., 2022). The gel is water equivalent due to large proportion of water (Izewska *et al*., 2012). For steep dose gradients such as IMRT and stereotactic treatment these advantages become more prominent. (Baldock *et al*., 2010).

3.7.2 Verification plan analysis

To compare the measured and planned dose for IMRT/VMAT/SBRT, a verification plan is generated and recalculated on the CT images of the 2D/3D array equipped with water equivalent material (Park *et al*., 2017). The verification plan is irradiated with the same MU and beam setup as the patient treatment setup using a linear accelerator (Linac). Software is used for comparing the gamma distribution of the TPS calculated dose and the measured dose using films or arrays (Elawady *et al*., 2014).

The Gamma index is employed with a planar dose distribution using a 2D/3D array detector (Park *et al*., 2017). The measured and calculated doses are compared using a combined dose difference (DD) and distance-to-agreements (DTA) for composite analysis (Mohamed *et al*., 2018). The composite analysis can be used for both high and low dose gradients (Bak *et al*., 2012). The DTA is the distance between the measured data point and the nearest point in the calculated dose distribution that exhibits the same dose (Low *et al*., 1998).

Consider an ellipsoid surface chosen to represent the acceptance criterion. The defining surface is given by the equation

$$1 = \sqrt{\frac{(\Delta r)^2}{(DTA)^2} + \frac{(\Delta D)^2}{(\Delta D_{max})^2}} \quad \text{..... (3. 11)}$$

Where

$\Delta r = |r_c - r_m|$: the distance between the calculated (r_c) and the measured (r_m) point.

$\Delta D = D_m(r_m) - D_c(r_c)$: the dose difference at rm relative to calculated dose D_c in r_c.

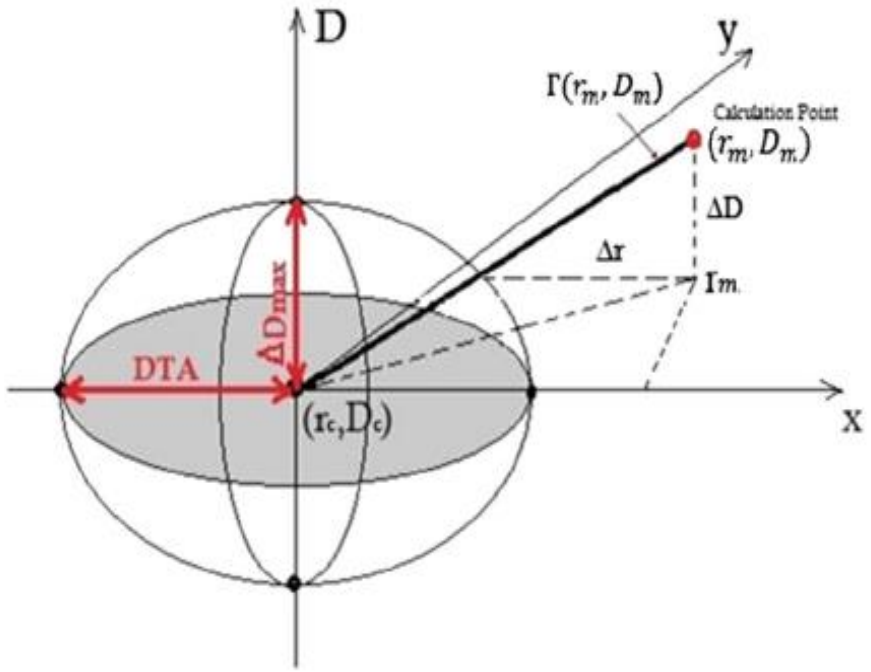

Figure 3. 10: The principle of gamma verification: x, y, D positions, and dose dimension; DTA (Distance To Agreement), $\Delta \boldsymbol{D_{max}}$ (Maximum deviation), $\Delta \boldsymbol{r}, \Delta \boldsymbol{D}$ local position and dose divergence of analyzed point (Mohamed *et al*.,2018).

For the compared distribution to match the reference dose in r_m, it must contain at least one point (r_m, D_m) i.e., one point for which

The gamma index $\gamma(r_c, r_m\ )$ for every point in the test distribution is calculated using the formula:

$$\gamma(r_m) = \{\Gamma(\ r_m, D_m)\} \ = \left\{ \sqrt{\frac{|r_c - r_m|^2}{(DTA)^2} + \frac{|D_m(r_m) - D_c\ (r_c)|^2}{(\Delta D_{max})^2}} \right\} \quad \text{..... (3. 12)}$$

Where $Ir_c\text{-}r_mI=\Delta r$ which is the distance between analyzed points (calculated (r_c) and the measured (r_m) point)

$|D_m(r_m) - D_c\ (r_c)| = \Delta D$ the dose difference at r_m relative to calculated dose D_c in r_c.

The accuracy of compatibility is determined by the point with the smallest deviation from the reference point, i.e., the point of $\Gamma(\ r_m, D_m)$ is minimum. The minimum value is the quality index $\gamma(r_m)$ of the reference point.

The pass-fail criterion therefore becomes

$\gamma(r_m) \leq 1$, calculation passed

$\gamma(r_m) > 1$, calculation failed (Mohamed *et al*., 2018)

3.8 Prostate motion management

The prostate is a mobile organ located below the bladder and in front of the rectum. The bladder and rectum can influence the movement of the prostate during and between fractions because the volume continuously changes. The bowel movement may also shift the bladder position. Prior to CT scan, the patient is given instructions on how to prepare the rectum and bladder. The patient is treated the same way as the scan in terms of bladder and rectum preparation.

To minimize the daily variability patient must maintain an empty rectum and fill the bladder. Empty rectum and full bladder reduce the movement of the prostate and reduce the dose to the rectum and bladder. Precise patient setup is obtained by acquiring the CBCT for soft tissue or fiducial in prostate (for post brachytherapy patients) or bone matching prior to treatment. CBCT is acquired before each treatment fraction to verify the actual status of the bladder and rectum and the position of the prostate with respect to the planned position.

The adaptation of the PTV margin has helped with the intrafraction prostate motion but results in more dose to the organ at risk and toxicity (Oehler *et al*., 2022). Hypofractionation SBRT technique for prostate cancer treatment is commonly used for patients with low- to intermediate-risk (Gorovets *et al.,* 2020). However, tighter margins, high dose gradients, and strict adherence to planning objectives in terms of patient positioning and organ motion management are required for hypofractionation (Panizza *et al*., 2022 and Faccenda *et al*., 2023).

Stereotactic treatment delivery time is longer than that of the IMRT and VMATs due to large, prescribed dose per fraction. Treatment length plays a crucial part in the intrafraction of prostate motion. Oehler *et al*., (2022) indicated that treatment time longer than 10 minutes may move the prostate by 3 mm and more as compared 5 minutes. This is as a result of continuous rectal and bladder filling during treatment.

Uncertainties regarding organ motion can limit SBRT success (Gorovets *et al*., 2020). The prostate tracking system are needed when using these techniques because of the decreased margin and longer delivery fraction time. As mentioned in 3.5.4 IGRT can be used to monitor daily setup.

3.9 Monte Carlo simulation

The Monte Carlo simulation is based on a statistical method which performs numerical integrations to solve a problem (Chetty *et al.*, 2007) and it has a powerful role in different radiotherapy aspects (Salemi *et al*., 2011). The Monte Carlo method for the simulation of radiation transport is a numerical means of solving the Boltzmann transport equation in an arbitrary geometry (Salvat-Pujol *et al*., 2013). Monte Carlo techniques have become a gold standard in medical physics to simulate electron and photon transport in materials and especially to calculate dose distributions in an inhomogeneous phantom (Yani *et al*., 2016). The use of the Monte Carlo technique has increased exponentially since the 1970s (Salvat-Pujol *et al*., 2013).

The Monte Carlo simulation of radiation transport used for predicting dose distribution in the radiation treatment of patients is known to be the only algorithm to model high-density scatter accurately (Cecen, 2013) by accounting for the effects of the different atomic composition of the high-density material relative to water (Keall *et al*., 2003).

The Monte Carlo technique used for radiotherapy photon and electron transport is available in codes such as the Electron-Gamma-Shower (EGSnrc), Monte Carlo N-particle Transport (MCNP), GEANT4, Penetration, and Energy Loss of Positron and Electrons (PENELOPE) etc. (Cecen, 2013). Electron-Gamma-Shower (EGSnrc) will be employed in this study, and only this EGSnrc will be described.

3.9.1 Electron-Gamma-Shower (EGSnrc)

EGSnrc software package was released in 2000, however the original software package was developed in the1970s at the Stanford Linear Accelerator Center (SLAC) (Kawrakow *et al*., 2017). EGSnrc models ionizing radiation transport through matter (Zadehrafi *et al*., 2020). It models particles such as photons, electrons and positrons with kinetic energies ranging from 1 keV and 10 GeV matter (Zadehrafi *et al*., 2020 and Kawrakow *et al*., 2017).

It simulates the photoelectric effect, Compton scattering, pair-production, positron annihilation, Rayleigh (incoherent) scattering processes (Lloyd, 2011) and Bremsstrahlung production using Bethe-Heitler cross sections. The interaction of photons with matter is explained in Chapter 2 section 2.1.2.

The total probability of these interactions happening is related to their individual interaction cross section and is given by

$$\sum_{tot} = \sum_{photoelec} + \sum_{compton} + \sum_{pair} + \sum_{Rayleigh} \quad \text{..... (3.13)}$$

Mohamed *et al.*, (2017) validated the MC model by calculating the PDDs and lateral profiles curves of a 6 MV photon beam at a 10 × 10 cm^2 field size in a homogeneous water phantom and compared it with experimental data provided by the LINAC manufacturer. The results were comparable as shown in Fig.3.11 below.

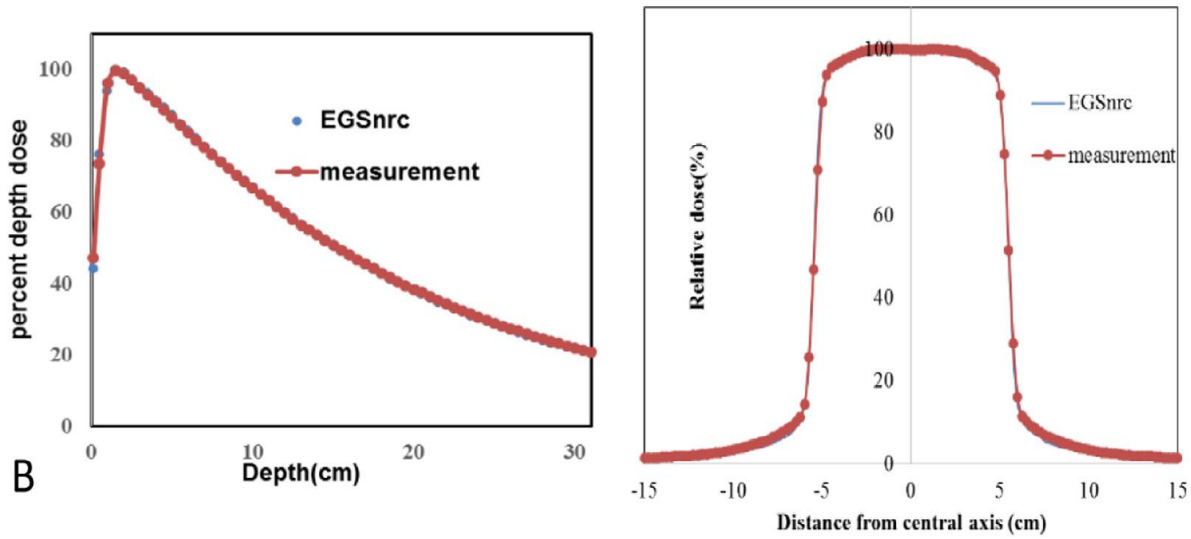

Figure 3. 11: An example of calculated PDDs and beam profile curves compared with those measured in water for a 6 MV photon beam (Mohammed *et al.*, 2017).

Israngkul-Na-Ayuthaya *et al.*, (2015) also compare the MC calculation and the ionization chamber measurements of PDD and beam profiles for a high energy 15 MV photon beam with a 10 × 10 cm^2 field size at a source to surface distance (SSD) of 100 cm. The results were comparable as shown in Fig.3.12 below (Israngkul-Na-Ayuthaya *et al*., 2015).

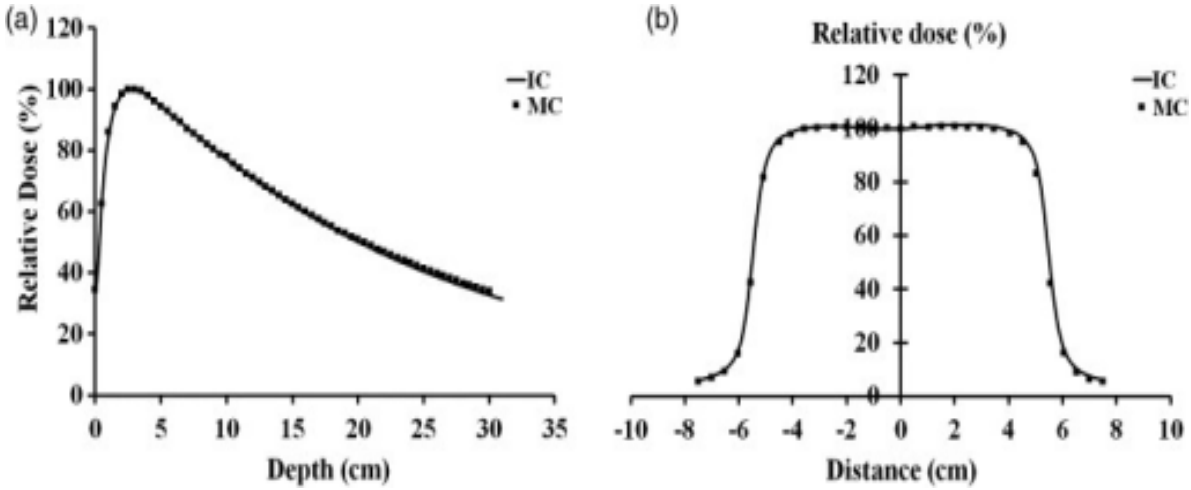

Figure 3. 12: Comparison between Monte Carlo simulation and ionization chamber measurements of (a) Percent Depth Dose (PDD) for 15 MV and (b) Dose Profile curve 15 MV (Israngkul-Na-Ayuthaya *et al*., 2015).

3.10 Phantom design in the literature

In literature, different authors designed phantoms based on their research interest and various methods were used to evaluate the dose to the organ of interest.

Figure 3.13 shows various in-house phantoms created by different authors based on area of interest. (A) Parenica *et al*., (2019) used slabs of gel bolus and placed the hip prosthesis within the slabs and the ionization chamber at the isocenter. Since they have created a cut-out on the superflab gel bolus to fit the prosthesis this could have created an air gap and added precaution is needed to avoid air gaps in-between the slabs. In our study dental wax was used to avoid air gaps around the hip prosthesis, bone and prostate insert.

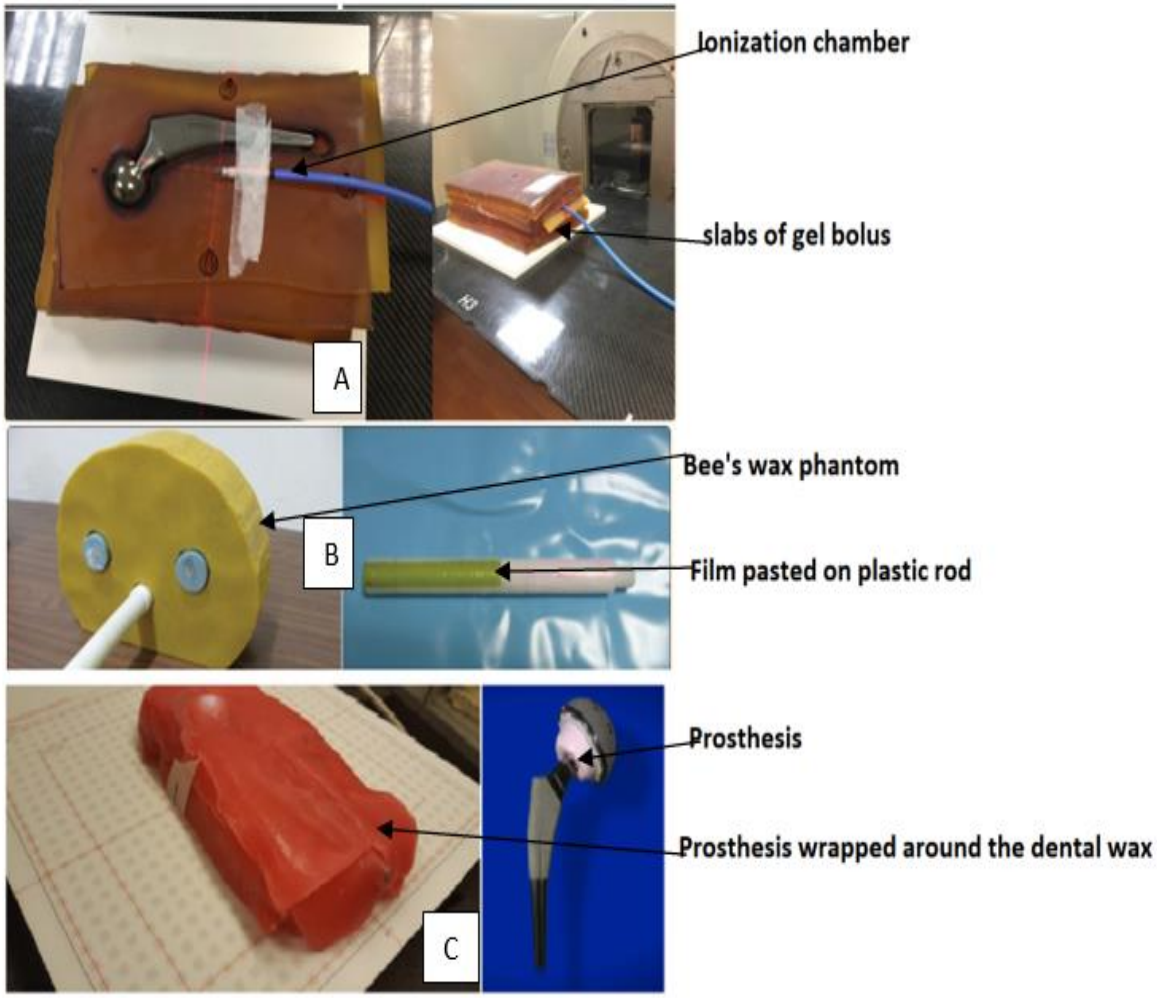

Figure 3. 13: (A) A hip prosthesis placed within the slabs of gel bolus, (B) a film pasted on the plastic rod inside the rectum and (C) a hip prosthesis wrapped around the dental wax on top of the 2D array.

(B) Ganapathy *et al*., (2013), designed a phantom using bee's wax to mimic a human pelvis. The phantom has an opening on the rectum to accommodate films pasted on the plastic rod as shown in Fig.3.13 (B). This phantom was utilized to evaluate the dose to the organ at risk (rectum) during prostate treatment. In our study, we adopted pasting the film on the plastic rod to measure the point dose to the prostate. (C) Koutsouvelis *et al*., (2021) wrapped the hip prosthesis using dental wax and placed it on top of the array to assess the discrepancies between the TPS calculated dose and measured dose.

Ade *et al*., (2017) created a phantom using Nylon-12 slices with unilateral titanium hip prosthesis and the bone to simulate femoral heads. Their Nylon-12 pelvic

phantom size is 25 x 30 x 17 cm^3. The phantom was designed to accommodate the film between the slices and their focus was to measure the dose perturbation effects of titanium prosthesis on 6 and 15 MV using static fields and compare with TPS calculated dose.

In their 2013 study, Gruen *et al*. used a cheese phantom for measuring point doses, sandwiching ionisation chambers and film between the phantom's spheres. To verify the prostate IMRT pre-treatment dose, McDermott *et al*. (2006) used an electronic portal imaging device (EPID) dosimetry. Gafchromic EBT3 film and a 2D diode array were utilised by Nalbant *et al*. (2014) to confirm the pre-treatment dose of IMRT. The issue with the studies mentioned above is that the phantoms have homogeneous density.

In previous studies the focus was on measuring the dose to the area close to the prosthesis whereas with this study prostate point dose is the focus. Section 4.1 below explains the concept of the intended phantom design and phantom design that was used for the experiment.

CHAPTER 4: MATERIALS AND METHODS

The objective of this work is to optimise the volumetric-modulated arc therapy (VMAT), intensity-modulated radiotherapy (IMRT), and prostate 3D conformal treatment dose distribution in a metallic hip prosthesis phantom. The study's objective was accomplished by the creation of an in-house pelvic phantom, evaluation of prostate point dose measurements for 3DCRT, IMRT, and VMATs plans.

Additionally, a MC simulation using EGSnrc is run for comparison. The MC simulated prostate point dose is then compared with the measured dose distribution (prostate point dose) obtained from the ionisation chamber, the Gafchromic EBT3 film, and treatment planning system calculations. A variety of tissue-equivalent materials were used in the construction of an in-house pelvic phantom. The material and methodology that were utilised in this study to assess the prostate point doses are the main topics of this chapter.

4.1 Phantom design

Radiotherapy phantoms are objects that simulate human body, and they can be composed of water or materials with similar characteristics to human tissue (Biglinetal, 2019). A phantom unlike a water phantom or simplified solid phantom slab setup, is a realistic representation of human anatomy and should reflect actual clinical outcomes and geometry. Phantoms have a variety of uses in radiation therapy and play a crucial role in patient-specific dosimetry. Most commercially available phantoms for patient specific dose measurements in radiotherapy are made of water equivalent (homogeneous) material.

In-house phantoms that mimic the anatomy of human structures are commonly used to measure dose at a specific point of interest, as with the prostate in this experiment. Tissue mimicking materials contained within the phantoms used to model a human body part are used worldwide in radiotherapy studies. An in-house phantom can be

used to simulate the treatment conditions and obtain the measurements which wouldn't be possible to measure on an actual patient.

4.1.1 Intended original phantom design

The use of a human-like phantom is crucial since it is more accurate in representing human anatomy and should represent true clinical outcomes than the use of a water phantom or a simplified phantom slab setup geometry.

The original conceptual design of the phantom is shown in Fig. 4.1. A Custom-made 3D-printed pelvic phantom reconstructed from anonymous prostate cancer CT data set with a hip prosthesis present using Fusion 360 and blender 3D printing software. The phantom is printed using a Prodways Selective Laser Sintering (SLS) 3D printing machine. The phantom is produced by powdered materials that are bond together to form a solid structure by using lasers controlled by the 3D system (Lu *et al*., 2021). The reconstructed phantom is modified to accommodate film and chamber insert.

The original dual dosimetric phantom design for the organ-specific pelvic prosthesis phantom consists of different removable inserts for ionization chamber (cylindrical hole crossing the prostate gland) and spiral slot to enclose the film. Ion chamber insert is suitable for cavity volume of ≤ 0.8 cm^3, while film inset can accommodate a thin sheet and size of 0.3 mm and 8" × 17" respectively. The 25 cm thick dosimetric phantom also contains organ substituted materials with densities of bladder, rectum, bony structures, and prostate (cancer cell composition) embedded in water-equivalent nylon-12 as shown in Fig.4.1 below. 1 cm nylon sandwiched between the titanium implant of 2.5 cm geometrical radius and the right hip bony structure for a tight grip.

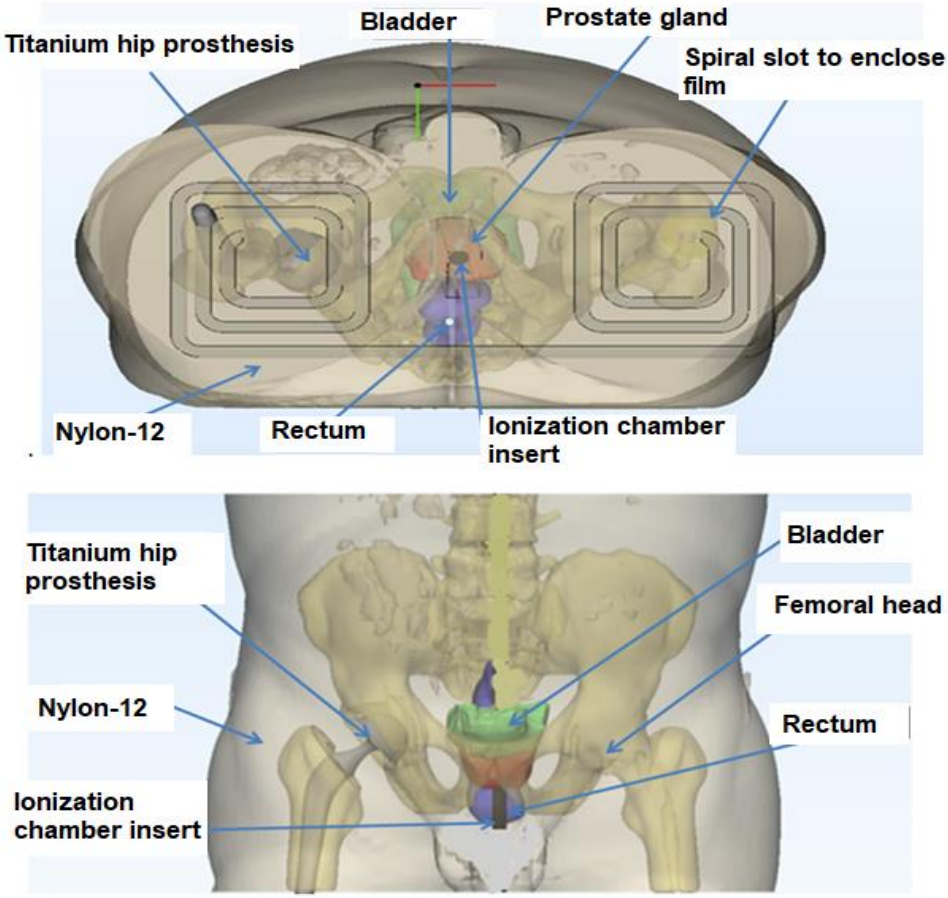

Figure 4. 1 : Intended original pelvic phantom design with hip prosthesis.

Due to cost constraints and the availability of the specified component materials, the above design was not implemented but instead adapted to create the below mentioned Pelvic Phantom as depicted in Fig. 4.2. Section 4.1.2 below explains in detail the concept of the phantom design that was used for the experiment.

4.1.2 In-house pelvic phantom design

An in-house pelvic phantom was constructed from superflab gel bolus slices, prostate insert (Nylon-12), dental wax, femoral bone inserts, and a titanium hip prosthesis. Superflab gel bolus and dental wax are widely used in radiotherapy for compensation of missing tissue.

Superflab gel bolus is made of proprietary synthetic gel. 30 cm square superflab gel bolus slices of 0.5 cm and 1 cm thickness were used in the phantom construction. Superflab gel bolus was used to simulate the rectum and bladder. The rectum and bladder have an irregular shape with the equivalent sphere diameters of 3.1 cm and 4.8 cm, respectively. Nylon-12 was used to replicate the prostate and the replica included a central cavity in which to insert the ionization chamber and film.

Nylon-12 is a water equivalent material and can be used to mimic human tissue with an electron density of 1.01 close to that of water. 3D-printed Nylon-12 was created using Fusion 360 and blender 3D printing software by Red Apple 3D printing company (Red Apple 3D Inc, SA). The prostate insert measures an equivalent sphere diameter of 4.6 cm and a volume of 52.20 cm^2. This diameter and the volume were adapted from the average size of the prostate from all patients with prostate cancer. The prostate gland measures $3 \times 3 \times 5$ cm approximately or a volume of 25 cm^2 (Mitterberger *et al*., 2010).

The prostate insert (Nylon-12) was printed from powdered materials bonded together to form a solid structure by using Prodways Selective Laser Sintering (SLS) 3D printing machine. The reconstructed prostate insert was modified to accommodate film and chamber insert. The central cavity was made to accommodate a volume of ≤ 0.9 cm^3. The volume of the central cavity was chosen to accommodate the 0.6 cc ionization chamber and the film strip. The central cavity on the Nylon was made smooth to ensure that it doesn't damage the ionization chamber and make scratches on the film.

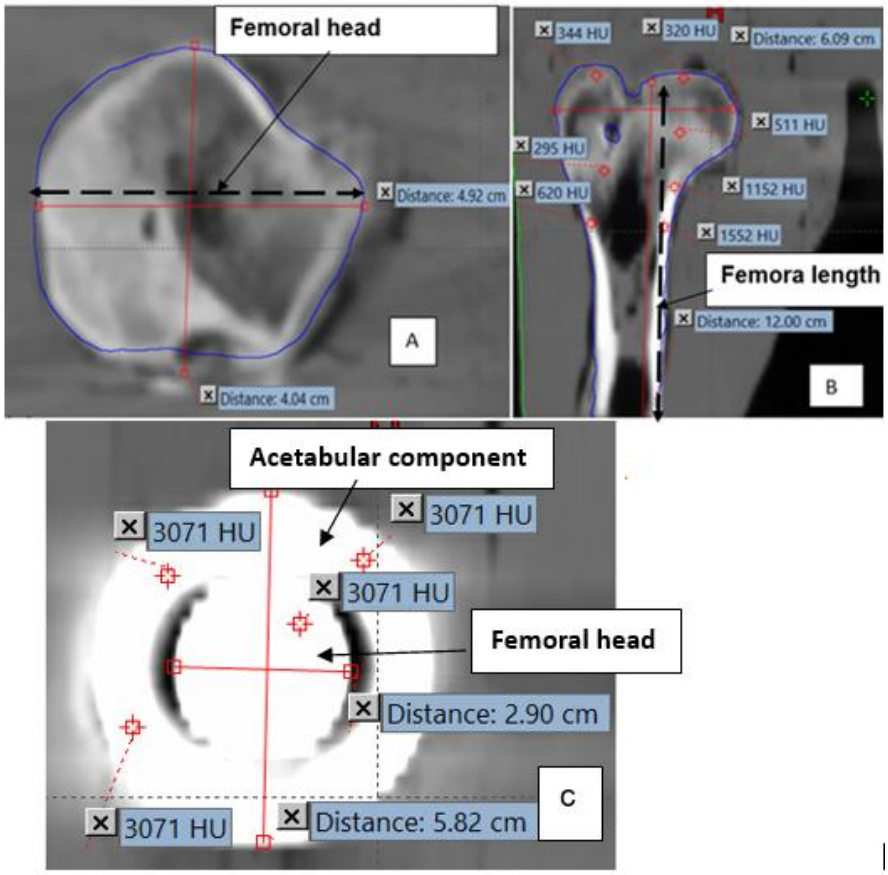

Figure 4. 2 : (A) Diameter of the pig femoral head bone, (B) the length and the CT number of the pig femur bone and (C) the diameter of the titanium acetabular component and femoral head.

The pig bone with an average femur diameter of 4.6 cm and femora length of about 12 cm as shown in Fig.4.2 was used to simulate the right human femoral head. The human femoral head ranges from 3.9 cm to 5.5 cm (Akinmokun *et al*., 2020). The femoral head of the pig bone is within the range of the human femoral head diameter. Various studies have investigated the bones or femurs of different animals and compared them to human femur. Pigs were reported to have similar cross-sectional diameters of the human femur and have a similar lamellar bone structure as humans (Li *et al*., 2015). The comparison of the electron densities of the pig and human bone are comparable as shown in Table 4.2. However, pigs were found to have smaller femoral lengths (average of 12 cm) compared to human male adults (48 cm). This is not a concern in our study since the concentration is on the femoral head and therefore the area of interest is covered. The hip prosthesis femoral head diameter is also indicated in Fig.4.2 (C).

Dental wax is pink in colour and is available in different forms and thicknesses. Dental was chosen because it melts easily in high temperature (45-60 °C) and ease molding. In the first process of construction the wax was melted using a heat gun and poured into a box mould containing the femoral bone insert, prostate insert, and hip prosthesis to minimize air gaps between these three materials, as they are not flat. These components were secured in position by masking tape to avoid shift during the moulding process as shown in Fig.4.3 (A).

Table 4. 1: Properties of materials used in an in-house pelvic phantom.

Material	**Relative density (g/cm^3)**	**Composition (% weight fraction)**	**Organ simulated**
Titanium alloy (Ti6AL4V)	3.74 Mass density of 4.5	Titanium (89.17) Aluminium (6.20) Vanadium (4.00) Iron (0.30) Oxygen (0.20) Carbon (0.08) Nikel (0.05)	Hip prosthesis (left femoral head)
Dental wax	1.02	Paraffin wax (70-80) Bees wax (12) Carnauba wax (2.5) Resins (3) Synthetic wax (2.5)	Soft tissue
Superflab gel bolus	0.907	Synthetic oil gel	Bladder and rectum
Nylon-12 (Prostate insert)	1.01	Nylon polymer ($(CH_2)_{11}CONH$)	Prostate
Pig Bone	1.193-1.824	Mineral Collagen Non-collagenous Proteins Water	Right femoral head

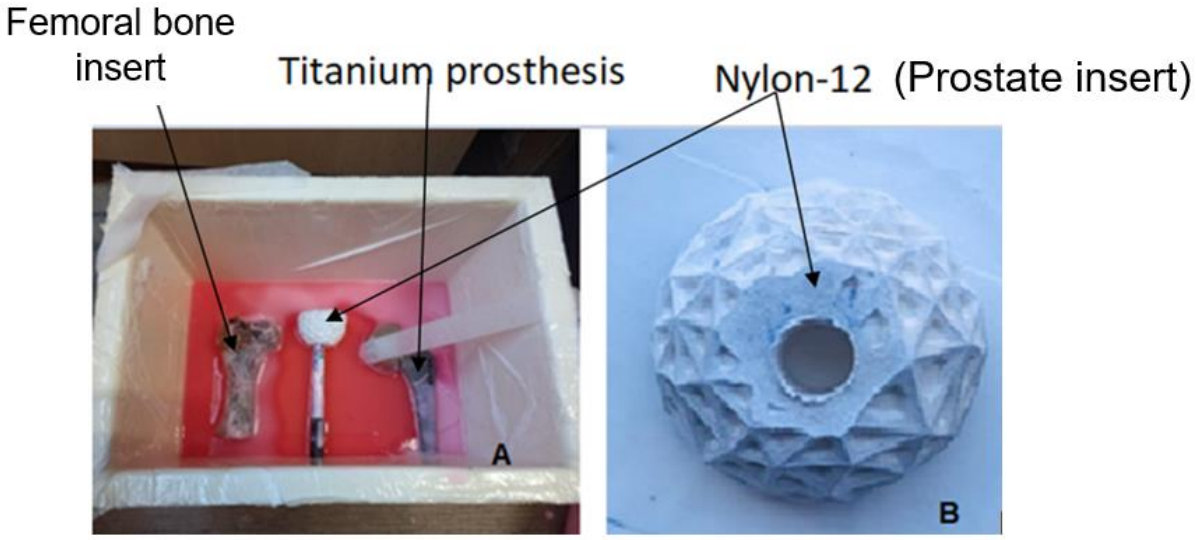

Figure 4. 3 : (A) prostate insert, prosthesis, and femoral bone insert in the mould and (B) The Nylon-12 (prostate insert) piece with the cavity for the ionization chamber and film insert.

The wax was decanted to a total depth of 5 cm to cover the titanium alloy, bone and prostate insert. The titanium alloy hip prosthesis and femoral bone inserts were used to replicate the femora. The titanium hip prosthesis consists of a titanium alloy (Ti6AL4V) head, stem and acetabular component. The diameter of the titanium alloy is 2.9 cm as shown in Fig. 4.2 (C). The titanium alloy used was the old prosthesis that was used on a patient, and it was donated by the orthopaedic surgeon. Once the dental wax had hardened, it was removed from the mould and placed between layers of superflab gel bolus slices.

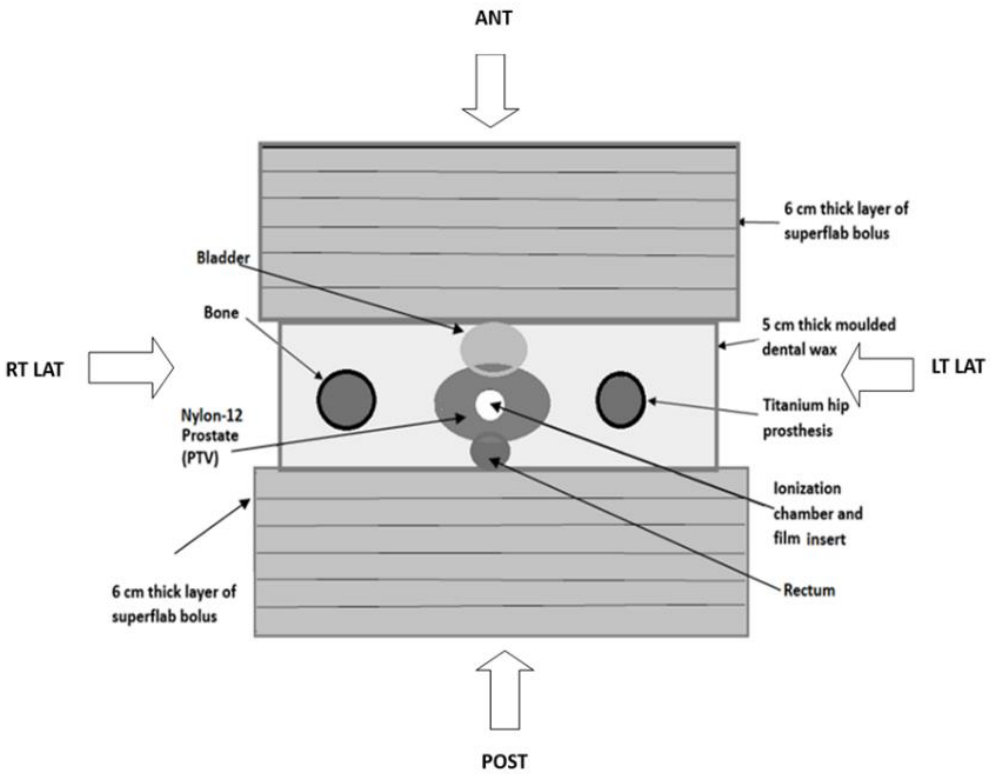

Figure 4. 4: Schematic diagram of the transverse plane of an in-house pelvic phantom.

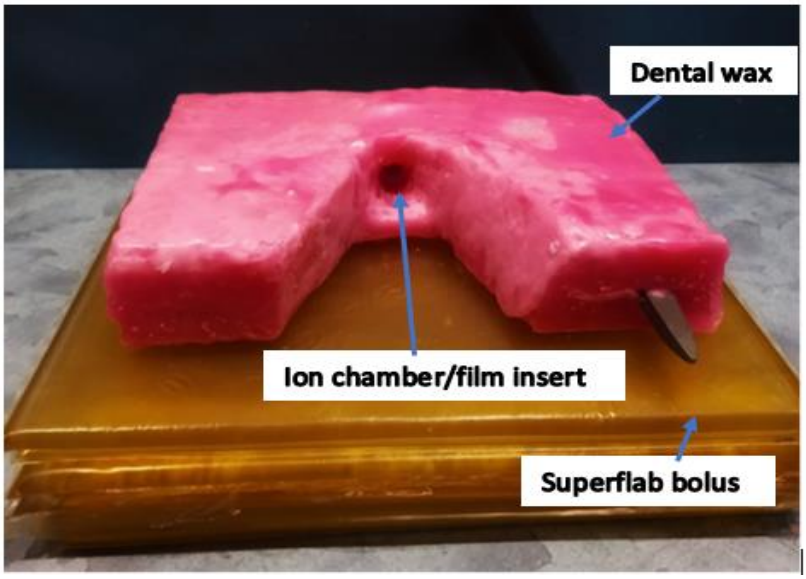

Figure 4. 5: Picture of the pelvic phantom showing the 5 cm thick moulded dental wax resting on a 6 cm thick layer of superflab gel bolus.

An in-house pelvic phantom is 30 cm in height, 30 cm in width and 17 cm thick (30 × 30 × 17 cm^3), which was the average dimensions of an adult male. This is a quick

assembly phantom that is more convenient for ionization chamber and film dosimetry. Figure 4.5 shows the 5 cm thick moulded dental wax on top of 6 cm of superflab gel bolus. 5 cm dental wax encompasses the bone, Nylon-12 (prostate insert) and hip prostheses, then 12 cm superflab gel bolus was added to make the thickness of the phantom to be 17 cm, representing the standard human male adult pelvis thickness. The TPS axial, coronal and sagittal view of the pelvic phantom is shown in Fig.C.9 in the appendix.

Table 4. 2: The densities obtained from the TPS of the material used for the phantom and for the actual human.

Material	**Mean relative density (g/cm^3) (SD)**	
	Pelvic phantom	**Actual human/titanium prosthesis**
Nylon-12 (Prostate insert)	0.969 ± 0.007	1.026 ± 0.006
Titanium prosthesis	2.504	3.74 (Expected)
Superflab bolus (Bladder) (Rectum)	0.997 ± 00.015	 1.008 ± 0.003 1.016 ± 0.015
Femoral bone insert	1.193-1.551	1.163-1.597
Dental wax (soft tissue)	0.950 ± 0.013	0.987 ± 0.125

Table 4.2 shows the relative density of the phantom obtained from the TPS and of the actual patient. The relative density of the Nylon-12 is known to be 1.01 g/cm^3, however due to the scatter the measured relative density was found to be 0.969 g/cm^3. The relative density of Nylon-12, superflab bolus and dental wax are affected by the scatter due to high density prosthesis. The CT number of titanium observed is 3071. The CT scanner used has a maximum CT number of 3071. The CT number exceeding the maximum limit is taken as 3071 (density of 2.504 g/cm^3). The titanium CT number obtained directly from the CT scanner is 3071 as shown in Fig.4.9 (B).

4.2 The radiological water-equivalence of superflab gel bolus and dental wax

The radiological water equivalence is an important quality of materials proposed for dosimetric applications that rely on the attenuation and scattering characteristics of water (Gargett *et al*., 2020). The water-equivalence of superflab gel bolus, and dental wax was investigated using two methods: (1) By measuring central axis (CAX) transmission (the linear attenuation coefficient) and calculating mass linear coefficient and (2) Relative density using CT number (HU) to calculate the density of the material.

4.2.1 Linear attenuation coefficient

The linear attenuation, as previously discussed in Chapter 2 section 2.3.1, of each material was obtained by measuring the transmission factors through different thicknesses of superflab gel bolus and dental wax. These measurements were compared to those taken with an RW3 Solid Water Phantom (PTW, Freiburg, Germany). The measurements were carried out using a PTW farmer 0.6 cc ionization chamber connected to a PTW MULTIDOS electrometer.

Figures 4.6 and 4.7 below show an experimental setup of 2 × 2 cm^2 defined at 100 SSD for 6 MV photon beam linear attenuation coefficient measurements of RW3 water equivalent, superflab gel bolus and dental wax materials. The AAPM recommends small dosimetry field sizes for linear attenuation coefficient measurements. The thickness of each material was placed at an SSD of 100 cm on top of the treatment table/couch. The ionizing chamber was set at an SSD of 150 cm (50 cm distal to the plane over which bolus slabs were placed) inside RW3 solid water slabs along the central axis of the beam below the treatment table. The resulting field size at 150 SSD is 3 × 3 cm^2 enough to cover the 2.4 cm sensitive length of the 0.6 cc ionization chamber.

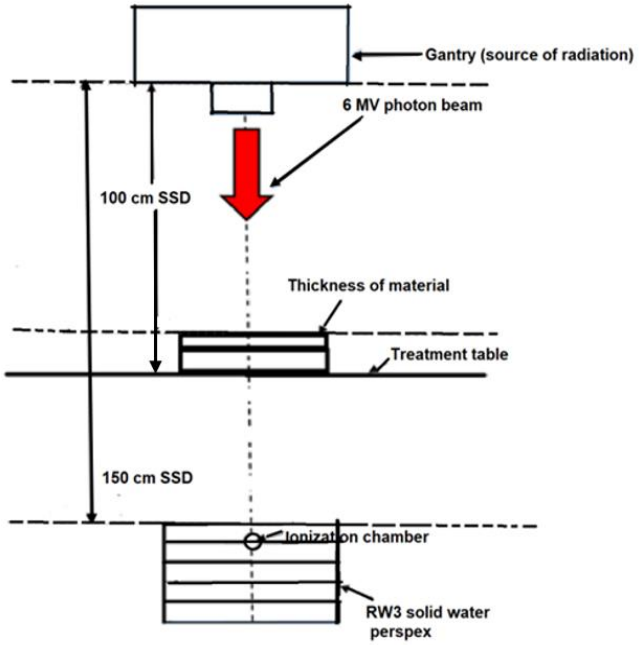

Figure 4. 6 : A schematic setup of 2 x 2 cm^2 beam geometry defined at 100 cm SSD for 6 MV transmission measurements using an ionization chamber positioned below the treatment table.

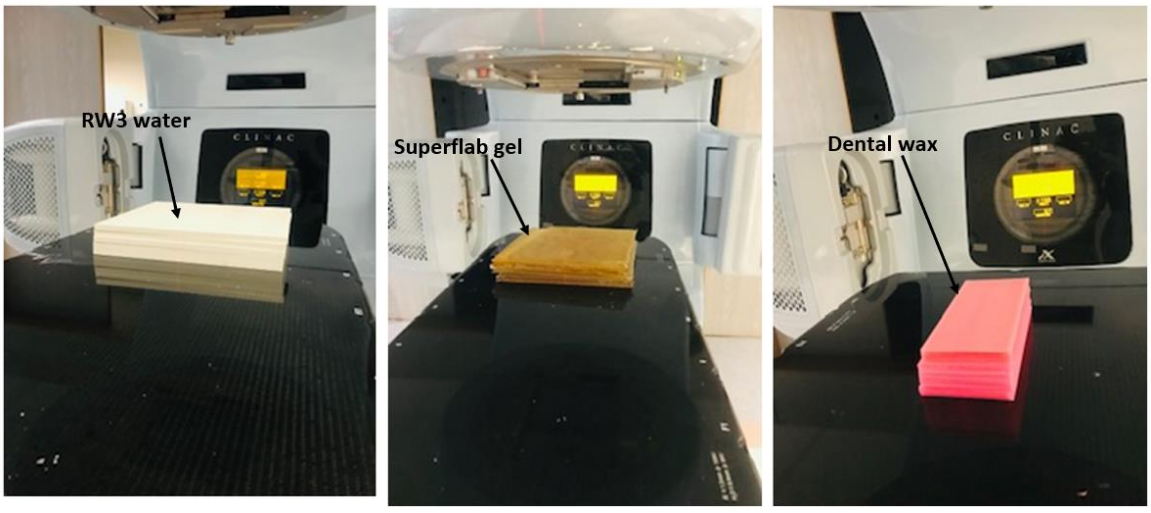

Figure 4. 7 : 5 cm thickness of RW3 solid water phantom, superflab gel bolus and dental wax on top of the treatment table**.**

200 monitor units were delivered to the centre of a 0.6 cc PTW farmer ionization chamber by a 6 MV photon beam using a 2 x 2 cm^2 field size for each measurement with gantry and collimator angles set to zero degrees, respectively. The AAPM recommends the use of small dosimetry field sizes for transmission measurements

to avoid more scatter. The large number of monitor units is used to ensure high signal-to noise ratio (SNR) (Ade *et al*., 2017). The first reading (0 reading) was the ionization chamber response with no material on the couch. Subsequently, the same amount of exposure was given to slabs of superflab gel bolus and dental wax placed at an SSD of 100 cm. The readings were acquired for different thicknesses with an increment of 1 cm each time. A maximum of 5 cm thickness was used for each material. The charge (nC) readings collected for different thicknesses were normalized to that of the first zero reading.

The transmission factor is the ratio of doses with and without the attenuating material.

$$\textit{Transmission factor} = \frac{N_x}{N_0} = e^{(-\mu.x)} \quad \text{..... (4. 1)}$$

Where N_x is the charge reading through an attenuating material and N_0 is the charge reading without an attenuating material.

The graph was plotted, and the exponential square fit was applied to determine the linear attenuation coefficient of the materials. The mass attenuation coefficient was calculated using Equation 2.7 by dividing the linear attenuation coefficient by the density of the material.

4.2.2 Relative density and Hounsfield units calculation

An in-house pelvic phantom was scanned using a Philips ingenuity CT scanner as shown in Fig.4.8. Two CT image sets were acquired: (1) standard pelvis 3 mm slice thickness protocol with a scan exposure parameter of 120 kV and 30 mA. (2) using O-MAR metal reduction artifact algorithms. An in-house pelvic phantom CT data sets were imported into an Eclipse (Varian Medical System, Palo Alto, USA) version 16.1 treatment planning system for both scans (with and without artifacts correction).

The organs of interest were delineated as shown in Fig. 4.9. The organs of interest for this experiment are the bladder, rectum, and left and right femoral heads (bone) as these are all in the treatment area when planning radiation therapy to the prostate.

The relative densities of the materials were recorded directly from the normal CT scan data sets using the physical property tool on the treatment planning system.

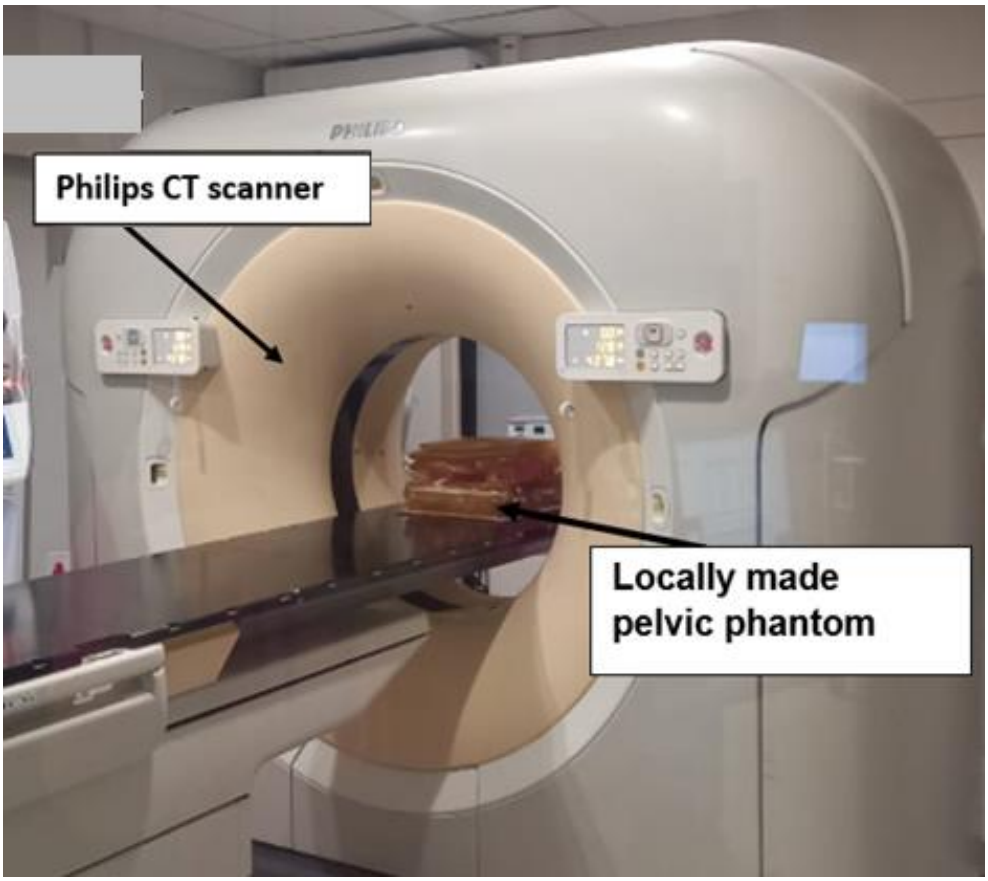

Figure 4. 8: In-house pelvis phantom placed inside the CT-scanner.

The CT scanner used has a standard 12bit depth image and the data sets can only store CT values between −1024 to 3071 HU, with 3071 being the upper CT number shown in Fig.4.9. This range can therefore only accurately represent tissues in patients which are under normal conditions without any high-density materials present. High density materials with CT numbers exceeding the upper limit of 3071 HU will be assigned a value of 3071 HU which leads to inaccuracies in dosimetry later.

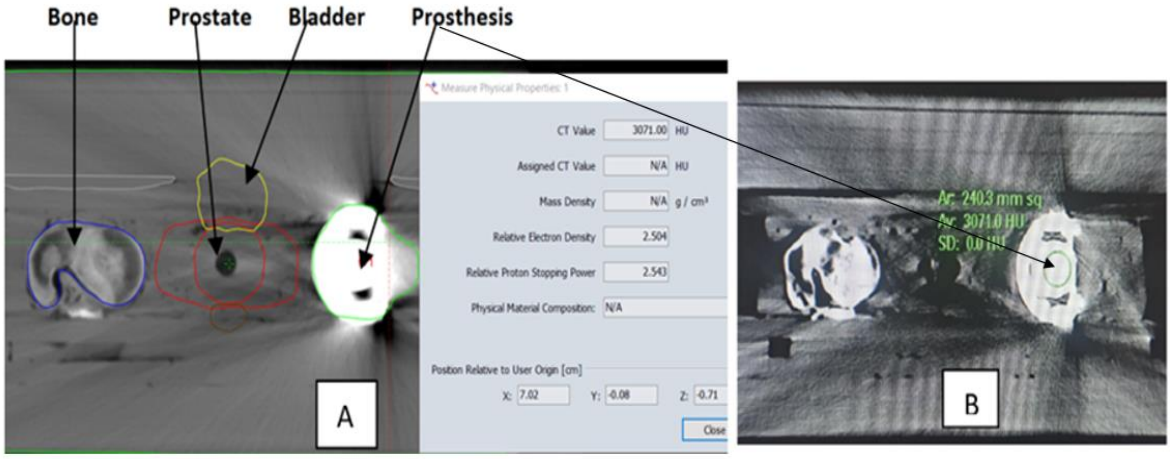

Figure 4. 9 : Relative electron density obtained from (A) TPS CT scan dataset and (B) the O-MAR CT data from the CT scanner.

The CT number (Hounsfield unit) and relative electron density of the material obtained from the CT data were verified by calculating the HU number (Equation 3.1) and the relative electron density of superflab gel bolus and dental wax. The experimentally measured Hounsfield unit of the material was then used to calculate the relative electron density of the material.

4.3 Radiation Dosimetry Experiment

Radiation dosimetry is the measurements, calculation, and assessment of an absorbed dose of ionizing radiation by the human body (Izewska, 2021). Radiation dosimetry is divided into two categories: absolute and relative radiation dosimetry. Absolute dosimetry is defined as the direct measurement of absorbed dose using dosimeter material under a standard condition. Relative dosimetry uses a dosimeter that has a secondary standard, such as film dosimetry, which requires calibration of dose in a known radiation field (Podgorsak, 2006). In this study treatment plans created using the planning system were used to estimate the prostate point doses using the ionization chamber and Gafchromic EBT3 film. The point dose location is chosen in the centre of the prostate volume (PTV).

4.3.1 Prostate cancer treatment technique plans

The organs of interest were delineated in an in-house pelvic phantom and the prostate was defined as the target volume of the diameter of 4 cm. The first experimental measurements were done without artifact density corrections using normal CT data sets. The goal of treatment planning is to achieve a uniform dose inside the PTV (Prostate). Achieving a homogeneous dose inside the PTV can be challenging when the patient has a hip prosthesis. Different treatment planning techniques were used to create treatment plans.

4.3.1.1 Static plans

The doses for four different plans using 6 MV and 15 MV photon beams were calculated using the Analytical Anisotropic Algorithm (AAA) on a Varian Eclipse 16.1 treatment planning system (TPS). The static 4-field treatment plans consist of anterior (gantry 0°) and posterior (180°) fields and left (90°) and right (270°) lateral fields. The field sizes used were 6 x 6 cm^2 for right and left lateral and 10 x 10 cm^2 for anterior and posterior. The fit to the collimator with a margin of 1 cm to PTV was used to get the field size. One lateral field passed through the bone of the normal hip and the opposing lateral passed through the hip prosthesis. The treatment plans were calculated for 20 Gy in 10 fractions. The plans were optimized to ensure that the prescribed dose covered at least 100 % of the dose of the ionization chamber/film insert.

4.3.1.2 IMRT plans

6 MV photon beams were used to produce two IMRT plans. IMRT plans frequently employ 6 MV photon beams. The fields going through the hip replacement were used to calculate the initial plan. The first plan made use of seven fields, each of which was placed at gantry angles that were 51° apart. The first IMRT plan's prescription was 72 Gy in 40 fractions (1.8 Gy each fraction) to the PTV (Prostate).

The most typical external beam prescription for prostate cancer is between 45 and 74 Gy in 25 to 40 fractions. For prostate patients who have had brachytherapy, the 45 Gy prescription is frequently used. Brachytherapy is the internal irradiation of the prostate using Iodine 125 (I125) or other low dose rate radioactive seeds or pellets (Zaorsky *et al*., 2017).

The optimization process is used in the planning of IMRT treatment. To specify the upper and lower bounds of feasible goals and desired dose distribution, physical constraints are defined using objective functions. Dynamic MLC movements are produced using an optimised fluence distribution for several chosen beams (Chung *et al*., 2011). To ensure that the 95% PTV (prostate) volume got at least 95% of the specified dose while keeping dose limitations to the organ at risk established by QUANTEC, dose targets and priorities were determined during the optimization process.

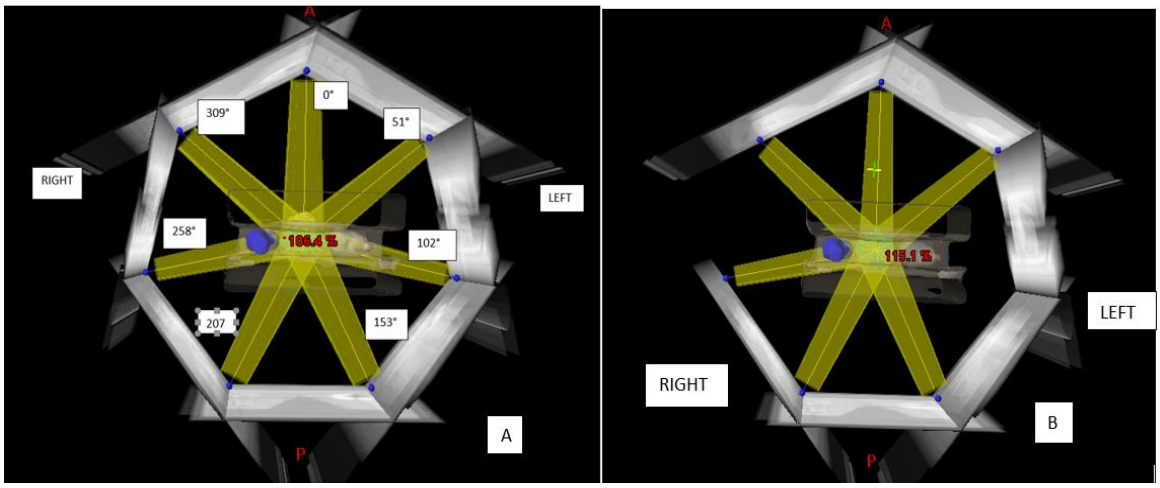

Figure 4. 10 : Illustration of the (A) IMRT 7 fields beam arrangement and (B) 6 fields IMRT avoiding the beam passing through the prosthesis (Eclipse treatment planning system (TPS) (Varian Medical Systems, Palo Alto, CA)).

The fields in the second design were set up as indicated in Fig. 4.10 (B) to prevent beams from passing through the prosthesis.

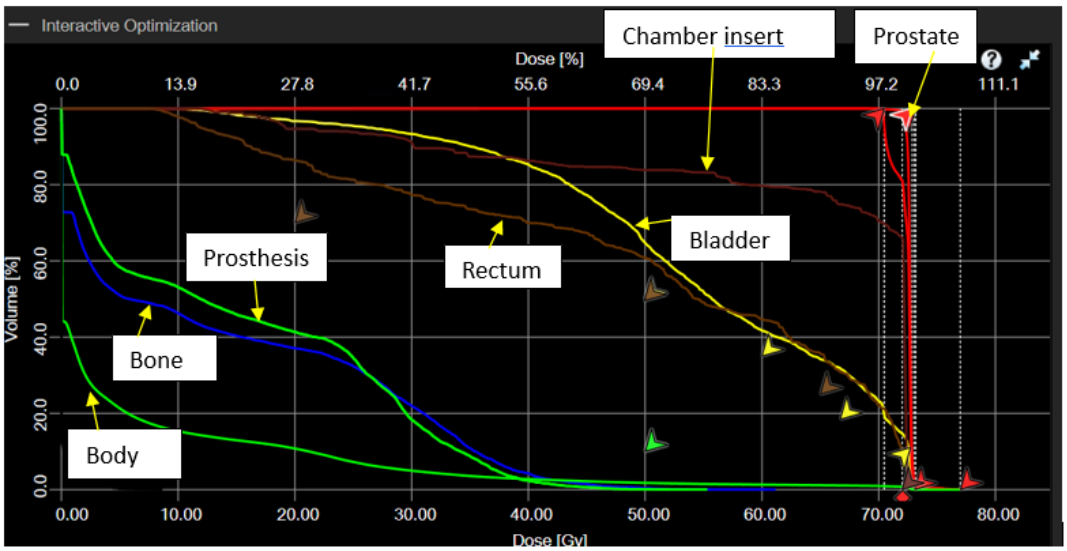

Figure 4. 11 : Eclipse interaction optimization window for prostate cancer patients, showing the DVH-lines of the prostate and organ at risk (Eclipse treatment planning system (TPS) (Varian Medical Systems, Palo Alto, CA)).

Following optimization, the plans' dose distribution was calculated using Anisotropic Analytical Algorithm (AAA) dose calculation algorithm utilizing 2.5 mm × 2.5 mm calculation grid. To further achieve the ideal prostate dose distribution following calculations, a plan normalization mode is employed. To ensure that the dose to the PTV and OAR limitations were met, the plans were assessed using the dose volume histogram (DVH) produced by the TPS. The 6 MV photon beams were used to deliver the 7 fields IMRT plan at gantry angles of 0°, 51°, 102°, 153°, 207°, 258°, and 309° to an in-house pelvic phantom on a Clinac IX linear accelerator. The ionisation chamber and film were placed inside the phantom to quantify the dose, which was then compared to the dose calculated by the TPS.

4.3.1.3 VMAT plans

The VMAT treatment planning technique is extensively utilised in the treatment of prostate cancer patients who have a hip prosthesis. On the standard CT (without artefact reduction) and the O-MAR CT data set, VMAT plans were also made. To accurately predict the intended dose distribution during the inverse planning

process, the optimizer is utilised with VMAT plans to identify differences in field shapes, dose rate, and gantry speed.

72 Gy in 40 fractions (1.8 Gy per fraction) was the prescribed dose for the PTV. A VMAT plan consists of one field arc rotating counter-clockwise from 179° to 181°, with the collimator rotated to 30°, and a dose rate of 600 MU/min, which is set as the upper limit. This is the highest photon energy dose rate available in the department. Another VMAT plan was then created using two opposing arcs, one clockwise and one counter-clockwise, with an avoidance sector to restrict radiation from passing through the prosthesis. The avoidance sector tool found in the Eclipse optimization window was used to avoid the hip prosthesis during optimization. During the actual delivery of the plan the beam switches off when it passes the avoidance region (hip prosthesis).

Plans were created using 6 MV photon beams on the Varian Eclipse treatment planning system, conforming to the prostate structure with 1 cm margins around it. The VMAT plans utilised the same optimisation goals as IMRT.

The plan's goal is to provide optimal PTV coverage. It is recommended that the suggested dose cover at least 95% of the PTVs. By not overexposing the OAR, the rectum, bladder, and femoral heads are spared. Table 3.2 lists the dose/volume objectives of OAR. This study employed the Anisotropic Analytical Algorithm (AAA) dose calculation algorithm with a 2.5 mm × 2.5 mm calculation grid.

4.3.2 Ionization chamber prostate point dose measurement

Prior to starting the experiment, the output, and mechanical functions of the Varian Clinac IX linear accelerator were checked. The check was performed using TRS 398 protocol to verify that the machine delivered 1 Gy at 10 × 10 cm^2 at a depth of 10 cm and SSD of 100 cm. The Varian Clinac iX linear accelerator passed all checks.

Before the use of the ionization chamber for prostate dose measure, the chamber leakage, polarity correction, recombination correction, linearity and reproducibility

were checked. These are explained in section 4.4.2. Figure 4.12 shows the PTW farmer chamber.

Figure 4. 12: Waterproof PTW Farmer chamber type 31013.

The phantom was positioned on the Varian Clinac IX linear accelerator as scanned as shown in Fig.4.13. Three marks (left, right and top) on the phantom marked during CT scan is used to accurately position the phantom with the guide of lasers. A PTW Farmer 0.6 cc ionization chamber connected to a Multidose electrometer was placed inside the cavity of an in-house pelvic phantom.

The irradiations were performed on the pelvic phantom and the prostate point dose was measured. The measurements were repeated three times and the average were calculated. The charge reading collected from the ionization chamber was converted into dose (Gy) using the IAEA TRS 398 protocol (IAEA, 2006). IAEA TRS-398 is the protocol used to determine the absorbed dose in external beam radiotherapy.

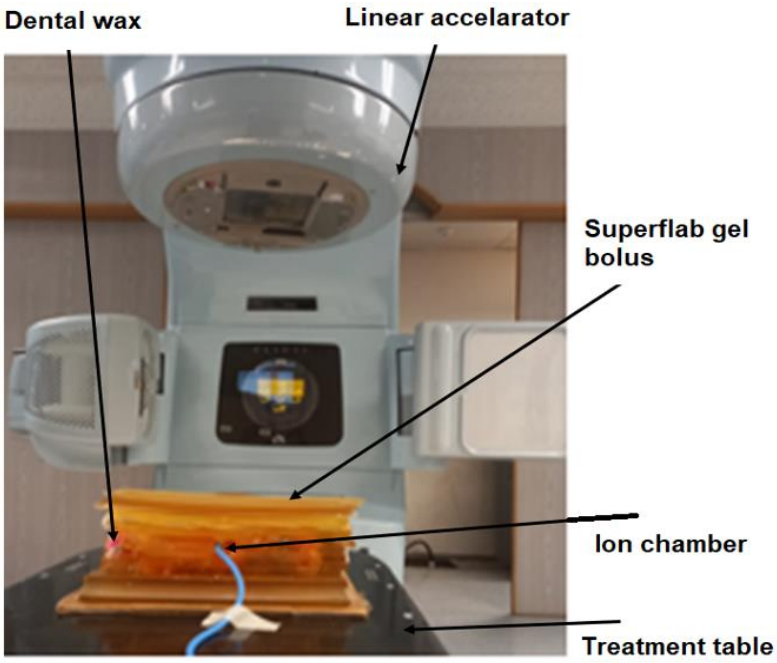

Figure 4. 13: Pelvic phantom setup on the linear accelerator.

The phantom was positioned on the machine using setup marks created during the CT scan to ensure that it was positioned the same way as scanned. To confirm the positioning and setup of the ionisation chamber inside the phantom, a cone beam CT (CBCT) image was taken. As shown in Fig.4.14. CBCT with a plastic rod is acquired without the film pasted on the rod to avoid verification dose added to the film. A mark is made on the rod to indicate the correct position.

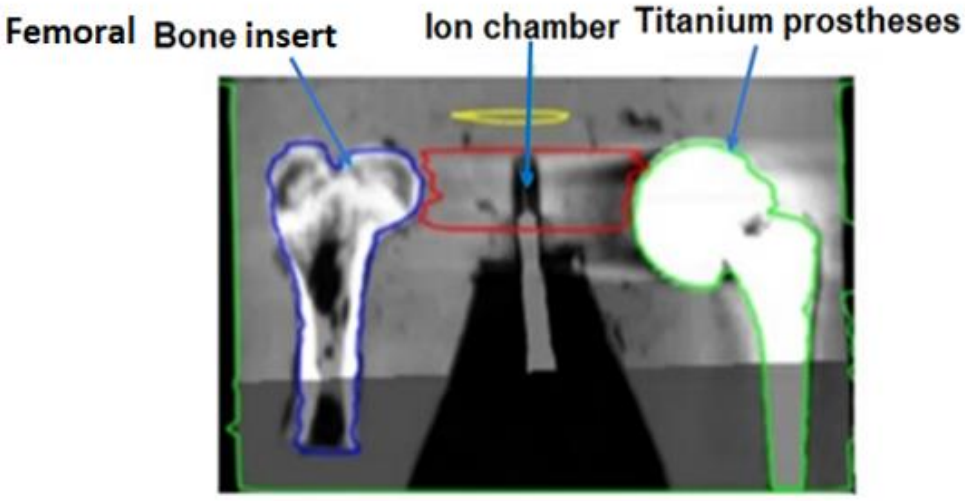

Figure 4. 14: Registration of CBCT and planning CT image position with the ionization chamber inside the prostate cavity (in red) (Eclipse treatment planning system (TPS) (Varian MedicalSystems, Palo Alto, CA)).

4.3.3 Gafchromic EBT3 film prostate dose measurements

Before using EBT3 film for the prostate point dose measurement, the dose calibration curve was obtained by irradiating small pieces of film using doses ranging from 0.25 - 6 Gy. Film calibrations allow the conversion of optical density to dose. The optical density can be related to the dose by applying a fitted function known as a calibration curve. A calibration curve is used as a dosimetry tool to convert optical density to dose for future measurements.

The films were subsequently used to measure the dose in a pelvic phantom. The scanner reproducibility, scanner uniformity, scanner parameters, film orientation dependence, scanner lateral response, film dose rate dependence, film energy dependence, and film uniformity are some factors which contribute to the total uncertainty of dose determining. These factors were assessed for both Gafchromic EBT3 film and Epson scanner, and the uncertainties were deemed acceptable.

4.3.2.1 Gafchromic EBT3 film

Gafchromic EBT3 film (International Specialty Products, ISP, Wayne, NJ) is one tool used in radiation therapy for pre-treatment quality assurance of IMRT and VMAT (Borca *et al*., 2013) and it was introduced in 2011 (Toossi *et al.*, 2016). Gafchromic EBT3 films are used to measure an absorbed dose of ionizing radiation. EBT3 films are distributed in a standard size of 20.3 × 25.4 cm^2 and have 25 sheets per box. These films are separated from one another by sheets of paper and stored in a black envelope. The manufacturer recommends keeping the unexposed films at a temperature of less than 25°C.

Gafchromic EBT3 film is made of a single 28 µm thick sensitive active layer of microcrystalline diacetylene suspended in gelatin (Battaglia *et al*., 2016) coated on all surfaces with a symmetric polyester substrate. The substrate protects the inner active layer making EBT3 films suitable for use in water. The active layer has yellow marker dye that helps to decrease UV/light sensitivity and films can be used for

multichannel dosimetry when used together with an RGB film scanner (Barco *et al*., 2013).

The matte surface polyester substrate contains microscopic silica particles which create a gap between the film surface and the glass window of the flatbed scanner. This gap, together with the matte substrate, helps prevent the formation of Newton's rings (interference patterns) in images obtained using flatbed scanners (Leon Marroquin *et al*., 2016 and Borca *et al*., 2013).

The elemental composition of EBT3 Gafchromic EBT3 films is as follows: the active layer consists of H (56.8 %), Li (0, 6%), C (27, 6 %), O (13.3 %), and Al (1, 6 %). The matte surface clear polyester base consists of H (36.4 %), C (45.5 %), and O (18.2 %) (Loen Moarroquin *et al*., 2016). The active layer has a density of 1.20 g/cm^3, and the matte polyester base density is 1.35 g/cm^3 (Bekerat *et al*., 2014).

The most convenient material for a dosimetric procedure is water, with an effective atomic number of Z_{eff} = 7.42 and a density of 1g/cm (Hossein, 2015). Gafchromic EBT3 film has an effective atomic number Z_{eff} of 7.26, as stated by the manufacturer, which corresponds closely to the Z_{eff} of water when compared to similar films. Gafchromic EBT3 film has an optimum dose range of 0.2 -10 Gy which makes the film suitable for IMRT and VMAT quality assurance (Gafchromic EBT3 specifications, 2020).

Dosimetry using Gafchromic EBT3 film is based on the colour change during irradiation exposure (Loen Moarroquin *et al.,* 2016). The colour of the film changes to shades of blue when exposed to ionizing radiation. The darkening of the film increases with increasing absorbed dose. The dose information, as shown in Fig. 4.15. is retrieved by a light transmission measurement through the darkened area given by (Papaconstadopoulos *et al.*, 2014)

$$T = \frac{I_T}{I_O} \quad \text{.....} \quad (4.\ 2)$$

where I_T is the transmitted light intensity and I_O is the incident light intensity.

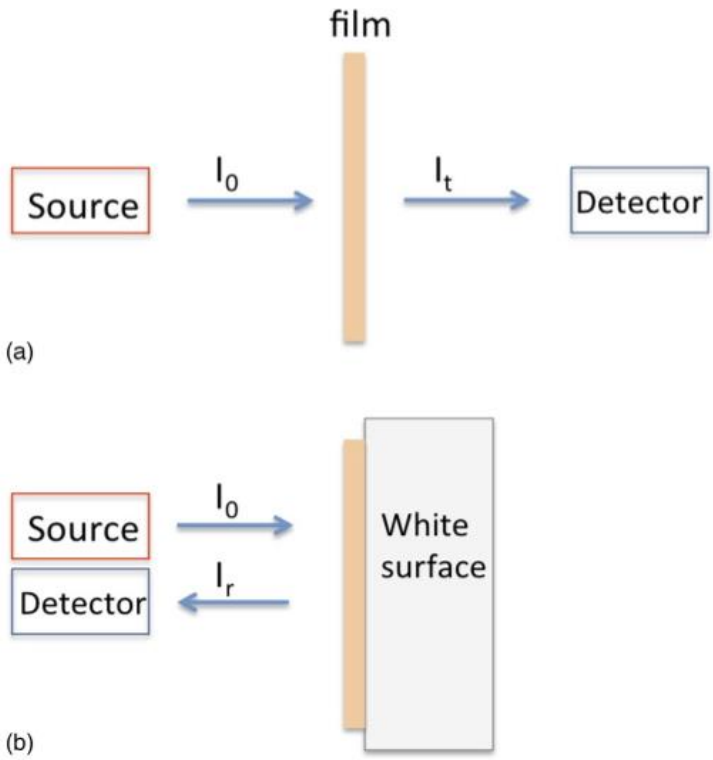

Figure 4. 15: Graphical representation of film scanning using the transmission (a) and reflection (b) measurements.

The change in intensity during the passage of film material is measured as the optical density d_x *(OD)* of the film,

$$OD = log\frac{I_T}{I_o} \quad \text{..... (4. 3)}$$

The film calibration curve is plotted in terms of netOD versus dose.

The equation that is recommended by the manufacturer to fit the calibration curve is given by

$$d_x\,(OD) = \frac{a+b}{D+c} \quad \text{..... (4. 4)}$$

Where $d_x\,(OD)$ is the optical density of the film scanner *x* at dose *D*, and *a*, *b*, *c* is the equation parameter to be fitted (Gafchromic EBT3 specification, 2020).

4.3.2.2 Film scanner

The optical density d_x of the film is determined by digitizing the image using a colour flatbed scanner and measurement of the film pixel value/response value in three colour channels, red, green, and blue (RGB) of the visible spectrum (Hossein, 2015). The absorbance spectrum of the active layer has a peak at 636 nm after exposure to ionizing radiation. The use of the red channel is recommended for analysing films (di Scienze, 2017). The red colour channel has a sensitive response to radiation for EBT3 up to 10 Gy, while the green colour channel enables high dose measurements between 8 - 40 Gy and the blue colour channel is used to enhance the uniformity due to a marker dye in the active layer (Gafchromic EBT3 specification, 2020).

Figure 4. 16: Epson perfection V750 PRO scanner used in this study.

The scanner used in this study is an Epson perfection V750 PRO (US Epson, Long Beach, CA) shown in Fig. 4.16 and its technical detains are tabulated in Table 4.3.

Table 4. 3: Technical details of EPSON perfection V750 PRO

Manufacturer	Epson
Model	Perfection V750 Pro
Maximum document size	216 mm X 297 mm
Supported document type	Transparencies, plain paper, films
Optical resolution	Main 6400 dpi x sub 9600 dpi
Optical resolution	640 dpi (horizontal and vertical)
Optical density	4 D_{max}
Scanner type	Flatbed scanner
Optical sensor	Matrix CCD
Scanning colour depth	48-bits
Light source	Cold cathode fluorescence lamp

4.4 Film calibration methods

The film calibration curve for the 6 MV and 15 MV photon beams was created using the RW3 solid water phantom. The dependence of film energy was also assessed using these beam energies.

4.4.1 Treatment planning preparation

Dose distribution plans of various doses ranging from 0.25 – 6 Gy were generated using 6 MV and 15 MV photon beams of 10 × 10 cm^2 field size in an Eclipse treatment planning system (TPS) version 16.1 (Varian medical system, Palo Alto, CA). Ten treatment plans for these doses were calculated using the Analysis Anisotropic Algorithm (AAA) at a depth of 10 cm and SSD of 90 cm in a solid water phantom for 6 MV and 15 MV photon beams.

Twelve plans were also calculated with six plans prescribed to 1 Gy at different dose rates (100, 200, 300, 400,500 and 600 MU/min) and another six plans prescribed to 2 Gy prescription at different dose rates. These plans were used for the dose rate dependence check of the Gafchromic EBT3 film.

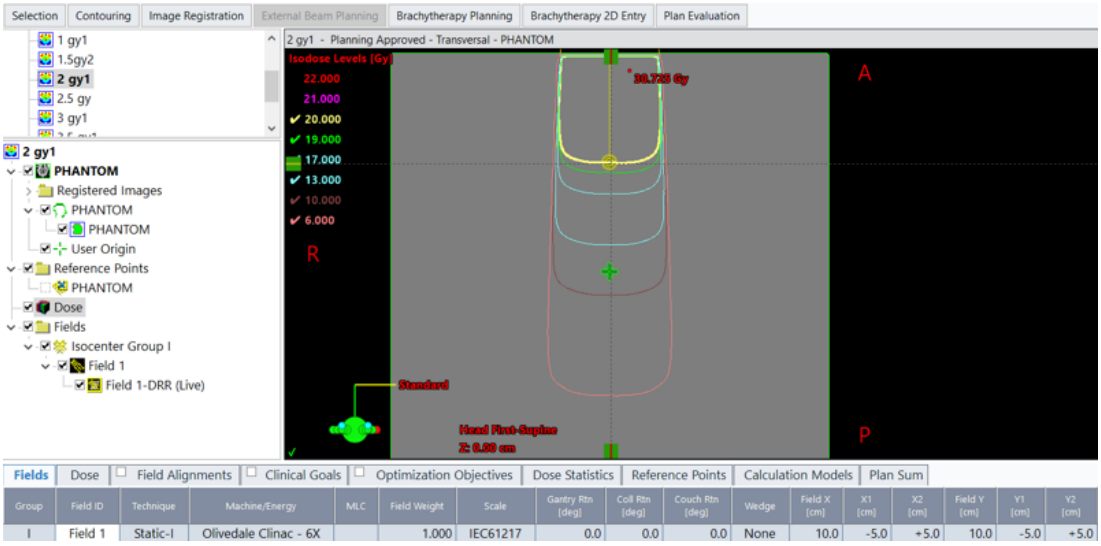

Figure 4. 17: Treatment plan dose distribution of a 6 MV photon beam of 2 Gy prescription dose normalized at isocentre (yellow isodose line) from the Varian Eclipse treatment planning system (Eclipse treatment planning system (TPS) (Varian Medical Systems, Palo Alto, CA)).

4.4.2 Verification of the TPS calculated dose

The Linac was calibrated using the International Atomic Energy Agency Technical Report Series (IAEA TRS) 398 protocol, which is based on standards of absorbed radiation to water, to deliver 1 cGy per monitor unit (MU) at dose maximum (D_{max}) of all energies. The output of the Clinac IX linear accelerator machine (Varian Medical System, Palo Alto, CA) was examined prior to the calibration of the films. The 0.6 cc PTW 30013 waterproof calibrated Farmer ionisation chamber (PTW, Freiburg, Germany) was used for photon beams.

The dose at a depth for both the 6 MV and 15 MV photon beams in which film irradiation was carried out was verified using the TRS 398 protocol. The ten generated plans for the field size of 6 MV and 15 MV photon beams with prescribed doses ranging from 0.25 – 6 Gy were verified in a water phantom at a depth of 10 cm and source to surface distance (SSD) of 90 cm using a 0.6 cc PTW waterproof farmer ionization chamber.

The PTW Multidos electrometer connected to the chamber gave the readings (charges nC) which were converted into dose (Gy) using the following formula:

The absorbed dose to water for high-energy photons is calculated using

$$D_{w,Q}(Z) = M_Q N_{D,W,Qo} K_{Q,Qo}\ K_P\ K_s\ K_{TP} \quad \text{..... (4. 5)}$$

where: M_Q is the dosimeter reading obtained under reference conditions with the chamber's reference point positioned at Z_{ref},

$N_{D,W,Qo}$ is the calibration factor (absorbed dose to water) for the dosimeter at the reference beam quality Q_o.

$K_{Q,Qo}$ is the chamber-specific adjustment factor that balances the variations between the reference beam quality and the actual beam quality,

Only the reference circumstances that are used for the calibration are valid for an ionization chamber's calibration factor. When using the ionization chamber, any deviation from the reference conditions should be compensated for using the relevant factor.

Polarity correction factor

K_P is the polarity correction factor, and it is typically brought on by the collecting electrode of the ionisation chamber capturing some of the initial electrons.

The correction factor for polarity in a given radiation beam is given by:

$$k_{pol} = \frac{|M_+| + |M_-|}{2M} \quad \text{..... (4. 6)}$$

Where M is the electrometer measurement acquired at the commonly used polarity, M_+ and M_- are the electrometer readings obtained at positive and negative polarity, respectively. The polarity that is often utilised is the same as the polarity that is used to calibrate the ionisation chamber.

Ion recombination factor

K_s is the ion recombination factor, and the employment of a correction factor k_s is necessary due to the incomplete collection of charge in an ionisation chamber cavity caused by ion recombination. There are two distinct effects: (i) general (or volume) recombination, which is the recombination of ions formed by various ionising particle tracks and is dependent on the density of ionising particles and, consequently, on the dose rate; and (ii) initial recombination, which is the recombination of ions formed

by a single ionising particle track and is independent of the dose rate. The applied polarising voltage and the chamber shape affect both effects. K_s is the ion produced by and is measured at +400V and 200V.

$$k_s = \frac{\left(\frac{V_1}{V_2}\right)^2 - 1}{\left(\frac{V_1}{V_2}\right)^2 - \frac{M_1}{M_2}} \quad \text{(4. 7)}$$

Where M_1 is the reading in volts (V_1) at 400V, and M_2 is the measurement in volts (V_2) at 200V. In conventional radiotherapy beams, initial recombination is less than 0.2%.

- **Pressure and temperature air polarity correction**

K_{TP} is the adjustment to the air polarity. All the chambers are exposed to outside air, causing variations in the air cavity's mass. Applying the adjustment factor will bring the cavity air mass into compliance with the reference conditions.

$$K_{TP} = \left(\frac{273.2+T}{273.2+To}\right)\left(\frac{Po}{P}\right) \quad \text{(4. 8)}$$

Where P and T represent the temperature and amount of cavity air present at the moment of the measurement, and P_o and T_o represent the standard values. Table 4. 4 below lists these values.

Table 4. 4: Parameters used for dose calculation for photon beams.

Energy	N_{DW} (x 10^7)	Depth (cm)	T & P $_{corr}$	$K_{Q,Q0}$	Field size (cm^2)	SSD (cm)
6 MV	0.05396	10	1.17	0.993	10 x10	90
15 MV	0.05396	10	1.17	0.974	10 x 10	90

4.4.3 Film calibration and Irradiation procedure

The films used in this study were obtained from batch number 11091601. Gafchromic EBT3 film sheets of 20.3 × 25.4 cm^2 were divided into pieces with dimensions of 3 × 4 cm^2. The films were handled with care using gloves to avoid fingerprints. Three EBT3 films from the same batch were used for this study.

The film pieces were exposed to 0.25, 0.5, 1.0, 1.5, 2.0, 2.5, 3.0, 3.5, 4.0, and 6.0 Gy consecutively, at a depth of 10 cm in an RW3 solid water phantom with 10 cm of solid water placed below the film to provide backscatter radiation. A source to surface distance (SSD) of 90 cm was set for the 6 MV and 15 MV photon beams with a dose rate of 600 MU/min. This is the highest photon dose rate produced by a Clinac IX linear accelerator (Varian Medical Systems, Palo Alto, CA). The field size was set at 10 × 10 cm^2 and the gantry was positioned at 0^o as planned on TPS. An illustrative diagram for the set-up is provided in Fig.4.18 below.

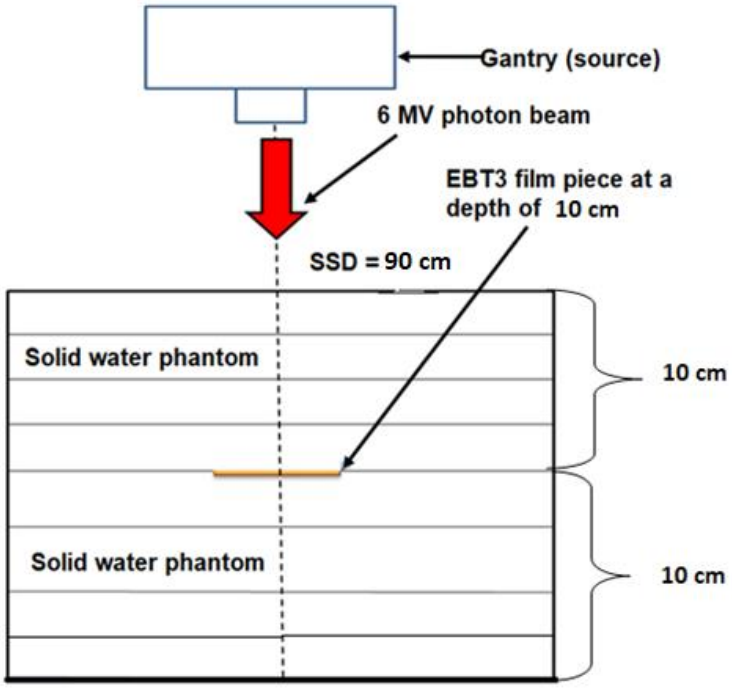

Figure 4. 18: Schematic diagram showing the Gafchromic EBT3 film setup sandwiched in a RW3 solid water phantom for irradiation.

The film pieces were placed at the isocenter of the linear accelerator, with a source –axis distance (SAD) setup at 100 cm as shown in Fig.4.19 below. The films were sandwiched between the 20 cm (10 cm at the bottom and 10 cm at the top) solid water phantom plates and the plates were taped together to close the gap between them.

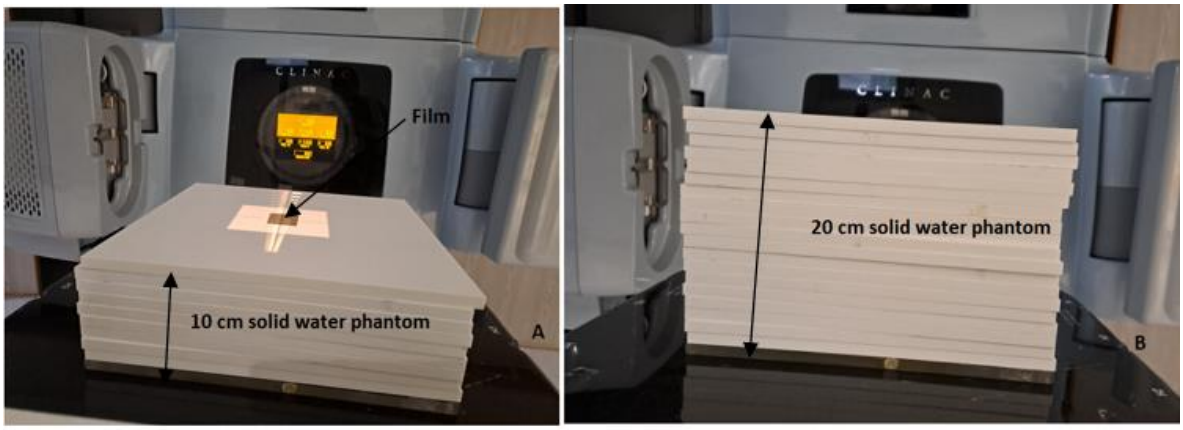

Figure 4. 19: The placement of film (A) on top of the 10 cm RW3 solid water phantom (30 x 30 cm^2) and (B) the film is sandwiched between the 20 cm solid water phantom.

There are factors which contribute to the total uncertainty of the dose determination that must be assessed to ensure that the uncertainty is acceptable. These factors include scanner reproducibility, scanner uniformity, scanner parameters, film orientation dependence, scanner lateral response, film dose rate dependence, film energy dependence, and film uniformity, as depicted in Fig.4.20 and explained further below.

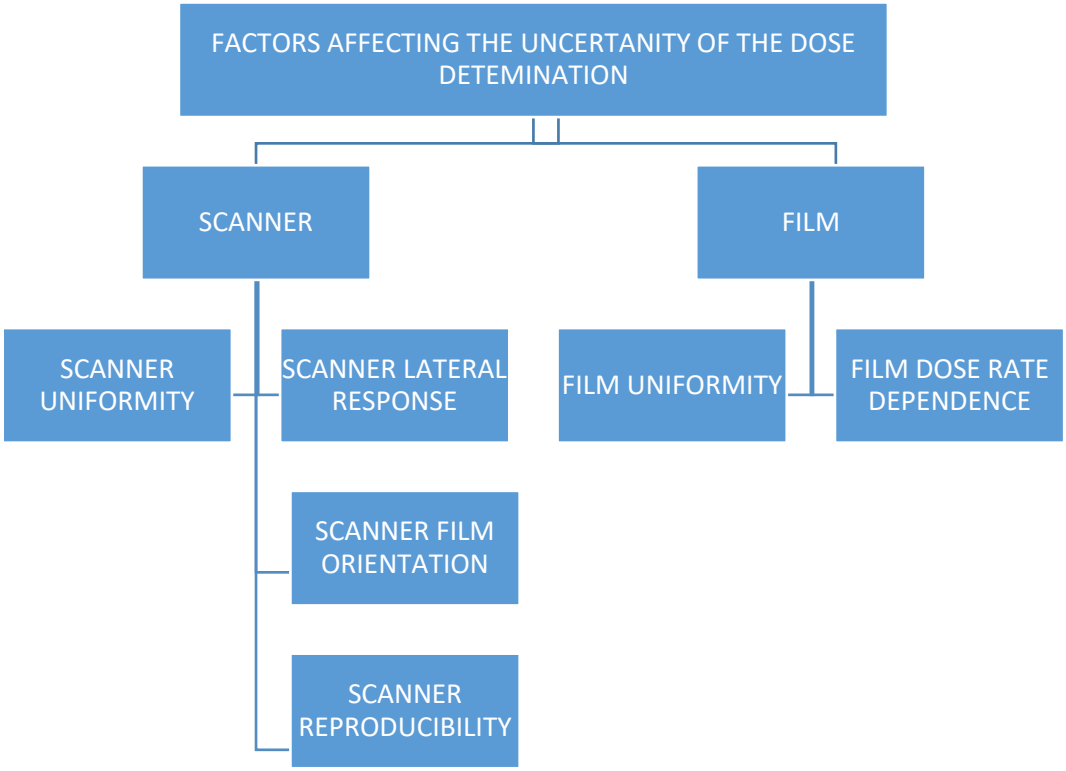

Figure 4. 20: The factors affecting the uncertainty of the dose determination**.**

4.4.3.1 Scanner reproducibility

Before scanning the film, 5 blank scans without films and zero-light transmitted intensity, were performed to warm up the lamp of the scanner and to eliminate the effects of scanner noise. The exposed films were scanned by an Epson Expression V750 PRO flatbed colour scanner (Epson America Inc., Long Beach, CA, USA) 24 hours after irradiation and in landscape orientation. Epson Scan software was applied to read all the transmitted raw intensity values used in this study.

There are two types of scanner reproducibility namely: short term and long-term reproducibility.

- The short-term reproducibility of the scanner was evaluated by performing 5 consecutive scans of a single unexposed (zero dose) 3 × 4 cm^2 film piece obtained from the same sheet of film. This test is to assess the change in scanner lamp output by determining the effect of variation in the background optical density. The standard deviation in the mean response used to estimate the uncertainty of pixel value at the center of the scanner is given by

$$SD = \sqrt{\frac{1}{N}\sum_{i=1}^{N}(x_i - \overline{x})^2} \quad \text{..... (4. 9)}$$

where x_i is the pixel value and $\overline{x}$ is the average pixel value

The standard deviation (SD) of the film piece calculated shows the highest uncertainty of 1.2, 2.8, and 1.7 for red, green, and blue channel, respectively. The highest percentage difference of 0.02 %, 0.05 % and -0.05 %, respectively as shown in Table B.1 in the appendix.

- The long-term reproducibility was evaluated according to Hanušová *et al.,* (2016) by scanning the same pieces of films at set intervals after irradiation (3 hours, 7 days, and 13 days). This determines the uncertainty of the mean response value for all red-green-blue (RGB) channels. For better uniformity each exposed film with dose levels from 0.25 – 6 Gy was scanned 3 consecutive times at the center of the scanner bed with an image resolution

of 72 dots per inch (dpi) (0.35 × 0.35 mm^2 pixel size) and a 48-bit (16 bits per colour channel) RGB colour scheme.

At the beginning of the scanning procedure, the image colour corrections were turned off to ensure that only raw data was obtained as shown in Fig. B.1 in the appendix. All films were positioned in landscape orientation at the center of the scanner. Each film was catalogued with a number to reference information such as dose, energy, dose rate, etc. The raw images of films were saved as tagged image file format (TIFF). The scanned images were exported to ImageJ (version 152) software (National Institutes of Health, Bethesda, MD) for analysis. A 2 × 2 cm^2 at the center of each film was selected to obtain the mean value of the transmitted light intensity (I).

The standard deviation to estimate the uncertainty of long-term reproducibility was computed using Equation 4.9 and the percentage difference was computed using the following formula.

$$\% \, difference = \left| \frac{x_0 - x_i}{x_0} \right| X \, 100 \quad \text{.....} \quad (4.10)$$

where x_0 is the response value on the first day of the scan and x_i is the response value obtained on different days after the first scan. The graph of the response/pixel response versus the time is plotted.

Figure B.2 and Table B.2 in the Appendix shows the dose-response of different prescribed dose levels (0.25 - 6 Gy) of the film scanned at different time intervals. The films used for this test were irradiated at 10 cm in a solid water phantom for a 6 MV photon beam at a field of 10 × 10 cm^2. The long-term reproducibility of the Epson Perfection V750 flatbed scanner was evaluated for time intervals of 0 minutes (day 1) (24 hours after film irradiation, 3 hours (day 2), 7 days (day 3) and 13 days (day 4) between scans.

The standard deviation of the long-term reproducibility of the scanner was evaluated based on the dose-response of the films scanned on a different day with respect to dose-response of film scanned on the first day (day 1). The highest percentage difference of dose-response calculated is 0.58 % obtained on day 4 for the 2 Gy prescribed dose for the red channel.

4.4.3.2 Scanner uniformity

The scanner non-uniformity response correction is important because each charge-coupled device detector of a document scanner has a different sensitivity, and the light source may have non-uniform light intensity. In addition, the light source of scattered light photons depends on the film location on the scanner bed (Wen *et al*., 2016).

The uniformity of the scanner was evaluated by scanning 3 × 4 cm^2 pieces of unexposed film (0 Gy), 1 Gy film and 2 Gy film at different positions (positions at the center of the scanner, 1, 4, 13 and 16) within the scanner glass window. The positions considered are indicated in Fig.4.21 below with 1 being the top left, 4 top right, 13 bottom left, and 16 bottom right of the scan glass window.

For each position, the same films were scanned 3 times and the average of the response/pixel value was calculated. The mean response value of each scanned image is denoted by *x*.

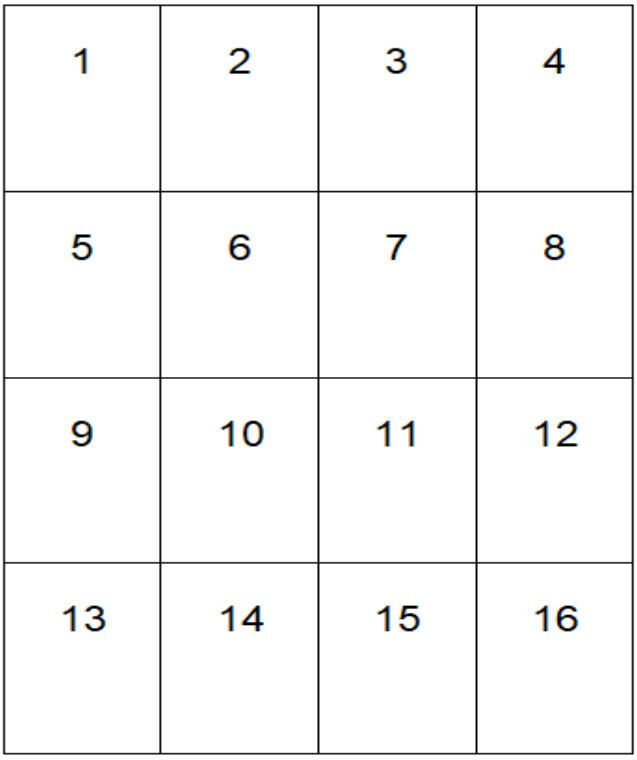

Figure 4. 21: The position of the film in a scanner glass window for scanner uniformity.

The uniformity of the scanner denoted by U_S over a given region is calculated as

$$U_S = \frac{x_{max} - x_{min}}{x_{mean}} \quad \text{..... (4. 11)}$$

where x_{max} is the maximum response value, x_{min} is the minimum response value and x_{mean} is the mean response value of the positions considered in the scanner. If the response value across the scanner is the same the uniformity would be zero.

The scanner uniformity was calculated by subtracting the lowest dose-response from the maximum dose-response and dividing it by the mean dose-response for each channel obtained from different positions of the scanner glass widow. The dose responses obtained in different scanner positions are shown in Table B.3 in the appendix. The scanner uniformity of the Red channel was 0.057 (5.7 %), the green channel was 0.038 (3.8 %) and the blue channel was 0.041 (4.1 %) for 1Gy prescribed dose. For the 2Gy prescribed dose, the red channel uniformity is 0.058 (5.8 %), the green channel was 0.034 (3.4 %) and the blue channel was 0.045 (4.5 %).

The dose-response at a different position for 1 Gy and 2 Gy prescribed dose uniformity results were almost the same for both channels. The difference in the dose-response of the film placed further away from the central axis of the flatbed scanner was 5.8 % for the red channel, 3.8 % green channel, and 4.5 % for the blue channel. These results were consistent with those reported by Loen Marroquin *et al.*, (2016). They found that the difference in the response of the films placed furthest from the central axis of the scanner was 5.0 % for the red channel, 7.0 % for the green channel and 10.0 % for the blue channel.

4.4.3.3 Scan Lateral response

The lateral direction is defined as being perpendicular to the scaling direction of travel of the scanning lamp, with zero lateral displacements representing the center of the scan plane (Palmer *et al.*, 2015). The lateral scan effect was evaluated by scanning the same film in portrait orientation at a different specific lateral position of

the scanner. A paper graph was attached to the scanner window from the user's left and the right of the scanner as shown in Fig. 4.22 below.

Three films of different dose levels (0 Gy, 1 Gy, and 2 Gy) were used for this test. Each film was scanned 3 times in the same position and the average was calculated. The lateral positions in which the film pieces were scanned were 4 cm, 8 cm, and 12 cm in both directions (left taken as negative direction and right as positive direction) from the center of the scanner.

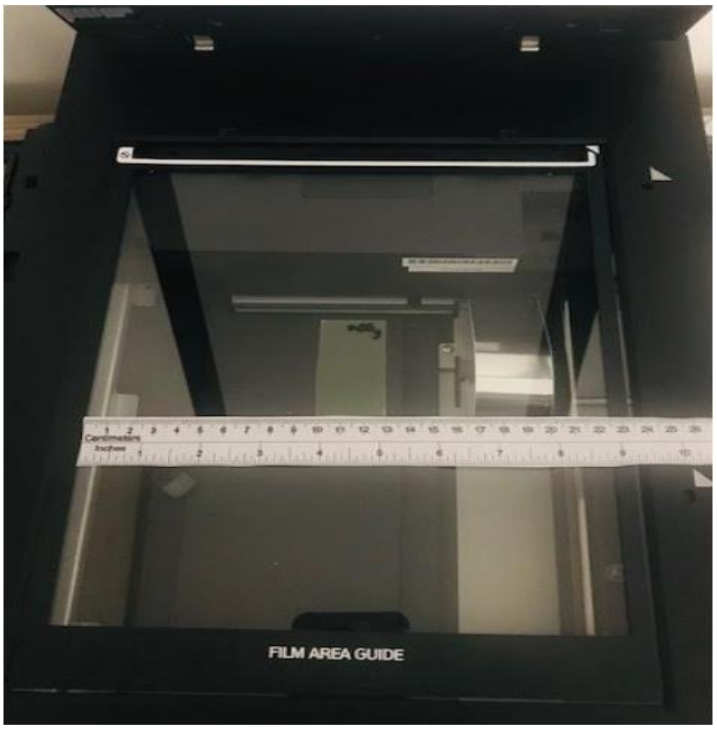

Figure 4. 22: A film positioned at the center of the scanner and a paper graph attached from left to right of the user.

The standard deviation of the different locations was computed using the following equation

$$SD = \sqrt{\frac{1}{N}\sum_{lp=1}^{N}\left(x_{Lp} - \overline{x}\right)^2} \quad \text{..... (4. 12)}$$

where x_{Lp} is the response value at a specific lateral position and $\overline{x}$ is the average response value at the centre of the scanner and a specific lateral position.

The percentage difference in film dose at 4 cm, 8 cm, and 12 cm in both positive and negative directions of lateral distance compared to the film dose on the central axis of the scanner was computed by using equation 4.13 below.

$$\%\, difference = \left|\frac{x_c - x_{lp}}{x_c}\right| X\ 100 \quad \text{..... (4. 13)}$$

where x_c is the response value at the center of the scanner and x_{lp} is the response value of a different lateral position.

Table B.4 in the Appendix shows the lateral scanner responses effect of film doses of 0.5 Gy, 1.0 Gy, and 2.0 Gy. The highest percentage difference in film dose-response was found to be at a 9 cm lateral distance compared to the film dose on the central axis of the scanner. At 0.5 Gy there was 2.4 % for both red and green channel and at 1 Gy was 2.6 % at -9 cm lateral distance for the red channel and at 2 Gy was 1.6 % at 9 cm lateral distance for the red channel.

The results show diminishing accuracy for the films scanned further away from the central axis of the scanner. The results for positive and negative displacements in the lateral direction, suggest that the higher the film prescribed dose the less the percentage difference.

4.4.3.4 Scanner film orientation

The scan response of radiographic films is sensitive to the orientation of the film on the scanner for two reasons: (1) the anisotropic scattering of photons emitted by the scanner when passing through the polymer network. (2) The polarization of the transmitted light by needle shaped particles in the film active layer aligned parallel to the direction in which the film was coated (Barca *et al*., 2013).

The dependence of the film orientation on the relative scanning orientation was investigated by scanning the 3 × 4 cm^2 film pieces with dose levels ranging from 0.25 - 6 Gy and irradiated with a 10 × 10 cm^2 6 MV photon beam at a depth of 10 cm in an RW3 solid water phantom in the landscape and portrait orientations at the center of the scanner.

Landscape orientation is defined as the long axis of the film being parallel to the linear light source. Portrait orientation is defined as the long axis of the film being perpendicular to the linear scanner light source (Matney *et al*., 2010) as illustrated in Fig.4.23 below.

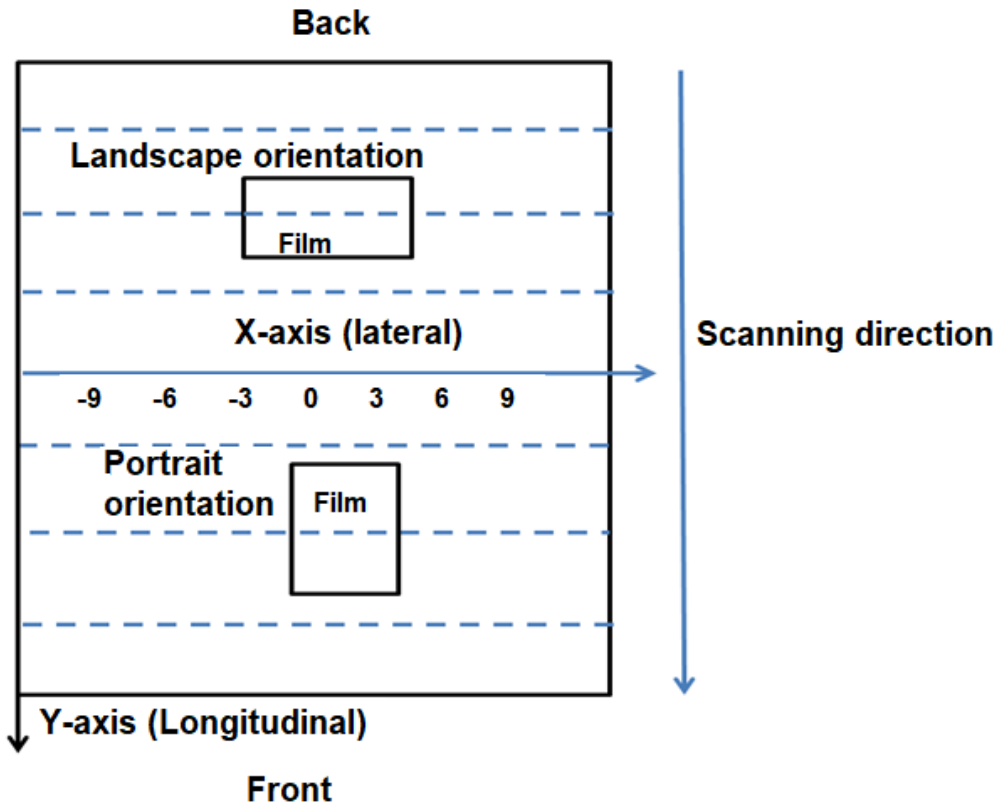

Figure 4. 23 : Schematic diagram of the coordinate axes x (lateral) and y (longitudinal), and the film orientations on the scan window for calibration films.

As shown in Fig.4.23 above, the scanning direction is from back to front, while the lateral position on the scanner is from the user's left (negative side) to right (positive side) paralleled to the x-axis from the center of the scanner. The light tube of the scanner moves along the longitudinal direction (Y-axis). Avoiding the edges of the glass plate is recommended since scan response in that area can be inaccurate (van Battum *et al*., 2008).

The percentage difference between the landscape and portrait response was computed using the following equation.

$$\%\, difference = \left| \frac{X_{landscape} - X_{Portrait}}{X_{landscape}} \right| X\ 100 \quad \text{..... (4. 14)}$$

where $x_{landscape}$ and $x_{Portrait}$ are the mean film response at each dose level in landscape and portrait respectively

The graph of response value versus the dose for 6 MV photon beam was plotted for both landscape and portrait measurements as illustrated in Fig.B.3 in the Appendix. The results indicate that the dose-response between portrait and landscape for the EBT3 film shows the highest percentage difference of 1.6 % for the red channel and 1.7 % for the green channel as shown in Table B.5 in the appendix.

4.4.3.5 Film uniformity

To evaluate the film uniformity, half sheet of Gafchromic EBT3 film sheet was cut into 6 pieces, each one of them exposed to 1Gy of 6 MV photon beam in a solid water phantom at a depth of 10 cm at an SSD of 90 cm. The films were analyzed by selecting a region of interest of 2 × 2 cm^2 and each film piece read 3 times at the center of the scanner. The readings for each film were averaged.

The film uniformity was computed by using

$$U_f = \frac{X_{max} - X_{min}}{X_{mean}} \quad \text{..... (4. 15)}$$

where X_{max} is the maximum response value, X_{min} is the minimum response value and x_{mean} is the mean response value of the positions in the film sheet.

The film uniformity is calculated by subtracting the lowest dose-response from the maximum dose-response and dividing by the mean dose-response for each channel obtained from different positions of the scanner glass widow. The dose-response for the different position of the film is tabulated in Table B.6 in the appendix. The non-uniformity of the film was 0.0041 (0.4%) for the red channel, 0.0014 (0.14%) for the green channel, and the 0.0027 (0.3%) for the blue channel for 1Gy prescribed dose. These results are consistent with those reported for EBT3 film by Loen Marroquin *et al.* (2016) and Barco *et al*. (2013). They both found a non-uniformity of less than 0.2 % and less than 1 % respectively for the red channel.

4.4.3.6 Film dose rate dependence

12 pieces of film (3 × 4 cm^2) were used to test the dose rate dependence. Each film piece is catalogued by a number that corresponds to the dose and dose rate of that film piece. The dose rates considered in this test are 100, 200, 300, 400, 500, and 600 MU/min for 1 Gy and 2 Gy prescribed plans. These are the dose rates available for the linear accelerator used for photon beam energies. The film pieces were positioned at the center of the scanner and scanned 3 consecutive times. The average was calculated with the corresponding standard deviation of each dose rate for 1 Gy and 2 Gy and was computed using Equation 4.9.

The measurement results showed no significant differences in dose-response were detected for the six dose rate values, which confirms that EBT3 films are independent of dose rate as shown in Table B.7 and Fig.B.4. Differences between the dose rates were negligible with a standard deviation of less than 10 and the highest percentage difference of 0.5 % at 1 Gy prescribed dose and 0.4 % at 2 Gy prescribed dose. The percentage difference is calculated by taking the response obtained at 600 MU/min dose rate as the reference. This dose rate is the highest dose of the photon energy and is mostly used for all static fields for the photon beam at the unit.

4.4.4 Film calibration curve

Before determining the film calibration curve the following tests were done: Comparing the dpi for different channels and comparing the different bits keeping the same dpi for different channels,

The film scanning procedure is explained in section 4.4.3. These films shown in Fig.4.24 were used to determine the calibration curve for 6 MV photon beam. The film piece number that corresponds to the dose and energy is also indicated. The Gafchromic EBT3 film calibration pieces irradiated to doses in the range 0 - 6 Gy using 15 MV photon beam are shown in Fig.B.5 in the appendix.

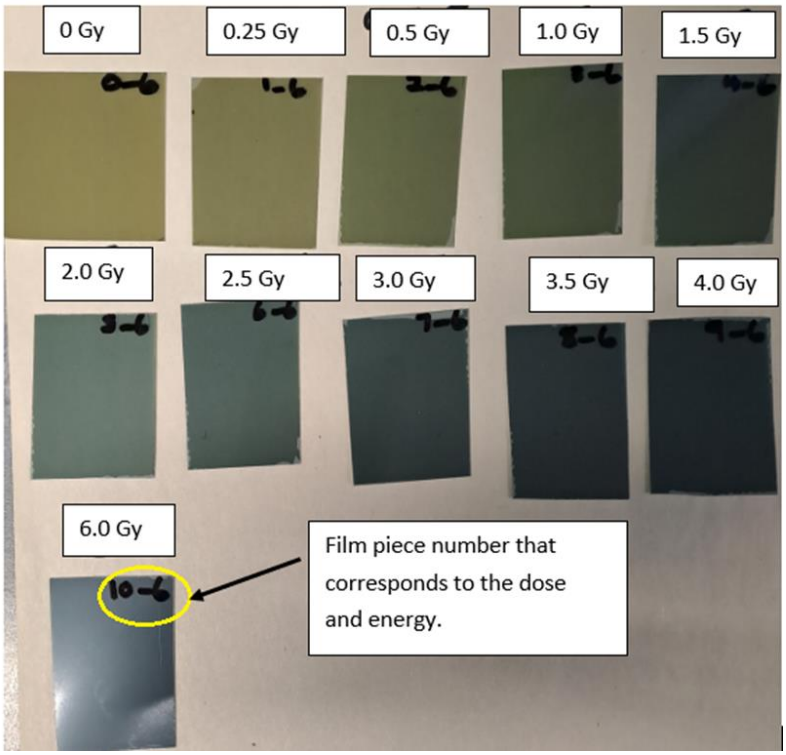

Figure 4. 24: Gafchromic EBT3 film calibration pieces irradiated to doses in the range 0 - 6 Gy using a 6 MV photon beam.

The physical principle of Gafchromic EBT3 film is represented by a colour change in response to radiation exposure. The Gafchromic EBT3 film is characterized by the net optical density (netOD). The netOD is related to the intensity (I) by the Lambert-Beer law (Loen Marroquin *et al*., 2016) and expressed as

$$netOD = -log_{10}\frac{I_T}{I_O} \quad \text{..... (4. 16)}$$

where I_o and I_T are the response values for the unexposed (mean response value of films) and exposed film pieces, respectively. For film analysis, raw response values from the red and green channels are converted into net optical density value (netOD).

A plot of netOD versus delivered dose was made for all ten dose points for the 6 MV photon beam and another ten points for the 15 MV photon beam. This served as the calibration curve for the film batch used. Film dosimetry uncertainty is defined as the fluctuation in dose-response across the irradiated field.

The overall uncertainty of the net optical density (SD (netOD)) is computed using the following equation

$$SD(netOD) = \frac{1}{ln\,10}\sqrt{\left(\frac{SD\ (I_O)}{I_O}\right)^2 + \left(\frac{SD(I)}{I}\right)^2} \quad \text{..... (4. 17)}$$

Where *SD (I_o)* and *SD (I)* are the associated standard deviations I_o and *I* respectively.

The highest net optical density standard deviation for both red and green channels was found to be 0.0013.

4.4.5 Prostate point dose measurements using Gafchromic EBT3 film

Gafchromic EBT3 film from the same batch of films used for determining the calibration curve was cut into rectangular strips of 0.8 × 5 cm^2. A mark was made on a corner of each film strip to monitor the orientation of the strip. The film strips were then placed onto a plastic rod with the film parallel to the axis of the rod as shown in Fig.4.25 below.

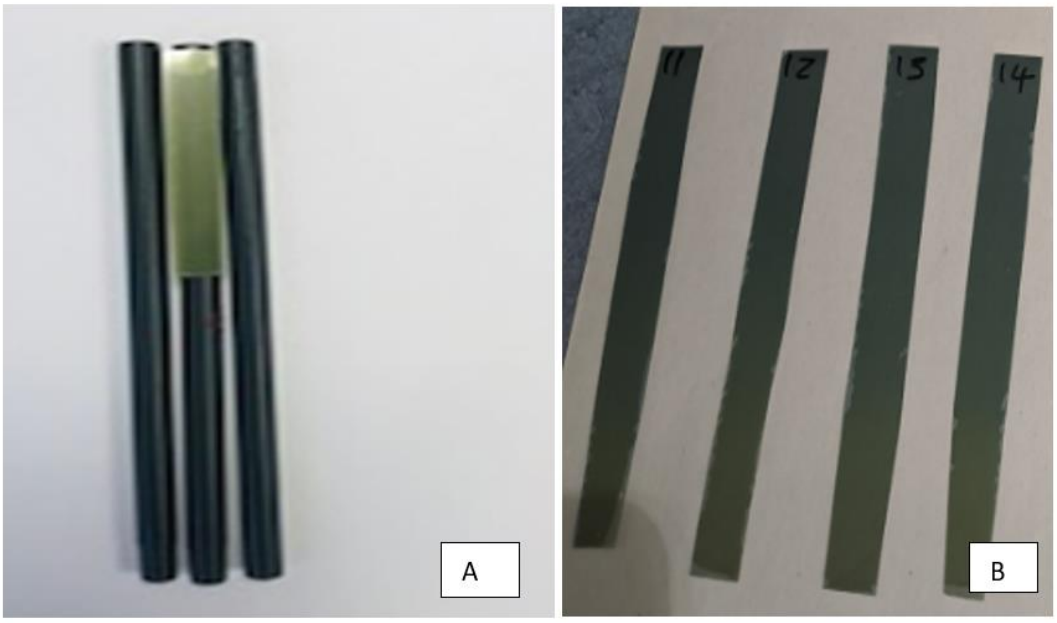

Figure 4. 25: (A) The Gafchromic EBT3 film pasted on a plastic rod and (B) numbered exposed films.

The rod with Gafchromic EBT3 films attached was inserted inside the prostate cavity and irradiated for each plan. IMRT and VMAT plans were delivered on the phantom. A line was drawn on the surface of the rod to ensure the unrotated insertion of the rod into the cavity (Ganapathy *et al*., 2013). After irradiation, the films were scanned using the Epson scanner by applying the red channel of RGB colour as shown in Fig.4.26. The pixels were converted into doses using the film calibration curve.

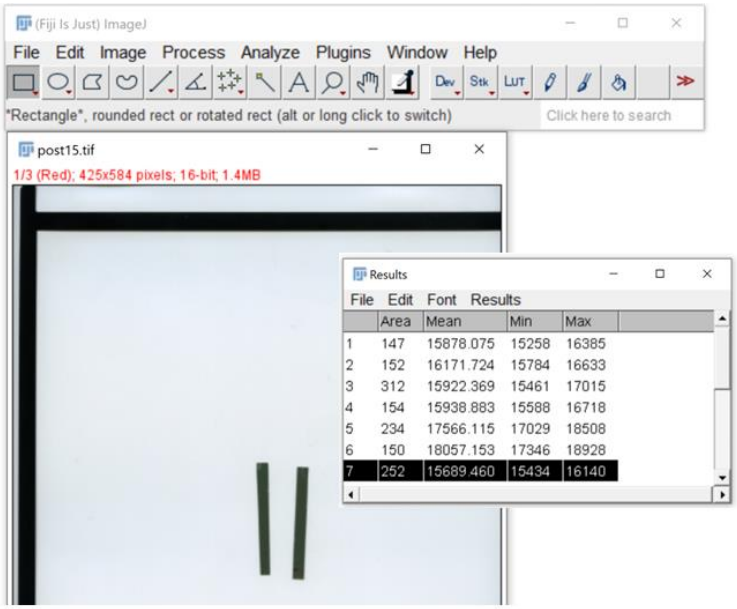

Figure 4. 26: Example of analysis of scanned irradiated Gafchromic EBT3 film using ImageJ program and corresponding pixel readings**.**

The doses measured with the ionization chamber and Gafchromic EBT3 films were compared with the prostate point dose from TPS-generated plans.

4.5 Artifact correction

For the second experiment, the O-MAR CT data sets were registered/fused to the CT data sets without artifact reduction. The contoured structures from the CT data without artifact reduction were copied into the O-MAR CT data sets. All the plans including IMRT and VMATs created in the first experiment were copied into the registered O-MAR CT data sets and calculated. The dose volume histogram of the plans with and without artifact density corrections were compared.

The Gafchromic films were also used to evaluate the discrepancy between the TPS calculated dose and measured dose for plans created using O-MAR CT data sets.

According to TECDOC 1540, the relative error $\delta(\%)$ between the film measurements and TPS calculations is computed as follows

$$\delta(\%) = \left[\frac{(D_{TPS} - D_{film})}{D_{film}}\right] X100 \quad \text{..... (4. 18)}$$

Where D_{film} is the dose obtained from film measurements and D_{TPS} is the TPS calculated dose.

4.6 EGSnrc Monte Carlo simulation

This section covers the Monte Carlo simulation on the Varian Clinac IX linear accelerator for validation of MC code and verification of prostate point dose calculations in an in-house pelvic phantom. The validation of MC code is done by simulation the dose distribution (PDD and profiles) and compare to the commissioning or experimental dose distribution.

Radiotherapy treatment aims to give the target/tumour volume a suitable absorbed dose to obtain tumour control with low-risk complications. The knowledge of absorbed dose distribution within a patient is based on its measurements in water in terms of PDD and the beam dose profiles or off-axis ratio (OAR). Detailed analysis of PDD helps to select the appropriate beam for radiotherapy treatment when a variety of beam energies are available as the attenuation and penetration parameters of photon beams differ with different parameters such as field size.

Dose distribution along the beam central axis is used in conjunction with off-axis profiles to deliver an accurate dose prescription inside the patient. The procedure used to measure the experimental/commissioning dose distribution using the linear accelerator is discussed in this section.

4.6.1 Linac Beam Commissioning Data

Successful radiotherapy treatment depends on the accuracy of the dose delivered to the patient which directly depends on the accuracy of the beam data used in the TPS. Beam data commissioning plays a vital role in accurate radiation treatment. The commissioning process involves measuring all data required for treatment planning system dose calculation in different field sizes (Lui *et al*., 2023). The data collected must also meet the manufacturer's performance standards.

The photons and electrons of different energies travel different distances in the medium, allowing treatment of tumours at various depths. In the case of photons, the energy is specified in terms of the nominal accelerator potential/beam energy (MV or MeV), as well as in terms of a parameter which indicates a penetrative quality of the beam. The penetrative quality indicator of the photon is the percentage depth dose at 10 cm depth for 10 × 10 cm^2 field size at the phantom surface and 100 cm source surface distance (SSD) (Jui, 2017).

The percentage depth dose on the central axis and flatness and symmetry of the beam in-plane and cross-plane profiles are scanned. This type of beam is often used to deliver a uniform dose distribution. Beam Output factors are also measured for different field sizes during commissioning. The beam output factor is defined as the ratio of the dose per monitor unit relative to the dose per monitor unit in a reference field (10 × 10 cm^2). The beam data collected during commissioning is to configure and model the algorithms (e.g., AAA) of the treatment planning system (e.g., Eclipse).

Prior to percentage depth dose (PDD) and dose profile measurements, mechanical tests on the linear accelerator were done. Mechanical checks such as mechanical positioning accuracy, positioning repeatability and radiation checks including field light and radiation field coincidence. They were all within the tolerance ± 2 %.

4.6.1.1 Scanning water tank and ionization chamber setup

Commissioning/experimental measurements were performed in a computer controlled PTW-MP3 water scanning system (tank) and 0.125 cm^3 semiflex

ionization chamber (PTW Freiburg, Germany). The water tank was filled with distilled water and was aligned to the beam's central axis by using the crosshairs and the localizing lasers. An SSD of 100 cm was set using the front pointer device on the Varian Clinac IX (Varian Medical System, Palo Alto, CA, USA) linear accelerator.

Ionization chamber alignment was done using PTW Centre-Check scanning software, this set the ionization chamber to the chamber effective point of measurement at the central axis. The scanning setup with the reference chamber placed at the corner of the field the X, Y, and Z scanning directions are showed in Fig.4.27.

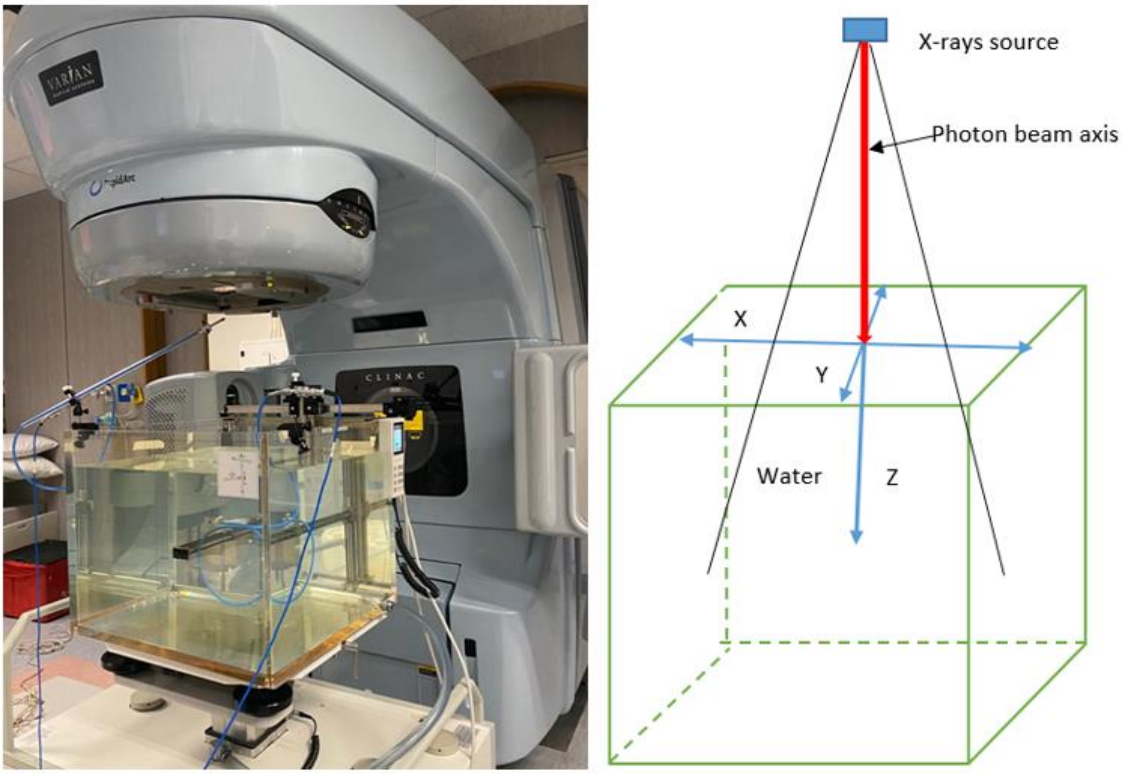

Figure 4. 27: The scanning water tank used in physical dose distribution measurements and the coordinates.

4.6.1.2 Measurements of percentage depth dose for 6 MV and 15 MV

In radiotherapy, the percentage depth dose (PDD) is given by the ratio of the absorbed dose at a given depth *Q* to the absorbed dose at a fixed reference depth

d_P (maximum dose) along the central axis of the beam, expressed as a percentage as shown in Fig.4.28 (Sruti *et al.*, 2016).

$$PDD\ (d, r, SSD) = \frac{D_Q}{D_P} X100 \quad \text{..... (4. 19)}$$

where *r* represents the edge of equivalent field size at the surface of the phantom and SSD is the source-surface distance, which is kept fixed during measurements (Hussain *et al*., 2017). The PDD is normalized to 100 % of its highest dose.

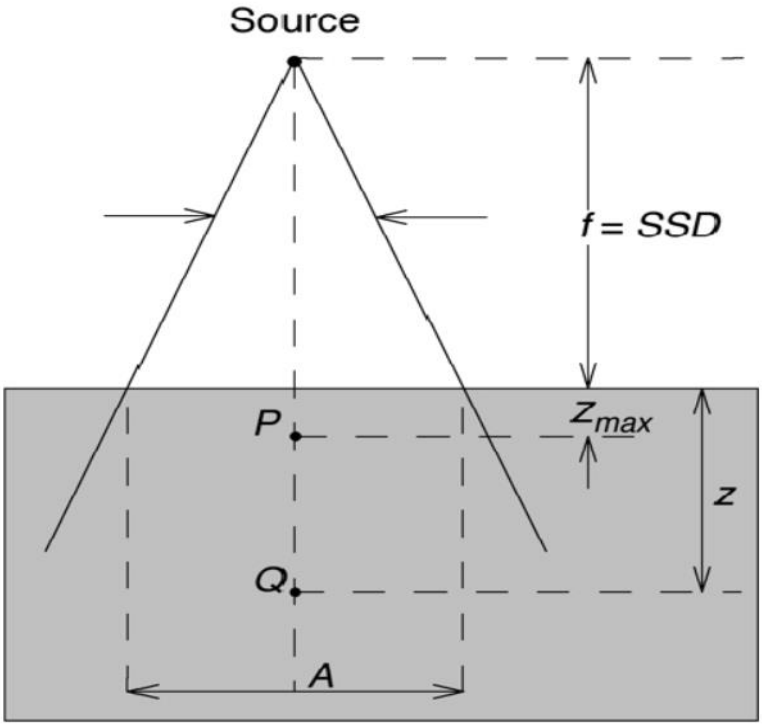

Figure 4. 28: The beam setup of PDD measurement (Sruti *et al.*, 2016**)**

Percentage depth dose (PDD) curves were acquired along the central axis (CAX) of the beam at an SSD of 100 cm for a field size of 3 × 3 cm^2, 6 × 6 cm^2, 10 ×10 cm^2 and 15 × 15 cm^2 on a Varian Clinac IX LINAC operating at two nominal photon energies of 6 MV and 15 MV.

PTW Mephysto software is used to drive the ionization chamber in an upstream direction starting at depths 300 mm to the depth of 0 mm with a 2.5 mm increment. This is to prevent errors due to the bending of the water surface (capillary effects). The percentage depth dose curves at 10 cm depth (D_{10}) and value of D_{max} (R100) in

water for 3 × 3 cm^2, 6 × 6 cm^2, 10 × 10 cm^2 and 15 × 15 cm^2 field sizes for both 6 MV and 15 MV photon beams were analyzed using Mephysto software and compared to specified references. The uncertainties obtained in this study were found to be within 2 %, which is attributed to inaccurate ionization chamber positioning of up to 1 mm and fluctuations of the chamber and electrometer, air pressure, and temperature during the time frame of one scan (Mishra *et al.*, 2018).

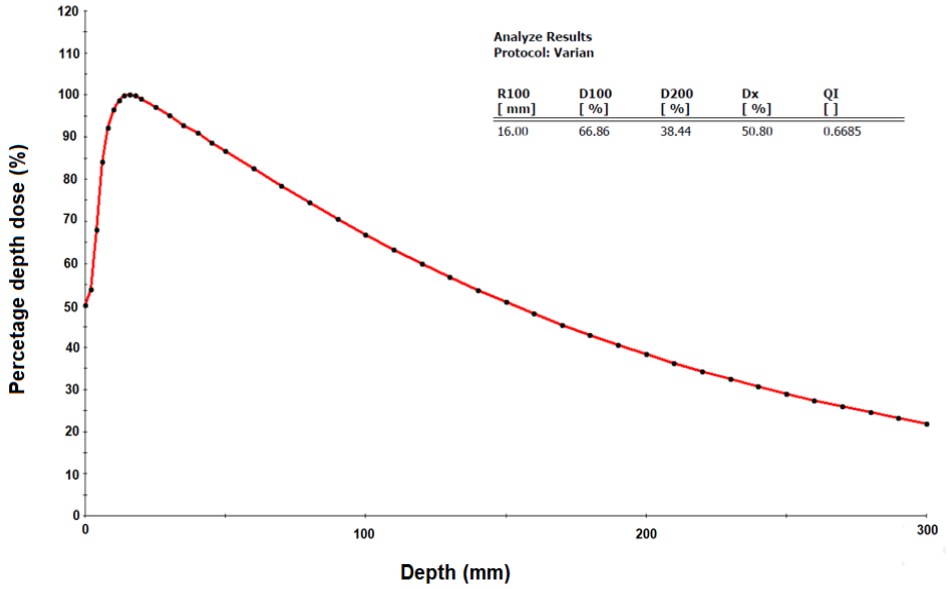

Figure 4. 29: The PDD of the 6 MV photon beam for 10 × 10 cm^2 field size of a Varian Clinac IX form PTW Mephysto software.

Figure 4. 29 shows the experimental results of the 6 MV photon beam PDD for field size 10 × 10 cm^2. The depth of dose at maximum D_{max} (R100) was found to be 16 mm, which corresponds with the value from the red book provided by the manufacturer of the Varian Linac.

4.6.1.3 Measurement of beam profile for 6 MV and 15 MV photon beam

Photon beam profiles are measured at several depths with a required minimum of 3 and a recommended number is 5 depths for 3 × 3 cm^2, 6 × 6 cm^2, 10 × 10 cm^2 and

15 × 15 cm^2 field sizes for both 6 MV and 15 MV photon beams. The 6 MV and 15 MV photon beams are the energies available at our centre and clinically used for prostate cancer treatment. Profiles are measured using an ionization chamber or a profiler/LA48 chamber array. For chamber measurements the ionization chamber was mounted onto the scanning tank in an upright orientation (axial chamber irradiation), to minimize stem and cable effects. Profiles were measured across the centre of the field in two different orientations, cross plane (X-axis direction) and in-plane (Y -axis direction) with the SSD set to 100 cm. The acquired cross and in-plane beam profiles are normalized at 100% on the central axis (CAX) of the beam and analyzed to obtain the flatness, symmetry, and penumbral width. The beam flatness for a photon beam is defined as the variation of dose relative to the central axis over the central 80% of the field size (reference region), at a 10 cm depth in a plane perpendicular to the central axis.

$$Beam\ flatness\ F = \left(\frac{D_{MAX} - D_{MIN}}{D_{MAX} + D_{MIN}}\right) X\ 100 \quad \text{..... (4. 20)}$$

It is calculated by finding the maximum D_{max} and minimum D_{min} dose point values on the beam profile within the central 80 % of the beam full width half maximum dose. It should be within 2 %.

Symmetry is defined as a maximum variation of the area left dose from the area right dose of a beam over the central 80% of full width half maximum.

$$Beam\ symmetry = \left(\frac{Area_{left} - Area_{right}}{Area_{left} + Area_{right}}\right) X\ 100 \quad \text{..... (4. 21)}$$

MEPHYSTO mc² software was used for data acquisition and analysis with a PTW water scanning system. The analysis displayed variations of the beam flatness, symmetry, field size and penumbra. The field size is defined as the lateral distance between the 50% isodose lines at a reference depth. Penumbra is the distance between the positions of 20% and 80% of the normalized profile. An example of the results obtained is shown in Fig. 4.29 and 4.30 for the PDDs and profiles.

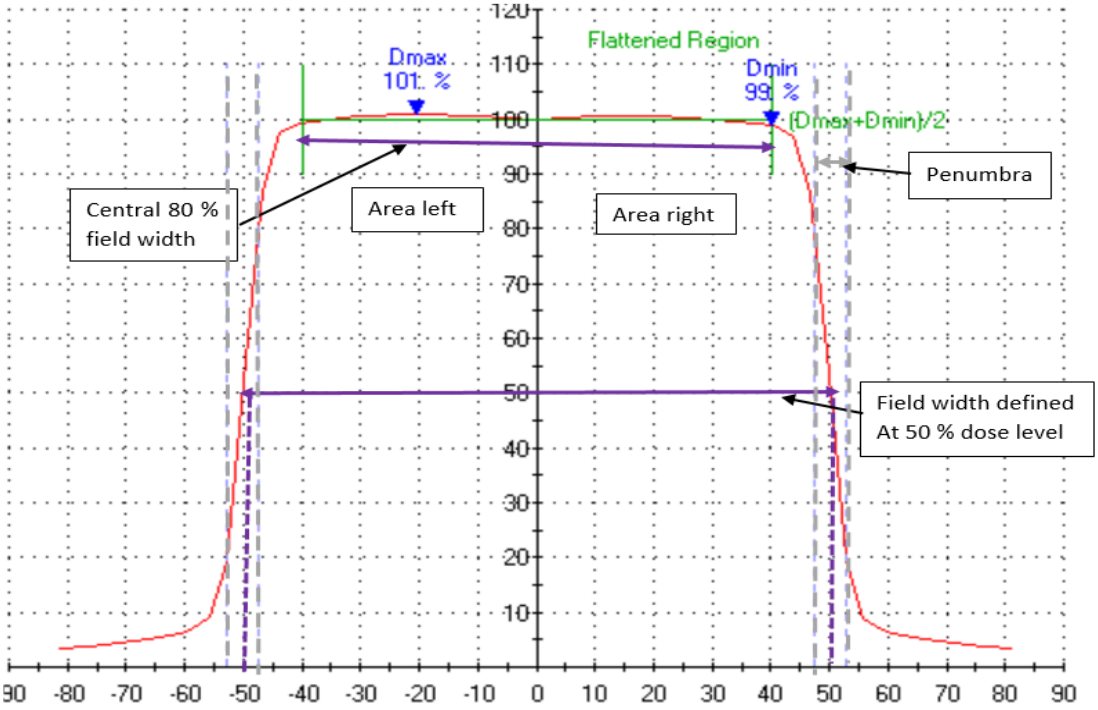

Figure 4. 30: The experimental result of the 6 MV 10 x10 cm^2 in-plane beam profile of the Varian Clinac IX linear accelerator analyzed using PTW Mephysto software**.**

Figures C.3, C.4, C.5, and C.6 in appendix displays the PDDs and beam profiles acquired for 6 MV and 15 MV photon beams for various field sizes.

4.6.2 Validation of EGSnrc Monte Carlo simulation on Varian Clinac IX Linear accelerator

In this study, the Electron-Gamma-Shower (EGSnrc) Monte Carlo (MC) code developed by the National Research Council of Canada (NRC) was used.

EGSnrc codes run using cross-section data of different materials stored in a PEGS4 (processor for Electron Gamma Shower) file. The files 521icru.pegs4dat and 700icru.pegs4dat contain data for a large number of commonly used materials (Rogers *et al*., 2021). In this study, all materials used were obtained from 700icru.pegs4dat which is recommended for high photon energies (Baluti, 2015). The PEGS4 file defines the “density effect corrections in ICRU report 37” and is in the HEN HOUSE inside EGSnrc (McKinney, 2018).

The EGSnrc package consists of BEAMnrc code and DOSXYZnrc code. The BEAMnrc Monte Carlo code system is used to model the linear accelerator head based on the manufacturer's information (Yani *et al*., 2016) by breaking the geometry down into component modules (CMs). The geometrical components of the Linear Accelerator head are used to design a particular shape.

DOSXYZnrc is a dose calculating code that simulates the passage of the source particles through a phantom comprised of dose calculation voxels of variable density and composition. It permits a variety of radiation source geometries and energies including monoenergetic point sources confined to a square field and sources read directly from phase-space files (Campos *et al*., 2009).

BEAMnrc/DOSXYZnrc user codes photon cross section packages are based on “Storm-Israel” (standard PEGS4 cross-sections), “epdl” and “xcom”, the format is of log cross section versus log energy for photoelectric, pair production, coherent scattering, and triplet production cross sections. The “epdl” setting uses cross sections from the evaluated photon data library (EPDL) from Lawrence Livermore and the “xcom” setting uses the XCOM photon cross-sections from Burger and Hubbell (Mohammed *et al*., 2019).

BEAMDP is used to analyse the phase space (phsp) parameters from BEAMnrc MC simulation and can also be used to combine multi-source models of the radiation beam used in MC radiotherapy treatment planning (Rogers *et al*., 2011 and Setiawan *et al*., 2019).

Before using Monte Carlo codes, they need to be validated by comparing the simulated dose distribution with the one measured in water. Validating the Monte Carlo simulations gives us the opportunity to use an accurate model for further dosimetric studies even in a complicated environment where physical measurement is unattainable. In this study, the Electron-Gamma-Shower (EGSnrc) Monte Carlo (MC) code was used to simulate the 6 MV and 15 MV photon beam generated by Varian Clinax IX linear accelerator.

4.6.2.1 Modelling of linear accelerator head

EGSnrc Monte Carlo simulation starts with the excited electron beam incident on a high-density material tungsten (W) coupled with a copper (Cu) layer target to produce bremsstrahlung photons (X-rays), with the origin taken at the front face of the target (Mishra *et al*., 2018) as shown in Fig.4.31. The direction of the X-ray beam produced is uncertain. The X-ray beam is guided by the tungsten primary collimators placed under the target. The primary collimator defines the maximum circular field and absorbs scattered photons leaving the treatment head in any direction other than that of the primary beam.

At this stage the X-ray beam is not uniform. To achieve uniformity, the beam must pass through the flattening filter attached to the lower end of the primary collimators. The flattening filter will create a flat dose profile. The material and thickness of the flattening filters depend on the beam energy E. Photons are scattered as they pass through the flattening filter reducing the mean photon energy by pair production and Compton scattering. The flattening filter also absorbs low-energy photons and therefore hardens the beam. The beam hardening is discussed in section 3.3.2.1.

After the flattening filter, the beam passes through the dual transmission ionization/monitor chamber, which is used to measure the radiation beam output of the machine in terms of Monitor Units (MU) as well as the symmetry and flatness of the X-ray beam. The mirror below the ionization chamber is used to project the light from the optical source to replicate the shape of the X-ray field. It is positioned at an angle so that the light field coincides with the radiation field.

From modelling perspective, the ionization chamber and mirror components are included in the Linac head model for consistency reasons only. The effect is minor compared to the other components of the Linac head. All components described above are patient independent.

The beam then passes through two sets (four blocks) of adjustable secondary tungsten collimator jaws situated below the mirror. Two blocks forming the upper jaws (Y-jaws) and two forming the lower jaws (X -jaws). The thickness of the jaws must be sufficient to shield out the unwanted radiation and effectively define the field

size. The jaws define a maximum field size of 40 × 40 cm^2 and can provide rectangular or square fields at the Linac isocentre.

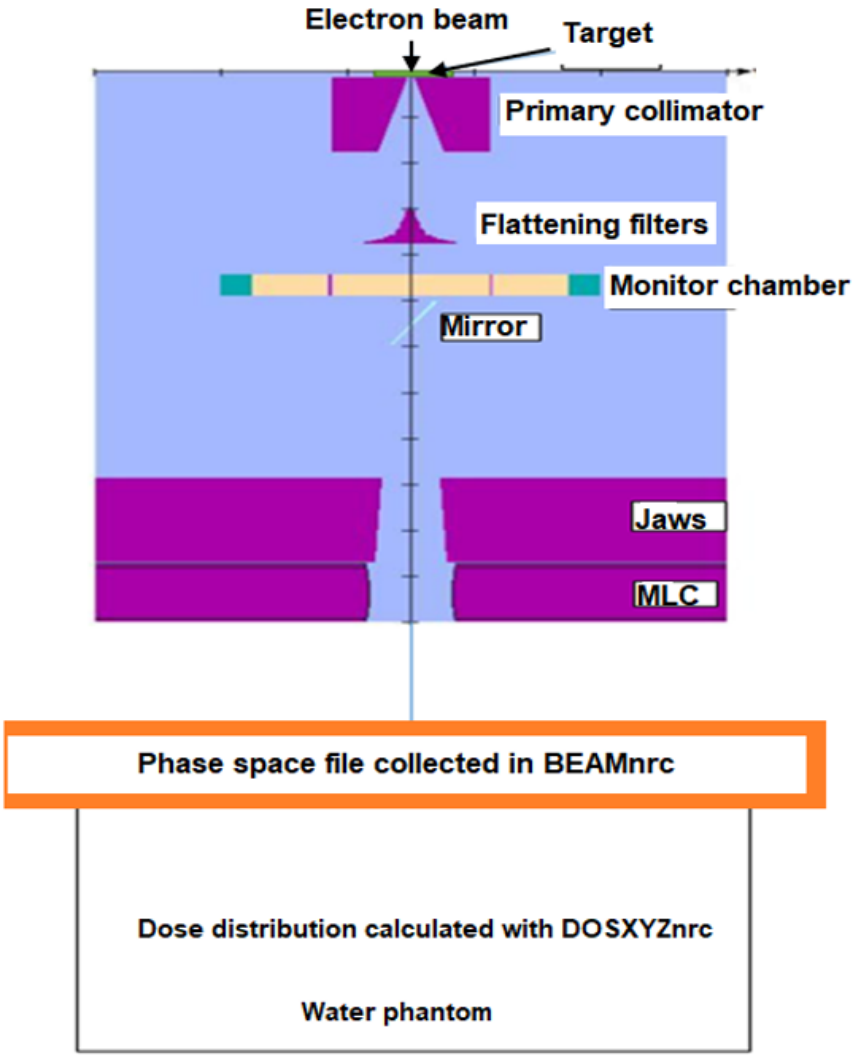

Figure 4. 31: Schematic view showing the linear accelerator head and phase space file collection simulated in this work.

Below the jaws are patient specific beam shaping multileaf collimators (MLC). The number of leaves in commercial MLCs differs according to different models. The models with 120 leaves (60 pairs) cover fields up to 40 × 40 cm^2 and require 120 individually computer-controlled motors. The jaws and MLC are patient dependent. To obtain accurate results from Monte Carlo simulations in radiotherapy calculations, precise modelling of the LINAC gantry and a sufficiently large number of particles (9×10^9) histories are required.

4.6.2.2 BEAMnrc user code

In the first step, the Linac head components were modelled using the BEAMnrc user code (Graphical User Interface 2.0) and simulated with field sizes of 3 × 3 cm^2, 6 ×6 cm^2, 10 ×10 cm^2 and 15 × 15 cm^2 for 6 MV and 15 MV photon beams. Modelling the Linac head involves specifying the linear accelerator, with the geometry and material of each component defined.

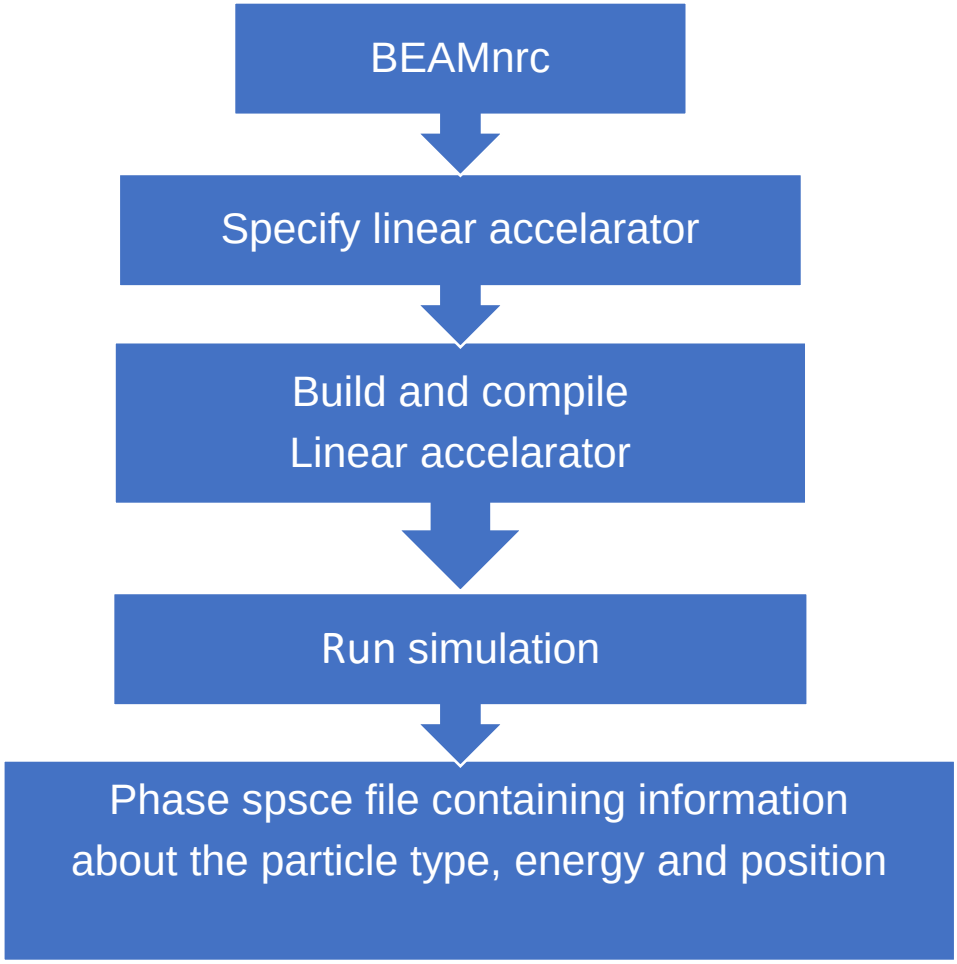

Figure 4. 32: The flowchart illustrating the working processes of EGSnrc BEAMnrc Monte Carlo simulation.

The geometry and material descriptions of the treatment head components of the Linac head were modelled using the manufacturer's (Varian Medical Systems, Palo Alto, CA) detailed information. Figure 4.32 shows the working process of EGSnrc BEAMnrc Monte Carlo simulation.

Components of the treatment head such as the target, primary collimators, flattening filters, ion chamber, mirror, jaws, multi-leaf collimators (MLCs) were simulated using the following component modules (CMs): SLAB, CONS3R, FLATFIL, CHAMBER, MIRROR, JAWS and VARMLC (120MLC) respectively as shown in Fig.4.33 below and the component modelled names, materials and their density is shown in Table 4.5. These component modules are found on BEAMnrc user code.

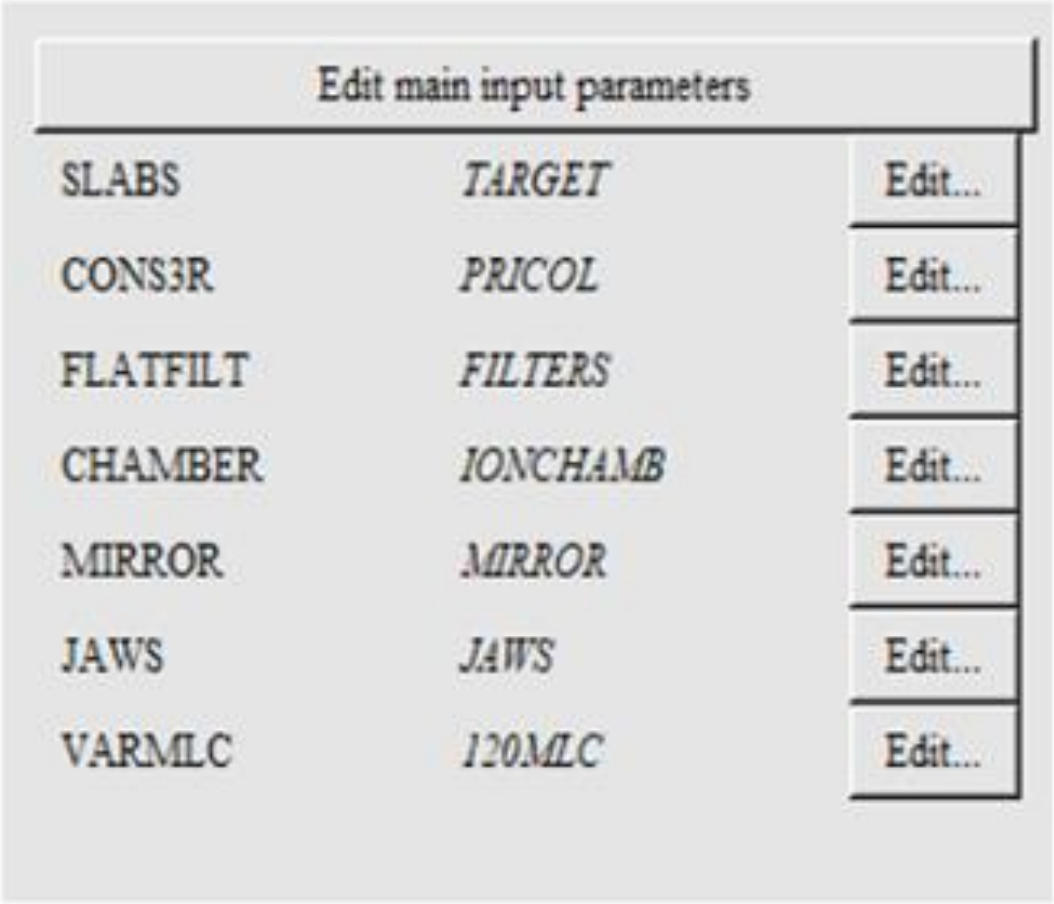

Figure 4. 33: The list of the component modules (CM) used in this study characterizing the Clinac IX linear accelerator in BEAMnrc.

Table 4. 5: Details of the component modules parameters

Component modules type	Component modelled names	Materials	Density (g/cm^3)
(1) SLABS	Bremsstrahlung Target	Tungsten Copper	19.3 8.92
(2) CONS3R	Primary Collimators	Tungsten	19.3
(3) FLATFILT	Flattening Filter	Copper (6 MV) Tungsten (15 MV)	8.92 16.9
(4) CHAMBER	Ion chamber	Kapton Air	1.42 0.0012
(5) MIRROR	Mirror	Mylar (Angled at 35° relative to the x- axis)	1.38
(6) JAWS	Secondary collimator jaws	Tungsten	19.3
(7) VARMLC	Multileaf collimators	92.5% Tungsten and alloy of Nickel, Copper & Iron	19.3

The summary of 7 materials and component modules used for modelling the Linac head is also shown in Fig.D.1 and D.4 in the Appendix.

BEAMnrc user code models the path of electrons and photons from the target to a predefined scoring plane position below the jaws (McKinney, 2018) and above the MLCs. The BEAMnrc simulation parameters were set to an electron transport cutoff (ECUT) of 0.7 MeV and a photon transport cutoff (PCUT) of 0.01 MeV. If the energy of the electron or photon drops below the cutoff value, it will no longer be tracked (Baluti, 2015).

Global electron cutoff was turned on with the ESAVE_GLOBAL range rejection value set to 2 MeV to eliminate the particles that have no significant contribution to the dose in the region of interest. The region and rejection range summary are shown in Fig.D.3 in the Appendix. All these particle transport parameters save simulation time. The linear accelerator was built and compiled by summing the required components.

Calculations were done for 9×10^9 particles (number of histories) to achieve less statistical uncertainty. After running the simulation, the output of the BEAMnrc simulation results in a phase space file (*. egsphsp) containing information about the types of the particle, position (X, Y and Z), energy E, direction, weight, and a tag that

records the particle history at any specified plane in the simulation geometry (Campos *et al*., 2009) and orientations of all particles in a scoring plane. An example of a phase space file is shown in Fig.D.5 for a 15 MV photon beam using 10 ×10 cm^2. All the DOSXYZnrc input parameters, including EGSnrc parameters, can be incorporated into an input file with extension *. egsinp.

4.6.2.3 DOSXYZnrc user code

In the second step, the dose calculation code DOSXYZnrc is used. Figure 4.34 shows the working process of BEAMnrc.

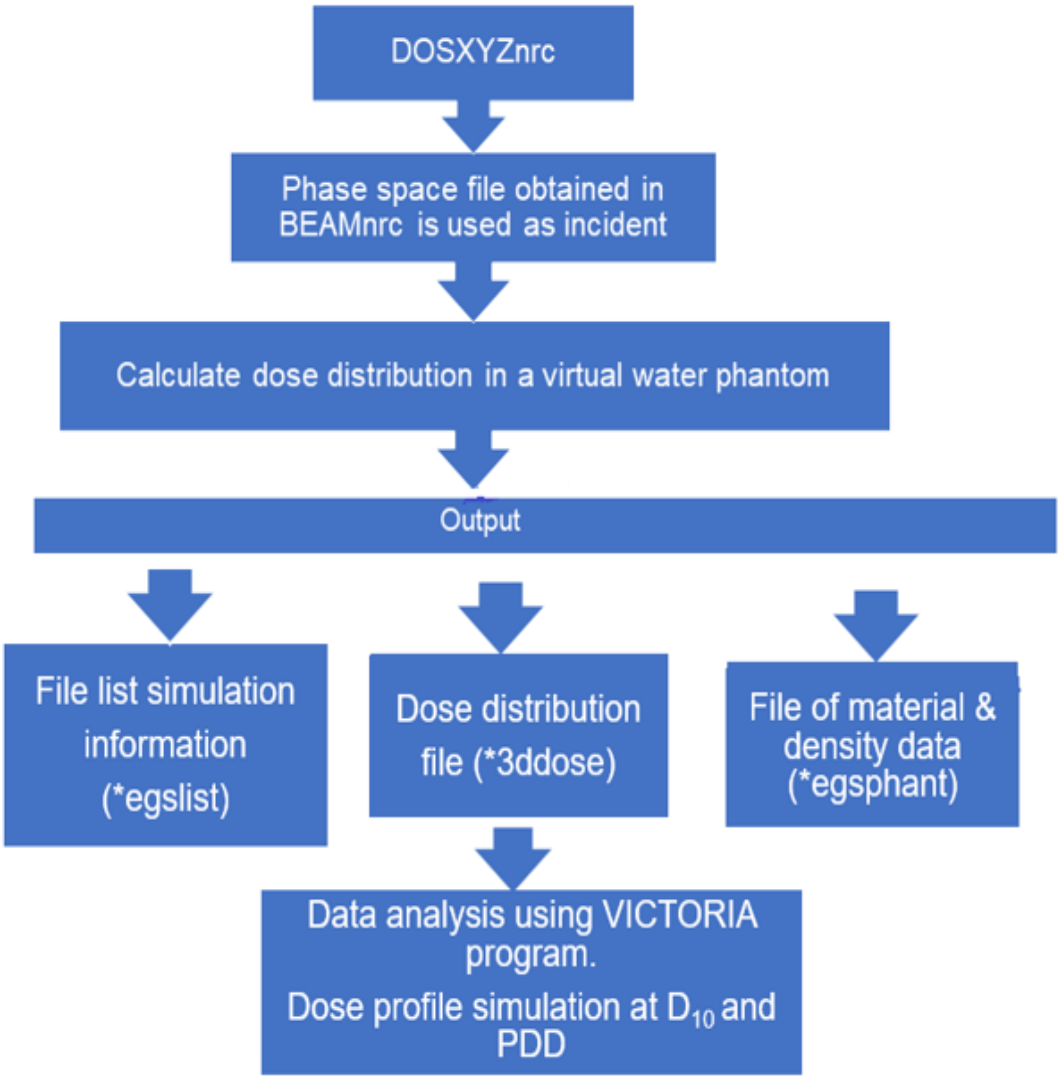

Figure 4. 34: The flowchart illustrating the working processes of EGSnrc BEAMnrc Monte Carlo simulation.

DOSXYZnrc user code can perform 3D absorbed dose calculations in Cartesian coordinates in a water phantom. The scored phase space file in BEAMnrc for a million particles existing in the treatment head (Campos *et al*., 2009) is used as an incident on a 60 × 60 × 24 cc virtual water phantom to calculate the dose distribution. The source to surface distance (SSD) is kept at 100 cm i.e., the same as the measurements done in a water phantom. No range rejection was used.

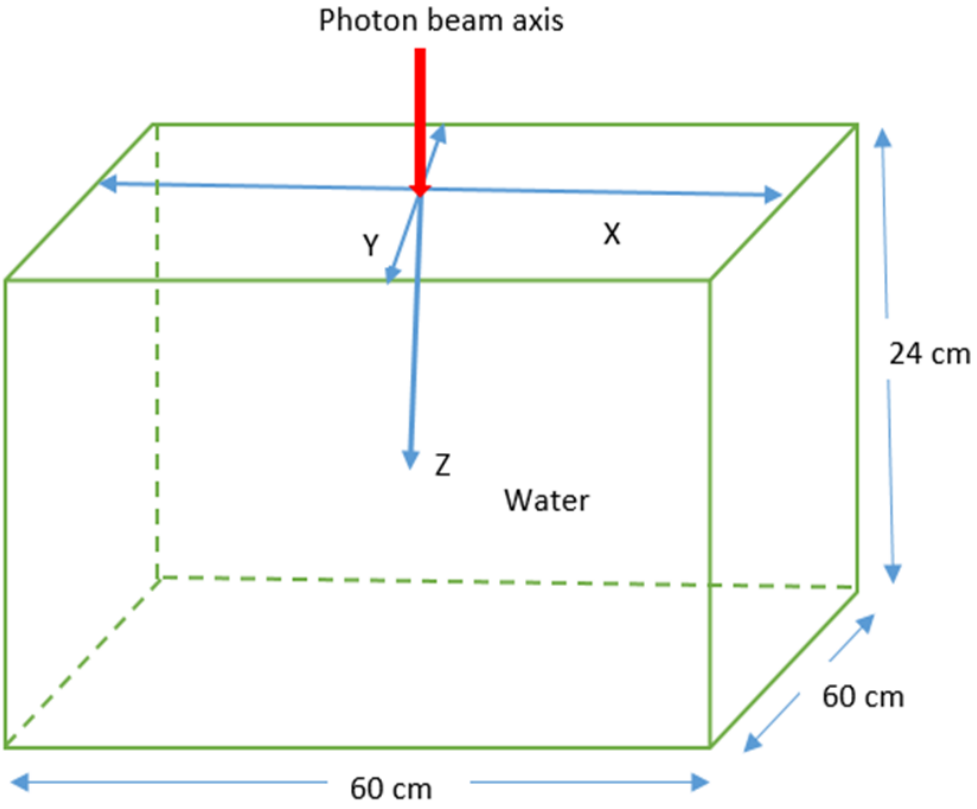

Figure 4. 35: Phantom design depicting how dose profiles are measured in the X and Y axes and PDD are measured in Z-axis.

The geometry of the phantom is defined on DOSXYZnrc user code as shown in Fig.4.35. In this code CT data can also be imported and translated to voxels with certain materials and densities. The position and size of the virtual water phantom were described by the Cartesian coordinate system with lateral (X-axis), longitudinal (Y-axis) and vertical (Z-axis) directions as in the radiotherapy treatment room. The voxel dimension of the virtual water phantom was 0.5 × 0.5 × 0.5 cm^3 for both X and Y axes. And for the Z-axis (towards the direction of the photon beam) a resolution of 0.2 cm was used. The number of histories for DOSXYZnrc Monte Carlo calculation was set to 9 × 10^9 particles. The dose distributions within the Cartesian geometry in

the virtual water phantom are calculated (Campos *et al*., 2009 & Yani *et al*., 2016). The outputs of a DOSXYZnrc calculations are 3D dose distribution data (*.3ddose).

4.6.2.4 Data comparison and analysis

The EGSnrc Monte Carlo simulated dose distribution data was analyzed using the Voxel Interactive Contour Tool for Online Radiation Intensity Analytics (VICTORIA) program to obtain the central axis percentage depth dose (PDD) and dose profile (off-axis ratio). The accuracy of the Monte Carlo model was evaluated by comparing the central axis percentage depth dose (PDD) and lateral dose profile (off-axis ratio) with the beam commissioning data. The EGSnrc dose distributions were compared with the experimental measurements using a gamma analysis, employing a 2 %/ 2 mm distance-to agreement criterion. The 6 MV and 15 MV photon beams EGSnrc MC calculated dose agreed well with experimental measurements within 2 % for all tested field sizes. Figures D.7 to D.17 in appendix displays the Monte Carlo simulated PDDs and beam profiles for 6 MV and 15 MV photon beams for various field sizes.

4.6.3 Verification of prostate point dose calculations for the Monte Carlo code

This section describes the modelling of an in-house pelvic phantom and the simulation of prostate point dose.

4.6.3.1 Monte Carlo modelling of pelvic phantom

The Monte Carlo pelvic phantom was created using an in-house pelvic phantom planning data set as an input of the DICOM RT toolbox. An in-house pelvic phantom CT-data sets were converted from DICOM (.dcm) format to text (.txt) format. CTCREATE was used to convert .txt files to *egsphant to be used in an EGSnrc

DOSXYZnrc code to simulate the dose. CTCREATE is a standalone code included in the EGSnrc package and was used to define the materials and their densities. The *egsphant file that contains file material and density data is shown in Fig. D.18. DOSXYZ/CTCREATE conversion ramp (Fig. D.19) for four materials, AIR700ICRU (air), ICRUTISSUE700IC (tissue), ICRPBONE700ICRU (bone), and TI700ICRU (titanium hip replacement) was used to convert CT data into the material and mass density (Zarza-Moreno *et al*., 2012).

Figure 4.36 shows the modified default ramp for converting CT values to material and density for air, tissue, bone and titanium materials in CTCREATE. An in-house pelvic phantom has no lung, so the lung calibration was excluded from conversion. Since the phantom has a high-density hip prosthesis, an additional calibration point was added to obtain agreement between exact geometry for MC dose calculations and dose calculations based on CT image geometry (Bazalava *et al*., 2006).

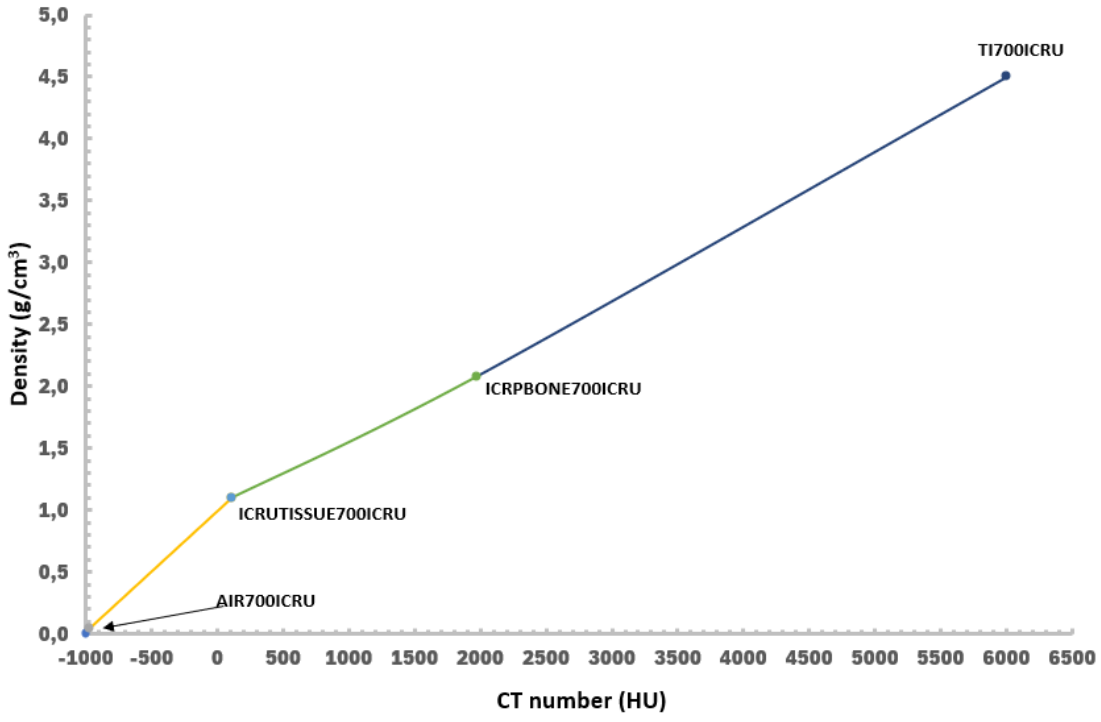

Figure 4. 36: Modified default ramp for converting CT values to material and density in CTCREATE.

Table 4.6 shows the CT number (HU) used for the conversion of HU into densities and materials in CTCREATE. Titanium was added to the standard DOSXYZnrc

calibration. Many authors use the exact CTCREATE ramp with the default HU and density limits, while other authors keep the four media and slightly modify the HU and density limits. In this study, the media was modified to accommodate titanium alloy with a CT number of 6000 HU and a density of 4.5 g/cm^3.

Table 4. 6: The CT number used for Hounsfield conversion into density and materials for MC calculation.

Material	CT NO range (HU)	Density range (g/cm^3)
Air	[-1000: -974]	[0.001: 0.044]
Tissue	[-974: 110]	[0.044: 1.101]
ICRP cortical bone	[110: 1976]	[1.101: 2.088]
Titanium alloy	6000	4.5

An in-house pelvic phantom was simulated for different static fields (anterior, posterior, left lateral and right lateral). The lateral fields were simulated using a 6 × 6 cm^2 field size and the anterior/posterior fields using a 10 × 10 cm^2 field size for both 6 MV and 15 MV photon beams as performed during the experimental measurements phase in section 4.3.1.1. The number of histories used was 9 ×10^9, the global electron cutoff energy was 0.7 MeV, and the global photon cutoff was 0.01 MeV.

The resultant 3ddose files from DOSXYZnrc were analyzed using the Voxel Interactive Contour Tool for Online Radiation Intensity Analytics (VICTORIA) program. The Monte Carlo Simulated prostate point dose for anterior, posterior, left lateral and right lateral fields were then compared with the dose measured by the ionization chamber and films on the linear accelerator. The dose measurements by the ionization chamber are discussed in section 4.3.2.

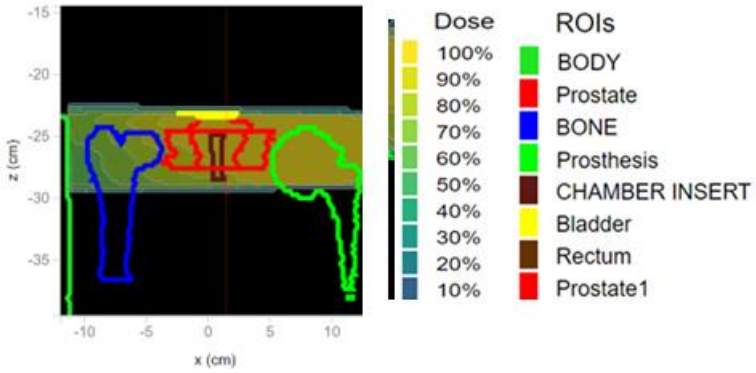

Figure 4. 37: The Y-axis view dose distribution obtained with MC simulation for the left lateral field 6MV photon beam.

Figure 4.37 shows a dose distribution of the beam passing through the titanium hip prosthesis for a 6 MV photon beam.

According to TECDOC 1540, the percentage error $\delta(\%)$ between the Monte Carlo simulated dose and ionization chamber measured dose is defined as

$$\delta(\%) = \frac{(D_{MC} - D_{ION\ CHAMBER})}{D_{ION\ CHAMBER}} \quad \text{..... (4. 22)}$$

where D_{MC} and $D_{ION\ CHMABER}$ are MC simulated dose and ionization chamber measured doses, respectively. The same formula is used to compare MC simulated dose with TPS calculated dose or MC simulated dose with film measured dose.

The highest percentage difference between the MC simulated dose and TPS calculated dose was found to be 3.9 % for 6 MV photon for the Anterior field and 2.0 % for 15 MV photon beam for the posterior field.

The dose distribution of the left lateral field of a 6 MV photon beam is visualised in Figure 4.38, which was generated using the Voxel Interactive contour Tool for Online Radiation Intensity Analytics (VICTORIA) wed viewer in an in-house pelvic phantom. The EGSnrc files, such as .egsphant and 3ddose, which are formatted plain text files carrying phantom and dose information, can be analysed using the VICTORIA programme. DICOM RT structures, DICOM radiotherapy (RT) dose, and DICOM CT image file types are also supported by the application.

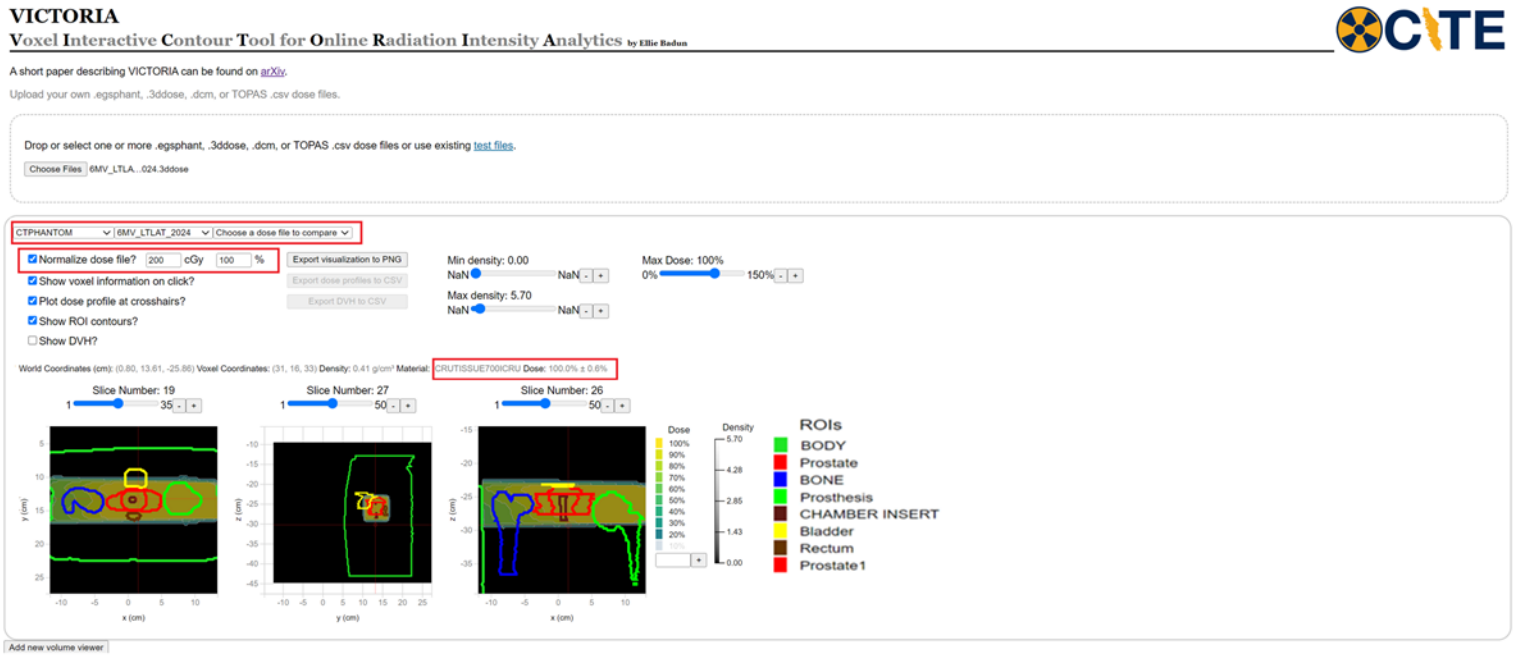

Figure 4. 38: Axial, coronal, and sagittal views of the 6 MV photon beam left lateral field dose distribution in an in-house pelvic phantom generated using CTCREATE on VICTORIA programme.

The density of the materials used in constructing the phantom is also displayed in the VICTORIA programme. This tool also allows for the visualisation of the dose volume histogram and the profiles of the axes (X, Y, and Z). The contours of the region of interest are displayed. The region of interest contours is shown. The dose has been normalized to 2 Gy at 100 %. The dose distribution of the 6 MV photon beam right lateral, anterior, and posterior field is showed in appendix Fig.D.21, Fig.D22 and Fig.D23, respectively.

4.7 Backscatter dose perturbation factor

Quantification of the prosthesis induced backscatter dose perturbation was acquired through the backscatter dose perturbation factor (BSDF). BSDF is defined as the ratio of the doses with and without the presence of the prosthesis for an identical setup. The BSDF measurements were acquired using 6 MV and 15 MV equally weighted lateral fields with a set field size of 6 × 6 cm^2 at an SSD of 87.5 cm. This is the same plan used for the verification of the TPS calculated dose using the ionization chamber and Gafchromic EBT3 film. One set of measurements was performed with the beams passing through the prosthesis and one set without passing through the prosthesis.

The plan was prescribed to 2 Gy. The doses were measured at different distances in 0.1 cm increments and different thicknesses of the prosthesis. The measurements were repeated three times and the averages were calculated.

The backscatter dose perturbation factor (BSDF) of the high-density hip replacement was calculated using the following.

$$BSDF = \frac{D_i}{D_h} \quad \text{..... (4. 23)}$$

Where D_i and D_h are the doses with and without the prosthesis respectively.

The highest BSDF value obtained is 1.13 for both 6MV and 15 MV photon beam. However, the BSDF is energy dependent.

CHAPTER 5: RESULTS AND DISCUSSION

This chapter presents, in tabular form, the results of the linear attenuation coefficient measurements of the materials used to construct the phantom and the verification of the CT number abstained from the CT scanner. The MC simulated prostate point dose is compared with the results of the prostate point dose measurements in an in-house pelvic phantom utilising the ionisation chamber and Gafchromic film. In addition, the MC simulated dose is compared with the TPS calculated prostate point dose, ionisation chamber, and Gafchromic film prostate point dose measurements. Tables and graphs are used to display the results.

5.1 Radiological properties of the materials

Since the materials utilised to generate an in-house phantom must be as close to the human body as possible for effective radiation dosimetry, evaluating the tissue-equivalency of these materials is essential.

5.1.1 Linear attenuation coefficient measurements

The linear attenuation coefficients of superflab gel bolus, dental wax and RW3 solid water slabs which were obtained by measuring the transmission for different thicknesses of these materials are indicated in Fig. 5. 1 and Table 5.1.

The zero-reading obtained without attenuating material was 9.063 nC.

Table 5. 1: The average charge reading collected for measurement of linear attenuation coefficient and the standard deviation (SD) included.

Thickness (cm)	Average charge reading (nC)		
	RW3 slabs	Dental wax	Superflab gel bolus
1	8.703 (SD ±0.0011)	8.715 (SD ±0.0001)	8.704 (SD ±0.0001)
2	8.150 (SD ±0.0060)	8.280 (SD ±0.0058)	8.154 (SD ±0.0058)
3	7.876 (SD ±0.0001)	7.877 (SD ±0.0057)	7.869 (SD ±0.0001)
4	7.490 (SD ±0.0006)	7.560 (SD ±0.0006)	7.498 (SD ±0.0058)
5	7.125 (SD ±0.0058)	7.233 (SD ±0.0001)	7.153 (SD ±0.0001)

Table 5.1 shows the average charge reading of the collected from the ionization chamber over 3 measurements. The transmission was obtained by dividing the zero reading with the reading obtained from different thicknesses of the material and plotted (Fig. 5. 1) against the thickness of the material.

Table 5. 2: Summary of calculated linear attenuation and mass attenuation coefficient of superflab gel bolus, dental wax and RW3 slabs and the standard deviation (SD) included.

Phantom material	Linear attenuation (μ) cm^{-1}	Mass attenuation coefficient (μ/ρ) cm^2/g	p-value
RW3	0.048 (SD± 0.0001)	0.0478 (SD± 0.0001)	
Dental wax	0.046 (SD± 0.0002)	0.0480 (SD± 0.0002)	0.086
Superflab gel bolus	0.047 (SD± 0.0001)	0.0481 (SD± 0.0001)	0.084

The mass attenuation coefficient is obtained by dividing the measured linear attenuation coefficient by the density of the material is shown in Table 5.2. The linear attenuation coefficient of RW3 slabs reported in the literature is 0.0465 cm^2/g. The calculated relative density of the superflab bolus and dental wax is 0.997g/cm and 0.958 g/ cm respectively. A difference in mass attenuation coefficient between the superflab gel bolus and dental wax when compared to water equivalent RW3 was found to be 0.63% and 0.4 % respectively.

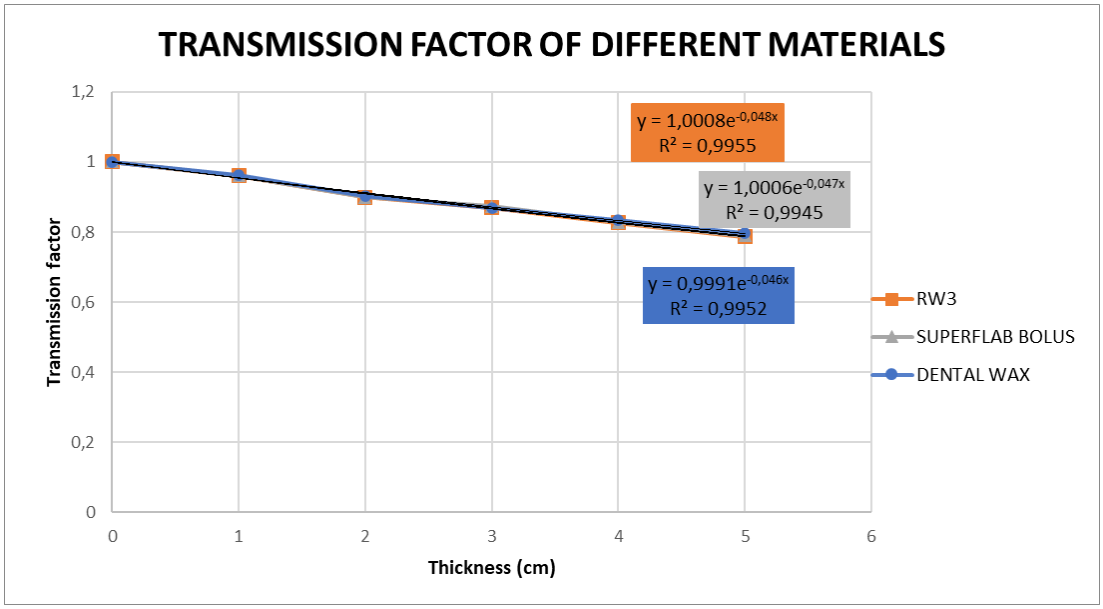

Figure 5. 1: Transmission factor as a function of thickness of superflab gel bolus, dental wax and RW3 slabs.

The calculated linear attenuation coefficient of the RW3, dental wax and superflab gel bolus were found to be 0.048 cm^{-1}, 0.046 cm^{-1} and 0.047 cm^{-1} and the mass attenuation coefficients were 0.0457 cm^2/g, 0.0449 cm^2/g, and 0.0451 cm^2/g respectively. The deviation of mass attenuation coefficient was found to be 0.63% and 0.4 % for superflab gel bolus and dental wax respectively when compared to the RW3 slab mass attenuation coefficient. The percentage value is statistically insignificant ($p > 0.05$).

Ade *et al*., (2017) reported the RW3 slab linear attenuation coefficient of 0.0486 cm^{-1} measured using a 2 × 2 cm^2 field size for a 6 MV photon beam. The results were comparable with a small discrepancy of 1.2 %. Verma *et al*., (2019) reported a linear attenuation coefficient of water, dental wax and superflab gel bolus for a telecobalt-60 (average energy of 1.25 MeV) beam measured using a field size of 5 × 5 cm^2 of 0.065 cm^{-1}, 0.062 cm^{-1} and 0.060 cm^{-1} respectively. There is a huge discrepancy between the results reported in the literature and our result due to the different field sizes and energy used. The linear attenuation coefficient of the material is energy dependent (Seif *et al*., 2017).

The mass attenuation values of the superflab gel bolus and dental wax were comparable with that of the RW3 solid water phantom and the calculated CT numbers were comparable with the ones obtained from CT data in the TPS. These materials were chosen as they are regularly used in the radiotherapy setting to compensate for missing tissue.

Only having access to a small piece of Nylon-12, meant that the linear and mass attenuation coefficients were not done. However, the CT number and relative density obtained from TPS were compared with the ones reported in the literature. In the literature, a difference of 1.5 % was found between the mass attenuation coefficient of Nylon-12 (0.0458 cm^2/g) and RW3 slabs (0.0465 cm^2/g) (Ade *et al*., 2017).

5.1.1.1 Verification of CT number obtained from TPS

The CT number calculated using Equation 3.1 was compared with the CT number obtained directly from the CT data set without an artifact correction. The comparison

is shown in Table 5.3 below. The comparison of the CT number should be within ± 20 HU IAEA guidelines (McLean *et a*l., 2012).

Table 5. 3: Comparison of calculated and TPS CT number and relative density.

Phantom material	Hounsfield number (HU)		Relative electron density (g/cm³)	
	Calculated	TPS	Calculated	TPS
Dental wax	-65.00	-68.000	0.958	0.950
Superflab gel bolus	-21.73	-8.000	0.967	0.997
Femoral of pig bone	Expected value=110-1978	295-1552	Expected value=1.193-1.824	1.193-1551
Titanium	Expected value=6000	3071	Expected value= 3.74	2.54

Expected value is the theoretical value (Akyol *et al*., 2019)

Verma *et al*., (2019) reported the calculated relative density of 0.958 and 0.923 g/cm³ for dental wax (paraffin wax) and superflab gel bolus, respectively. There is no discrepancy between the dental wax relative density reported in the literature compared to the one obtained in this study. However, there is a huge discrepancy in the calculated superflab bolus relative density.

5.2 Prostate point dose comparison

In the literature, dose distributions in the vicinity of a high-density hip prosthesis have been evaluated by the use of film, ionization chambers, diodes and ion/diodes arrays and other dosimeters. Algorithms used in different planning systems have also been evaluated in addition to the Monte Carlo simulation. In these studies, the high-density material was placed either in a cadaver, water or tissue equivalent medium or in-house fabricated phantom, but several studies have used tissue-equivalent phantoms. Different external beam radiotherapy machines were used.

Fevre *et al.*, (2020) evaluated the effect of metallic implants on a human cadaver. In their study, an alanine electron spin resonance dosimeter was used to evaluate the discrepancies between the TPS calculated dose and measured dose. The results showed that the measured dose was lower than the TPS calculated dose. The

advantage of using the human cadaver for dose measurements is that the dosimeter can be implanted into individual organs depending on what need to be measured.

For a hip prosthesis with an unknown composition, Rijken *et al*., (2017) evaluated the dose uncertainties with a specified density override using a water bath on top of the device. In the TPS, the density override was set to 6 g/cm3. The unknown hip prosthesis composition was checked against the known hip prosthesis composition. The dosimetric uncertainty for beams passing through the hip prosthesis was found to be 10 %. They have recommended careful consideration when assigning density for unknown titanium.

In this study, Ionization chamber measurements, EBT3 film measurement and MC simulation were done on the normal CT data set of an in-house pelvic phantom using four different plans (two equally weighted laterals and two opposite and equally weighted anterior and posterior fields). For each plan the prostate point doses were measured and recorded. Ionization chamber measurements and EBT3 film measurement were done on IMRT and VMATs plans.

5.2.1 Ionization chamber measurements

Ionisation chamber dosimetry is the technique most usually used to measure absorbed doses in radiation. Ionisation chambers with absorbed-dose-to-water calibration factors are used in some dosimetry protocols (TRS 398 and TG 51) to assess radiation beam dose.

5.2.1.1 Static field measurements

The charge (nC) readings collected using the ionization chamber were converted into dose (Gy) using the TRS 398 protocol.

Table 5. 4: The comparison of the TPS calculated dose and ionization chamber measured dose of each field of 6 MV photon beam.

Field	SSD (cm)	TPS calculated dose (Gy)	Average Ion chamber measured dose (Gy)	% Difference
Anterior	91.5	2.066 (SD±0.002)	2.030 (SD±0.006)	1.8
Posterior	91.5	2.030 (SD±0.001)	1.996 (SD±0.001)	1.7
LT lateral	87.5	1.997 (SD±0.006)	1.878 (SD±0.012)	6.3
RT lateral	87.5	2.006 (SD±0.001)	2.053 (SD±0.006)	-2.2

Table 5. 5: The comparison of the TPS calculated dose and ionization chamber measured dose of each field of 15 MV photon beam.

Field	SSD (cm)	TPS calculated dose (Gy)	Average Ion chamber measured dose (Gy)	% Difference
Anterior	91.5	2.038 (SD±0.001)	2.049 (SD±0.006)	-0.5
Posterior	91.5	2.036 (SD±0.002)	2.041 (SD±0.012)	-0.2
LT lateral	87.5	2.008 (SD±0.002)	1.927 (SD±0.015)	4.2
RT lateral	87.5	2.008 (SD±0.001)	2.050 (SD±0.001)	-2.1

Only the reference conditions used for the calibration are valid for the calibration factor for an ionisation chamber. When using the ionisation chamber, any deviation from the reference conditions should be compensated for using the relevant factor.

The corrected charge (nC) reading was calculated by multiplying the reading by polarity effects, electrometer calibration**,** ion recombination, pressure, and temperature. The corrected charge (nC) reading was then used to calculate the dose. The ionization chamber calibration factor ($N_{Dw, Q0}$ (cGy/nC)) used was 5.432 cGy/nC. The chamber was calibrated at the National Metrology Institute of South Africa (NMISA).

A calibrated PTW Farmer ionisation chamber with a traceable calibration certificate was used to measure the prostate point dose. The difference between the measured dose for the 6 MV photon beam and the prostate point dose calculated by TPS was found to be 1.8%, 1.7%, 6.3%, and -2.2%, respectively, for the four anterior (gantry 0°), posterior (gantry 180°), left lateral (gantry 90°) and right lateral (gantry 270°) fields, respectively. The percentage difference was calculated using Equation 4.18 taken from TECDOC 1540.

The values for the anterior, posterior, left lateral, and right lateral fields, respectively, for the 15 MV photon beam, were -0.5%, -0.2%, 4.2%, and -2.1%. The left lateral beams passing through the prosthesis showed the maximum deviation. The prostate dose was overestimated by the treatment planning system.

A study by Parenica *et al*., (2019) used a superflab gel bolus, hip prosthesis and ionization chamber to create a phantom as shown in Fig.3.13 (A). The hip prosthesis was placed within the slabs of the bolus and the chamber placed at the isocenter of the beam. The plans (with and without density override) were created with a lateral field passing through the prosthesis using the Pinnacle and Monaco planning system. When density override is used the Pinnacle had an error of 4.4 % when compared to the ionization chamber measured dose and when the density override is not used the error was 9.2 %. When the density override was used, an error of 0.2% was seen, and when it was not used, an error of 3.6% was seen for the Monaco planning system using MC dose calculation. Their phantom is a simple assembly phantom; however, care needs to be taken when placing the hip prosthesis and ionization chamber to avoid air gaps between the slabs of the phantom, especially between the slabs that sandwich the prosthesis and ionization chamber.

A phantom with a hip replacement that can contain TLDs at various points was created as part of a study by Paulu *et al*., (2017) to assess the accuracy of dose computation using the Pinnacle Collapsed Cone Convolution (CCC), Eclipse Acuros XB, and AAA algorithms. They sandwiched the hip prosthesis between two hemicylindrical pieces of urethane cast to create their phantom. The phantom had a diameter of 8.89 cm. TLDs were positioned along the prosthesis at various locations. For the Pinnacle (CCC algorithm), Eclipse AXB, and Eclipse AAA, respectively, the discrepancy between the TPS calculated dose and TLDs measured dose was 5-22%, 2-23%, and 6-25% greater measured than TPS calculated dose. Their phantom was only made to fit hip prostheses, TLD, and for comparing dose algorithms.

In our study, different tissue equivalent materials were used to construct a pelvic phantom. The phantom was constructed with the ionization chamber insert and film insert to measure the prostate point dose at the same point. The two different energies that are most frequently used in our centre were the subject of

investigations. This investigation was carried out to show how two different photon energies responded differently to the presence of a prosthesis, and it was discovered that high Z titanium prostheses attenuate 6 MV and 15 MV photon beam energies to varying degrees.

5.2.1.2 IMRT measurements

The doses to the prostate, rectum and bladder were significantly increased with the IMRT technique, when comparing the CT normal and O-MAR plans with the beam passing through the prosthesis. However, there was a slight reduction of dose to the right femur (bone). Similarly, with the IMRT plans with the field avoiding the prosthesis, the doses to the prostate, rectum and bladder were significantly increased. There is no apparent difference between the two plans' conformity index. Overall, the IMRT plans with hip prostheses' dosimetric parameters showed that the plans made using O-MAR CT data would not have been acceptable due to the increased maximum dose to the PTV.

The prostate, rectum, and bladder dose volume histogram (DVH) characteristics for normal CT data plans and O-MAR CT data plans were examined for the beam avoiding the prosthesis. In comparison to normal CT-plans, O-MAR plans exhibit improved prostate coverage, and they were in compliance with the maximum tolerated dose of 107%.

The CT normal was used as the reference to calculate the percentage difference in Table 5.6.

Table 5. 6: Dosimetric parameters for IMRT plans with hip prosthesis.

	IMRT			IMRT with avoidance		
	CT normal	**O-MAR**	**% Difference**	**CT normal**	**O-MAR**	**% Difference**
PTV (prostate)						
Maximum dose (%)	107.2	114.4	6.7	104.1	105.3	1.2
D2 (%)	100	100	0.0	100	100	0.0
D98 (%)	99.5	100	0.5	96.2	98.5	2.4
Rectum						
V50 (%)	74.2	77.0	3.8	79.9	83.3	4.3
V60 (%)	68.9	71.7	4.1	74.6	78.2	4.8
V70 (%)	60.4	62.9	4.1	68.9	72.5	5.2
Bladder						
Maximum dose	107.5	110.2	2.5	104.7	105.3	0.6
V50 (%)	88.3	90.1	2.0	79.2	78.4	-1.0
V70(%)	60.9	61.1	0.3	61.6	61.3	-0.5
Right femur (Bone)						
V10 (%)	49.5	48.4	-2.2	44.2	43.2	-2.3
Left Femur(prosthesis)						
V10 (%)	56.1	56.3	0.4	48.6	49.1	1.0
Conformity index	1.50	1.52	1.3	1.05	1.12	6.7

PTV (prostate): Except for the O-MAR plan without avoiding the prosthesis, which showed the highest dose percentage difference of 6.7% when compared to the normal CT plan presented in Table 5.6, all plans were able to reach an acceptable maximum dose.

Bladder: All approaches, except for the O-MAR plan, were successful in achieving the bladder's goal. It was found that IMRT with an avoidance beam spares the bladder better. For both the normal CT and O-MAR plans, no statistically significant difference was discovered. When comparing the CT normal plans with the O-MAR plans, a maximum difference of 2.5% was seen.

Rectum: For the two plans, the dose given to the rectum was sufficient to meet its constraint. The normal CT and O-MAR plans differed significantly from one another. When comparing the plans with the beam avoiding the prosthesis, the sparing of the rectum in the normal CT plans is lower than in the O-MAR plans by 5.2% for V70, 4.8% for V60, and 4.3% for V50.

Right femoral head: the right femoral head was adequately spared by both plans. The O-MAR avoided beam plans show better sparing for the femoral head.

Left femoral head (prosthesis): There was no significant difference between the two plans for the left femoral head (prosthesis).

The most common practice is to prevent the beam from passing through the prosthesis, however as demonstrated in Fig. 5.2, it is not possible to deliver a homogeneous dose inside the PTV prostate.

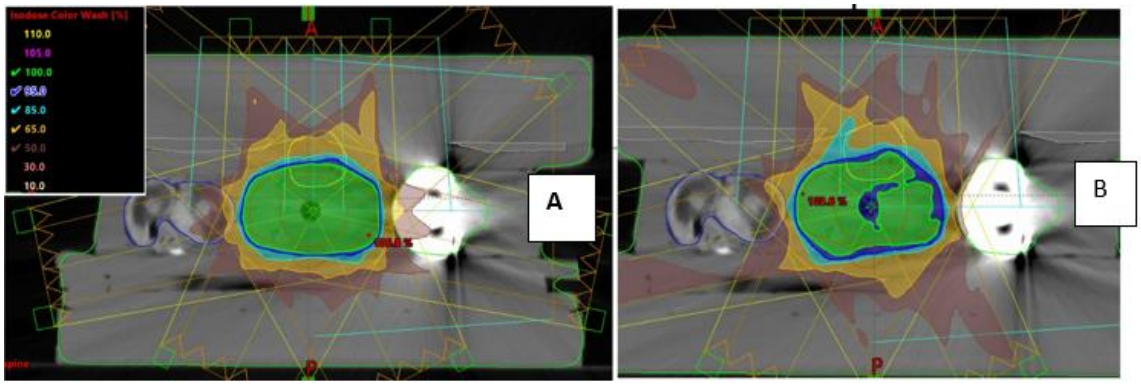

Figure 5. 2: IMRT plans (A) 7 field plans without avoiding the prosthesis and (B) six field plans avoiding the prosthesis (Eclipse treatment planning system (TPS) (Varian Medical Systems, Palo Alto, CA)).

Table 5. 7: Comparison of TPS calculated IMRT prostate point doses of 6 MV photon beam and ionization chamber measured prostate point doses.

PLANS	CT NORMAL (non-O-MAR) dataset			CT O-MAR dataset		
	TPS calculated dose (Gy)	Ionization chamber (Gy)	% Difference	TPS calculated dose (Gy)	Ionization chamber (Gy)	% Difference
IMRT	1.827 (SD±0.007)	1.787 (SD±0.0010)	2.2	1.801 (SD±0.00001)	1.731 (SD±0.0001)	4.1
IMRT (with avoidance sector)	1.817 (SD±0.0002)	1.783 (SD±0.0058)	1.9	1.839 (SD±0.00001)	1.781 (SD±0.0010)	3.2

The ionization chamber measured doses were the average doses obtained over the whole IMRT fraction for plans passing through the prosthesis and one avoiding passing through the prosthesis. For the IMRT plan with the beam passing through

the hip prosthesis, the prostate point dose discrepancies between the measured and TPS calculated doses were 2.2% and 4.1% for normal CT and O-MAR, respectively.

For the IMRT plan with the field arrangement to prevent the beam from going through the prosthesis, the dose discrepancies between the measured and TPS estimated doses were 1.9% and 3.2% for normal CT and O-MAR, respectively. The prostate coverage in the DVH is better in IMRT plans with the beam passing through the prosthesis, whereas the PTV (prostate) dose distribution is not uniform in plans with a beam arrangement to avoid passing through the prosthesis. However, when the two plans are verified in a phantom using an ionisation chamber, the avoidance-free O-MAR plans show the highest percentage difference as compared to the normal CT plan.

5.2.1.3 VMAT measurements

The VMATs plan with and without avoidance sector is shown in Fig. 5.3 below.

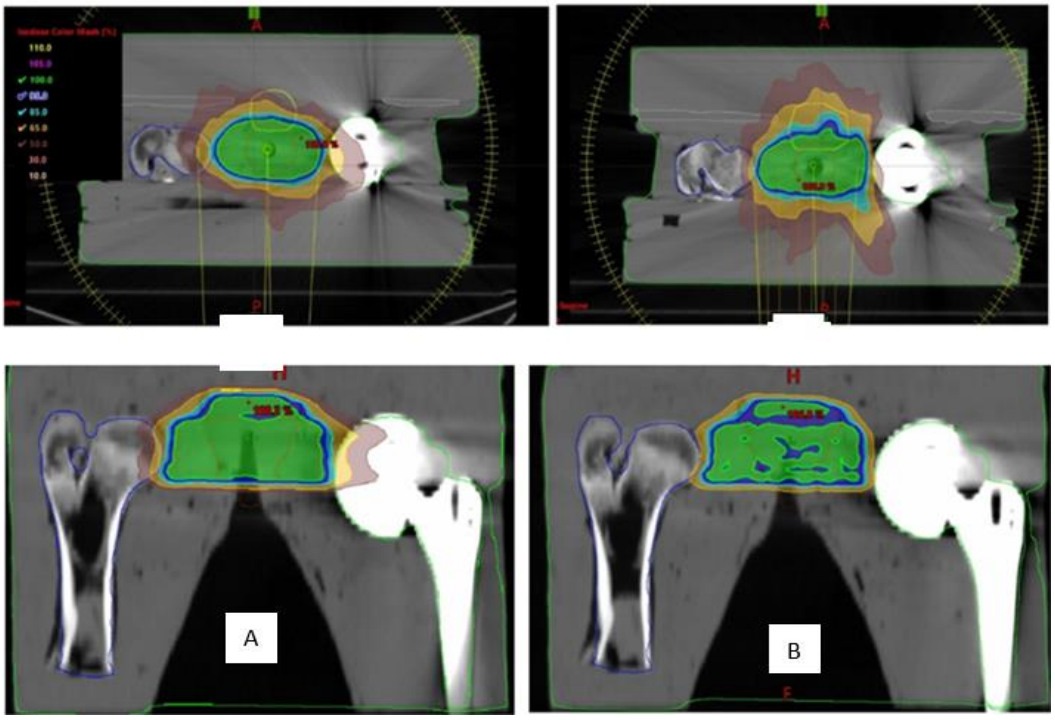

Figure 5. 3: VMAT plans (A) without the avoidance sector and (B) with the avoidance sector (Eclipse treatment planning system (TPS) (Varian MedicalSystems, Palo Alto, CA)).

PTV (prostate): All plans were able to achieve a desirable maximum dose except for the O-MAR plan without avoiding the prosthesis, which showed a maximum dose percentage difference of 3.5 % when compared to the CT normal plan shown in Table 5.8.

Bladder: All plans, except for the O-MAR plan, were successful in achieving the bladder's goal. VMAT with an avoidance beam has proven to be more bladder sparing. When comparing the CT normal plans with O-MAR plans, a maximum discrepancy of -2.8% was found on V70.

Rectum: For all six plans, the dose to the rectum met its constraint. In contrast to normal CT plans, there was a dose increase in O-MAR plans. When comparing the plans with the beam avoiding the prosthesis, the sparing of the rectum in the 2 arcs normal CT plans is better than in the O-MAR plans by 4.4% for V70, 3.8% for V60, and 3.9% for V50.

Right femoral head: Both plans adequately spared the right femoral head. The O-MAR avoided beam plans display superior femoral head sparing. There was a small discrepancy between the two plans for the left femoral head (prosthesis).

In contrast to using a single arc, using two arcs to avoid the beam passing through the hip prosthesis resulted in lower doses to vital organs and improved coverage of the PTV (prostate). Except for the O-MAR 2 arcs plans, which indicated an increase in dose to the prostate and the organ at risk.

The main benefit of VMAT over IMRT is the ability to lower the dose to crucial structures, which has been shown to lower the risk of side effects. Less time is required to treat the patient with VMAT plans than with IMRT since they use fewer monitor units.

Table 5. 8: Dosimetric parameters for VMAT plans with hip prosthesis.

Structures	VMAT (1arc)			VMAT (1 arc with avoidance)			VMAT (2 arcs)			VMAT (2 arcs with avoidance)		
	CT normal	O-MAR	% Difference	CT normal	O-MAR	% Difference	CT normal	O-MAR	% Difference	CT normal	O-MAR	% Difference
PTV (prostate)												
Maximum dose (%)	107.8	111.6	3.5	109.1	111.5	2.2	105.4	107.5	2.0	105.3	107.1	1.7
D2 (%)	100	100	0.0	100	100	0.0	100	100	0	100	100	0.0
D98 (%)	98.3	99.8	1.5	97.8	99.5	1.7	97.6	99.3	1.7	96.5	98.5	2.1
Rectum												
V50 (%)	83.3	86.7	4.1	82.8	85.8	3.6	80.5	83.5	3.7	82.7	85.9	3.9
V60 (%)	79.2	82.3	3.9	78.6	81.6	3.8	75.9	79.0	4.1	78.0	81	3.8
V70 (%)	70.5	73.9	4.8	72.1	75.4	4.6	69.9	73.1	4.6	72.8	76.0	4.4
Bladder												
Maximum dose	107.1	106.4	-0.7	106.9	106.4	-0.4	105.2	105.1	-0.1	104.1	104.1	0.0
V70 (%)	50.6	49.2	-2.8	60.6	59.6	-1.7	61.4	60.8	-0.9	60.7	60.3	-0.7
V50 (%)	78.9	77.9	-1.3	79.2	78.8	-0.5	77.1	76.4	-0.9	75.9	75.2	-0.9
Right femur (Bone)												
V10 (%)	48.5	47.8	-1.4	48.8	48.1	-1.4	48.3	47.7	-1.24	47.3	46.6	-1.5
Left Femur (prosthesis)												
V10 (%)	54.5	55.1	1.1	51.7	51.6	-0.2	53.8	54.4	1.1	47.6	47.8	0.4
Conformity index	1.32	1.32	0.0	1.30	1.30	0.0	1.22	1.21	0.8	0.97	0.96	-1.0

Table 5. 9: Comparison of TPS calculated VMAT doses of 6 MV photon beam and ionization chamber measured doses.

PLANS	CT NORMAL (non-O-MAR) dataset			CT O-MAR dataset		
	TPS calculated dose (Gy)	Ionization chamber (Gy)	% Difference	TPS calculated dose (Gy)	Ionization chamber (Gy)	% Difference
VMAT (1 arc)	1.827 (SD±0.0070)	1.787 (SD±0.0010)	2.2	1.801 (SD±0.00001)	1.731 (SD±0.0001)	4.1
VMAT (1 arc with avoidance sector)	1.817 (SD±0.0002)	1.783 (SD±0.0058)	1.9	1.839 (SD±0.00001)	1.781 (SD±0.0010)	3.2
VMAT (2 arcs)	1.805 (SD±0.0060)	1.786 (SD±0.0058)	1.1	1.816(SD±0.00010)	1.791 (SD±0.0001)	1.4
VMAT (2 arc with avoidance sector)	1.844 (SD±0.00001)	1.789 (SD±0.00001)	3.0	1.846 (SD±0.00001)	1.789 (SD±0.0002)	3.1

The average doses acquired over the 1 arc VMAT fraction for arc plans going through the prosthesis and plans with an avoidance sector were those that were measured in the ionisation chamber. For normal CT and O-MAR, dose discrepancies between measured and TPS estimated doses were 2.2 % and 4.1%, respectively. For 2 arcs plans without an avoidance sector, the dose discrepancies between measured and TPS estimated doses were 1.1 % and 1.4 % for normal CT and O-MAR, respectively. For two arcs plans with an avoidance sector, the dose discrepancies between the measured and TPS calculated doses were 3.0 % and 3.1% for normal CT and O-MAR, respectively. The percentage difference is calculated using equation 4.18.

Avoiding the beam passing through the prosthesis is recommended by the AAPM TG 63. According to our research, the 2 arcs VMATs technique is the best way to treat pelvic cancer while having a hip replacement. The contribution of the beam to the prosthesis is decreased when beam avoidance sectors are used to block radiation from reaching the prosthesis. Although Prabhakar *et al*. (2013) found comparable results in the literature, they constructed a structure for the prosthesis in their investigation rather than employing the avoidance sector.

The advantage of using an ionization chamber for dose measurements is that it gives direct readings. However, the electrometer's readout of charges needs to be converted to absorbed dose (Gy). An ionization chamber's calibration factor $N_{D,W,Qo}$ is only valid under the reference conditions that are used during the calibration. Any deviation from the reference conditions while using the ionisation chamber must to be corrected by applying the proper factor when converting the charges into an absorbed dose.

5.3.2 Gafchromic EBT3 film measurements

Gafchromic EBT3 film has been widely used for dosimetry in the volumetric region due to its flexible nature and high spatial resolution. The most convenient material for the dosimetric procedure is water with an effective atomic number of Z_{eff} = 7.42 and a density of 1g/cm. The Gafchromic EBT3 film has an effective atomic number Z_{eff} of 7.26.

5.3.2.1 Verification of the dose

The comparison of TPS calculated and Gafchromic film measured dose for a 6 MV photon beam in a solid water phantom is shown in Table 5.10. The ionization chamber measured doses were calculated using TRS 398 protocol.

Table 5. 10: Comparison of TPS calculated and ionization chamber measured dose for a 6 MV photon beam in a solid water phantom at a depth of 10 cm.

Monitor units delivered	TPS calculated dose (Gy)	Average measured charges (nC)	Ionization chamber TRS 398 Calculated doses (Gy)	% Difference
31	0.250	3.28 (SD±0.0057)	0.251	-0.39
61	0.500	64.49 (SD±0.0057)	0.501	-0.19
123	1.000	13.03(SD±0.0000)	1.001	-0.09
184	1.500	19.45 (SD±0.0058)	1.501	-0.07
246	2.000	25.98 (SD±0.0058)	2.004	-0.19
307	2.500	32.45 (SD±0.0000)	2.502	-0.08
369	3.000	38.97 (SD±0.0057)	3.002	-0.07
430	3.500	45.41 (SD±0.0058)	3.503	-0.09
492	4.000	52.03 (SD±0.0057)	4.001	-0.02
738	6.000	77.98 (SD±0.0000)	5.999	0.02

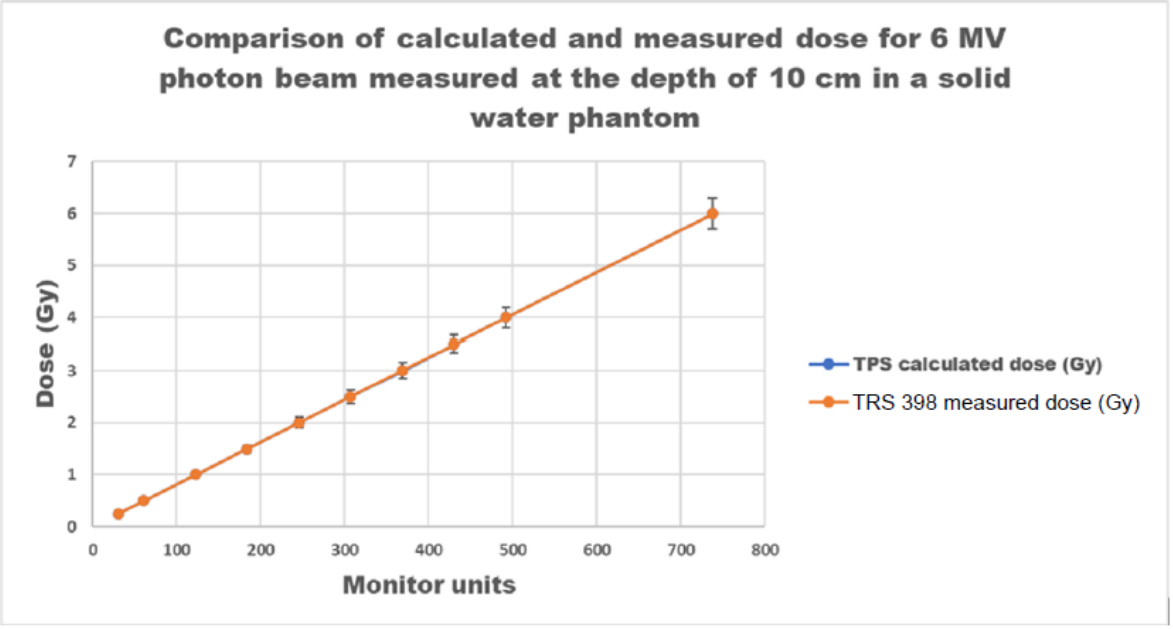

Figure 5. 4: Comparison of the dose calculated and measured (TRS 398) for a 6 MV photon beam at 10 cm in a solid water phantom.

The results in Table 5.10 and Fig.5.4 shows the comparison of the measured dose and the planned dose for the 6 MV photon beam at 10 × 10 cm^2 field size measured at a depth of 10 cm and SSD of 90 cm in a solid water phantom for different prescribed dose levels. The measured dose per TRS 398 shows a good agreement with the planned dose with a percentage difference of less than 0.40 %.

Table 5. 11: Comparison of calculated and ionization chamber measured dose for 15 MV photon beam measured at a depth of 10 cm in water.

Monitor units delivered	TPS calculated dose (Gy)	Average measured charges (nC)	Ionization chamber TRS 398 Calculated doses (Gy)	% Difference
27	0.250	3.370 (SD±0.0057)	0.249	0.40
54	0.500	6.739 (SD±0.0058)	0.501	-0.20
109	1.000	13.68 (SD±0.0057)	1.001	-0.09
163	1.500	20.50 (SD±0.0000)	1.501	-0.07
217	2.000	27.19 (SD±0.0058)	2.001	-0.05
272	2.500	34.14 (SD±0.0000)	2.501	-0.04
326	3.000	40.93 (SD±0.0057)	2.998	0.07
381	3.500	47.79 (SD±0.0057)	3.501	-0.03
435	4.000	54.55 (SD±0.0057)	4.001	-0.03
652	6.000	81.80 (SD±0.0000)	6.002	-0.03

Table 5.11 and Fig.5.5 show the comparison of the planned dose and the measured dose for a 15 MV photon beam per TRS 398 protocol. A point dose in a planning system was used to estimate the planned dose at the depth of 10 cm since all plans were calculated at the depth of 10 cm and SSD of 90 cm in a water phantom. These plans were normalized to give 100 % of the prescribed dose at isocentre (depth of 10 cm) in a solid water phantom. The comparison between the planned dose and the measured dose shows a percentage difference of less than 0.5 %.

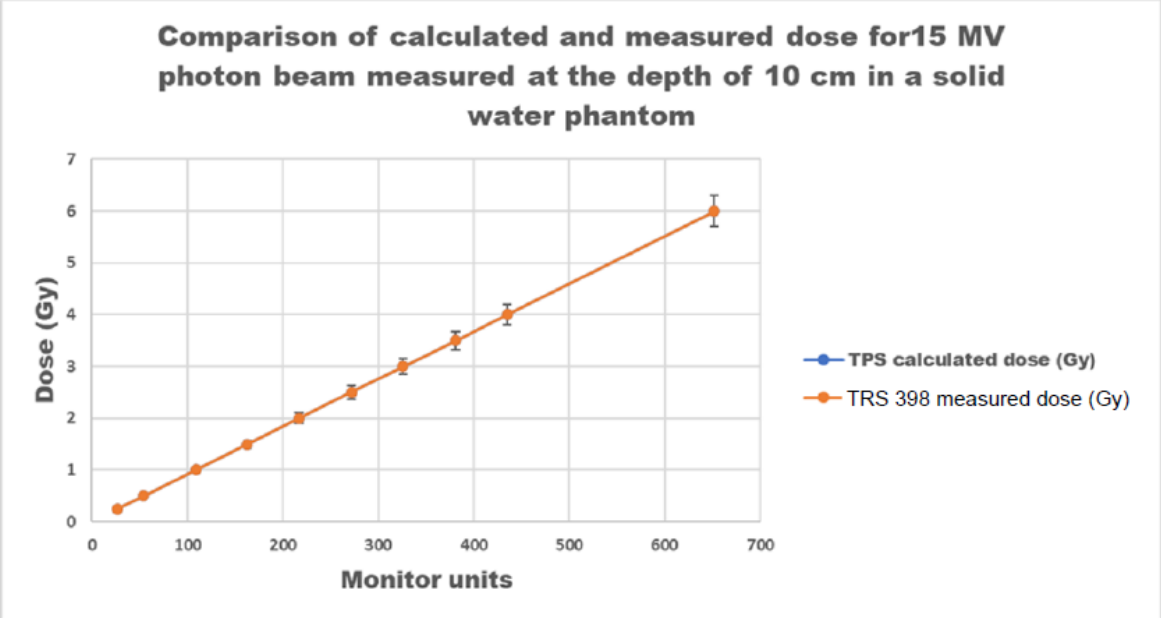

Figure 5. 5: Comparison of the calculated and measured (TRS 398) dose measured at 10 cm in a water tank for 15 MV photon beam.

Comparing the TPS calculated and measured doses for a 15 MV photon beam according to the TRS 398 protocol is shown in Table 5.11 and Fig. 5.5. The film calibration curve was also created using a 15 MV photon beam and compared with the one from a 6 MV electron beam to examine the energy dependency of the films.

5.3.2.2 Gafchromic EBT3 film calibration curve

Before the determination of the Gafchromic EBT3 film calibration curve, readings of the films scanned using different image resolutions were compared by scanning the

same films with different dpi. The dose-response results and standard deviation are presented in Table 5.12 below.

Table 5. 12: Comparison of dose-response of scanner resolution 400 dpi, 72 dpi and 50 dp.

Monitor Units	Dose (Gy)	400dpi	72dpi	50dpi
0.00	0.00	28854.58 (SD±37.8)	28751.31 (SD±21.9)	28761.71 (SD±159)
25.00	0.25	25905.02 (SD±83.4)	25552.51 (SD±120.1)	25824.27 (SD±36.8)
51.00	0.50	23763.49 (SD±62.6)	23510.05 (SD±83.7)	23691.61 (SD±21.1)
101.00	1.00	20493.74 (SD±10.1)	20443.22 (SD±19.1)	20491.72 (SD±8.94)
151.00	1.50	18247.45 (SD±29.8)	18130.56 (SD±37.7)	18209.59 (SD±7.92)
201.00	2.00	16505.45 (SD±2.6)	16564.87 (SD±36.9)	16432.41 (SD±39.5)
251.00	2.50	15260.32 (SD±43.9)	15103.97 (SD±46.3)	15188.28 (SD±2.36)
301.00	3.00	14181.15 (SD±37.1)	14116.16 (SD±0.5)	14053.62 (SD±223.2)
351.00	3.50	13521.61 (SD±60.1)	13345.05 (SD±41.8)	13385.92 (SD±18.3)
401.00	4.00	13006.10 (SD±90.9)	12840.80(SD±4.5)	12698.83 (SD±86.5)
602.00	6.00	11546.90 (SD±79.3)	11402.11 (SD±4.4)	11279.90 (SD±74.9)

Figure 5. 6: The comparison of film readings from different scanner resolution 400 dpi. 72 dpi and 50 dpi.

The film calibration curves were obtained in red and green channels as shown in Fig.5.7. The formulas for each curve were calculated in 0.25 - 6 Gy doses using Microsoft Excel software. The calibration curve data were fitted with second-order polynomial for the 0.25 - 6 Gy dose range for all calibration curves. The fitting equation and the regression squared of the fit are displayed on the curve. The red channel curve presented more sensitivity than the green channel.

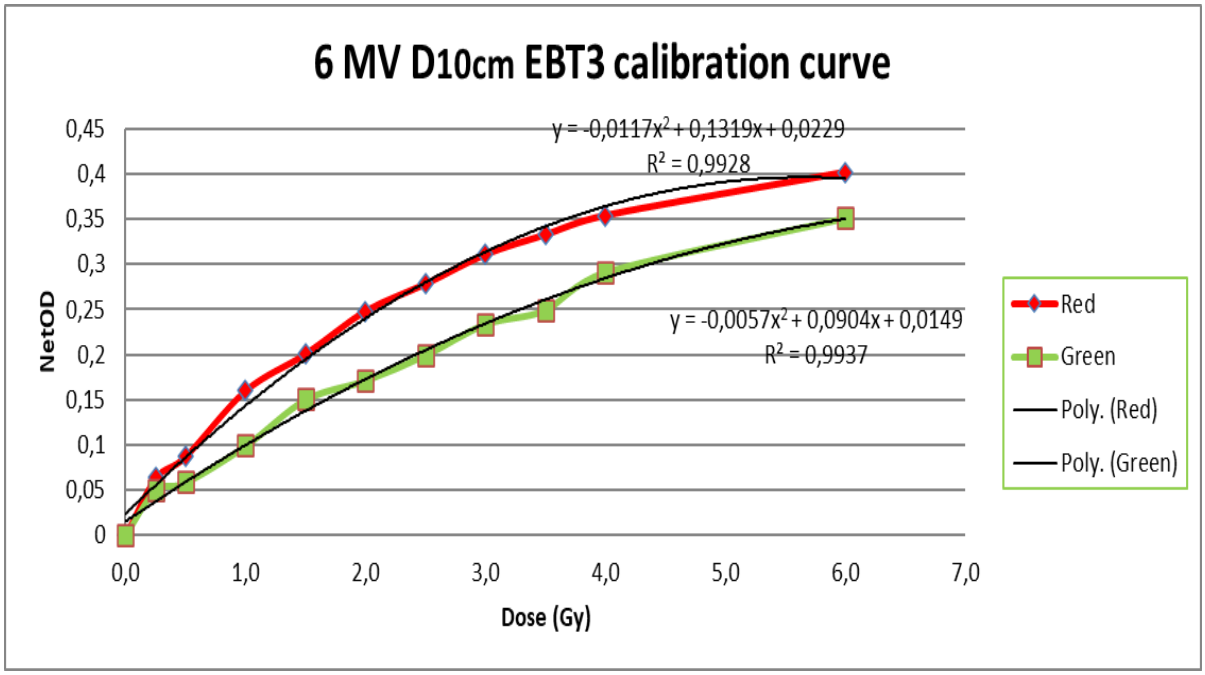

Figure 5. 7: Dose-response calibration curves for EBT3 film to 6 MV photon beam for Red and Green measured in a solid water phantom, showing greater sensitivity to the red colour channel.

Figure 5.7 shows the regression of $R^2 = 0.9928$ for the red channel, $R^2 = 0.9937$ for green channel and for the green channel, the regression of the fitted curve was very similar to that of the red channel.

Table 5. 13: Net optical density of the EBT3 film dose-response acquired at a depth of 10 cm for 6 MV in a solid water phantom.

Dose (Gy)	6MV Red channel at a depth of 10 cm NetOD	6MV Green channel at a depth of 10 cm NetOD
0.00	0.0	0.0
0.25	0.061 (SD±0.0009)	0.044 (SD±0.0011)
0.50	0.087 (SD±0.0013)	0.059 (SD±0.0011)
1.00	0.161 (SD±0.0011)	0.103 (SD±0.0013)
1.50	0.201 (SD±0.0012)	0.151 (SD±0.0010)
2.00	0.246 (SD±0.0013)	0.178 (SD±0.0012)
2.50	0.273 (SD±0.0011)	0.211 (SD±0.0011)
3.00	0.313 (SD±0.0012)	0.237 (SD±0.0011)
3.50	0.338 (SD±0.0011)	0.262 (SD±0.0012)
4.00	0.358 (SD±0.0011)	0.293 (SD±0.0009)
6.00	0.401 (SD±0.0009)	0.348 (SD±0.0012)

The calibration curve was also obtained by exposing the films in solid water for 6 MV photon and 15 MV photon beams. Figure 5.9 was done to compare the calibration curve measured in a solid water phantom to check the energy dependence of the Gafchromic EBT3 film. The results confirmed that Gafchromic EBT3 films are nearly independent of energy.

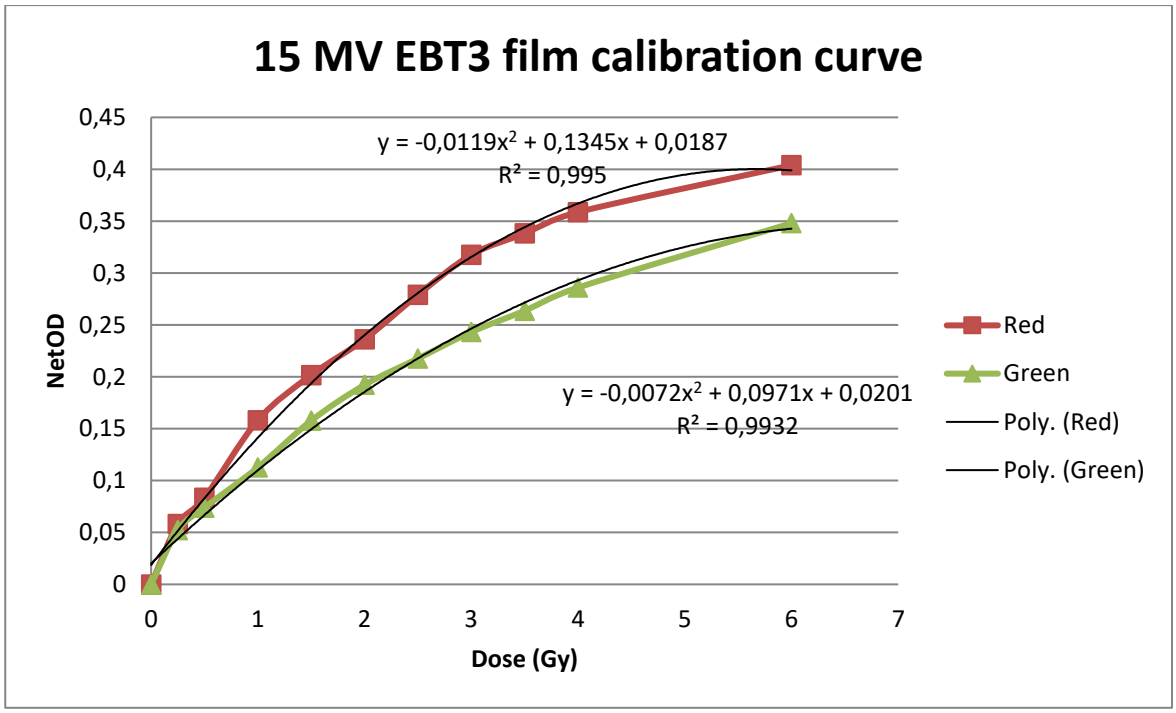

Figure 5. 8: Dose-response calibration curves for EBT3 film to 15 MV photon beam for Red and Green channels measured in a solid water phantom.

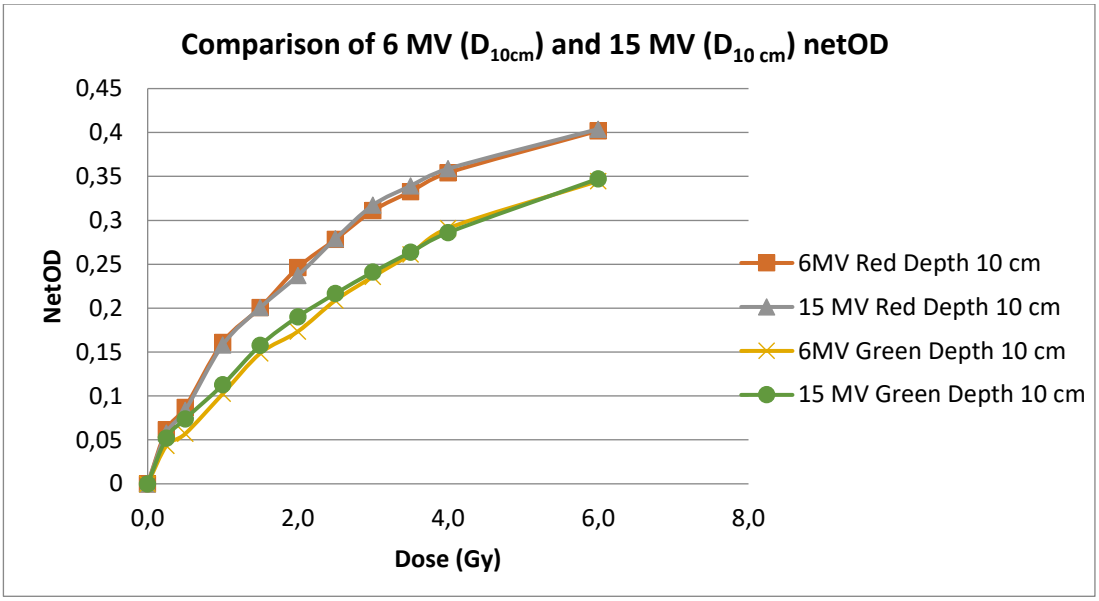

Figure 5. 9: Comparison of net optical density versus the absorbed dose curve for 6 MV and 15 MV photon beams.

The net optical density values for a 15 MV photon beam obtained by irradiating films in a solid water phantom at the depth of 10 cm are comparable to the net optical values for the Gafchromic EBT3 film for the 6 MV photon energy obtained by irradiating films at the depth of 10 cm.

Table 5. 14: Comparison of the net optical density values for 6 MV photon beam and 15 MV photon beam and the standard deviation (±) indicated.

Dose (Gy)	Net optical density (OD)			
	6MV Red Depth 10 cm	15 MV Red Depth 10 cm	6MV Green Depth 10 cm	15 MV Green Depth 10 cm
0.0	0.000	0.000	0.000	0.000
0.3	0.061±0.0009	0.059±0.0011	0.044±0.0011	0.046±0.0012
0.5	0.087±0.0013	0.086±0.0011	0.059±0.0012	0.063±0.0012
1.0	0.161±0.0011	0.160±0.0013	0.103±0.0011	0.115±0.0009
1.5	0.201±0.0012	0.203±0.0010	0.151±0.0011	0.155±0.0011
2.0	0.246±0.0013	0.239±0.0012	0.178±0.0011	0.186±0.0012
2.5	0.273±0.0011	0.282±0.0011	0.211±0.0012	0.214±0.0011
3.0	0.312±0.0012	0.318±0.0011	0.237±0.0011	0.241±0.0011
3.5	0.335±0.0011	0.341±0.0012	0.262±0.0012	0.264±0.0011
4.0	0.356±0.0011	0.362±0.0009	0.293±0.0011	0.286±0.0011
6.0	0.401±0.0009	0.406±0.0012	0.348±0.0009	0.347±0.0009

5.3.2.3 Gafchromic EBT3 film prostate point dose measurements

Irradiated films were scanned using an Epson scanner and the pixel reading was obtained using the red channel. The pixel readings for each field were converted into dose by using the film calibration curve obtained in Section 4.4.4. Table 5.15 and Table 5.16 show the mean pixel readings used to calculate dose for 6 MV and 15 MV photon beams.

Table 5. 15: Comparison of TPS calculated dose with Gafchromic EBT3 film measured prostate point dose for 6 MV and 15 MV photon beam

	6 MV PHOTON BEAM				**15 MV PHOTON BEAM**			
Field	**Average TPS calculated dose (Gy)**	**Average mean pixel reading**	**Average Film Calculated dose (Gy)**	**% difference**	**Average TPS calculated dose (Gy)**	**Average mean pixel reading**	**Average Film Calculated dose (Gy)**	**% Difference**
Ant	2.066 (SD±0.001)	15965.328 (SD±11.2)	2.02 (SD±0.004)	2.3	2.038 (SD±0.0006)	16021.685 (SD±10.5)	2.01 (SD±0.001)	1.3
Post	2.030 (SD±0.0006)	16039.428 (SD±9.86)	2.05(SD±0.0006)	-0.9	2.036 (SD±0.002)	16146.826 (SD±11.3)	2.04(SD±0.001)	0.2
LT LAT	1.997 (SD±0.001)	17863.682(SD±10.85)	1.91(SD±0.006)	4.5	2.008 (SD=0.000)	17570.204 (SD±10.1)	1.94 (SD±0.001)	3.5
RT LAT	2.006 (SD±0.0006)	16102.675(SD±12.04)	2.05(SD±0.002)	-2.1	2.008 (SD±0.0004)	15924.85 (SD±11.8)	2.06 (SD±0.0006)	-2.5

The prostate point doses for the 6 MV and 15 MV photon beams are shown in Table 5.15 from the treatment planning system. Plans were developed to ensure that the prostate cavity received at least 100% of the specified dose.

Gafchromic EBT3 film was used to measure the prostate point dose. The dose calibration curve was generated by irradiating small pieces of film with doses ranging from 0.25 Gy – 6 Gy before using EBT3 film for prostate point dose measurement. Some elements that contribute to estimating the overall dose uncertainty. Both the EBT3 film and the Epson scanner had these aspects evaluated, and the uncertainties were found to be acceptable.

The comparisons of the measurements between the TPS calculated prostate point dose and measured dose calculated using equation 4.18 for the 6 MV photon beam were found to be 2.3 %, -0.9%, 4.5 % and -2.1 % for the anterior (gantry 0°), posterior (gantry 180°), left lateral (gantry 90°) and right lateral (gantry 270°) fields, respectively. For 15 MV the values were 1.3 %, 0.2%, 3.5 % and -2.5 %. The maximum deviation was again observed in the left lateral beam passing through the prosthesis. The treatment planning system overestimated the dose to the prostate.

The Gafchromic EBT3 dosimeter's performance is completed by higher film homogeneity and energy independence. The manufacturer recommends scanning the Gafchromic film after 24 hours. When cutting the film, caution must be used, gloves must be worn, and there must be no dust. Accurate results necessitate strict adherence to scanning procedure and Gafchromic film handling. The fact that slicing film causes the film to tear at the edges is an important disadvantage.

5.3.3 Comparison of doses obtained from normal CT data and O-MAR CT data

The physical parameters of all materials used in the pelvic phantom obtained directly from the CT data set of the normal CT and CT with O-MAR algorithm applied were compared and shown in Table 5.16 below. The CT numbers and relative densities of the superflab gel bolus and dental wax on the O-MAR scans were higher than those of the normal scans because the CT data was smooth and without artifacts.

Table 5. 16: Physical parameters of all the materials used in the pelvic phantom obtained from CT data set on Eclipse treatment planning system.

O-MAR CT VALUES

MATERIAL	CT NO	Relative density	Mass density	Stopping power
Titanium	3071	2.504	2.628	2.543
Bone	427	1.22	1.275	1.234
Superflab Bolus	6	1.003	1.006	1.013
Dental Wax	-38	0.974	0.98	0.989
Nylon	-64	0.953	0.967	0.972

NORMAL CT VALUES

MATERIAL	CT NO	Relative density	Mass density	Stopping power
Titanium	3071	2.504	2.628	2.543
Bone	454	1.226	1.282	1.24
Superflab Bolus	-8	0.997	0.999	1.009
Dental Wax	-68	0.95	0.965	0.97
Nylon	-44	0.969	0.977	0.985

Four field box plans of the same field size, SSD and energies (6 and 15 MV photon beams) were created using the CT data set (normal CT) without artifact correction and CT data set with artifact correction (O-MAR algorithms) for dose volume histogram comparison purpose.

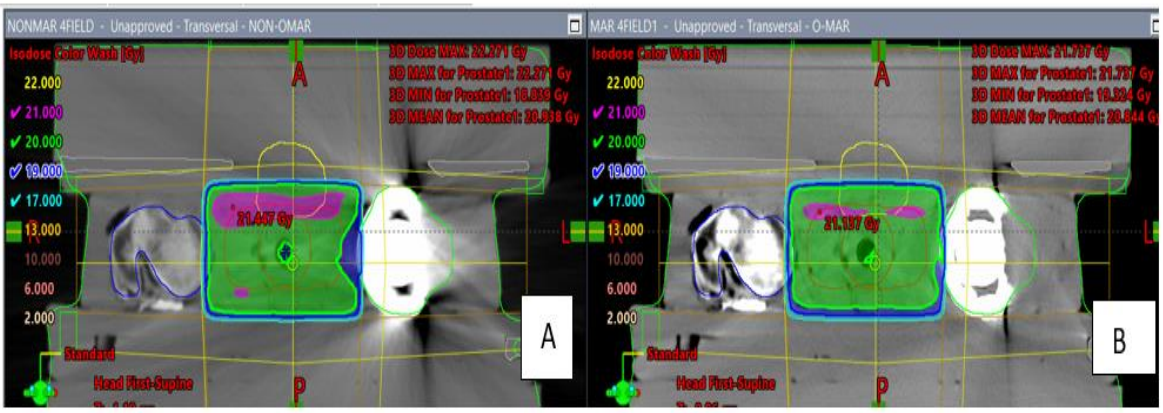

Figure 5. 10: The dose distribution for a four-field box plan of 6 MV photon beam (A) without artifact correction, (B) with artifact correction by applying O-MAR algorithms on the CT scanner (Eclipse treatment planning system (TPS) (Varian Medical Systems, Palo Alto, CA)).

The O-MAR algorithms reduced the artifact in the reconstructed image as shown in Fig.5.10. (B). The results of a comparison of the normal CT plan and O-MAR plan were compared using dose volume histogram (DVH) as shown in Fig.5.11 below for the 4-field plan. From both phantom plans, O-MAR did not affect dose distributions and DVHs while minimizing metal artifacts.

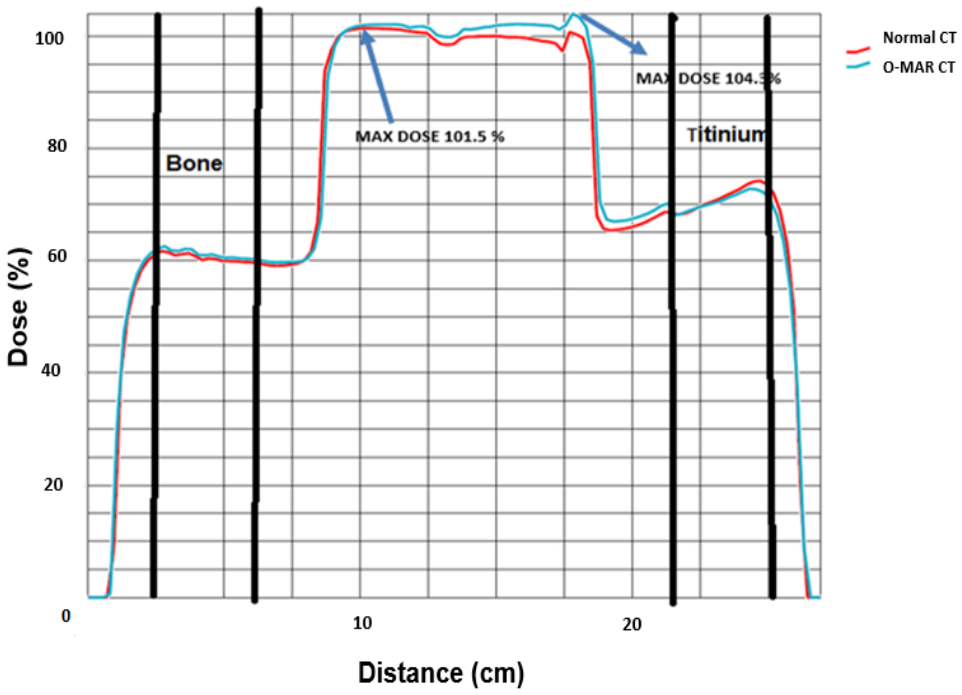

Figure 5. 11: Normal CT and O-MAR comparison of the lateral dose profile of TPS external beam planning calculation for four fields for 6 MV photon beam (Eclipse treatment planning system (TPS) (Varian Medical Systems, Palo Alto, CA)).

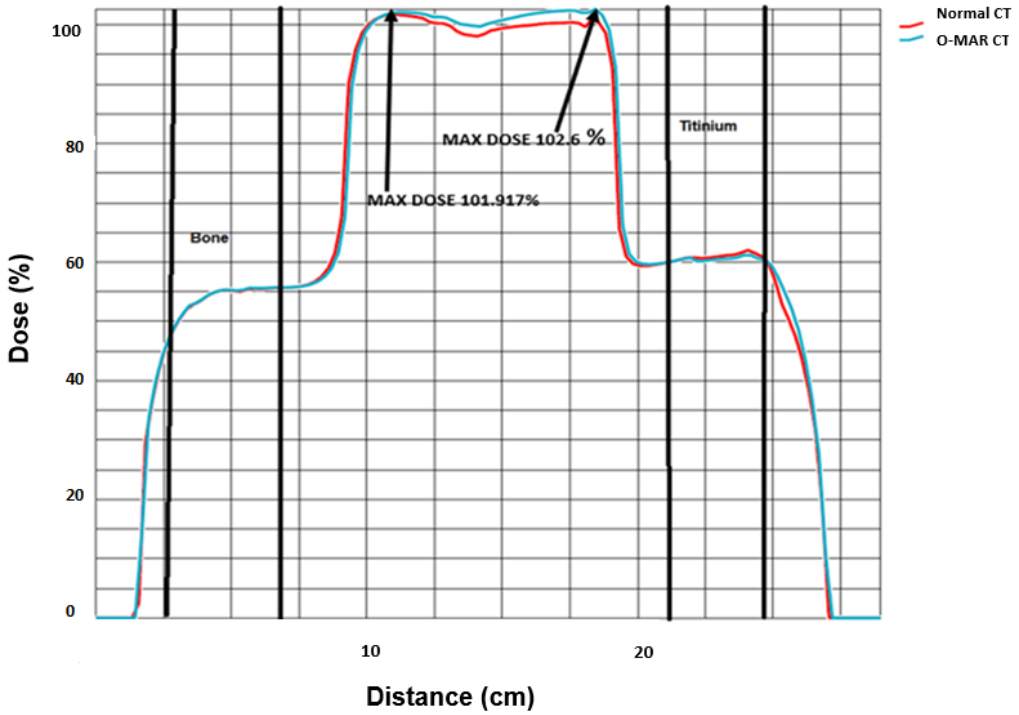

Figure 5. 12: Normal CT and O-MAR comparison of the lateral dose profile of TPS external beam planning calculation for four fields for 15 MV photon beam (Eclipse treatment planning system (TPS) (Varian Medical Systems, Palo Alto, CA)).

The lateral dose profiles for the normal scan (non-O-MAR) and O-MAR scan derived from the treatment planning system for the 6 and 15 MV photon beams are compared in Figures 5.11 and 5.12. There was a statistically significant difference at p=0.024 in the dose distribution for the dosimetric effect of O-MAR. A maximum dose of 104.3% was observed in the prostate tissue close to the titanium of the O-MAR plans for the 6 MV photon beam plan as opposed to a maximum dose of 101.5% in the prostate close to the bone of the normal CT scan plan. The titanium side of the phantom received a maximum dose of 102.6% for the 15 MV photon beam plan, whereas the bone side of the normal CT scan plan received a maximum dose of 101.9%. O-MAR usage led to a substantial reduction in CT number except for the prostate insert as shown in Table 5.16 above.

The plans were also compared by delivering the 6 MV photon beam plans in an in-house pelvic phantom with an ionization chamber. The comparison of the prostate point dose between the normal CT and the O-MAR CT using an ionisation chamber is shown in Table 5.17. The % difference between the ionisation chamber measured dose and the TPS calculated dose (calculated using equation 4.18) is indicated.

Table 5. 17: Comparison of the TPS calculated prostate point dose of normal CT and O-MAR CT with ion chamber measurements.

FIELDS	**CT NORMAL**			**CT O-MAR**		
	TPS (Gy)	**Average ion chamber (Gy)**	**% Difference**	**TPS (Gy)**	**Average ion Chamber (Gy)**	**% Difference**
Anterior	2.066	2.020 (SD±0.001)	2.2	1.998	2.04 (SD±0.006)	-2.1
Posterior	2.030	2.020 (SD±0.006)	0.5	1.989	2.01 (SD±0.001)	-1.1
LT lateral	1.997	1.910 (SD±0.001)	4.5	1.996	1.92 (SD±0.006)	3.7
RT lateral	2.006	2.03 (SD±0.001)	-1.2	2.014	2.03 (SD±0.006)	-0.8

The maximum HU for the CT scanner is 3071. Because the CT scanner in use has an upper limit HU value of 3071 HU, it was not possible to identify the precise CT number of the titanium prosthesis.

For this study, two CT data sets were acquired, one with an O-MAR (Metal artifact reduction) algorithm applied to reduce image artifacts and one without artifact correction. The doses from the series (previously described) generated on a TPS for both CT data sets were compared using DVH as shown in Fig. 5.13, 5.14 and 5.15 and prostate point dose measurements delivered by a linear accelerator and measured using an ionization chamber. The plans using O-MAR CT data show the highest maximum dose on the prosthesis side for both 6 MV and 15 MV.

With artefact correction, an appropriate distribution coverage of the prostate was seen in the plan. However, the plans with artefact correction (O-MAR) for both the 6 MV and 15 MV photon beams had the maximum discrepancy between the TPS predicted prostate dose and the ionisation chamber measurement. The highest deviation for both the 6 MV and 15 MV CT data plans for the ionisation chamber is seen on the left lateral field (Prosthesis side).

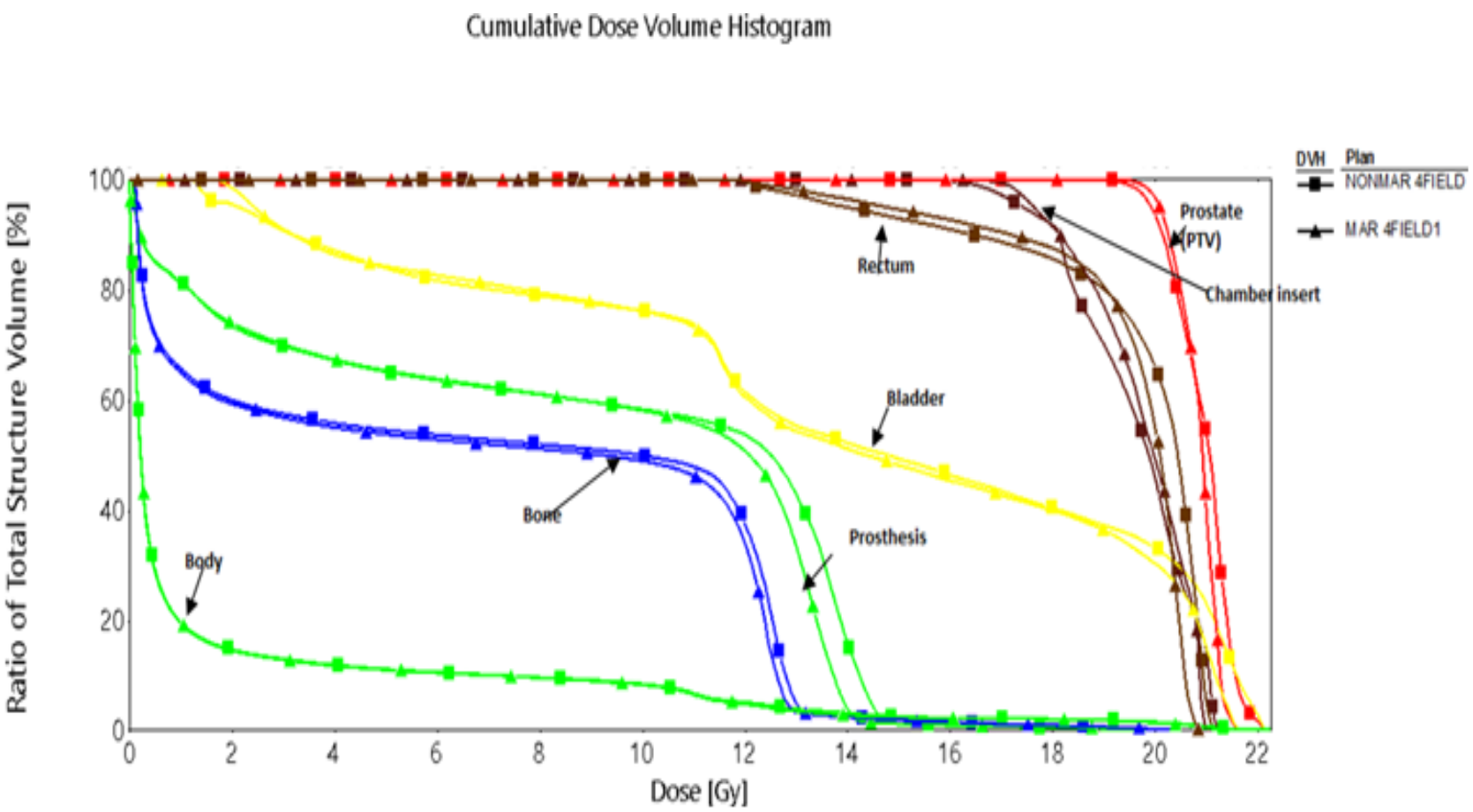

Figure 5. 13: DVH comparison of 6 MV 4-field 3D conformal plans using CT with and without artifact correction.

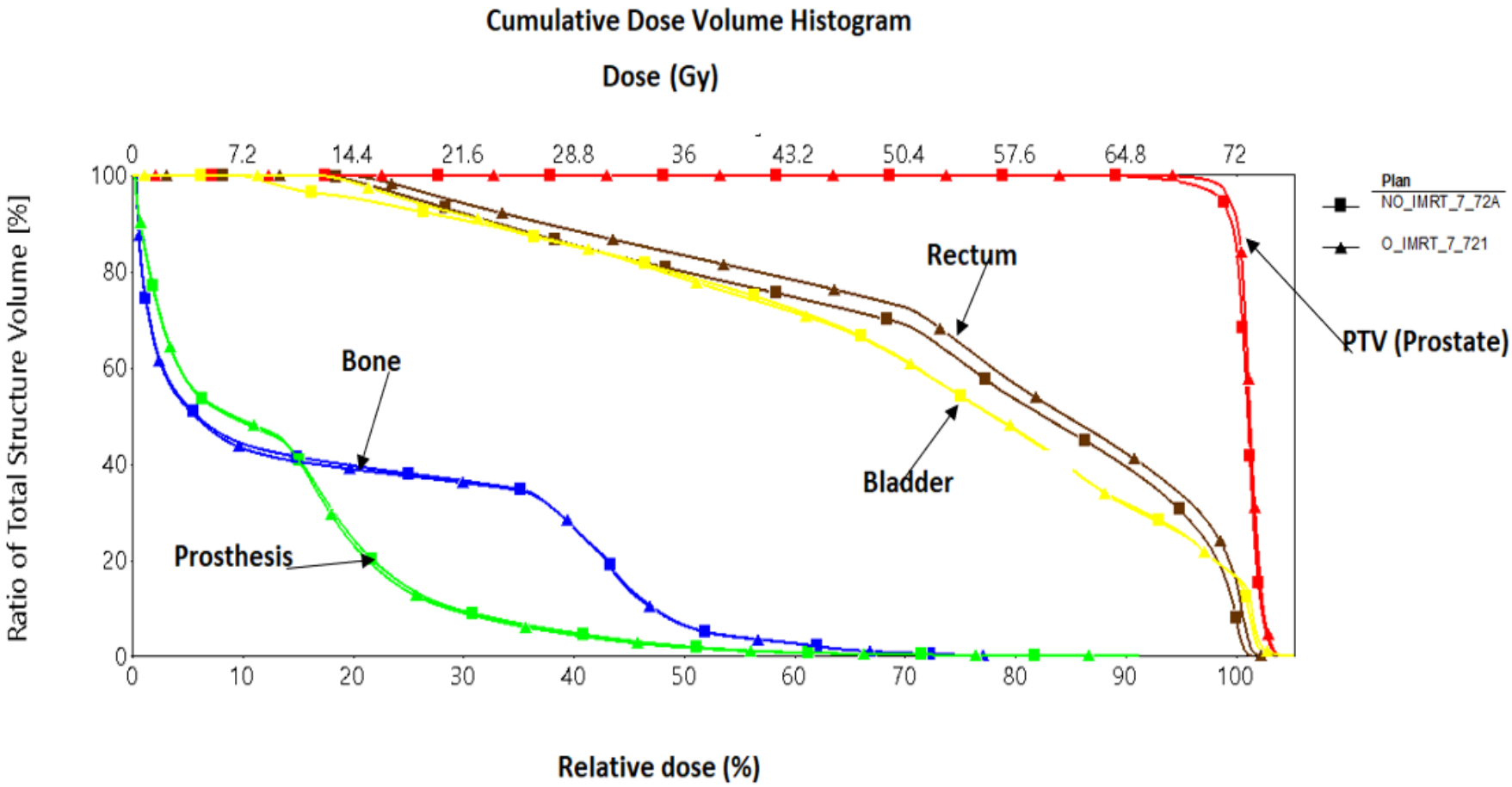

Figure 5. 14: DVH comparison of 6 MV IMRT plans avoiding beams passing through the prosthesis using CT with and without artifact correction.

.

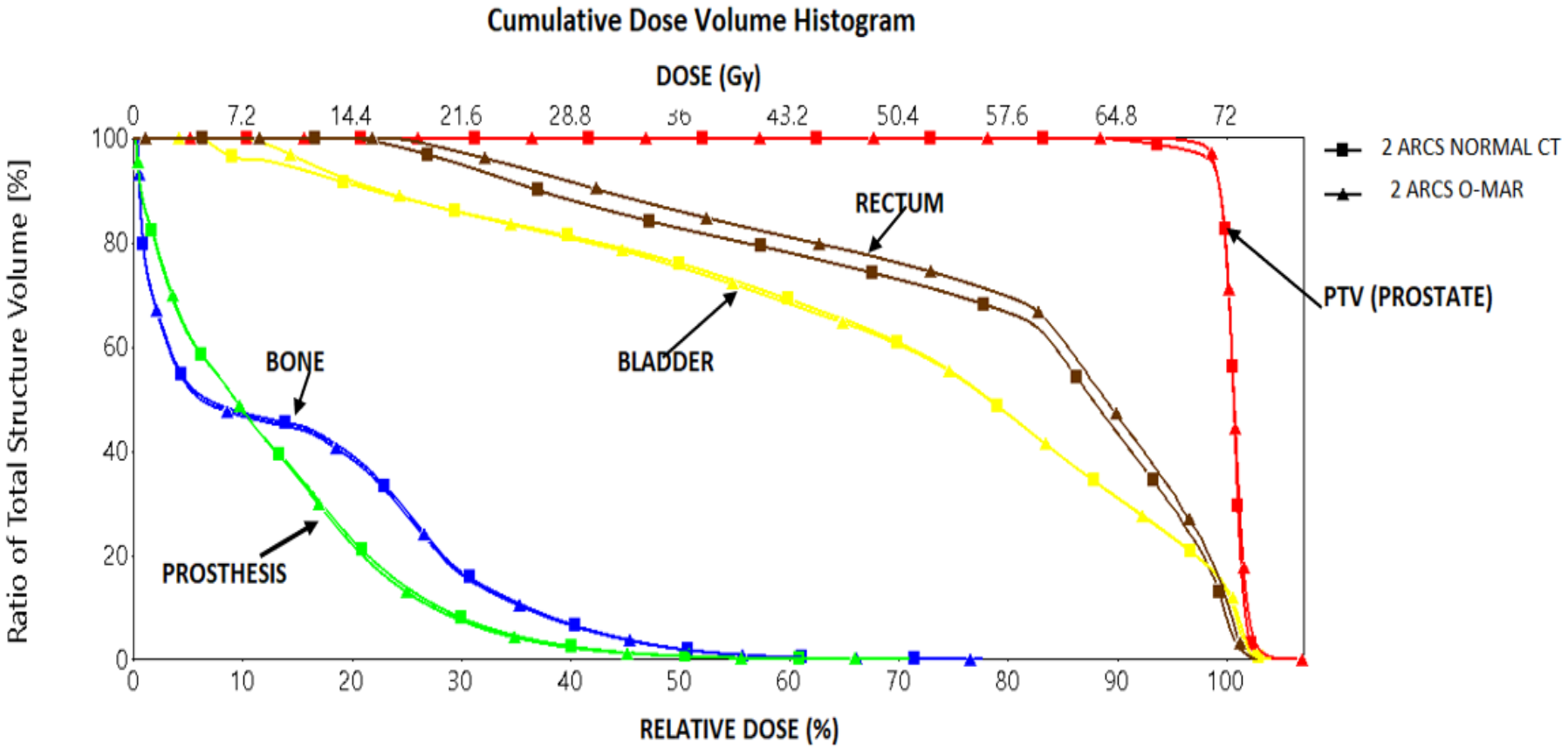

Figure 5. 15: DVH comparison of 6 MV VMAT plans avoiding beams passing through the prosthesis using CT with and without artifact correctio

Table 5. 18: Comparison of TPS calculated IMRT doses of 6 MV photon beam with film measured doses.

PLANS	NORMAL CT (non-O-MAR) dataset			CT O-MAR dataset		
	TPS calculated dose (Gy)	Gafchromic EBT3 Film dose (Gy)	% Difference	TPS calculated dose (Gy)	Gafchromic EBT3 Film dose (Gy)	% Difference
IMRT	1.827 (SD±0.0070)	1.768 (SD±0,0006)	3.3	1.801 (SD±0.00001)	1.751 (SD±0.0003)	2.3
IMRT (with avoidance sector)	1.817 (SD±0.0002)	1.763 (SD±0.0058)	3.1	1.839 (SD±0.00001)	1.758 (SD±0.0010)	4.0

Table 5. 19: Comparison of TPS calculated VMAT doses of 6 MV photon beam with film measured doses.

PLANS	NORMAL CT (non-O-MAR) dataset			CT O-MAR dataset		
	TPS calculated dose (Gy)	Gafchromic EBT3 Film dose (Gy)	% Difference	TPS calculated dose (Gy)	Gafchromic EBT3 Film dose (Gy)	% Difference
VMAT (1 arc)	1.827 (SD±0.006)	1.767 (SD±0.003)	3.4	1.801 (SD±0.00001)	1.761 (SD±0.006)	2.2
VMAT (1 arc with avoidance sector)	1.817 (SD±0.0002)	1.762 (SD±0.006)	3.1	1.839 (SD±0.00001)	1.769 (SD±0.006)	3.9
VMAT (2 arcs)	1.805 (SD±0.0060)	1.766 (SD±0.005)	2.2	1.816(SD±0.00010)	1.755 (SD±0.0003)	3.4
VMAT (2 arc with avoidance sector)	1.844 (SD±0.006)	1.773 (SD±0.005)	4.0	1.846 (SD±0.00001)	1.774 (SD±0.0002)	4.1

The comparison of IMRT and VMAT for film dose measured using plans made of normal CT data and the O-MAR data set is shown in Tables 5.18 and 5.19. When comparing the TPS computed dose to the normal CT plans, the O-MAR plans with the avoidance sector exhibit the greatest percentage difference.

5.4 EGSnrc Monte Carlo prostate dose simulation

This section shows the results of the validation of MC simulation results for 6 MV and 15 MV photon beam and EGSnrc prostate point dose simulation.

5.4.1 Validation of Monte Carlo simulation

EGSnrc Monte Carlo code was validated by comparing the MC simulated dose distribution with the one measured in water during the commissioning of the machine.

The central axis percentage depth doses (PDD) and dose profiles for 6 MV and 15 MV photon beams with 3 × 3 cm^2, 10 × 10 cm^2 and 15 × 15 cm^2 field sizes measured using Varian Clinac IX linear accelerator (commissioning data) were within the limits set by the manufacturer.

5.4.1.1 Percentage depth dose and dose profile

The percentage depth dose and dose profile obtained from commissioning data measured in water and MC simulations were compared using gamma analyses, employing a 2 %/2 mm distance-to agreement criterion. The gamma analysis evaluates the dose distribution point by point for PDD and profiles.

The PDD obtained in water for 6 MV at 3 × 3 cm^2 shows the maximum dose at the depth of 1.60 cm and 1.59 cm for MC simulation dose distribution. The EGSnrc Monte Carlo calculated dose distribution agreed well with experimental

measurements within 2 % as shown in Fig.5.16. The maximum deviation of PDD was found at a depth between 12 and 14 cm.

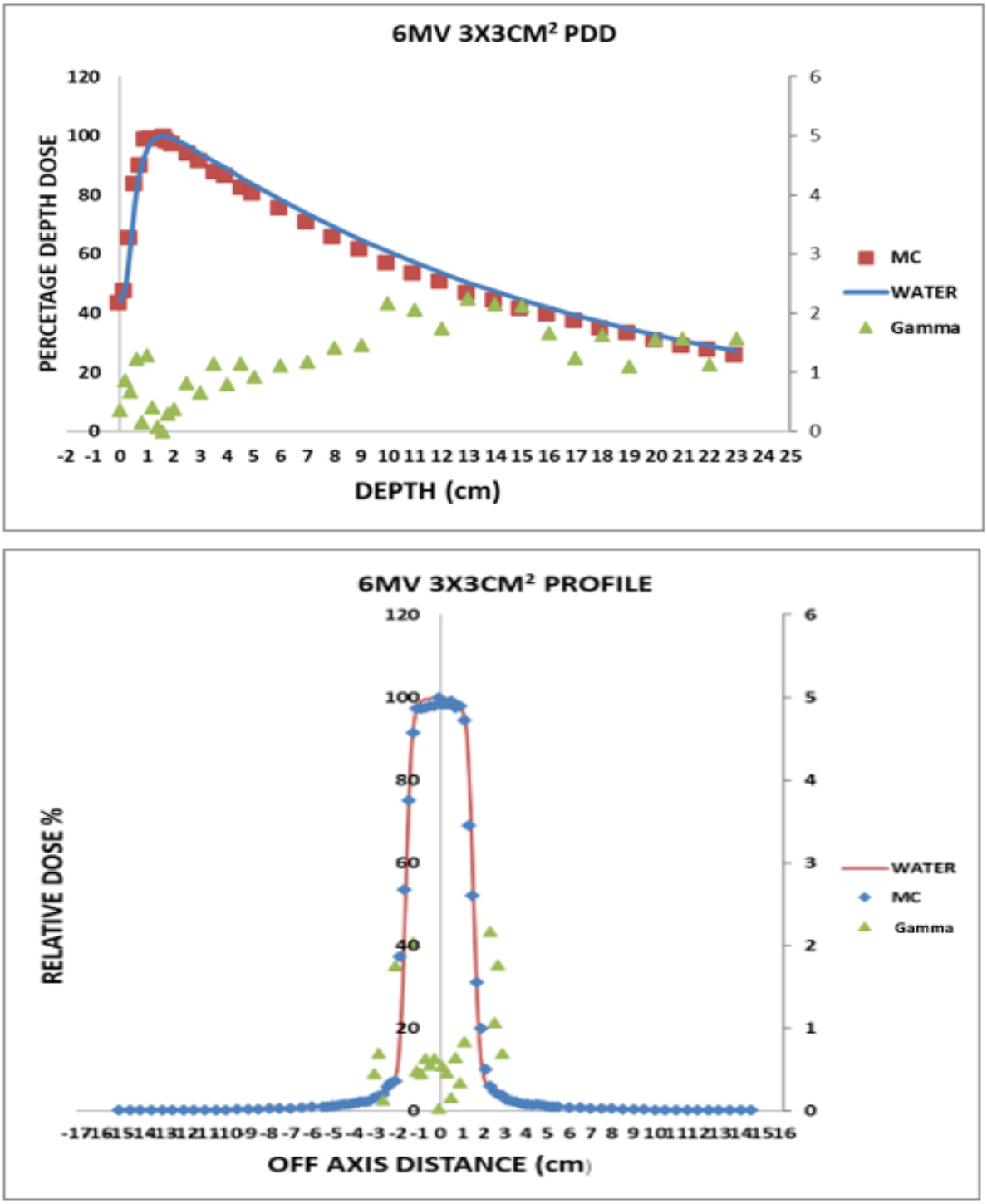

Figure 5. 16: The percentage depth dose and beam profile for 6 MV photon beam with 3 × 3 cm^2 field size and gamma analyses for each point indicated.

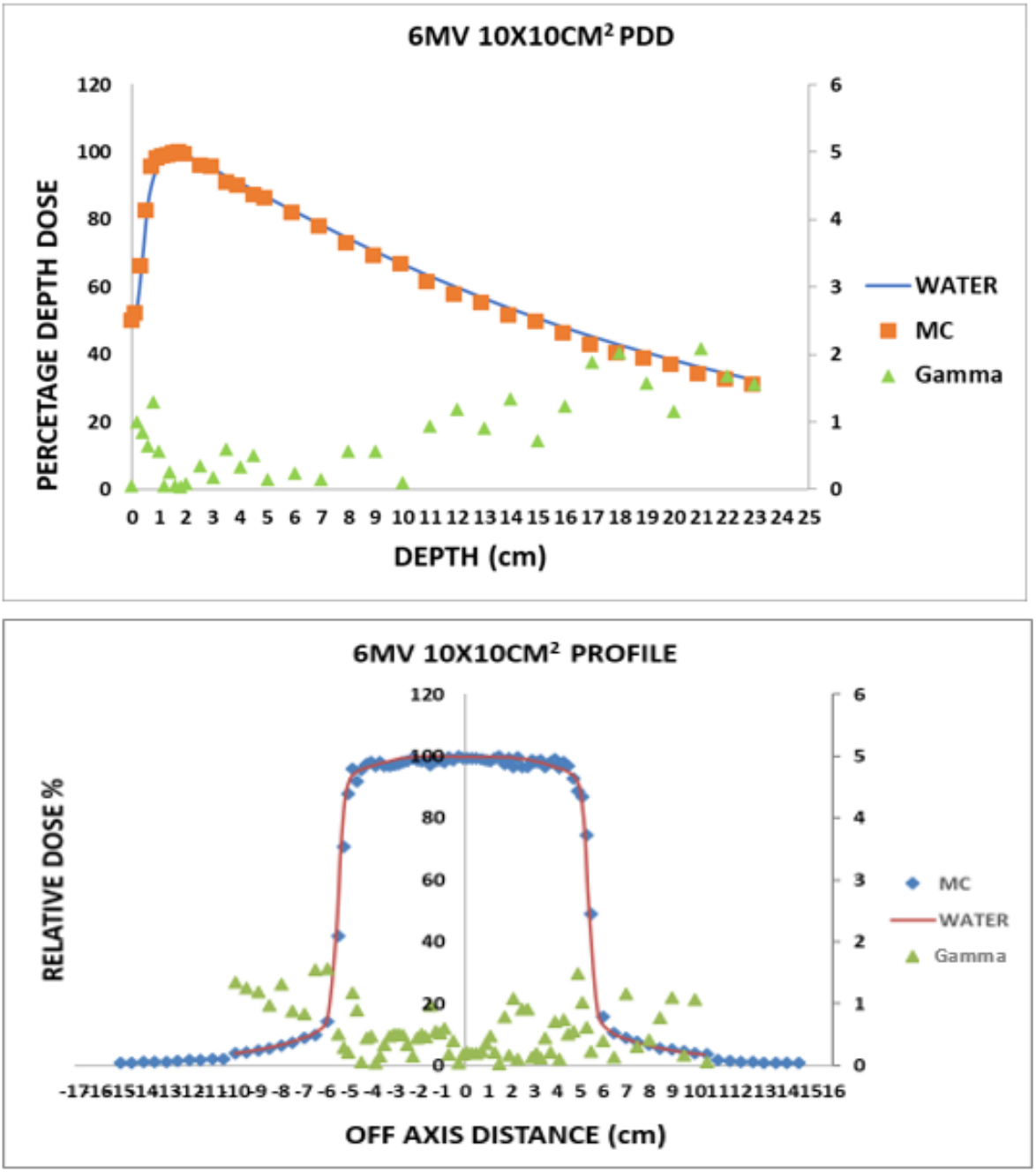

Figure 5. 17: The percentage depth dose and beam profile for 6 MV photon beam with 10 × 10 cm^2 field size and gamma analyses for each point indicated.

The PDD obtained in water for 6 MV at 10 × 10 cm^2 field size shows the maximum dose at a depth of 1.60 cm and 1.59 cm for MC simulation dose distribution. The EGSnrc Monte Carlo calculated dose distribution (PDD and dose profile) agreed well with experimental measurements within 2 % as shown in Fig.5.17. The maximum deviation was found at a depth of 21 cm.

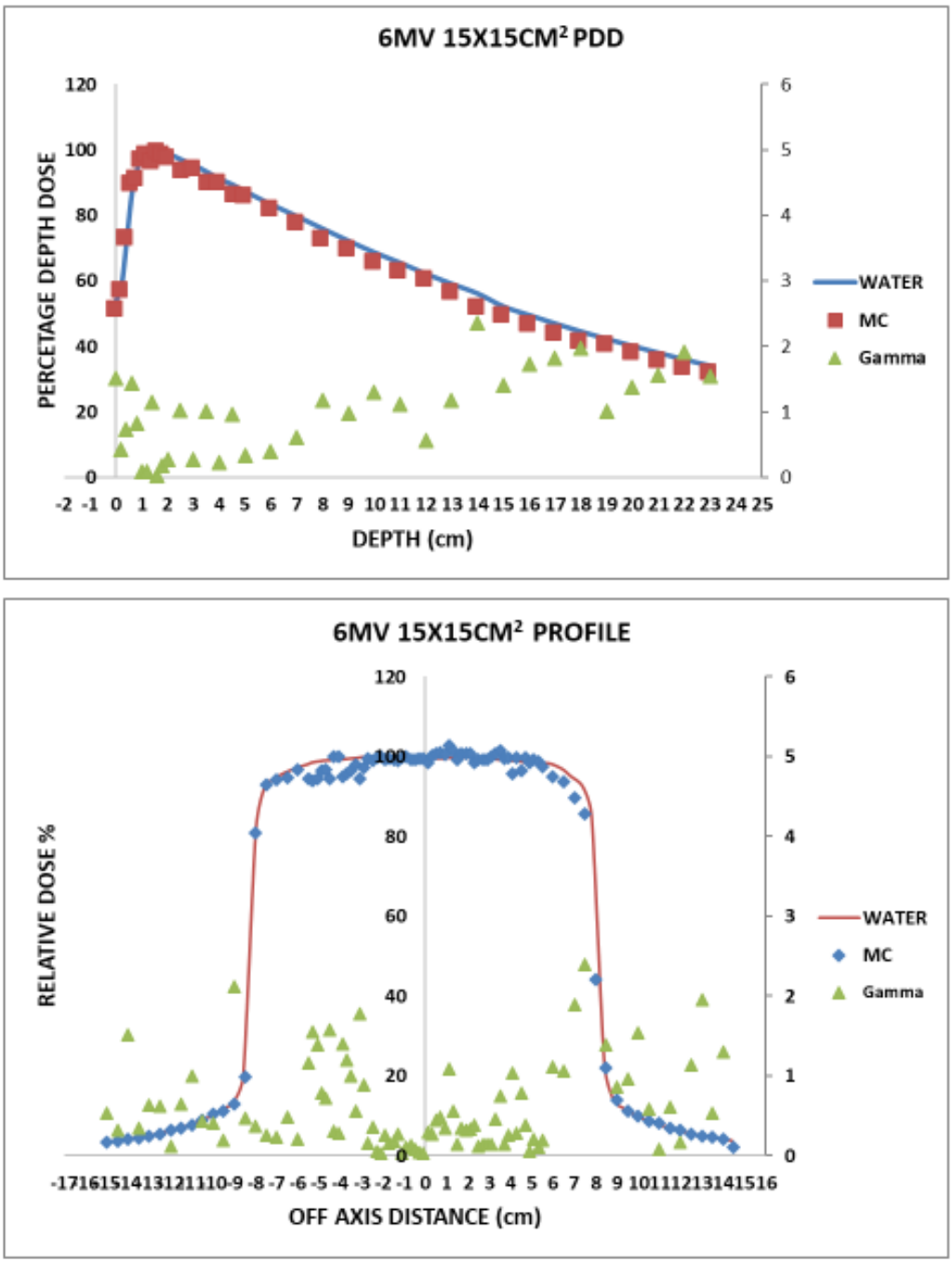

Figure 5. 18: The percentage depth dose and beam profile for 6 MV photon beam with 15 × 15 cm^2 and gamma analyses for each point indicated.

The PDD obtained in water for 6 MV at 15 × 15 cm^2 field size shows the maximum dose at a depth of 1.5 cm and 1.50 cm for MC simulation dose distribution. The EGSnrc Monte Carlo calculated dose distribution (PDD and dose profile) agreed well with experimental measurements within 2 % as shown in Fig.5.18. The maximum deviation of PDD was found at a depth of 21 cm.

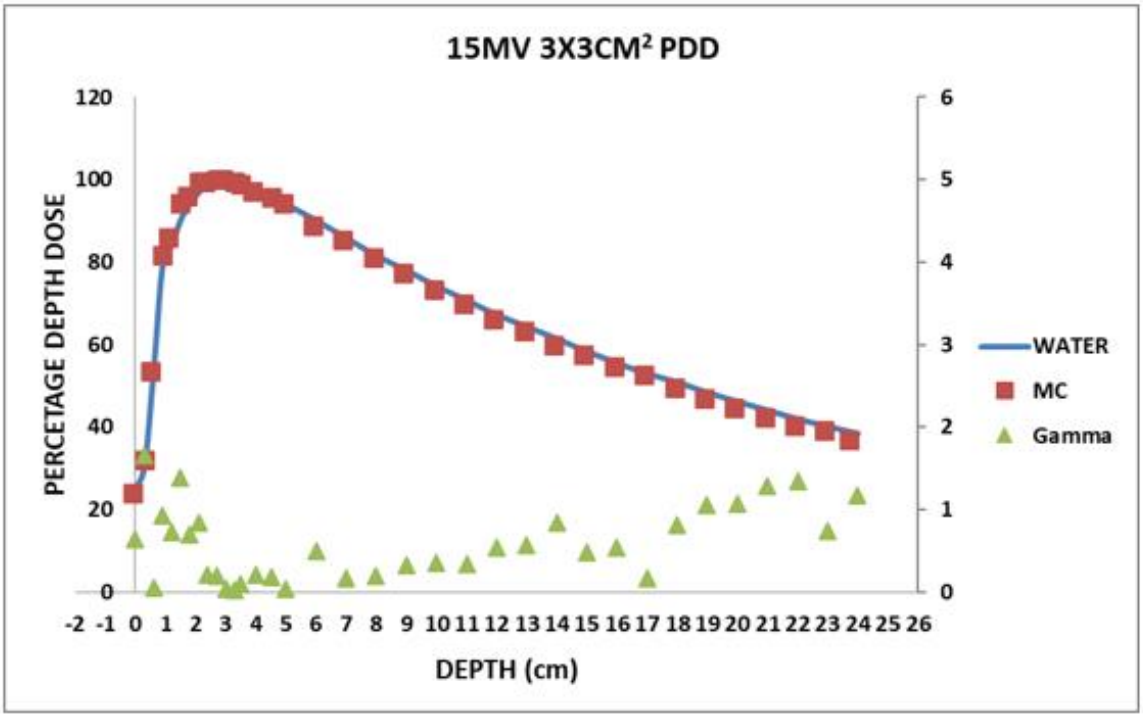

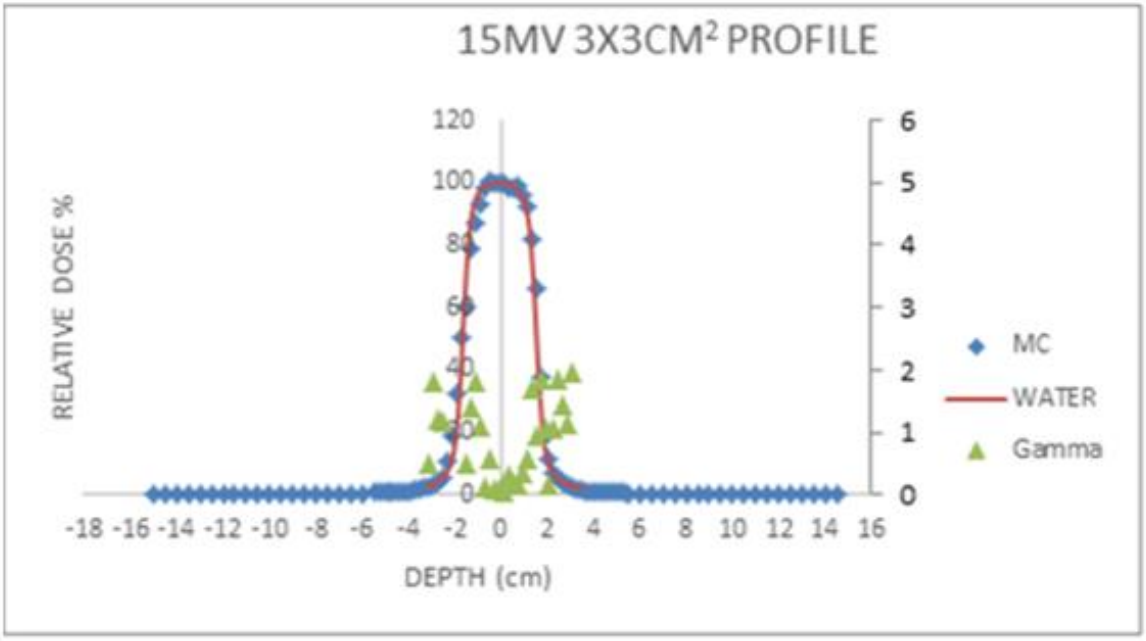

Figure 5. 19: The percentage depth dose and beam profile for 15 MV photon beam with 3 × 3 cm^2 field size and gamma analyses for each point indicated.

The PDD obtained in water for 15 MV at 3 × 3 cm^2 field size shows the maximum dose at a depth of 3.0 cm and 3.05 cm for MC simulation dose distribution. The EGSnrc Monte Carlo calculated dose distribution (PDD and dose profile) agreed well

with experimental measurements within 2 % as shown in Fig.5.19. The maximum deviation of PDD was found at a depth of 1 cm.

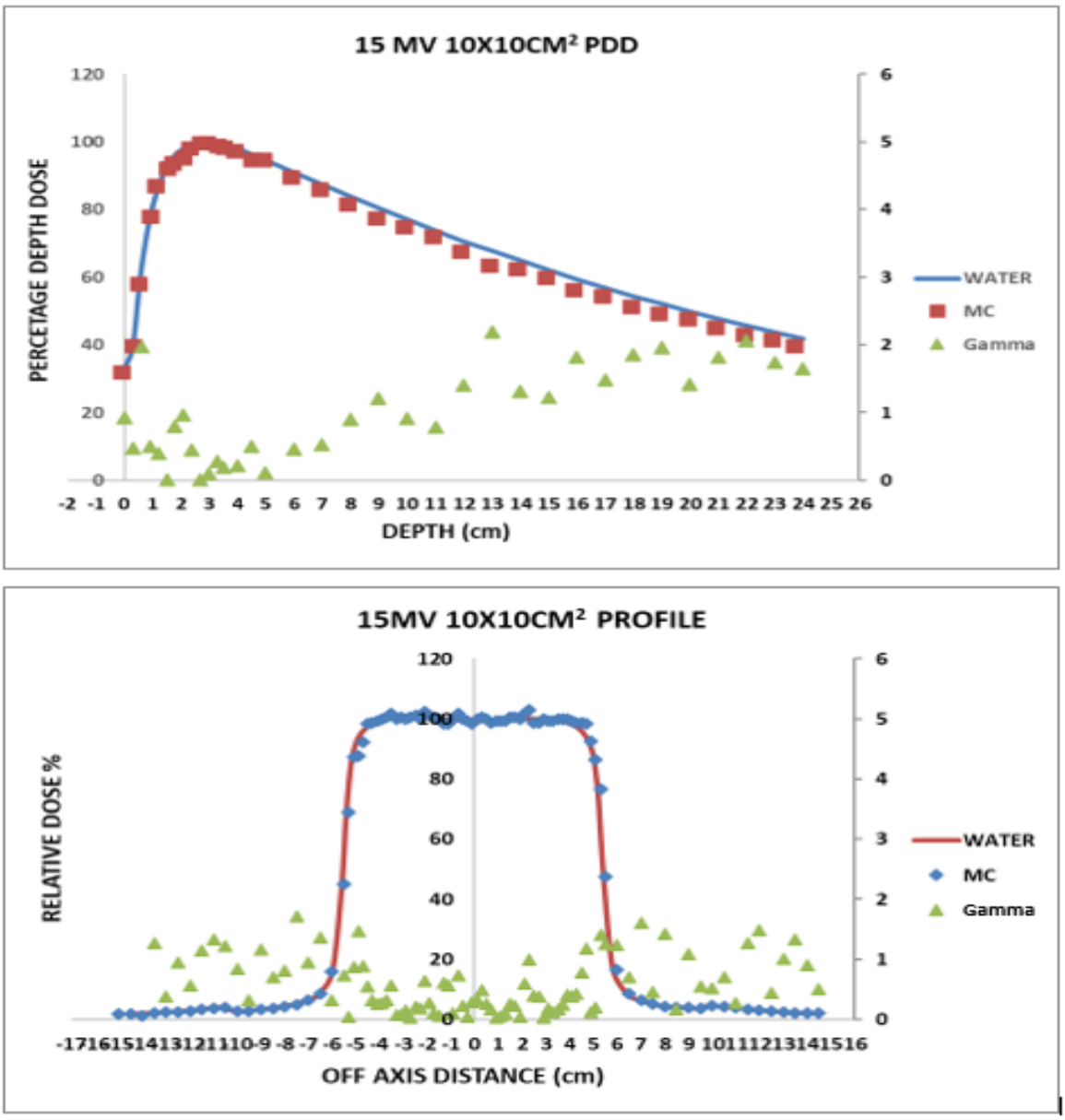

Figure 5. 20: The percentage depth dose and beam profile for 15 MV photon beam with 10 × 10 cm^2 field size and gamma analyses for each point indicated.

The PDD obtained in water for 15 MV at 10 × 10 cm^2 field size shows the maximum dose at a depth of 3.0 cm and 3.0 cm for MC simulation dose distribution. The EGSnrc Monte Carlo calculated dose distribution (PDD and dose profile) agreed well with experimental measurements within 2 % as shown in Fig.5.20. The maximum deviation of PDD was found at a depth of 21 cm.

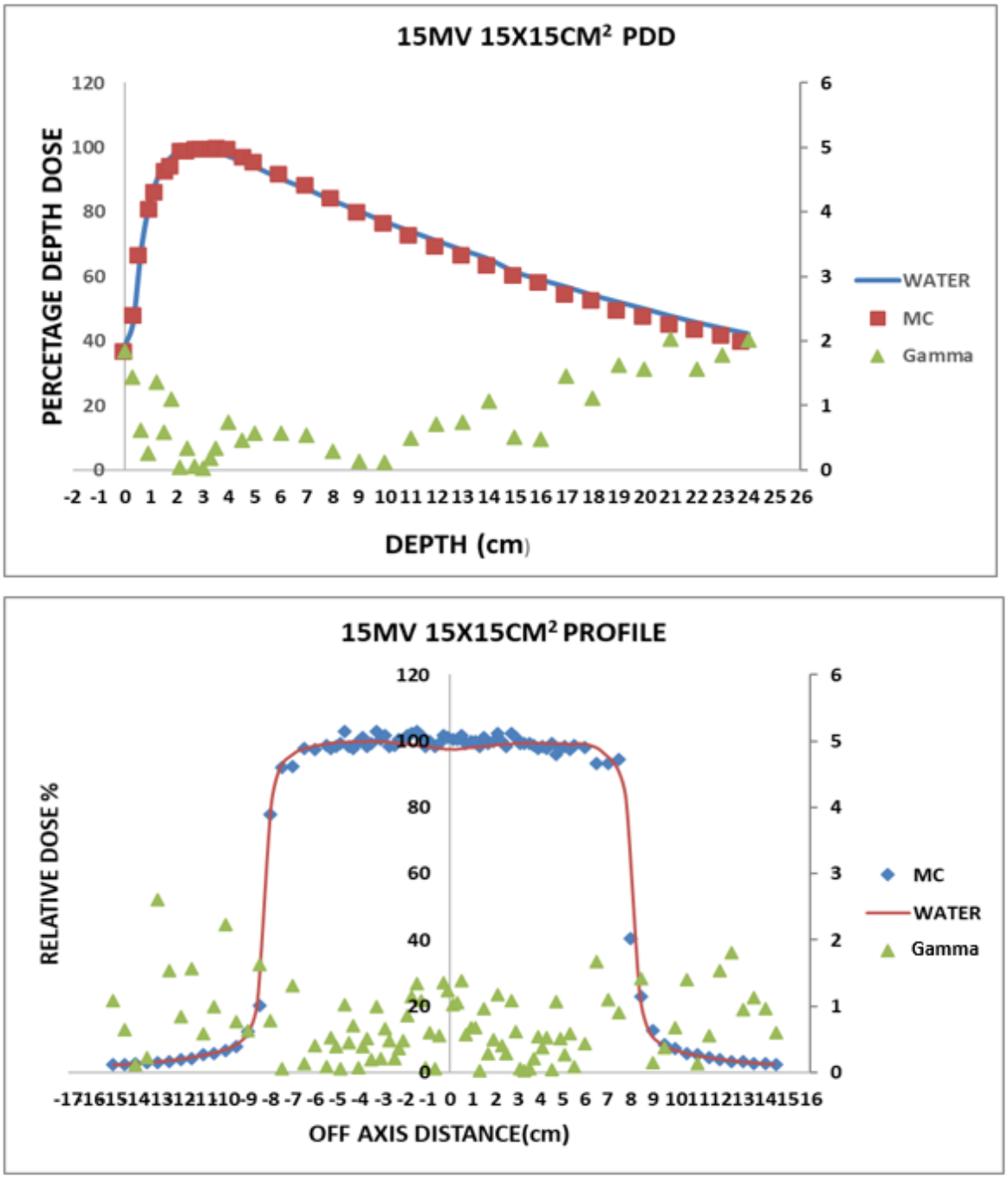

Figure 5. 21: The percentage depth dose and beam profile for 15 MV photon beam with 15 × 15 cm^2 field size and gamma analyses for each point indicated**.**

The PDD obtained in water for 15 MV of 15 × 15 cm^2 shows the maximum dose at a depth of 2.49 cm and 2.5 cm for MC simulation dose distribution. The EGSnrc Monte Carlo calculated dose distribution (PDD and dose profile) agreed well with experimental measurements within 2 %. The maximum deviation was found at a depth of 23 cm for PDD.

Table 5. 20: Depth dose comparisons between the Monte Carlo simulated and measured data at D_{max}

The depth of dose maximum (D_{MAX}) (cm)						
Field size (cm^2)	**6 MV Photon beam**			**15 MV Photon beam**		
	Experiment	**MC calculated**	**% Difference**	**Experiment**	**MC calculated**	**% Difference**
3 x 3	1.60	1.590	-0.6	3.00	3.05	1.6
10 x 10	1.60	1.590	-0.6	3.00	3.00	0.0
15 x 15	1.50	1.500	0.0	2.49	2.50	0.4

With field diameters of 3 × 3 cm^2, 10 × 10 cm^2 and 15 × 15 cm^2 for 6 MV and 15 MV photon beams for both PDD, as shown in Table 5.20 and profiles, the EGSnrc Monte Carlo predicted dose distribution in agreement with experimental results within 2%. Hence, this model shows the potential to be used for further dosimetric studies.

5.4.2 EGSnrc Monte Carlo prostate point dose

Table 5.21, Table 5.22, Fig. 5.22, and Fig. 5.23 below demonstrate a prostate point dose comparison between the treatment planning system (TPS) calculated dose, Ionisation chamber measurements, Gafchromic EBT3 film measurements, and the % difference relative to the MC simulated dose for 6 MV and 15 MV photon beam. The MC code is regarded as a gold standard since the code can accurately model the high-density materials. The percentage difference between TPS calculated dose, Ionization chamber measurement, EBT3 film measurement with MC simulated prostate point dose as reference was calculated using equation 4.22.

Table 5. 21: Comparing a TPS calculated dose, ionisation chamber, EBT3 film, and MC-simulated prostate point dose for 6 MV as well as the percentage difference with respect to MC simulated point dose, indicated.

	6 MV Prostate point dose (Gy)						
Fields	**MC simulation**	**TPS**	**% Difference**	**Ion chamber**	**% Difference**	**EBT3 film**	**% Difference**
ANT	1.987(SD±0.0006)	2.066 (SD±0.0010)	3.9	2.030 (SD±0.0010)	-2.1	2.020 (SD±0.0004)	-1.6
POST	1.995(SD±0.0006)	2.030 (SD±0.0000)	1.8	1.996 (SD±0.0006)	-0.1	2.050 (SD±0.0006)	-2.7
LT LAT (Prosthesis)	2.000(SD±0.0029)	1.997 (SD±0.0010)	-0.2	1.878 (SD±0.0006)	6.5	1.910 (SD±0.0060)	4.7
RT LAT (Bone)	1.999(SD±0.0005)	2.006 (SD±0.0006)	0.4	2.053 (SD±0.0006)	-2.6	2.050 (SD±0.0006)	-2.5

Table 5. 22. Comparison of a TPS calculated dose, Ionization chamber, EBT3 Gafchromic film measurements for 15 MV photon beam and the percentage difference compared to MC simulated point dose indicated.

	15 MV Prostate point dose (Gy)						
Fields	**MC Simulation**	**TPS**	**% Difference**	**Ion chamber**	**% Difference**	**EBT3 film**	**% Difference**
ANT	1.999 (SD ±0.0011)	2.038 (SD±0.0006)	1.9	2.079 (SD±0.0006)	-3.8	2.010 (SD±0.0010)	-0.6
POST	1.995 (SD± 0.0115)	2.036 (SD±0.0001)	2.0	2.041 (SD±0.0005)	-2.3	2.040 (SD±0.001)	-2.2
LT LAT (Prosthesis)	1.998 (SD± 0.0012)	2.008 (SD±0.0000)	0.5	1.927 (SD±0.0005)	3.7	1.940 (SD±0.001)	2.9
RT LAT (Bone)	2.000 (SD±000288)	2.008 (SD±0.0006)	0.4	2.050 (SD±0.0012)	-2.4	2.060 (SD±0.0006)	-2.9

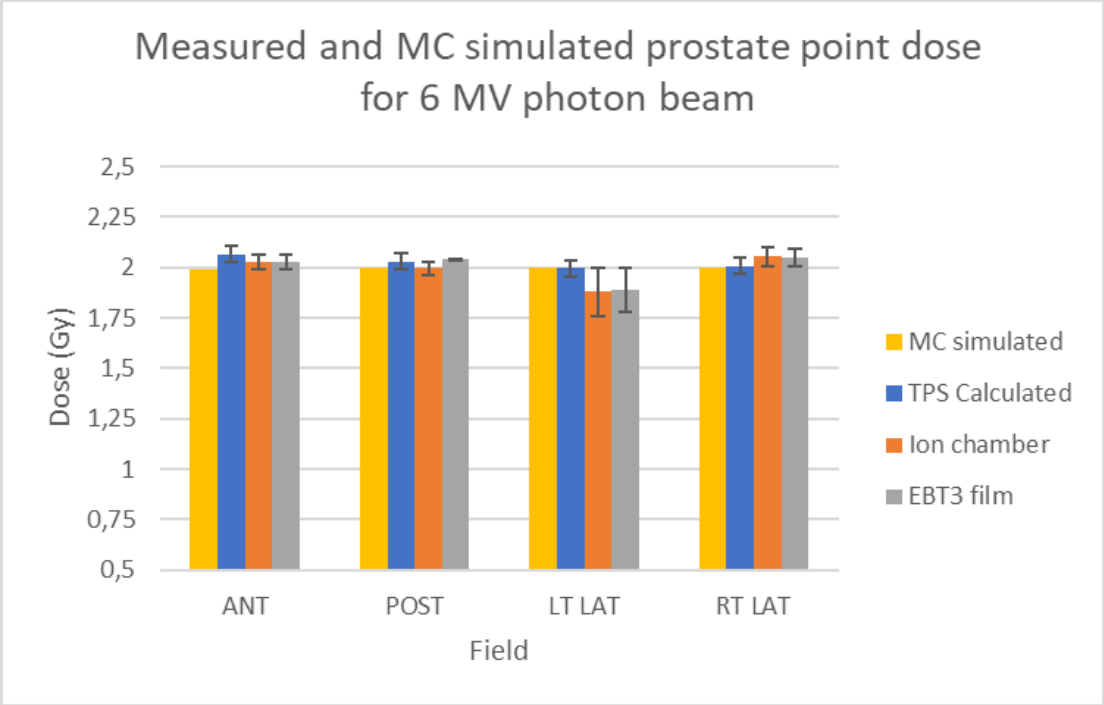

Figure 5. 22: Measured and MC simulated prostate point dose for ANT, POST, LT LAT and RT LAT of 6 MV photon beam. Error bars represent the percentage difference obtained when compared with the Monte Carlo simulated prostate point dose.

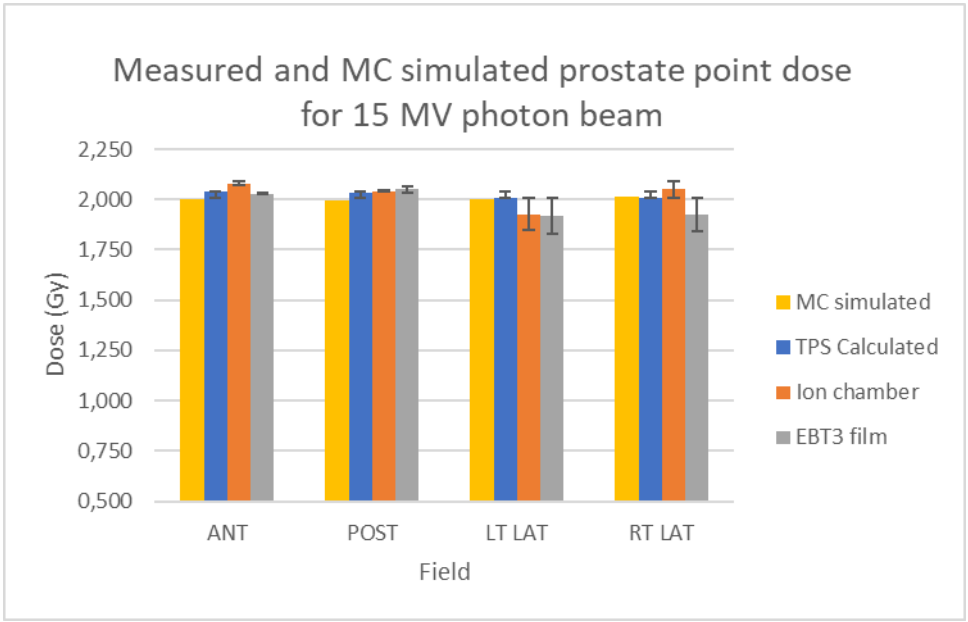

Figure 5. 23: Measured and MC simulated prostate point dose for ANT, POST, LT LAT and RT LAT of 15 MV photon beam. Error bars represent the percentage difference obtained when compared with the Monte Carlo simulated prostate point dose.

The percentage error of ionization chamber prostate point dose measurements, EBT3 film prostate dose measurements and EGSnrc Monte Carlo prostate dose calculations compared to AAA calculated plans are visualized in a bar graph as shown in Fig.5.22 and Fig.5.23.

Monte Carlo simulation for the prostate point dose for an in-house pelvic phantom was performed using the DOSXYnrc code used for simulating the dose. CTCREATE was used to define the materials and their densities. The EGSnrc user manual provides the default curve for converting CT values to material and density for air, lung, tissue, and bone. Since the phantom has a high-density hip prosthesis, additional calibration and lung were excluded from conversion. The conversion was done in a CTCREATE to convert the .dcm file into *. egsphant for dose simulation in DOSXYZnrc.

The resultant 3ddose file was analyzed using the VICTORIA programme. The percentage difference between the MC simulated prostate point dose and AAA TPS calculated prostate point dose was 3.9%, 1.8 %, -0.2 % and 0.4 % for the anterior (gantry 0^0), posterior (gantry 180^0), left lateral (gantry 90^0) and right lateral (gantry 270^0) fields respectively for the 6 MV photon beam. For the 15 MV beam the values were 1.9 %, 2.0%, 0.5 % and 0.4 % for the anterior, posterior, left lateral and right lateral fields, respectively. The difference of 3.9 % is larger than the values reported in the literature when comparing the TPS calculated dose and MC simulated dose. These might be due to the difference in the CT number used. The CT scanner used has a maximum of 3071 HU whereas the CT number used in the MC simulation was the expected value of 6000 HU.

Titanium could reduce relative dose variance to a lesser extent, but results would match the ±3% tolerance indicated by ICRU on measured and calculated doses. The implant presence causes a significant weakening of the beam in the space behind it, which affects the dose distribution in the region (small pelvis and prostate), there is a significant change in dose due to a radiation back scattering from the implant.

Numerous studies have also used EGSnrc MC simulation to evaluate the effect of hip prosthesis and compare it to the TPS algorithms. Jayamani *et al*., (2020) investigated the effect of titanium rod on 12-bit, 12-bit extended and 16- bit depth

CT data set for 6 MV photon beam using EGSnrc MC simulation and compared with Monaco TPS calculated dose.

In their study, the dose at D_{max}, at the entrance point prior to the titanium rod, at the point within the titanium rod, and at the exit point from the titanium rod were all evaluated using a wax phantom with a titanium rod. For the entrance point before titanium, the D_{max} agreement between the TPS calculated dose and MC estimated dose was determined to be 18.65%, 14.47%, and 18.56% for the 12-bit, 12-bit extended, and 16-bit depths, respectively. For the 12-bit, 12-bit extended, and 16-bits the agreement within the titanium rod was found to be 12.72%, 6.80%, and 4.95%, while the exit point from the titanium rod was found to be 0.72%, 13.68%, and 6.33%.

The 16-bits shows the CT number of 10006 ±73 HU with the physical density of > 4.34 $g.cm^{-3}$ (Jayamani *et al*., 2020). Titanium prosthesis has the physical density of 4.5 $g.cm^{-3}$ which is closer the 16-bit density obtained in the literature. The 16 bits CT scanner is not available at our facility.

To compare the accuracy of the Eclipse Acuros XB algorithms in the VMATS approach with the MC simulation for plans with avoidance sectors and static beams going through the implant, Ojala *et al*. (2014) employed a phantom with a wall constructed of PMMA, filled with water, and a hip prosthesis. The measured dose is overestimated by the AXB algorithm, with errors varying from -1.1% to -2.2%. The calculations performed using the original CT dataset had the biggest variances, with a mean difference of -1.9%; however, using the updated dataset, the mean difference is now -1.5%.

The overall differences between the MC model and measurements were less, with variances ranging from -0.9% to +0.7%. The original CT dataset showed the highest deviations, as with the AXB method and the mean difference of -0.6%, but with the corrected dataset, the average overestimation was only +0.5%. The measured and MC calculated doses in the area around the implant are both underestimated by the AXB method; the mean discrepancies are -2.4% and -2.5% for the original and corrected CT datasets, respectively. Again, for the MC model, the total deviations from the measurements were lower, with values between -3.1% and 0.1%. With the

original CT dataset, the biggest deviations, and the mean difference of -1.8% were identified.

The dose distribution of a 4-field box, 5-field 3DCRT, 6-filed IMRT, and a single arc VMAT plan for 6 MV and 15 MV with a titanium hip prosthesis in place was measured using Gafchromic EBT3 films by Ade *et al*. (2018). The gamma index is used to compare TPS calculations with film measurements. 3 mm distance-to-agreement (DTA) and 3% dose differential (DD) were chosen as the evaluation criteria. The dose increase in the prosthetic region was evident in the film measurements but was not in the TPS case. Inside the prosthesis, the difference between the film and PTS dose measurements is the largest. For 6 MV and 15 MV, respectively, the percentage dose increase ranges from 5% to 19% and 6% to 21%.

5.5 Statistical analysis

The statistical significance of the results was first assessed using an analysis of variance (ANOVA) to test, with an adjusted p-value of 0.05 indicating the statistical significance then followed by the Tukey's Honestly Significant Difference (HSD) test. ANOVA was used to test significant differences in the population mean measurements among the methods (TPS, Ion Chamber, Film Dose, and MC Dose) and different treatment angles for the 6 MV and 15 MV photon beam. The ANOVA test reveals compelling evidence that the choice of method has a significant impact on the measurements obtained.

Tukey's Honestly Significant Difference (HSD) test was used to evaluate the results' statistical significance; an adjusted p-value of 0.05 indicated the statistical significance. This post-hoc test is frequently used to identify which groups differ significantly from one another following the completion of an ANOVA. When making several pairwise comparisons, it accounts for the familywise error rate.

5.5.1 Comparing Anterior, posterior, left and right laterals plans

Tukey's Honestly Significant Difference (HSD) test was used to compared prostate point doses measured using ionization chamber, EBT3 film, MC simulated and TPS calculated.

6 MV photon beam

Left Lateral vs. Anterior: The estimated difference in mean measurements between the Left Lateral and Anterior treatment angles is -0.095278 Gy. This difference is statistically significant ($p < 0.001$), suggesting that the mean measurement at the Left Lateral angle is significantly lower than that at the Anterior angle.

Posterior vs. Anterior: The estimated difference in mean measurements between the Posterior and Anterior treatment angles is -0.036861 Gy. This difference is statistically significant ($p = 0.009$), indicating that the mean measurement at the Posterior angle is significantly lower than that at the Anterior angle.

Right Lateral vs. Anterior: The estimated difference in mean measurements between the Right Lateral and Anterior treatment angles is -0.004333 Gy. This difference is not statistically significant ($p = 0.982$), suggesting that there is no significant difference in mean measurements between these two angles.

Posterior vs. Left Lateral: The estimated difference in mean measurements between the Posterior and Left Lateral treatment angles is 0.058417 Gy. This difference is statistically significant ($p < 0.001$), indicating that the mean measurement at the Posterior angle is significantly higher than that at the Left Lateral angle.

Right Lateral vs. Left Lateral: The estimated difference in mean measurements between the Right Lateral and Left Lateral treatment angles is 0.090944 Gy. This difference is statistically significant ($p < 0.001$), suggesting that the mean measurement at the Right Lateral angle is significantly higher than that at the Left Lateral angle.

Right Lateral vs. Posterior: The estimated difference in mean measurements between the Right Lateral and Posterior treatment angles is 0.032528 Gy. This difference is marginally statistically significant (p = 0.026), indicating that the mean measurement at the Right Lateral angle is slightly higher than that at the Posterior angle.

These results provide insights into the specific differences in mean measurements between different treatment angles for the 6MV photon beam energy level, helping to identify which angles significantly differ from each other.

15 MV photon beam

Left Lateral vs. Anterior: The estimated difference in mean measurements between the Left Lateral and Anterior treatment angles is -0.068472 Gy. This difference is statistically significant (p < 0.001), indicating that the mean measurement at the Left Lateral angle is significantly lower than that at the Anterior angle.

Posterior vs. Anterior: The estimated difference in mean measurements between the Posterior and Anterior treatment angles is -0.007944 Gy. This difference is not statistically significant (p = 0.638), suggesting that there is no significant difference in mean measurements between these two angles.

Right Lateral vs. Anterior: The estimated difference in mean measurements between the Right Lateral and Anterior treatment angles is -0.018750 Gy. This difference is statistically significant (p = 0.030), indicating that the mean measurement at the Right Lateral angle is significantly lower than that at the Anterior angle.

Posterior vs. Left Lateral: The estimated difference in mean measurements between the Posterior and Left Lateral treatment angles is 0.060528 Gy. This difference is statistically significant (p < 0.001), suggesting that the mean measurement at the Posterior angle is significantly higher than that at the Left Lateral angle.

Right Lateral vs. Left Lateral: The estimated difference in mean measurements between the Right Lateral and Left Lateral treatment angles is 0.049722 Gy. This difference is statistically significant ($p < 0.001$), indicating that the mean measurement at the Right Lateral angle is significantly higher than that at the Left Lateral angle.

Right Lateral vs. Posterior: The estimated difference in mean measurements between the Right Lateral and Posterior treatment angles is -0.010806 Gy. This difference is not statistically significant ($p = 0.377$), suggesting that there is no significant difference in mean measurements between these two angles.

5.5.2 Comparing methods per energy

ANOVA and Tukey's Honestly Significant Difference (HSD) tests were employed to investigate the differences in prostate point dose measurement techniques for 6 MV and 15 MV photon energies.

6MV photon beam energy

Ion Chamber vs. Film Dose: The estimate of -0.082 Gy with a standard error of 0.014208 and a highly significant p-value (< 0.0001). This suggests that the mean measurement obtained using the Ion Chamber method significantly differs from that of Film Dose.

MC Dose vs. Film Dose: The estimate of 0.037764 Gy with a standard error of 0.006698 results in a t-value of 5.638 and a highly significant p-value (< 0.0001). This indicates a significant difference in mean measurements between MC Dose and Film Dose.

TPS vs. Film Dose: The estimate of 0.064042 Gy with a standard error of 0.006698 corresponds to a t-value of 9.562 and a highly significant p-value (< 0.0001). This suggests a significant disparity in mean measurements between TPS and Film Dose.

MC Dose vs. Ion Chamber: The estimate of 0.119764 Gy with a standard error of 0.014208 yields a t-value of 8.429 and a highly significant p-value (< 0.0001). This implies a significant difference in mean measurements between MC Dose and Ion Chamber.

TPS vs. Ion Chamber: The estimate of 0.146042 Gy with a standard error of 0.014208 results in a t-value of 10.279 and a highly significant p-value (< 0.0001). This indicates a significant disparity in mean measurements between TPS and Ion Chamber.

TPS vs. MC Dose: The estimate of 0.026278 Gy with a standard error of 0.006698 corresponds to a t-value of 3.923 and a significant p-value (0.000568). This suggests a significant difference in mean measurements between TPS and MC Dose, although the significance is slightly lower compared to the other comparisons.

In summary, all comparisons between dosimetry methods (MC Dose, Ion Chamber, and TPS) and Film Dose exhibit statistically significant differences in mean measurements. Additionally, comparisons between MC simulation and the other methods (Ion Chamber and MC Dose) also show significant difference. These findings underscore the importance of selecting an appropriate dosimetry method, as it significantly affects the measured outcomes**.**

15 MV photon beam energy

Ion Chamber vs. Film Dose: The mean measurement obtained using the Ion Chamber method is significantly lower than that obtained using the Film Dose method (estimate = -0.082 Gy, $p < 0.001$).

MC Dose vs. Film Dose: The mean measurement obtained using the MC Dose method is significantly higher than that obtained using the Film Dose method (estimate = 0.038 Gy, $p < 0.001$).

TPS vs. Film Dose: The mean measurement obtained using the TPS method is significantly higher than that obtained using the Film Dose method (estimate = 0.064 Gy, $p < 0.001$).

MC Dose vs. Ion Chamber: The mean measurement obtained using the MC Dose method is significantly higher than that obtained using the Ion Chamber method (estimate = 0.120 Gy, $p < 0.001$).

TPS vs. Ion Chamber: The mean measurement obtained using the TPS method is significantly higher than that obtained using the Ion Chamber method (estimate = 0.146 Gy, $p < 0.001$).

TPS vs. MC Dose: The mean measurement obtained using the TPS method is significantly higher than that obtained using the MC Dose method (estimate = 0.026 Gy, $p = 0.001$).

These results provide valuable insights into the effectiveness of different dosimetry methods in obtaining accurate measurements. The significant differences observed suggest that the choice of method can affect the measured outcomes, highlighting the importance of selecting an appropriate method based on the specific requirements of the radiation dosimetry process.

5.5.3 VMAT/IMRT plans

Ionisation chamber and film measurements were compared, and the test revealed a large discrepancy between the two. Less than 0.001 is the significant level. Between the distribution of film measurements and the TPS calculated dose, there is a significant difference of 0.0001 according to the test. The test revealed a significant difference between ion chamber measurements and TPS calculated dose with a significant level of less than 0.001 for ionisation chamber measurements and TPS calculated dose.

5.5.4 Normal CT data sets and O-MAR CT data sets plans

CT normal measurement and O-MAR CT data sets ionization chamber measurements the test show a statistically significant difference at p=0.024, with O-MAR having a higher value than CT normal measurements.

5.6 Backscatter dose perturbation factor

Table 5.22 shows the backscatter dose perturbation for 6 MV and 15 MV phantom calculated as the ratio of the dose with and without the prosthesis measured using a 6 x 6 cm^2 laterals field.

Table 5. 23: The mean backscatter dose perturbation for 6 MV and 15 MV photon beam using 6 × 6 cm^2 versus distance measured from the tissue-prosthesis interface backwards from the prosthesis.

Distance (mm)	6 MV photon beam	15 MV photon beam
1	1.07 (SD±0.006)	1.11 SD±0.001)
2	1.11 SD±0.006)	1.12 SD±0.006)
3	1.10 SD±0,000)	1.11 SD±0.001)
4	1.13 SD±0.005)	1.12 SD±0.006)
5	1.07 SD±0.006)	1.13 SD±0.006)

The thickness of the prosthesis shows no significant difference in backscattered radiation, but thickness does affect the transmission. A 15 MV photon beam has higher BSDF compared to that of a 6 MV photon beam. The BSDF is dependent on energy. The backscatter dose perturbation increases with increasing energy. A similar effect has been reported by Mohammadi *et al.*, (2017), and Ade *et al.*, (2017) in which comparable results for titanium were found to be 1.109 for a 6 MV photon beam and 1.117 for a 15 MV photon beam.

The transmission factor of titanium was also evaluated. The titanium transmission factor was measured by inserting a 0.6 cc ionization chamber inside the RW3 solid water phantom with the titanium piece placed on top of the RW3 solid water phantom. 100 monitor units were delivered using a 6 MV photon beam while varying the field size. The results obtained were similar to those reported in the literature (Table 3.3 in Chapter 3). The transmission increases with increasing field size due to scatter.

Table 5. 24: Titanium transmission factor for 6 MV and 15 MV photon beams of different field sizes.

FILED SIZE (cm^2)	Transmission factor	
	6 MV	15 MV
3 x 3	0.869	0.910
5 x 5	0.859	0.898
8 x 8	0.860	0.898
10 x 10	0.863	0.897
12 x 12	0.864	0.897
15 x 15	0.866	0.898

5.7 Limitation of the study

The fact that the phantom is not entirely anthropomorphic poses a constraint to the study. The adult male's shape is not the same as that of the phantom. Although the hip prosthesis should be inserted into the bone structure, it is not attached to the bone structure in an in-house pelvic phantom. Furthermore, the length of the pig bone used is not the same size as an adult human bone length.

CHAPTER 6: CONCLUSIONS AND RECOMMENDATIONS

The aim of this research study is to optimize the dose distribution of 3D conformal, IMRT and VMAT prostate treatment in a metallic (Titanium) hip prosthesis phantom. The aim was achieved through (1) the development of a novel patient-specific verification phantom with all organs defined and a prostate tumour. (2) Optimizing treatment planning using an Analytical Anisotropic Algorithm (AAA) TPS algorithm and (3) Perform Monte Carlo calculation of a static field.

This study set out to establish a methodology where the effects of high-density titanium implants could be quantified accurately and efficiently in an in-house pelvic phantom as there is no physical evaluation of the dose distribution for patients with implants. It is important to accurately quantify the dose to the prostate for the scan done on the CT scanner with the limited CT range. The investigation conducted in Chapter 4 quantified the dosimetric effects of the high-density titanium hip prosthesis material on the treatment of pelvic prostate cancer. Since there has been a worldwide increase in the number of elderly men with hip prostheses being referred for external beam radiotherapy, it has become crucial to understand the effects that a titanium prosthesis would have on photon dose distributions.

In this study, an in-house pelvic phantom consisting of superflab gel bolus, dental wax, femoral bone inserts, a titanium prosthesis and prostate insert made of Nylon-12 with a central cavity to accommodate an ionization chamber and film, was used to evaluate the dose distribution for the prostate with and without the hip prosthesis. The phantom was easily assembled for dosimetric measurements, and the insertion of the ionization chamber and film was achieved easily with this phantom.

The evaluation of prostate point dose performed in an in-house pelvic phantom using an ionization chamber shows that the dose calculated by the treatment planning system overestimated the dose by the maximum of 6.3 % on the lateral beam (gantry 90°) of a 6 MV photon beam passing through the prosthesis as shown in Table 5.4.

The effect of the prosthesis was greater for the 6 MV photon beam than for the 15 MV photon beam. The evaluation of the prostate point dose, performed using Gafchromic EBT3 film, shows that the treatment planning system dose calculation overestimated the dose by 4.5 % on the lateral beam (gantry 90°) on the 6 MV photon beam passing through the prosthesis as shown in Table 5.15.

The evaluation of prostate point dose for IMRT plan performed using the ionization chamber and Gafchromic film was found to be 1.9 % (Table 5.7) and 3.1 % (Table 5.18) respectively for the IMRT plans with the beam avoidance. The evaluation of prostate point dose for VMAT plan performed using the ionization chamber and Gafchromic film was found to be 1.9 % (Table 5.9) and 4.0 % (Table 5.19) respectively for the VMAT plans with the avoidance sector. For both IMRT and VMAT plans, the TPS overestimated the dose. Avoiding the beam passing through the prosthesis is recommended by the AAPM TG 63. According to our research, the 2 arcs VMATs technique is the best way to treat pelvic cancer while having a hip replacement. The contribution of the beam to the prosthesis is decreased when beam avoidance sectors are used to block radiation from reaching the prosthesis.

The limitation of the CT values of the phantom CT scan affected the uncertainty of the prostate dose distribution. The exact CT values of such prostheses cannot be determined through conventional CT scanning. Ionization chamber and film measurements did provide results of the prostate point dose which, when compared with the TPS calculated dose showed that the TPS overestimated the prostate point dose. However, CT values significantly exceeded the upper limit of 3071 HU because of the presence of a titanium prosthesis within the phantom. A better understanding of the dose distribution in the presence of a high atomic number titanium prosthesis was further evaluated using Monte Carlo code.

EGSnrc Monte Carlo simulation, known for accurately modelling a high-density material was used. Validation of MC codes was performed by comparing the dose distribution of the MC simulated dose distribution for 6 MV and 15 MV photon beams with those measured in water during the commissioning of the machine. The comparison of the EGSnrc MC code and experimental dose distribution agreed well within 2 % as shown in Fig.5.16 to Fig.5.21. Validating the linear accelerator gives

us the opportunity to use an accurate model for further dosimetric studies even in a complicated environment where physical measurement is unattainable.

During the EGSnrc Monte Carlo prostate point dose simulation, the pelvic phantom was created from the CT data set using the conventional four material ramp (CTCREATE) to convert CT numbers into material and mass density. The default HU to electron density curve was extended to accommodate high-Z titanium materials since an override correction was required for accurate dose calculations. Results of the comparison of the Monte Carlo simulated dose and TPS (AAA algorithm) calculated dose showed a maximum overestimation of the dose by 3.9 % in the anterior field for the 6 MV photon beam and 2.0 % in the posterior field for the 15 MV photon beam. In the lateral beam passing through the titanium prosthesis the results show a slight underestimation of the dose by -0.2 % and 0.5% for 6 MV and 15 MV photon beams (Table 5.21 and 5.22), respectively. Avoidance of the prosthesis is recommended when planning prostate EBRT.

It was recommended that a density override correction with the theoretical value of 4.5 g/cm^3 be applied to the titanium prosthesis when treatment planning takes place to ensure a more accurate dose calculation through the titanium prosthetic. However, as this is not always achievable on a CT scan with an upper limit of 3071 HU, it is advisable to avoid beams entering through the titanium prosthesis during treatment planning. A CT scanner with the extended CT number range can be utilised If it is available.

This study contributed to our understanding of how prostate cancer patients scanned with a CT scanner of a limited CT number were affected by high-density implants in terms of dose distribution. Since the dose distribution for patients with implants is only estimated using the treatment planning system and cannot be physically evaluated, the creation of an in-house pelvic phantom and the Monte Carlo model for the phantom demonstrated to be useful. For additional dosimetric analysis and precise prostate dose computation in the presence of high-density prostheses, the independent Monte Carlo dose calculation approach can be employed. The inability of the AAA algorithm to model dose distribution accurately requires caution in clinical settings for patients with titanium prosthetics (Pawałowski *et al.*, 2022).

6.1 Recommendation for future works

Although the investigation established the effects of titanium hip prostheses on prostate dose distributions and the results of the study showed that the treatment planning system overestimates the prostate dose when a titanium prosthesis is present, the study could be improved.

The recommendations for the future works are as follows:

1) Use a CT scanner with extended CT numbers and compare the results with the MC simulated.
2) Clinical application of an in-house pelvic phantom for prostate cancer patients' specific quality assurance.
3) Repeat the study to see the effects on VMAT planned treatments for patients with high density hip prosthesis and compare the prostate dose distribution to 3D plan results and also compare with Monte Carlo simulated dose.
4) To repeat the experiment with the use of the intended phantom design with spiral film.
5) To use Monte Carlo model for treatment planning of prostate cancer patients with metallic hip prosthesis.

REFERENCES

Ade, N., & du Plessis, F.C.P., (2017). Measurement of the influence of titanium hip prostheses on therapeutic electron beam dose distributions in a novel pelvic phantom. Physica Medica. 42: 99-107

Agazaryan, N., Solberg, T.D., DeMarco, J.J. (2003). Patient specific quality assurance for the delivery of intensity modulated radiotherapy. J Appl Clin Med Phys. Winter;4(1):40-50. doi: 10.1120/jacmp.v4i1.2540. PMID: 12540817; PMCID: PMC5724432.

Akça, B. & Erzeneoğlu, S.Z. (2014). The mass attenuation coefficients, electric, atomic and molecular cross-sections, effective atomic numbers, and electron densities for compounds of some biomedically important elements at 59.5 keV. Hindawi Publication Corporation. Article ID 901465.

Akinmokun, O.I., Ibeabuchi, N.M., Akinsulire, A.T., Nwachukwu, F.C. Estimation of Femoral Head Size from Palpable Bony Prominences of the Femur. West Afr J Med. 2020 Apr-Jun;37(2):173-177. PMID: 32150636.

Ali, A.M (2018). Evaluation of orthopedic metal artifact reduction application in three-dimensional computed tomography reconstruction of spinal instrumentation: a single Saudi center experience. Journal of Clinical imaging science. 8:11

Al-Mohammed, H.I. & Mahyoub, F.H. (2011). Patient-specific quality assurance for the treatment of intensity modality radiation therapy of nasopharyngeal carcinoma. Journal of Cancer Research and Experimental Oncology, Vol.3(5): 55-61.

American Cancer Society. (2018). Facts and Figures 2018. American Cancer Society. Atlanta.

Andersson, K.M,, Nowik, PT., Persliden, J., Thunberg, P., Norrman, E. (2015). Metal artefact reduction in CT imaging of hip prostheses-an evaluation of commercial techniques provided by four vendors. Br. J. Radiol. 88(1052):20140473. doi: 10.1259/bjr.20140473.

Arabloo, J., Hamouzadeh, P., Mousavinezhad, S. M., Mobinizadeh, M., Olyaeemanesh, A., & Pooyandjoo, M. (2016). Health technology assessment of image-guided radiotherapy (IGRT): A systematic review of current evidence. Medical Journal of the Islamic Republic of Iran, 30, 318. Retrieved from http://www.ncbi.nlm.nih.gov/pubmed/27390688.

Attix, F.A. (2019). Chapter 8 on charged particle interaction with matter. Introduction of radiological physics and radiation dosimetry.

Bailey, D.W. (2012). EPID dosimetry for pretreatment quality assurance with two commercial systems. *J Appl Clin Med Phys*. **13**(4): 82- 99.

Bak, J., Choi, J. H., Kim, J. S., & Park, S. W. (2012). Modified dose difference method for comparing dose distributions. *Journal of applied clinical medical physics*, *13*(2), 3616. https://doi.org/10.1120/jacmp.v13i2.3616.

Baldock C, De Deene Y, Doran S, Ibbott G, Jirasek A, Lepage M, McAuley KB, Oldham M, Schreiner LJ. Polymer gel dosimetry. *Phys Med Biol*. 2010 Mar 7;55(5):R1-63. doi: 10.1088/0031-9155/55/5/R01. Epub 2010 Feb 11. PMID: 20150687; PMCID: PMC3031873.

Baskar, R., Lee, K.A., Yeo, R., Yeoh, K.W. (2012). Cancer and Radiation Therapy: Current Advances and Future Directions. *Int J Med Sci*; 9(3):193-199. doi:10.7150/ijms.3635. Available from http://www.medsci.org/v09p0193.htm

Battaglia, M. C., Schardt, D., Espino, J. M., Gallardo, M. I., Cortés-Giraldo, M. A., Quesada, J. M., Lallena, A. M., Miras, H., & Guirado D. (2016). Dosimetric response of Gafchromic EBT3 films to protons of low energies in the Bragg peak region. Physical review accelerators and beams 19, 064701.

Bazalova, M., Beaulieu, L., Palefsky, S. and Verhaegen, F. (2007) Correction of CT Artifacts and Its Influence on Monte Carlo Dose Calculations. Medical Physics, 34, 2119.https://doi.org/10.1118/1.2736777

Bekerat, H., Devic, S., DeBlois, F., Singh, K., Sarfehnia, A., Seuntjens, J., Shih, S., Yu, X., & Lewis, D., (2014). Improving the energy response of external beam therapy (ebt) GafChromicTM dosimetry films at low energies (100 kev) Med. Phys. 41 022101

Benedict, S.H., Yenice, K.M., Followill, D., Galvin, J.M., Hinson, W., Kavanagh, B., et al. (2010). Stereotactic body radiation therapy: the report of AAPM Task Group 101. Med Phys. 37(8):4078–101.

Beni, M.S., Krstic, D., Nikezic, D. & Yu, K.N. (2018). Monte Carlo studies on photon interactions in radiobiological experiments. PLOS ONE.

Bentzen S.M, Constine L.S, Deasy J.O, Eisbruch A, Jackson A, Marks L.B, Ten Haken R.K, and Yorke E.D. Quantitative Analyses of Normal Tissue Effects in the Clinic (QUANTEC): an introduction to the scientific issues. Int J Radiat Oncol Biol Phys. 2010 Mar 1;76(3 Suppl):S3-9. doi: 10.1016/j.ijrobp.2009.09.040. PMID: 20171515; PMCID: PMC3431964.

Blum, A., Meyer,B., Raymond, A., Louis, M., Bakour, O., Kechidi, R., Chanson, A., & Gondim-Teixeira, P. (2016). CT of hip prosthesis: New techniques and new paradigms. Journal de Radioloque Diagnostique, volume 97, issue 3, pages 256-264.

Boas, F.E., & Fleischmann, D. (2012). CT artifacts: Causes and reduction techniques. Imaging Med.4(2), 229-240.

Bochorishvili, B. (2018). Physics of radiation therapy. Research institute of clinical medicine (RICM)-Todua's clinic. Ivane Javakhishvili Tbilisi state university (TSU).

Boike, T.P., Lotan, Y., Cho, L.C., *et al*. (2020). Phase I dose-escalation study of stereotactic body radiation therapy for low- and intermediate-risk prostate cancer. J Clin Oncol. 2011;29(15):2020-2026

Boos, J., Sawicki, L.M., Lanzman, R.S., Thomas, C., Aissa, J., Schleich, C., Heusch, P., Antoch, G. & Kropil, P. (2017). Acta Radiologica, vol.58 (1) 70-76.

Borca, V.C., Pasquino, M., Russo, G., Grosso, P., Cante, D., Sciacero, P., et al. (2013). Dosimetric characterization and use of GAFCHROMIC EBT3 film for IMRT dose verification J Appl Clin Med Phys, 14, p. 4111Google Scholar

Butson, M.J., Cheung, T. & and Yu, P.K.N. (2001). (Gafchromic EBT3 film dosimetry in water phantoms. Phys. Med. Biol. 46 N27–N31.

Cai, M., Archibald-Heeren, B., Wang, Y. & Metcalfe, P.E. (2017). Linearization of EBT3 film dose response and virtual film dosimetry for SRBT quality assurance. Journal of Physics: Conference Series, 777 (1), 012005-1-012005-4.

Campos, LT., Braz, D. & da Rosa, LAR. (2009). Monte Carlo simulation of regular fields for electrons beams from a medical accelerator using EGSnrc. International Nuclear Atlatic Conference. September 27-October 2.

Carl A Carlsson, C.A., and Carlsson, G.A. (1996). Department of Medicine and Care Radio Physics Faculty of Health Sciences. Series: Report / Linköpings högskola, Institutionen för radiologi; 8 ISRN: LIU-RAD-R-008. Second edition

Carlsson, C.A. & Carlsson, G.a. (1996). Basic physics of X-rays imaging. ISRN: LIU-RAD-008.

Cecen, Y. (2013). Monte Carlo radiation transport in external beam radiotherapy. Bitlis Eren univ J sci &Technol 3:1-5.

Chakarova, R., Cronholm, R., Andersson, P & Krantz. (2017). Swedish Radiation Safety Authority. 13

Chandarana H, Wang H, Tijssen RHN, Das IJ. Emerging role of MRI in radiation therapy. J Magn Reson Imaging. 2018 Dec;48(6):1468-1478. doi: 10.1002/jmri.26271. Epub 2018 Sep 8. PMID: 30194794; PMCID: PMC6986460.

Cherry, R.N. (2003) Chapter 48 Radiation: Ionizing. Avalilable from http://www.ilocis.org/documents/chpt48e.htm

Cherry, S.R.; Sorenson, J.A. and Phelps, M.E. (2003). Physics in Nuclear Medicine, 3rd ed, Saunders. ISBN 0-7216-8341-X.

Chetty, I.J., Curran, B., Cygler, J.E., DeMarco, J.J., Ezzell, G., Faddegon, B.A., Kawrakow, I., Keall, P.J., Liu, H., Ma, C.M., Rogers, D.W., Seuntjens, J., Sheikh-Bagheri, D., Siebers, J.V. (2007). Report of the AAPM Task Group No. 105: Issues associated with clinical implementation of Monte Carlo-based photon and electron external beam treatment planning. Med Phys. 34(12):4818-53. doi: 10.1118/1.2795842. PMID: 18196810.

Cho, S., Kim, S.H., Kim, C.H., Park, J.G, Park, J.H. & Jeong, J.H. (2011). Secondary cancer risks in out-of-field organs for 3D conformal radiation therapy. Progress in Nuclear Science and Technology, Vol. 1: 521-524.

Choudhary, S. (2018). Cancer Therapy & Oncology International Journal, ISSN: 2473-554X, Juniper Publishers.

Chung JB, Kim JS, Ha SW, Ye SJ. Statistical analysis of IMRT dosimetry quality assurance measurements for local delivery guideline. Radiat Oncol. 2011 Mar 28;6:27. doi: 10.1186/1748-717X-6-27. PMID: 21439096; PMCID: PMC3073875

Connolly, J.R. (2007). Interaction of X-ray with Matter and Radiation Safety, for EPS400-002, Introduction to X-ray Powder Diffraction.

Cunningham, J.R. & Dance, D.R. (2019). Interaction of radiation with matter. Diagnostic radiology physics. A handbook for teachers and students. IAEA publication. ISBN 978-92-0-131010

Dang A, Kupelian PA, Cao M, Agazaryan N, Kishan AU. Image-guided radiotherapy for prostate cancer. Transl Androl Urol. 2018 Jun;7(3):308-320. doi: 10.21037/tau.2017.12.37. PMID: 30050792; PMCID: PMC6043755.

Dang, A., Kupelian, P. A., Cao, M., Agazaryan, N., & Kishan, A. U. (2018). Image-guided radiotherapy for prostate cancer. *Translational andrology and urology*, *7*(3), 308–320. https://doi.org/10.21037/tau.2017.12.37

Daryanani A, Turkbey B. Recent Advancements in CT and MR Imaging of Prostate Cancer. Semin Nucl Med. 2022 May;52(3):365-373. doi: 10.1053/j.semnuclmed.2021.11.013. Epub 2021 Dec 18. PMID: 34930627; PMCID: PMC9038642

Derar,H. & Shahinpoor, M. (2015). Recent patents and designs on hip replacement prostheses. Biomed Eng J. 9:92-102. DOI: 10.1007/978-3-319-61540-0_4

Desouky, O., Ding, N., Zhou, G. (2015). Targeted and non-targeted effects of ionizing radiation, Journal of Radiation Research and Applied Sciences, Volume 8, Issue 2, 2015, Pages 247-254, ISSN 1687-8507, https://doi.org/10.1016/j.jrras.2015.03.003.

Di Scienze, S. (2017). Dosimetric characterization of GafChromic EBT3 Films in Volumetric Modulated Arc Therapy (VMAT) radiotherapy treatments. Alma Mater Studiorum _ Universit_a di Bologna

Dowsett, D.J.; Keerry, P.A. and Johnston, R.E. (1998). The Physics of Diagnostic Imaging, 1st ed, Chapman & Hall Medical. ISBN 0-412-460602.

Duffy, S., Gonzales, J., Khan, R., Lenards,N. (2018) Ashley Hunzeker, Dosimetric analysis of volumetric arc therapy on localized prostate cancer with unilateral hip prosthesis: the hip-skip method. Available from: https://sethrduffy.weebly.com/uploads/3/8/9/6/38968963/srj_final research_paper.pdf 27

Dyson, N. (1993). Radiation Physics with Application in Medicine and Biology, 2nd ed, Ellis Horwood. ISBN 0-13-741108-6.

Eclipse treatment planning system (TPS) version 16.1. Varian Medical Systems, Palo Alto, CA.

Elawady, R.A., Attalla, E.M., Eleshemey, W.M., Shouman, T. & Alsayed, A.A. (2014). Dose verification of intensity modulated radiotherapy in head and neck tumours. International Journoul of Cancer Therapy and Onclogy, volume 2, number 3.

Elcim, Y., Dirican, B., & Yavas, O. (2016). Dosimetric comparison of treatment planning systems using collapsed cone convolution and pencil beam algorithms. Journal or Radiotherapy in Practice; 15:364-377.

El-Ghossian, M.O. (2017). Calculations with different material and Range of electrons interaction with different material and human parts body. International journal of scientific & technology research volume 6, issue 01.

El-Kader, H.A., El-Leithy, M., El-Hadidy, A., & El-Ghaed, M. (2014). Dosimetry measurements of radiation fields. RRBS,8(8), 302-318.

Evans, M.D.C. (2012). Chapter 11: Computerized Treatment Planning Systems for External Photon Beam Radiotherapy. IAEA publication. ISBN 92-0-107304-6)

F.M. Khan, J.P. Gibbons, Khan’s the Physics of Radiation Therapy, Lippincott Williams & Wilkins, 2014.

Faccenda, V.; Panizza, D.; Daniotti, M.C.; Pellegrini, R.; Trivellato, S.; Caricato, P.; Lucchini, R.; De Ponti, E.; Arcangeli, S. Dosimetric Impact of Intrafraction Prostate Motion and Interfraction Anatomical Changes in Dose-Escalated Linac-Based SBRT. *Cancers* **2023**, *15*, 1153. https://doi.org/10.3390/cancers15041153

Fischer-Valuck, B.W., Rao, Y.J. and Michalski, J.M. (2018) Transl Androl Urol 2018; 7(3):297-307

GAFChromic™ EBT3 film specifications, Available at www.gafchromic.com

Gao, L., Sun, H., Ni, X., Fang, M. & Tao, L. (2018). Effects of 16-bit CT imaging scanning conditions for metal implants on radiotherapy dose distribution. Oncl Lett; 15 (2): 2373-2379.

Gargett, M. A., Briggs, A. R., and Booth, J. T. (2020). Water equivalence of a solid phantom material for radiation dosimetry applications. Phys. Imaging Radiat. Oncol. **14**, 43–7.

Garth, J. (2005). Electron/photon transport and its applications. American Nuclear Society Topical meeting in Monte Carlo, Chattoriooga, TN.

Giantsoundi,D., Deman, B., Verburg, J,. Trofimov, A., Jim, Y., Wang, G., Gjesteby, L., & Paganetti, H. (2017). Metal artifacts in computed tomography for radiation therapy planning: dosimetric effects and impact of metal artifact reduction. Phys.Med.Biol 62:R49-80

Gjesteby, L., De man, B., Jin, Y., Paganetti, H., Verburg, J., Giantsound, D., & Wang, G.E. (2016). Metal Artifact Reduction in CT: Where Are We After Four Decades? IEEE Access.Volume 4

Gluhcheva, Y, Dimitrova, T.L., Dukova, R., Zheleva, N., Koleva, I., & Encheva, E. (2015). Dosimetry acceptance test of linear accelerator Varian Clinac iX. Bulgarian Chemical Communications, Volume 47, Special Issue B (pp. 458–463).

Golgstein, (2003). Beam-specimen interactions 1) scattering. Available from http://geode.colorado.edu/~epma/PDF/5_beamSpecimen_scattering.pdf

Gorovets D, Burleson S, Jacobs L, Ravindranath B, Tierney K, Kollmeier M, McBride S, Happersett L, Hunt M, Zelefsky M. Prostate SBRT With Intrafraction Motion Management Using a Novel Linear Accelerator-Based MV-kV Imaging Method.

Pract Radiat Oncol. 2020 Sep-Oct;10(5):e388-e396. doi: 10.1016/j.prro.2020.04.013. Epub 2020 May 23. PMID: 32454176.

Gruen, A., Ebell, W., Wlodarczyk, W., Neumann, O., Kuehl, J.S., Stromberger, C., Budach, V., Marnitz, S. (2013). Total Body Irradiation (TBI) using Helical Tomotherapy in children and young adults undergoing stem cell transplantation. Radiat Oncol. 8(1):92. doi: 10.1186/1748-717X-8-92

Gurjar, O.P., Mishra, S.P., Bhandari, V., Pathak, P., Patel, P. & Shrivastav, G. (2014). Radiation dose verification using real tissue phantom in modern radiotherapy techniques. Journal of Medical Physics 39(1): 44-49.

Hanks, G.E. (1999). Progress in 3D conformal radiation treatment of prostate cancer. Acta Oncologica Suppl.13, pp.69-74

Hanušová, T., & Burýšková, S. (2016). Impact of calibration curve precision on results of imrt verification with ebt3 films. rad Conference Proceedings, vol. 1, pp. 49-54. www.rad-proceedings.org

Herman, T.deL., Schnell, E., Young, J., Hildebrand, K., Algan, O., Syzek, E., Herman, T., & Ahmad, S. (2013). Dosimetric comparison between IMRT delivery modes: Step-and-shoot, sliding window, and volumetric modulated arc therapy - for whole pelvis radiation therapy of intermediate-to-high risk prostate adenocarcinoma. *Journal of medical physics*, *38*(4), 165–172. https://doi.org/10.4103/0971-6203.121193

Hunter, W. (2011). Interactions of radiation with matter. Nuclear medicine basic science lectures. Available from http://www.rad.washington.edu/research/our-research/groups/irl/education/basic-science-resident-lectures

Hussain, A., & Muhammad, W. (2017). Treatment Planning in Radiation Therapy.

IAEA human health reports No. 16. (2019). Introduction of image guided radiotherapy into clinical practice. International atomic energy agency Vienna.

IAEA. TecDoc 1540. (2007). Specification and Acceptance Testing of Radiotherapy Treatment Planning Systems. Vienna: IAEA.

ICRU 91. Treatment Planning Algorithms. (2017). Journal of the International Commission on Radiation Units and Measurements, Volume 14, Issue 2, 1 December 2014, Pages 65–75.

Inkson, B.J. (2016). Scanning electron microscopy (SEM) and transmission electron microscopy (TEM) for materials characterization.

Inkson., B.J. (2016). Materials Characterization Using Nondestructive Evaluation (NDE) Methods. Pages 17-43. ttps://doi.org/10.1016/B978-0-08-100040-3.00002-X.

INTERNATIONAL ATOMIC ENERGY AGENCY. (2006). Absorbed Dose Determination in External Beam Radiotherapy, Technical Reports Series No. 398, IAEA, Vienna.

Israngkul-Na-Ayuthaya, I., Suriyapee, S., Pengvanich, P. (2015). Evaluation of equivalent dose from neutrons and activation products from a 15-MV X-ray LINAC. JOURNAL OF RADIATION RESEARCH, VOL.56, No.6 : 919-926.

Jabbari K. (2011). Review of fast monte carlo codes for dose calculation in radiation therapy treatment planning. *Journal of medical signals and sensors*, *1*(1), 73–86.

Jabbari, K., Amouheidari, A., & Babazadeh, S. (2012). The Quality Control of Intensity Modulated Radiation Therapy (IMRT) for ONCOR Siemens Linear Accelerators Using Film Dosimetry. Iranian Journal of Medical Physics Vol. 9, No. 2, 111-125

Jayamani, J., Osman, N.D., Tajuddin, A.A., Mohd Noor, N., Abdul Aziz, (2020). Dosimetric Comparison between Monaco TPS and EGSnrc Monte Carlo simulation on Titanium Rod in 12bit and 16bit Image Format. Journal of Radiation Research and Applied Sciences, Volume 13, Issue 1.

Kawrakow, I., Mainegra-Hing, E., Rogers, D.W.O., ET AL, (2006). EGSnrcMP: the multi-platform environment for EGSnrc. Natl. Res. Counc. Can. Ott.

Keall, P.J., Siebers, J.V. & Mohan, R. (2003). Radiotherapy dose calculations in presence of hip prosthese. Med Dosim; 28:107-12.

Khan FM, Gibbons JP. Khan's The physics of radiation therapy; 5th edition. Philadelphia, USA; 2014. Website: www.lww.com.

Khan FM. 4th ed. Baltimore: Lippincott; (2010). The Physics of Radiation Therapy

Khan, F.M. (2003). The Physics of Radiation Therapy 3rd ed, Lippincott Williams & Wilkins. ISBN 0-7817-3065-1 28

Kim, D.W., Park, K., Kim, H., Kim, J. (2020). History of the photon beam dose calculation algorithm in radiation treatment planning system. Progress in Medical Physics. 2020;3(31):54-62.

King, S.; Pitcher, E.M. and Smail, M.A. (2002). Optimizing Medical Radiation Exposures for Uroradiological Procedures, with Special Emphasis on the Paediatric Imaging, *BJU International*. 89:510-516.

Kling, J. and Patel, K.M. (2013). Prostate treatment with helical TomoTherapy in patients with bilateral hip prostheses--two case studies. Med Dosim. Spring;38(1):30-4. doi: 10.1016/j.meddos.2012.05.003. Epub 2012 Aug 10. PMID: 22884740.

Knőős, T. & Sweden, L. (2019). Dose calculation algorithms in 3DCRT and IMRT. Available from https://www.aapm.org/meetings/amos2/pdf/35-9832-6508-974.pdf

Koehn, C., Ebert, U., Angular distribution of Bremsstrahlung photons and of positrons for calculations of terrestrial gamma-ray flashes and positron beams, Atmos. Res. (2013), http://dx.doi.org/10.1016/j.atmosres.2013.03.012

Kroon PS, Hol S & Essers M. Dosimetric accuracy and clinical quality of Acuros XB and AAA dose calculation algorithm for stereotactic and conventional lung volumetric modulated arc therapy plans. Radiat Oncol. 2013;8(1): 149. DOI: 10.1186/1748- 717X-8-149.

Le Fèvre C, Brinkert D, Menoux I, Kuntz F, Antoni D, El Bitar Z, Thiery A, Fabbro R, Noël G. (2020). Effects of a metallic implant on radiotherapy planning treatment-experience on a human cadaver. Chin Clin Oncol. 14. doi: 10.21037/cco.2020.01.09. Epub 2020 Feb 11. PMID: 32075394.

Leon Marroquin, E.Y., Herrera González, J.A., Camacho López, M.A., Barajas, J.E, & García-Garduño, O.A. (2016). Evaluation of the uncertainty in an EBT3 film dosimetry system utilizing net optical density. Journal of Applied Clinical Medical Physics:17(5):466-481. DOI: 10.1120/jacmp.v17i5.6262.

Lewis, D., Micke, A., Yu, X., Chan, M.F. (2012). An efficient protocol for Gafchromic EBT3 film dosimetry combining calibration and measurement in a single scan. Med Phys.: 39(10):6339–50. [PubMed] [Google Scholar]

Liugang, G., Hongfei, S., Xinye, N., Mingming, F., Zheng, C., & Tao, L. (2016). Metal artifact reduction through MVCBCT and KVCT in radiotherapy. Scientific Report 6, article number: 37608.

Lloyd, S.A.M. (2011). Evaluation of a deterministic BOLTZMANN solver for radiation therapy dose calculation involving high-density hip prostheses. Thesis university of Victoria.

Low DA, Harms WB, Mutic S, Purdy JA. A technique for the quantitative evaluation of dose distributions. Med Phys. 1998 May;25(5):656-61. doi: 10.1118/1.598248. PMID: 9608475.

Ma CM, Li J. Dose specification for radiation therapy: dose to water or dose to medium? Phys Med Biol. 2011 May 21;56(10):3073-89. doi: 10.1088/0031-9155/56/10/012. Epub 2011 Apr 20. PMID: 21508447

Macchia G, Deodato F, Cilla S, et al. Volumetric modulated arc therapy for treatment of solid tumours: current insights. Onco Targets Ther. 2017;10:3755–3772. Published 2017 Jul 26. doi:10.2147/OTT.S113119

Mackie TR, Bielajew AF, Rogers DW, Battista JJ. Generation of photon energy deposition kernels using the EGS Monte Carlo code. Phys Med Biol. 1988;33:1-20.

Mahmoudi, R., Jabbari, N., Aghasi, M. and Khalkhali, H.R. (2016). Energy dependence of measured CT number on substituted materials used for CT number calibrated of radiotherapy treatment planning systems. PLOS ONE JULY 8

Mahmoudi, R., Jabbari, N., Aghdasi, M., & Khalkhali, H. R. (2016). Energy Dependence of Measured CT Numbers on Substituted Materials Used for CT Number Calibration of Radiotherapy Treatment Planning Systems. *PloS one*, *11*(7), e0158828. https://doi.org/10.1371/journal.pone.0158828.

Mahur, M., Gurjar, O.P., Grover, r.K., Negi, P.S., Sharma, R., Singh, A. & Singh, M. (2017). Evaluation of effect of different computed tompgraphy scanning protocols on

Hounsfield unit and its impact on dose calculation by treatment planning system. Iranian Journal of Medical Physics.; 14:149-154.

Maraghechi, B., Davis, J., Badu, S., Fleck, A., Darko, J. and Osei, E. (2017). Retrospective analysis of portal dosimetry pre-treatment quality assurance of prostate cancer volumetric-modulated arc therapy (VMAT) plans. Journal of radiotherapy in practice 00, (1-9).

Marroquin, E. Y., Herrera González, J. A., Camacho López, M. A., Barajas, J. E., & García-Garduño, O. A. (2016). Evaluation of the uncertainty in an EBT3 film dosimetry system utilizing net optical density. *Journal of applied clinical medical physics*, *17*(5), 466–481. https://doi.org/10.1120/jacmp.v17i5.6262.

Martin, J.E. (2006). Physics for Radiation Protection, 2nd ed, Wiley-VCH Verlag GmbH & Co.KGaA. ISBN 3-527-40611-5.

Matney, J.E., Parker, B.C., Neck, D.W,, Henkelmann, G., & Rosen II. (2010). Evaluation of a commercial flatbed document scanner and radiographic film scanner for Gafchromic EBT3 film EBT film dosimetry. J Appl Clin Med Phys:11:3165.

Maulana, A. & Pawiro, S.A. (2016). Dosimetry verification on VMAT and IMRT radiotherapy techniques: In the case of prostate cancer. Journal of Physics: Conference Series 694(2016) 012010.

McDermott, L.N., Wendling, M., van Asselen, B., Stroom, J., Sonke, J.J.,van Herk, M. & Mijnheer, B.J.(2006). Clinical experience with EPID dosimetry for prostate IMRT pre-treatment dose verification. Med Phys.33(10):3921-30

McLean ID *et al*. IAEA Human Health Series No. 19, Quality assurance programme for computed tomography: diagnostic and therapy applications (2012).

Min, S., Choi, Y.E., Kwak, J., Cho, B. (2015). Practical approach for pretreatment verification of IMRT with flattening filter free(FFF) beams using Varian Portal Dosimetry. J Appl Clin Med Phys.; 16(1): 40–50.

Mishra S, Dixit PK, Selvam TP, Yavalkar SS, Deshpande DD. Monte Carlo investigation of photon beam characteristics and its variation with incident electron beam parameters for indigenous medical linear accelerator. J Med Phys 2018;43:1-8.

Mitterberger M, Horninger W, Aigner F, Pinggera GM, Steppan I, Rehder P, Frauscher F. Ultrasound of the prostate. Cancer Imaging. 2010 Mar 3;10(1):40-8. doi: 10.1102/1470-7330.2010.0004. PMID: 20199941; PMCID: PMC2842183.

Mohammandi, K., Hassani, M., Ghorbani, M., Farhood, B., & Knaup, C. (2017). Evaluation of the accuracy of various dose calculation algorithms of a commercial treatment planning system in the presence of hip prosthesis and comparison with Monte Carlo. Journal of cancer Research and Therapeutics; 13:501-9.

Mohammed, M., Chakir, E., Boukhal, H., Mroan, S., & El-Bardouni, T. (2017). Evaluation of the dosimetric characteristic of 6 MV flattened and unflattened photon beam. Journal of King Saud University-Science. 29, 371-379. 29

Mohammed, S.H., Trabelsi, A. & and Manai, K. (2018). Stopping Power, CSDA Range, Absorbed Dose and Cross Sections Calculations of F18 Simulated in Water using Geant4 Code. Indian Journal of Science and Technology, Vol 11(6)

Morsbach, F., Bickelhaupt, S., Wanner, G.A., Krauss, A., & Schmidt, B. (2013). Hatem Alkadhi, MD, MPH Reduction of Metal Artifacts from Hip Prostheses on CT Images of the Pelvis: Value of Iterative Reconstructions. **Radiology:** Volume 268: Number 1.

Mousa, A.; Kusminarto, K.; Suparta, G.B. (2017). A New Simple Method to Measure the X-ray Linear Attenuation Coefficients of Materials using Micro-Digital Radiography Machine. Int. J. Appl. Eng. Res.12, 10589–10594

Muhammed, E. (2017). Transport of information-carries in semiconductors and nanodevices. A volume in the advances in computer and electrical engineering (ACEE) book series. Published in the United States by IGI Global.

Mullins, J.P., Grams, M.P, Herman, M.G., Brinkmann, D.H. & Antolak, J.A. (2016). Treatment planning for metals using an extended CT number scale. Journal of Applied Clinical Medical Physics, volume 17, number 6.

Nabavizadeh N., Elliott D.A., Chen Y., Kusano A.S., Mitin T., Thomas C.R., Holland J.M. (2016). Image Guided Radiation Therapy (IGRT) practice patterns and IGRT's impact on workflow and treatment planning: Results from a national survey of

american society for radiation oncology members. International Journal of Radiation Oncology Biology Physics, 94 (4), pp. 850-857.

Nalbant, N., Donmez, K.N & Blige, H. (2014). Pre-treatment dose verification of IMRT using Gafchromic Ebt3 film and 2D Array. J. Nucl. Med. Radiat Ther, 5(3):1-6.

National cancer registry. (2013). https://cansa.org.za/south-african-cancer-statistics/

Ng, WL., Brunt, J., Temple, S., Saipillai, M., Harridass, A., Wong, H., Malik, z. & Eswar, C. (2015). Volumetric modulated arc therapy in prostate cancer patients with metallic hip prostheses in a UK centre. Reports of Practical oncology and Radiotherapy 20:273-277.

Oderinde, OM & Oded, R. (2015). Variation of dose distribution with depth and incident energy using EGSnrc Monte Carlo simulation method. IOSR Journal of Applied Physics. Volume 7, issue 2 ver.1:33-40.

Oehler C, Roehner N, Sumila M, Curschmann J, Storelli F, Zwahlen DR, Schneider U. Intrafraction Prostate Motion Management for Ultra-Hypofractionated Radiotherapy of Prostate Cancer. Curr Oncol. 2022 Aug 31;29(9):6314-6324. doi: 10.3390/curroncol29090496. PMID: 36135065; PMCID: PMC9497512.

Oelfke, U. & Scholz, C. (2019). 15 dose calculation algorithms. Available from http://eknygos.lsmuni.lt/springer/315/187-196.pdf

Ogata, T., Ueguchi, T., Yagi, M., Yamada, S., Tanaka, C., Ogihara, R., Isohashi, F., Yoshioka, Y., Tomiyama, N., Ogawa, K. & Koizumi, M. (2013). Feasibility and accyracy of relative elctron density determined by virtual monochromatic CT value subtraction at two different energies using the gemstone spectral imaging. Radiat Oncol. 8:83.

Ojala J, Kapanen M, Sipilä P, Hyödynmaa S, Pitkänen M. The accuracy of Acuros XB algorithm for radiation beams traversing a metallic hip implant - comparison with measurements and Monte Carlo calculations. J Appl Clin Med Phys. 2014 Sep 8;15(5):4912. doi: 10.1120/jacmp.v15i5.4912. PMID: 25207577; PMCID: PMC5711096.S

Palmer, A.L., Dimitriadis, A., Nisbet, A., & Clark, C.H. (2015). Evaluation of Gafchromic EBT-XD film, with comparison to EBT3 film, and application in high dose radiotherapy verification. Phys Med Biol: 60:8741–8752.

Pang EPP, Knight K, Baird M, Loh JMQ, Boo AHS, Tuan JKL. A comparison of interfraction setup error, patient comfort, and therapist acceptance for 2 different prostate radiation therapy immobilization devices. Adv Radiat Oncol. 2017 Feb 16;2(2):125-131. doi: 10.1016/j.adro.2017.02.001. PMID: 28740923; PMCID: PMC5514259.

Panizza D, Faccenda V, Lucchini R, Daniotti MC, Trivellato S, Caricato P, Pisoni V, De Ponti E, Arcangeli S. Intrafraction Prostate Motion Management During Dose-Escalated Linac-Based Stereotactic Body Radiation Therapy. Front Oncol. 2022 Apr 7;12:883725. doi: 10.3389/fonc.2022.883725. PMID: 35463373; PMCID: PMC9021501.

Papaconstadopoulos, P., Hegyi, G., Seuntjens, J., & Devic, S. (2014). A protocol for EBT3 Gafchromic EBT3 film dosimetry using reflection scanning. United States: N. p. Web. doi:10.1118/1.4901308.

Park, S.Y., Park, J.M., Choi, C.H., Chun, M., Han, J.H., Cho, J.D. & Kim, J. (2017). Optimal density assignment to 2D diode array detector for different dose calculation algorithms in patient specific VMAT QA. Journal of Radiation Protection and Research, 42(1): 9-15

Paulu, D., Alaei, P. (2017). Evaluation of dose calculation accuracy of treatment planning systems at hip prosthesis interfaces. J Appl Clin Med Phys. May;18(3):9-15. doi: 10.1002/acm2.12060. PMID: 28317312; PMCID: PMC5689850.

Pawałowski, B., Ryczkowski, A., Panek, R., Sobocka-Kurdyk, U., Graczyk, K. and Piotrowski, T. (2022). Accuracy of the doses computed by the Eclipse treatment planning system near and inside metal elements. Sci Rep. Apr 8;12(1):5974. doi: 10.1038/s41598-022-10072-8. PMID: 35396569; PMCID: PMC8993896.

Pimthong, J., Kakanaporn, C., Tuntipumiamorn, L., Laojunun, P., Iampongpaiboon, P. (2016). Commissioning and validation of COMPASS system for VMAT patient specific quality assurance. J Phys: Conf Ser. 694:012025.

Podgorsak, E. B. (2005). Radiation Oncology Physics: A Handbook for Teachers and Students, Austria: International Atomic Energy Agency.

Podgorsak, E. B.(2010). Radiation Physics for Medical Physicists (Biological and Medical Physics, Biomedical Engineering). Chapter 7.

Potetnya VI, Koryakina EV, Troshina MV, Koryakin SN (2021) Use of the chemical Fricke dosimeter and its modifications for dosimetry of gamma neutron radiation of a pulsed reactor. Nuclear Energy and Technology 7(3): 231-237. https://doi.org/10.3897/nucet.7.74149

Prabhakar, r., Kumar, M., Cheruliyil, S., Jayakumar, S., balasubramanian, S., & Cramb., J. (2013). Volumetric modulated arc therapy for prostate cancer patients with hip prostheses, Reports of Practical Oncology and Radiotherapy 18:209-213.

Quan EM, Li X, Li Y, Wang X, Kudchadker RJ, Johnson JL, Kuban DA, Lee AK, Zhang X. A comprehensive comparison of IMRT and VMAT plan quality for prostate cancer treatment. Int J Radiat Oncol Biol Phys. 2012 Jul 15;83(4):1169-78. doi: 10.1016/j.ijrobp.2011.09.015. PMID: 22704703; PMCID: PMC3805837.

Rama, S.B. & Parkharel, S. (2014). A dosimetric study of volumetric modulated arc therapy planning thechniques for treatment of low-risk prostate cancer in patients with bilateral hip prostheses. South Asian J Cancer. Jan-Mar: 3(1):18-21.

Reft, C., Alec, R., Dad, I., Gerbi, BJ., Keall, P., Lief, E., Papanikolaou, N., Mijnheer, BJ., Sibata, C. & Van Dyk, J. (2003). Dosimetric considerations for Patients with HIP prostheses undergoing pelvic irradiation. Report of the AAPM Radiation Therapy Committee Task Group 63. Med Phys 30:1162–82

Reisz, J. A., Bansal, N., Qian, J., Zhao, W., & Furdui, C. M. (2014). Effects of ionizing radiation on biological molecules--mechanisms of damage and emerging methods of detection. *Antioxidants & redox signaling*, *21*(2), 260–292. https://doi.org/10.1089/ars.2013.5489

Research Article The Mass Attenuation Coefficients, Electronic, Atomic, and Molecular Cross Sections, Effective Atomic Numbers, and Electron Densities for Compounds of Some Biomedically Important Elements at 59.5 keV Burcu Akça and Salih Z. ErzeneoLlu. Hindawi Publishing Corporation Science and Technology of Nuclear Installations Volume 2014, Article ID 901465, 8 pages http://dx.doi.org/10.1155/2014/901465.

Rhee, D.J., Kim, S. & Joeng, D.H. (2019). Effects of the difference in tube voltage of the CT scanner on dose calculation.

Rijken J, Hu Y, Hiscoke K. (2023). Individualized breathing trace quality assurance for lung radiotherapy patients undergoing 4DCT simulation. *J Appl Clin Med Phys* :e13929. [PMID: 36807511 DOI: 10.1002/acm2.13929] [Reference Citation Analysis]

Rijken J, Hu Y, Hiscoke K. Individualized breathing trace quality assurance for lung radiotherapy patients undergoing 4DCT simulation. *J Appl Clin Med Phys* 2023;:e13929. [PMID: 36807511 DOI: 10.1002/acm2.13929] [Reference Citation Analysis]

Rijken, J. D., & Colyer, C. J. (2017). Dose uncertainties associated with a set density override of unknown hip prosthetic composition. Journal of applied clinical medical physics, 18(5), 301–306.

Rim, J., Choi, J., Lee, S, A. & Khil, E.K. (2018). Comparison of metal artifact reduction for orthopedic implants versus standard filtered back projection: value of postoperative CT after hip replacement. J Korean Soc Radiol; 78 (1):22-29.

Rogers DW, Kawrakow I, Seuntjens JP, Walters BR, Mainegra-Hing E. Ottawa, ON: National Research Council of Canada; 2010. NRC User Codes for EGSnrc. NRCC Report PIRS-702 (revB)

Rogers DW, Walters B, Kawrakow I. (2016) *PIRS 509(A) Rev.* Ottawa, ON: National Research Council of Canada. BEAMnrc user's Manual.

Rogers, D.W.O. (2017). The EGSnrc code system. NRC Rep. PIRS-701 NRC Ott,.

Rogers, D.W.O., Walters, B., Kawrakow, I., *et al*., (2017). BEAMnrc user's manual. NRC Rep. PIRS 509, 12.

RTOG 0126. (2014). A phase 111 randomized study of high dose 3D-CRT/IMRT versus standard dose 3D-CRT/IMRT in patients treated for localized prostate cancer.

RTOG 0938. Radiation therapy oncology group. https://www.nrgoncology.org/Clinical-Trials/Protocol/rtog-0938?filter=rtog-0938

Salvat-Pujol, F., Jeschke, H. O., & Valentí, R. (2013). Simulation of electron transport during electron-beam-induced deposition of nanostructures. *Beilstein journal of nanotechnology*, *4*, 781–792. https://doi.org/10.3762/bjnano.4.89.

Sandrini ES, da Silva AX, da Silva CM. Evaluation of collimator rotation for volumetric modulated arc therapy lung stereotactic body radiation therapy using flattening filter free. Appl Radiat Isot. 2018 Nov;141:257-260. doi: 10.1016/j.apradiso.2018.05.026. Epub 2018 May 25. PMID: 29861162.

Schmidt MA, Payne GS. Radiotherapy planning using MRI. Phys Med Biol. 2015 Nov 21;60(22): R323-61. doi: 10.1088/0031-9155/60/22/R323. Epub 2015 Oct 28. PMID: 26509844; PMCID: PMC5137785.

Seibert, J.A., Boone, J.M. (2005). X-ray Imaging Physics for Nuclear Medicine Technology. Part 2: X-ray Interactions and Image Formation, Journal of Nuclear Medicine. 33(1).

Seif F, Tahmasebi-Birgani M.J, Bayatiani M.R. An Analytical-empirical Calculation of Linear Attenuation Coefficient of Megavoltage Photon Beams. J Biomed Phys Eng. 2017 Sep 1;7(3):225-232. PMID: 29082214; PMCID: PMC5654129.

Seuntjens, J.P., Strydom. W, & Shortt, K.R. (2019). Chapter 2: Dosimetric principles, quantities and units. Available from http://www-naweb.iaea.org

Sharma, A., Singh, M., Singh, B. & Sandhu, B.S. (2009). Coherent and incoherent scatterings for measurement of mandibular bone density and stable iodine content of tissue. J med Phys: 34(3):192-187.

Silva, I.M.C.C., de Freitas, D.Q., Ambrosano, G.M.B., Boscolo, F.N. and Almeida, S.M. (2012). Bone density: comparative evaluation of Hounsfield units in multislice and cone-beam computed tomography. Braz Oral Res Nov-Dec; 26 (6): 550-6

Singh, R., Kainth, H.S., Dev, S., Singh, G., Mehta, D., Shahi, J.S., Singh, B., & Verma, T, R. (2019). Evaluation of positional accuracy of the Varian's exact-arm and retractable-arm support electronic portal imaging device using intensity-modulated radiotherapy graticule phantom. Volume 15, issue, page:204-210.

South Africa National Cancer Registry (NCR-SA) (2013). https://www.nicd.ac.za/centres/national-cancer-registry/

Sprawls, P. (1995). Physical principles of medical imaging, 2nd edition. ISBN 0-944838-54-5.

Sturk, D. (2019). Radiographic physics review. Presentation. Available from https://www.paho.org/hq/dmdocuments/2014/Radiographic-Physics-Review.pdf

Sutherland, K. (2019). Radiation Therapy in Patients with Implanted Hip Prostheses: Phantom Study Results. Radiation oncology department Cancer care Manitabo, Winnipeg Canada. Available from pubs.medicaldosimetry.org

Takahashi, Y. & Huri, S. (2014). Fast, simple, and informative patient specific dose verification method for intensity modulated total morrow irradiation with helical tomography. Radiation Oncology; 9:34.

Tanooka M, Doi H, Miura H, Inoue H, Niwa Y, Takada Y, Fujiwara M, Sakai T, Sakamoto K, Kamikonya N, Hirota S. (2013). Three-dimensional radiochromic film dosimetry for volumetric modulated arc therapy using a spiral water phantom. J Radiat Res. 1;54(6):1153-9. doi: 10.1093/jrr/rrt059. Epub. PMID: 23685667; PMCID: PMC3823780.

Tegaw EM, Geraily G, Etesami SM, Gholami S, Ghanbari H, Farzin M, Tadesse GF, Shojaei M. A Comparison between Electron Gamma Shower, National Research Council/Easy Particle Propagation (EGSnrc/Epp) and Monte Carlo N-Particle Transport Code (MCNP) in Simulation of the INTRABEAM ® System with Spherical Applicators. (2021). *J Biomed Phys Eng*. Feb 1;11(1):47-54. doi: 10.31661/jbpe.v0i0.2008-1171. PMID: 33564639; PMCID: PMC7859382.

Teoh, M., Clark, C.H., Wood, K., Whitaker, S. & Nisbet, A. (2011). Volumetric modulated arc therapy: a review of current literature and clinical use in practice. Br J Radiol, v.84 (1007)

The international commission on radiation unit and measurements (2010). Journal of the ICRU, Vol10 N 1, Report 83.

Thomas, S.J. (1999). Relative electron density calibration of CT scanners for radiotherapy treatment planning. The British Journal of Radiology, 72, 781-786.

To D, Xhaferllari I, Liu M, Liang J, Knill C, Nandalur S, Gustafson G, Lack D. Evaluation of VMAT Planning Strategies for Prostate Patients with Bilateral Hip Prosthesis. (2021). *Technol Cancer Res Trea*t. Jan-Dec;20:15330338211038490. doi: 10.1177/15330338211038490. PMID: 34490809; PMCID: PMC8427923.

Toossi, M.T.B., Khorshidi, F., Ghorbani, M., Mohamadian, N., & D. Davenport, D. (2016). Comparison of EBT and EBT3 Radio Chromic Film Usage in Parotid Cancer Radiotherapy J Biomed Phys Eng: 6(1): 1–12.

Tremthick, L.J. (2012). Characterization of dosimetry in electron radiotherapy under different bolus applications. Master of Applied Science thesis. RMIT university.

Trujillo-Bastidas, C.D., Garcia-Garduna, O.A,. Larraga-Gutierrez, J.M., Martinez-Davalos, A. & Rodrigues-Villafuerte, M. (2016). Effective atomic number and electron density calibration with a dual-energy CT technique. AIP Conference Proceedings 1747, 080009.

Tsai, J.Y., Chen, F.H., Hsieh, T.Y., Hsiao, Y.Y. (2015) Effects of indirect actions and oxygen on relative biological effectiveness: estimate of DSB induction and conversion induced by gamma rays and helium ions*. J Radiat Res*.;56(4):691-9. doi: 10.1093/jrr/rrv025. Epub. PMID: 25902742; PMCID: PMC4497398.

Tufan, M.C. (2006). Interaction of electrons with matter. 8th nuclear science training course with nuclides.net, solvenia.

Tukey's Honestly Significant Difference (HSD) test.

Utitsarn K, Alrowaili ZA, Stansook N, et al. Optimisation of output factor measurements using the Magic Plate 512 silicon dosimeter array in small megavoltage photon fields. (2017). *J Phys Conf Ser*.;777:12022. [Google Scholar]

Uysal B, Beyzadeoğlu M, Sager O, Dinçoğlan F, Demiral S, Gamsız H, Sürenkök S, Oysul K. Dosimetric evaluation of intensity modulated radiotherapy and 4-field 3-d conformal radiotherapy in prostate cancer treatment. Balkan Med J. 2013

Mar;30(1):54-7. doi: 10.5152/balkanmedj.2012.075. *Epub* 2013 Mar 1. PMID: 25207069; PMCID: PMC4116026.

van Battum, L.J., Hoffmans, D., Piersma, H., & Heukelom, S. (2008). Accurate dosimetry with GafChromic EBT film of a 6 MV photon beam in water: what level is achievable? *Med Phys:*35(2):704–16.

Van Eeden, D. (2014). Development of a particle source model for a synergy linear accelerator to be used in Monte Carlo radiation dose calculations for cancer therapy. Thesis Viewed on 25/03/2018

Veikutis, V., Budrys, T., Basevicius, A., Lukosevicius, S., Gleizniene, R., Unikas, R. & Skaudikas, D. (2015). Artifacts in computer tomography imaging: how it can really affect diagnostic image quality and confuse clinical diadnosis? Journal of Vibro engineering; volume 17, issue 2. ISSN 1392-8716.

Walters, B., Kawrakow, I., Rogers, D.W.O. (2005). DOSXYZnrc user's manual. NRC Rep. PIRS 794.

Wen, N., Lu, S., Kim, J., Qin, Y., Huang, Y., Zhao, B., Liu, C., & Chetty, I. J. (2016). Precise film dosimetry for stereotactic radiosurgery and stereotactic body radiotherapy quality assurance using Gafchromic™ EBT3 films. *Radiation oncology (London, England)*, *11*(1), 132. https://doi.org/10.1186/s13014-016-0709-4.

White P, Yee CK, Shan LC, Chung LW, Man NH, Cheung YS. A comparison of two systems of patient immobilization for prostate radiotherapy.(2014). *Radiat Oncol*. Jan 22;9:29. doi: 10.1186/1748-717X-9-29. PMID: 24447702; PMCID: PMC3905910

Yani, S., Dirgayussa, IGE., Rhani, MF., Haryanto, IA And Arif, I. (2016). Monte Carlo investigation of inhomogeneity phantom effects in 6MV photon beam. Transactions on Science and Technology. 3(2):336-344.

Yu, H., Zeng, K., Bharkhada, D.K., Wang, G., Madsen, M.T., Saba, O., Policeni, B., Howard, M.A. & Smoker, W.R.K. (2007). A segmentation-based method for metal artifact reduction. Acad Radiol; 14(4): 495-504.

Yu. L., Leng, S., McCollough, C.H. (2012). Dual-energy CT-based monochromatic imaging. *AJR Am J Roentgenol*. 199(5 Suppl):9–15. doi: 10.2214/AJR.12.9121.

Zaorsky NG, Davis BJ, Nguyen PL, Showalter TN, Hoskin PJ, Yoshioka Y, Morton GC, Horwitz EM. (2017). The evolution of brachytherapy for prostate cancer. Nat Rev Urol. Jun 30;14(7):415-439. doi: 10.1038/nrurol.2017.76. *PMID:* 28664931; PMCID: PMC7542347.

Zaorsky, N. G., Showalter, T. N., Ezzell, G. A., Nguyen, P. L., Assimos, D. G., et al (2016). ACR Appropriateness Criteria® external beam radiation therapy treatment planning for clinically localized prostate cancer, part I of II. Advances in radiation oncology, 2(1), 62–84.

Zhang, Y. (2018). Convolutional neutral network-based metal artifact reduction in X-ray computed tomography. *Physics.Med.Ph.*

Zhao, W., Patil, I., Han, B., Yang, Y., Xing, L., & Schüler, E. (2020). Beam data modeling of linear accelerators (linacs) through machine learning and its potential applications in fast and robust linac commissioning and quality assurance. *Radiotherapy and oncology: journal of the European Society for Therapeutic Radiology and Oncology*, *153*, 122–129. https://doi.org/10.1016/j.radonc.2020.09.057.

Ziemann, C., Stille, M., Cremers, F., Buzug, T.M. & Rades, D. (2018). Improvement of dose calculation in radiation therapy due to metal artifact correction using augmented likelihood image reconstruction. *J Appl Clin Med Phys*, 19(3): 227-233.

APPENDIX

A. CONFERENCE AND MANUSCRIPT

A.1 Conference presentations

(1) Preliminary study on the design of a novel pelvic prosthesis spiral phantom for advanced radiotherapy verification. 1ST SA Congress of Oncology 2019 (SACO 2019). 9-11 August 2019 in Cape Town.

(2) Validation of the Monte Carlo model for 6 MV and 15 MV photon beams of Varian Clinac ix Clinac. South African Institute of Physics Conference (SAIP 2021). 22-30 July 2021 at Northwest University.

(3) Comparing film measurements and Monte Carlo simulations of dose delivered in a pelvis phantom with titanium hip prosthesis. 28 28th International Nuclear Physics Conference (INPC 2022). 11-16 September 2022 in Cape town.

(4) Calibration of Gafchromic EBT3 Films for Pelvic Prosthesis Phantom Dosimetry. Congress of Oncology (SACO 2023). 1-3 September 2023 in Cape town.

A.2 Manuscript

(1) Comparing Film Measurements and Monte Carlo Simulations of Dose Delivered in a Pelvic Phantom with Titanium Hip Prosthesis. (INPC 2022 Conference proceedings). K E Dumela, O M Oderinde and I T Usman. Published under licence by IOP Publishing Ltd. *Journal of Physics: Conference Series,* Volume 2586, 28th International Nuclear Physics Conference (INPC 2022) 11/09/2022 - 16/09/2022 Cape Town, South Africa

B. GAFCHROMIC EBT3 FILM AND SCANNER

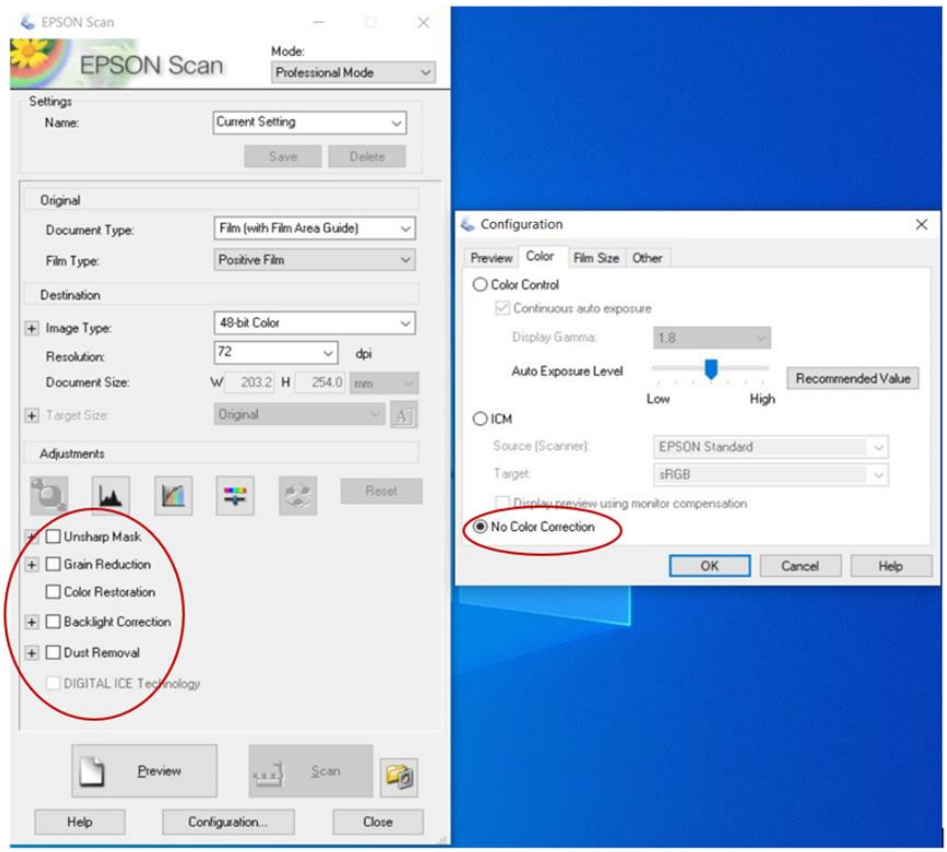

Figure B. 1: Epson scanner settings

1. Short term scanner reproducibility

Table B. 1: Dose-response for the scanner short term reproducibility

RGB Channels						
Scan no	Red		Green		Blue	
		% Difference		% Difference		% Difference
1	28747.057 (SD ± 1.2)		25877.582 (SD ± 2.8)		17939.295 (SD ± 0.1)	
2	28745.46 (SD± 0.5)	0.01	25871.1 (SD ± 0.5)	0.03	17939.385 (SD± 0.1)	-0.05
3	28744.175 (SD± 0.03)	0.01	25876.285 (SD ± 1.0)	0.05	17942.984 (SD ± 1.7)	0.02
4	28743.72 (SD ± 0.2)	0.01	25869.199 (SD ± 2.2)	0.03	17936.884 (SD ± 0.9)	0.01
5	28742.119 (SD ± 0.9)	0.02	25868.686 (SD ± 1.1)	0.03	17936.673 (SD ± 1.1)	0.02

2. Long term scanner reproducibility

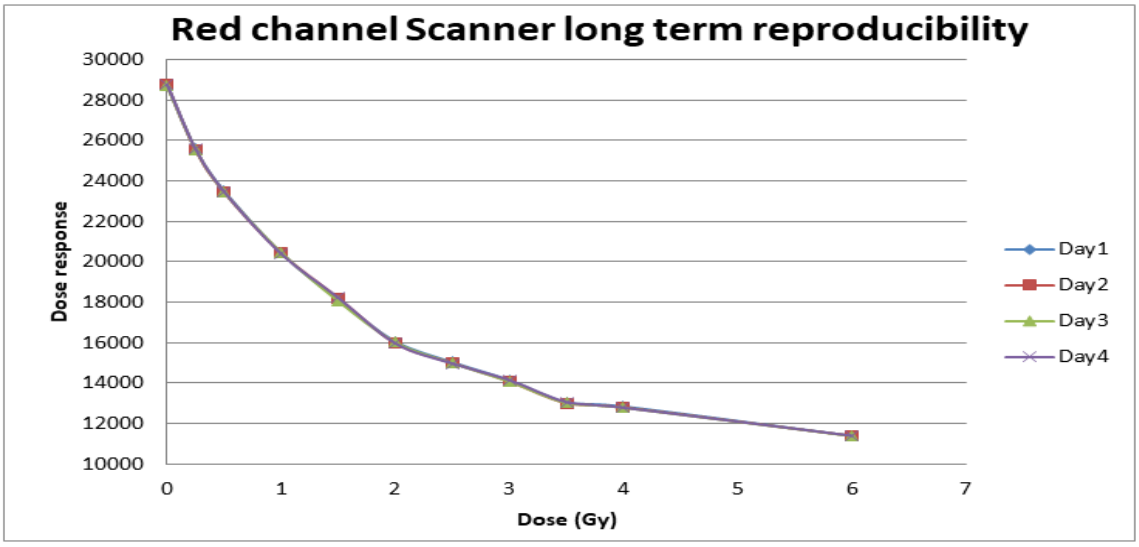

Figure B. 2: The scanner long term reproducibility for a red channel

Table B. 2: The dose-response for a long-term scanner reproducibility of a red channel, and the standard deviation (SD) and the percentage difference.

Dose (Gy)	Day 1-Red	Day 2-Red		Day 3-Red		Day 4-Red	
			% Difference		% Difference		% Difference
0.0	28773.633	28764.42 (SD ±63.3)	0.03	28698.51 (SD ±26.6)	0.26	28771.05 (SD ±0.7)	0.01
0.25	25578.218	25546.139 (SD ±11.3)	0.13	25566.702 (SD ±4.1)	0.05	25789.969 (SD ±9.8)	0.05
0.5	23516.742	23352.235 (SD ±22.8)	0.27	23413.565 (SD ±18.8)	0.23	23409.901 (SD ±1.6)	0.16
1.0	20443.224	20134.008 (SD ±3.3)	0.05	19967.265 (SD ±8.5)	0.12	20209.461 (SD ±10.3)	0.17
1.5	18135.906	18221.915 (SD ±30.4)	0.47	18059.974 (SD ±26.8)	0.42	18330.612 (SD ±18.3)	0.52
2.0	16064.868	15938.853 (SD ±30.4	0.54	15923.333 (SD ±14.7)	0.26	15971.732 (SD ±17.7)	0.58
2.5	15039.494	14904.131 (SD ±16.0)	0.30	14985.577 (SD ±19.1)	0.36	14972.005 (SD ±15.8)	0.45
3.0	14149.649	14083.462 (SD ±23.4)	0.47	14077.02 (SD ±25.7)	0.51	14153.898 (SD ±13.2)	0.03
3.5	13152.018	12913.05 (SD ±13.7)	0.30	12922.133 (SD ±10.6)	0.23	13067.605 (SD ±12.4)	0.12
4.0	12847.174	12748.465 (SD ±17.0)	0.38	12743.589 (SD ±22.5)	0.49	12687.137 (SD ±12.7)	0.47
6.0	11398.88	11395.32 (SD ±1.3)	0.03	11387.09 (SD ±4.2)	0.10	11401.23 (SD ±1.5)	0.20

Day 1 is the first day the films were scanned 24 hours after irradiation, Day 2 is 3 hours after the first scans, Day 3 is 7 days after the first day of scanning and day 4 is 13 days after the first day of scanning.

3 Scanner uniformity

Table B. 3: The dose responses obtained in different scanner position at 1 Gy and 2 Gy prescribed dose

Scanner Position	1Gy			2Gy		
	Red	Green	Blue	Red	Green	Blue
Centre	19619.726	19820.797	15987.696	15880.596	16798.194	15078.832
1	19449.626	19791.859	16046.341	15695.246	16683.724	15046.646
Between 2-3	19544.457	19706.481	15924.402	15729.524	16561.868	14847.184
4	18886.387	19507.465	15952.872	15297.775	16548.026	15027.543
Between 8 and 12	19407.264	19600.982	15780.411	15564.366	16518.113	14816.789
16	19385.068	19701.378	15922.834	16206.411	17121.433	15494.625
Between 14 and 15	19484.03	19885.403	16212.337	15688.671	16603.112	14946.207
13	19495.15	19896.608	16221.738	15709.351	16756.214	15173.61
Between 5 and 9	20010.66	20272.189	16435.889	16015.761	16846.253	15127.722
Average	19475.819	19798.129	16053.8356	15754.189	16715.2152	15062.1287

4 Scanner lateral response

Table B. 4: Scanner lateral response

Dose response (Standard deviation)												
Position (cm)	**0.5 Gy Green**		**0.5 Gy Red**		**1 Gy Green**		**1 Gy Red**		**2 Gy Green**		**2 Gy Red**	
		% Difference		**% Difference**		**% Difference**		**% Difference**		**% Difference**		**% Difference**
-9	**22273.076 (SD±176.9)**	**2.2**	**22822.164 (SD±169.3)**	**2.2**	**20024.873 (SD±87.8)**	**1.2**	**19450.818 (SD±187.1)**	**2.6**	**17034.493 (SD±21.4)**	**0.4**	**15963.169 (SD±1.5)**	**0**
-6	**22476.592 (SD±104.9)**	**1.3**	**23130.808 (SD±68.4)**	**0.8**	**20186.271 (SD±30.7)**	**0.4**	**19815.423 (SD±58.2)**	**0.8**	**17082.384 (SD±38.3)**	**0.6**	**16039.653 (SD±39.8)**	**0.5**
-3	**22700.012 (SD±25.9)**	**0.3**	**23269.181 (SD±19.5)**	**0.2**	**20291.478 (SD±6.0)**	**0.1**	**19979.799 (SD±0.09)**	**0.1**	**17075.016 (SD±35.7)**	**0.6**	**16032.533 (SD±36.2)**	**0.5**
0	**22773.398**		**23324.305**		**20273.198**		**19980.042**		**16973.967**		**15960.117**	
3	**22705.471 (SD±24.0.0)**	**0.3**	**23296.459 (SD±9.8)**	**0.1**	**20325.082 (SD±18.3)**	**0.3**	**19997.097 (SD±6.03)**	**0.1**	**17035.135 (SD±21.6)**	**0.4**	**15984.751 (SD±12.3)**	**0.2**
6	**22502.620 (SD±95.7)**	**1.2**	**23175.284 (SD±52.7)**	**0.6**	**20181.212 (SD±32.5)**	**0.5**	**19873.414 (SD±37.7)**	**0.5**	**16891.765 (SD±29.1)**	**0.5**	**15788.113 (SD±86.0)**	**1.1**
9	**22218.648 (SD±196.1)**	**2.4**	**22798.842 (SD±185.8)**	**2.3**	**20010.671 (SD±92.8)**	**1.3**	**19571.996 (SD±144.3)**	**2.0**	**16878.885 (SD±33.6)**	**0.6**	**15710.768 (SD±124.7)**	**1.6**

5 Scanner film orientation

Table B. 5: Dose-response acquired in a landscape and portrait orientation in a flatbed scanner.

Dose (Gy)	Red-Landscape	Green-Landscape	Red-Portrait		Green-Portrait	
				% Difference		% Difference
0.00	28773.633	25915.681	28773.633	0	25915.681	0
0.25	25566.702	23903.569	25789.969	0.9	24135.568	1.0
0.50	23213.565	22642.307	23409.901	0.9	22781.729	0.6
1.00	19967.265	20054.744	20209.461	1.2	20276.150	1.1
1.50	17659.974	18267.151	17730.612	0.4	18479.466	1.2
2.00	15923.333	16786.275	15971.732	0.3	16926.538	0.8
2.50	14585.577	15551.466	14772.005	1.3	15699.563	0.9
3.00	13627.02	14563.491	13753.898	0.9	14665.268	0.7
3.50	12922.133	13776.11	13067.605	1.1	13892.495	0.8
4.00	12293.589	12952.924	12487.137	1.6	13171.382	1.7
6.00	11195.081	11130.806	11368.880	1.6	11317.320	1.7

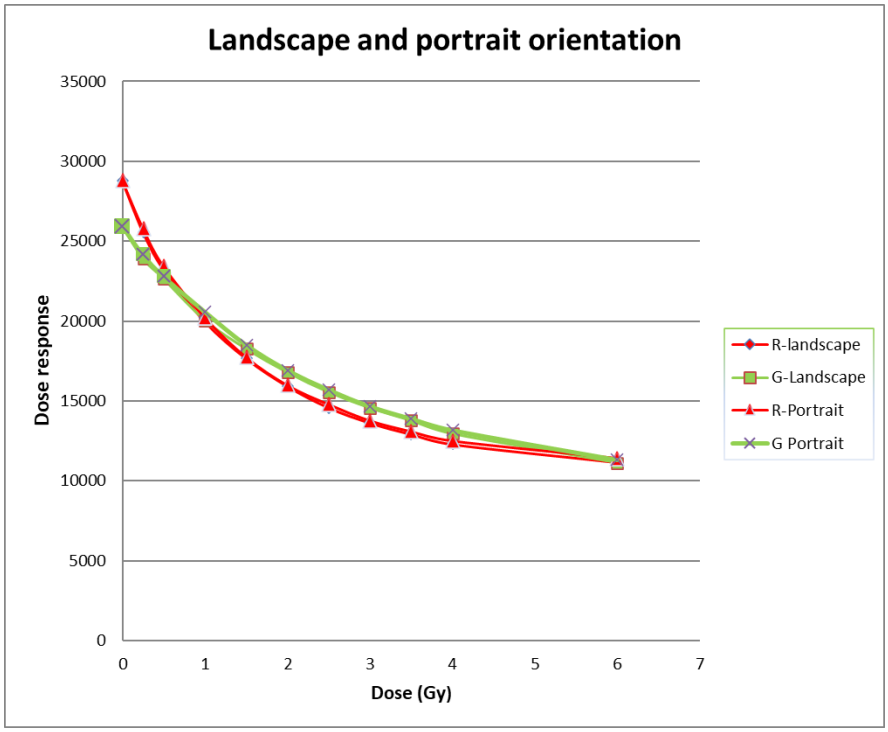

Figure B. 3: The dose-response acquired in a landscape and portrait orientation in a flatbed scanner.

6 Film uniformity

Table B. 6: Film uniformity results for the red, green, and blue channels

Film piece NO	Red	Green	Blue
1	20024.364	20154.555	16244.675
2	20018.935	20150.960	16243.261
3	20013.078	20152.367	16237.172
4	20020.683	20162.906	16245.569
5	20023.420	20150.202	16249.077
6	20016.708	20148.329	16251.191
Average	20019.531	20153.220	16245.158

7 Film dose rate dependence

Table B. 7: EBT3 film response to 6MV photon beam with a dose rate ranging from 100 to 600 MU/min

Dose rate (MU/min)	Dose response (Standard deviation)	
	1Gy	2Gy
100	20548.312 (SD ± 1)	16488.795(SD ± 6)
200	20432.242(SD ± 2)	16596.92 (SD± 1)
300	20455.227(SD ± 5)	16526.483 (SD± 1)
400	20445.58(SD ± 1)	16553.102(SD ± 3)
500	20532.321 (SD± 2)	16559.589 (SD± 1)
600	20443.224 (SD± 7)	16554.868 (SD± 9)

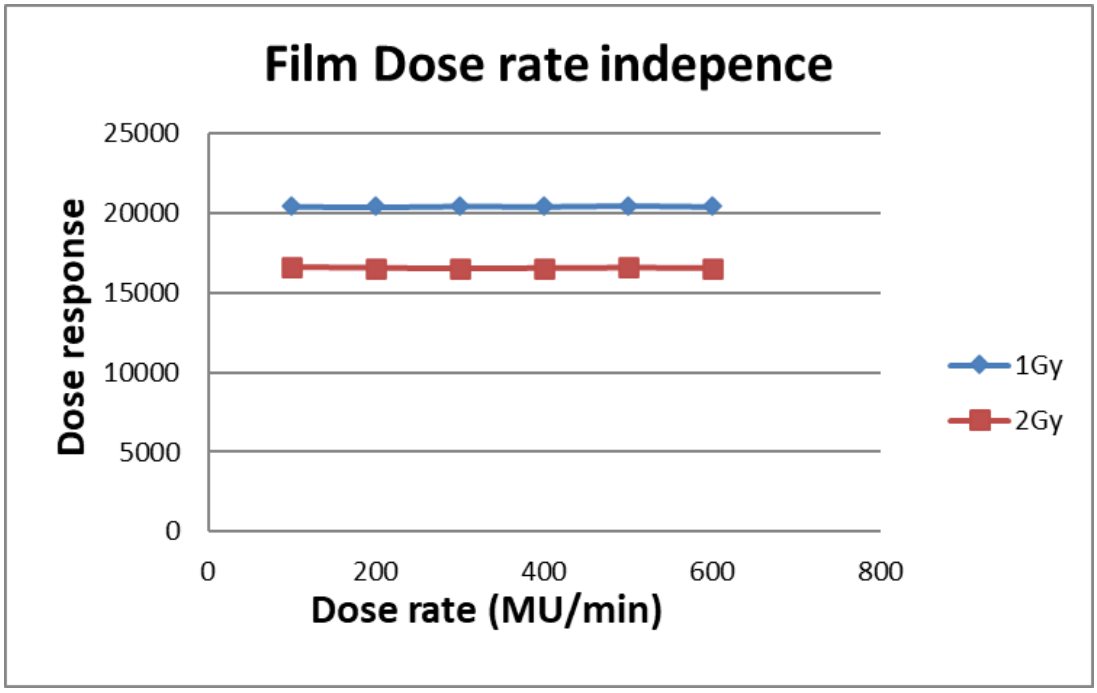

Figure B. 4: The dose responses for different dose rates

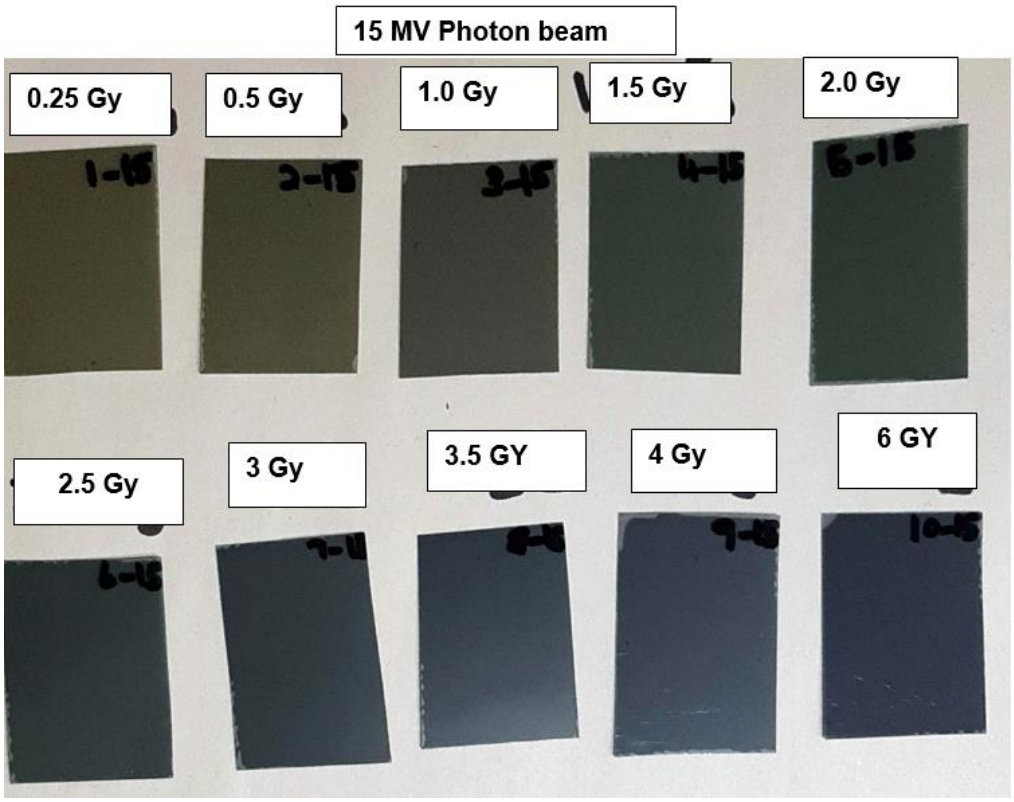

Figure B. 5: Gafchromic EBT3 film calibration pieces irradiated to doses in the range 0 - 6 Gy using 15MV photon beam.

C. EXPERIMENTAL MEASUREMENTS

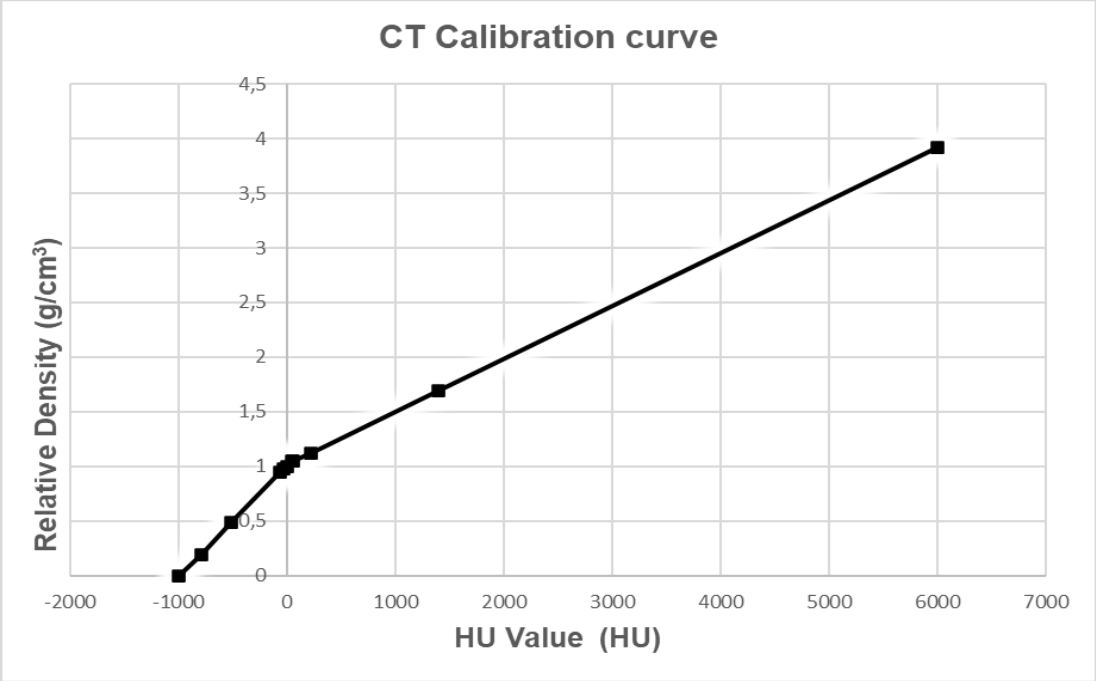

Figure C. 1: The calibration curve from treatment planning system. The calibration curve is extended to accommodate high density material.

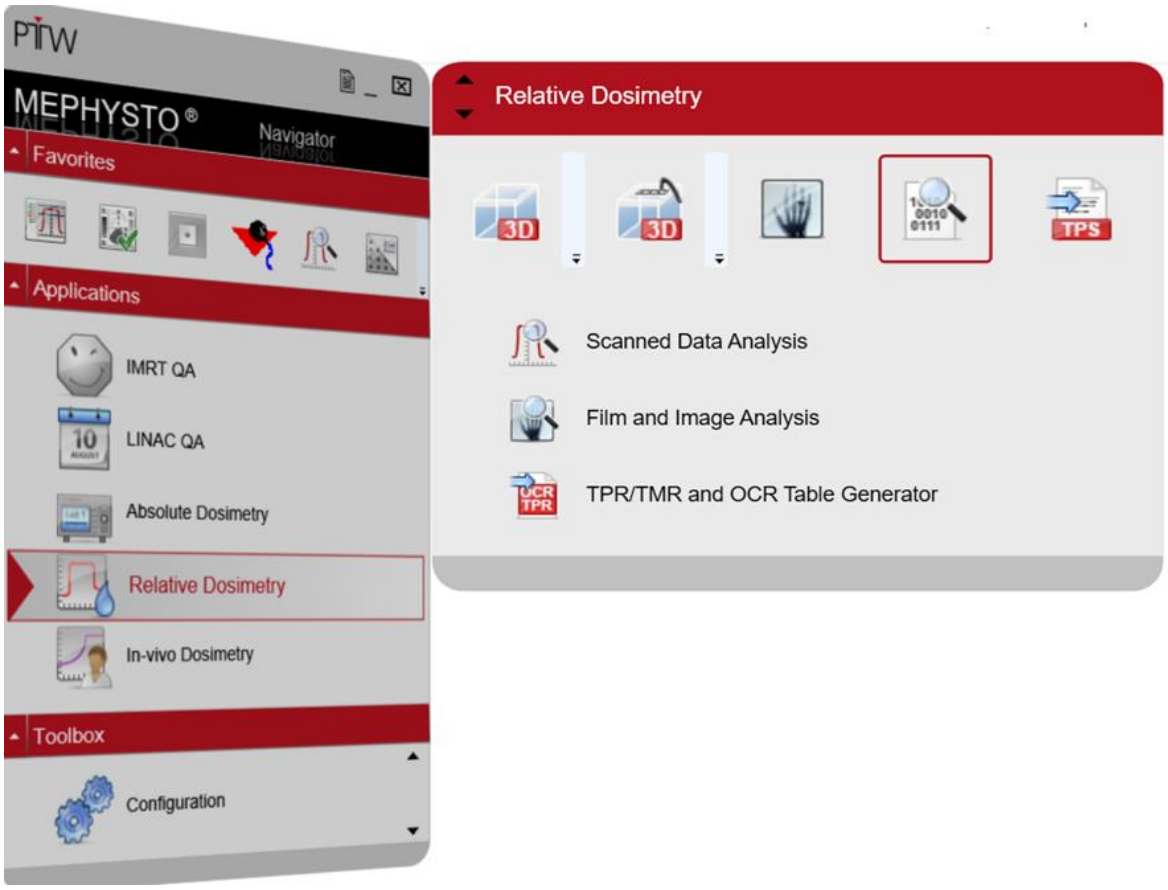

Figure C. 2: MEPHYSTO® mc^2 Navigator Software

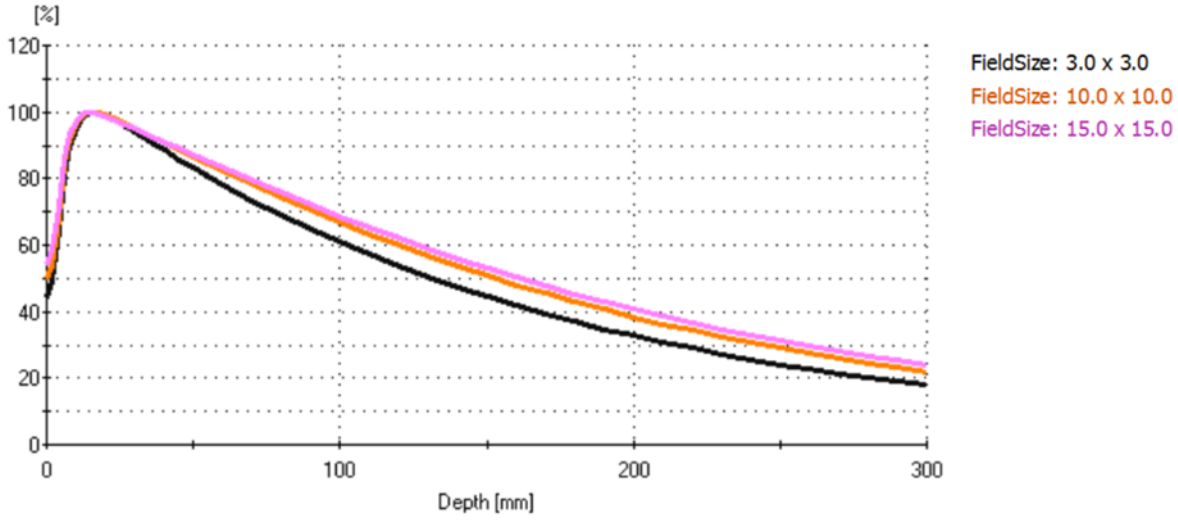

Figure C. 3: 6 MV photon beam percentage depth dose of the field sizes considered in this study.

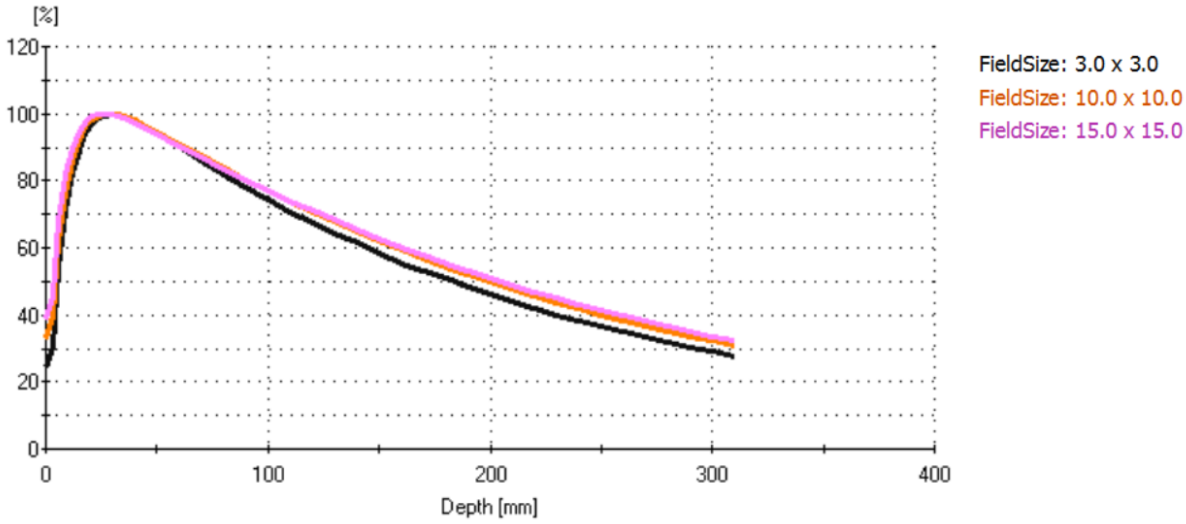

Figure C. 4: 15 MV photon beam percentage depth dose of the field sizes considered in this study

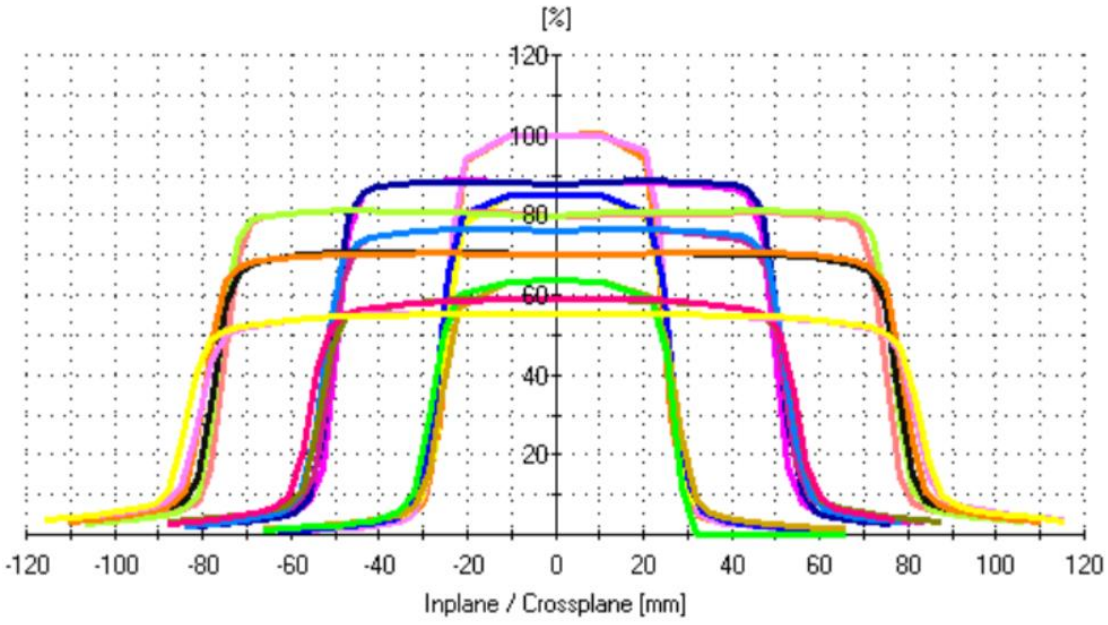

Figure C. 5: Experimental 6 MV photon beam for different field sizes

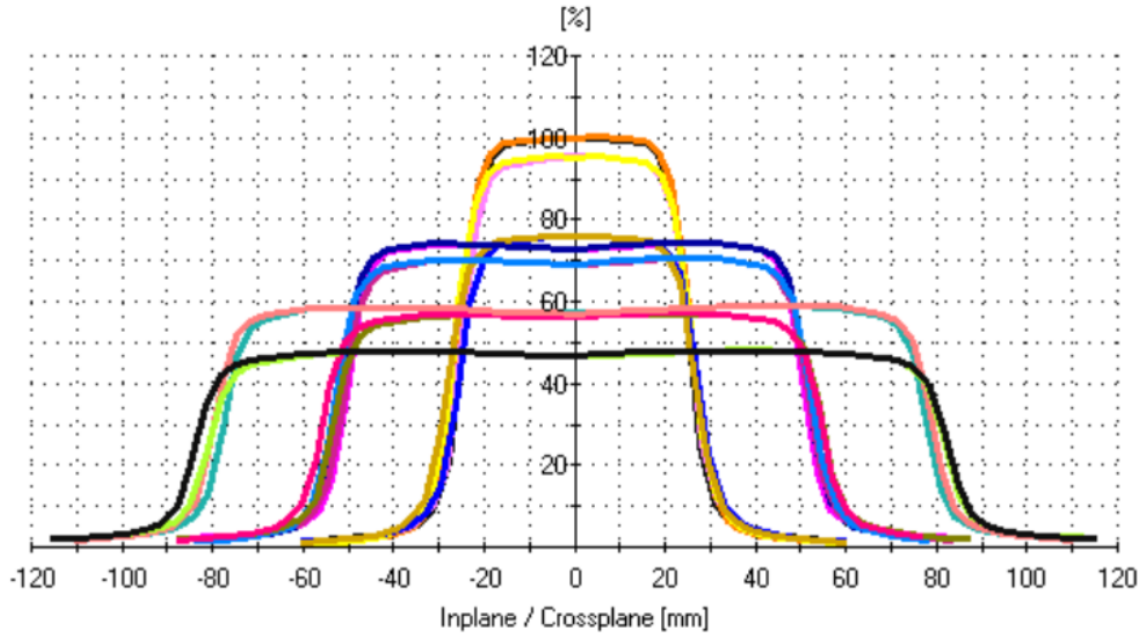

Figure C. 6: Experimental 15 MV photon beam for different field sizes

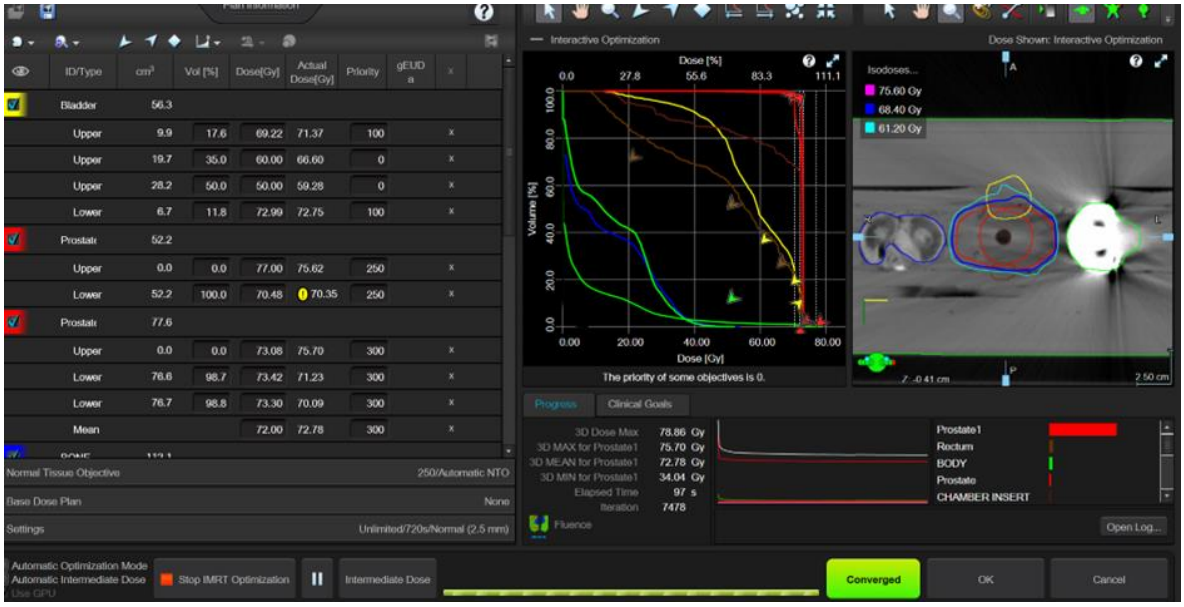

Figure C. 7: Eclipse optimization window for 7 FIELD IMRT

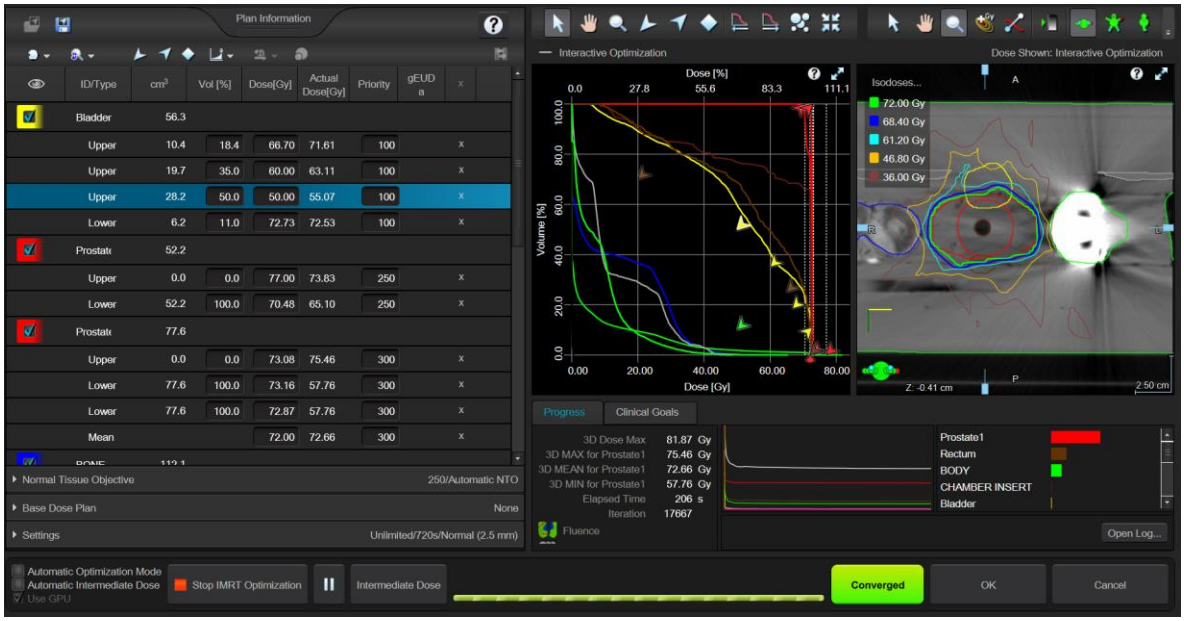

Figure C. 8: Optimization window for IMRT with beam avoidance

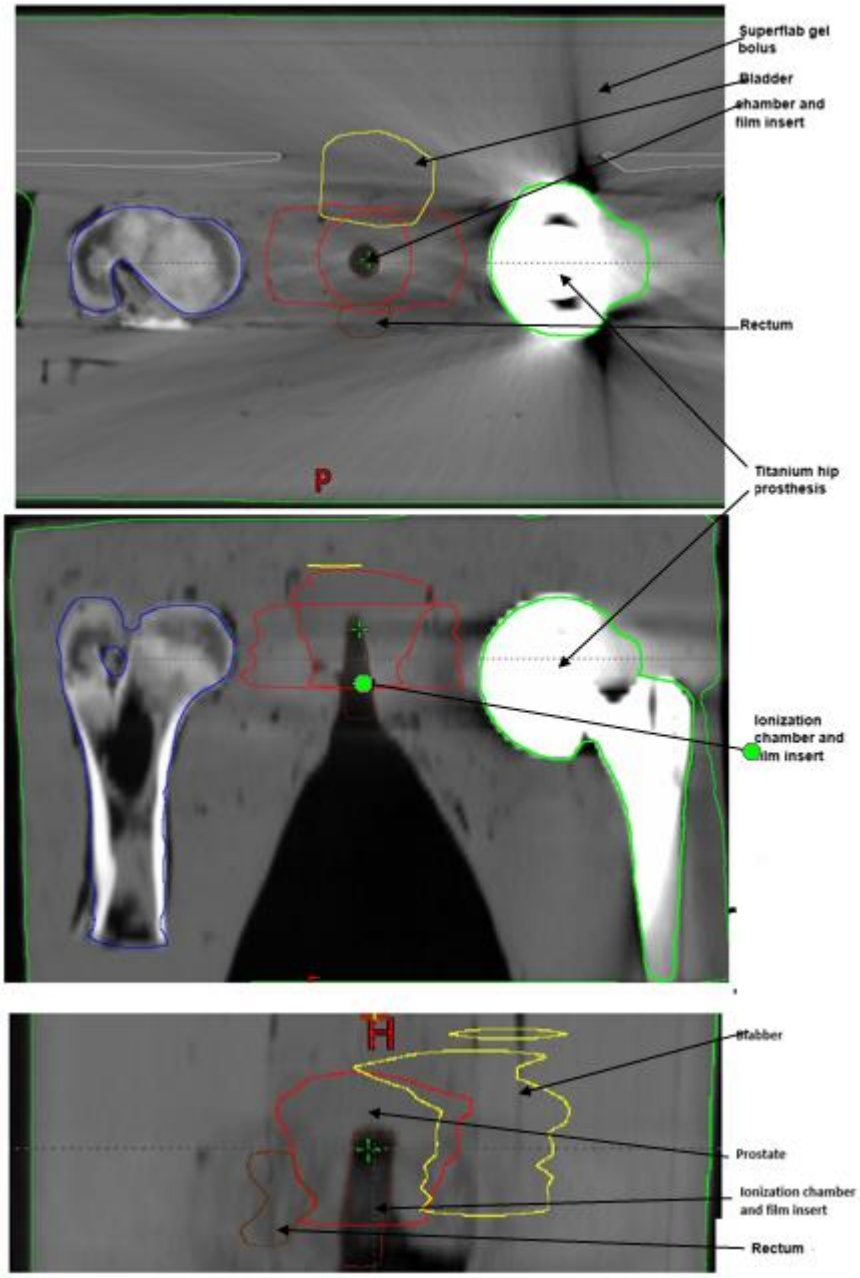

Figure C. 9: illustration of the (A) axial, (B) coronal and (C) sagittal view of an in-house pelvic phantom.

D. MONTE CARLO CODE

BEAMnrc Output Files

The outputs of a DOSXYZnrc calculations are:

(1) 3D dose distribution data (*.3ddose) that contains corresponding dose uncertainties of all the voxel, dose value and dose error.

(2) file list simulation (*. egslst) that contains the total CPU time during the simulation.

```
================================================================================

                  Material summary   7 Materials used
********************************************************************************
 # Material           density(g/cm**3)   AE(MeV)   AP(MeV)     UE(MeV)  UP(MeV)
-- -----------------  ----------------   -------   -------     -------  -------
 1 AIR700ICRU            1.205E-03        0.700     0.010      55.511    55.000
 2 W700ICRU              1.930E+01        0.700     0.010      55.511    55.000
 3 CU700ICRU             8.933E+00        0.700     0.010      55.511    55.000
 4 KAPTON700ICRU         1.420E+00        0.700     0.010      55.511    55.000
 5 H2O700ICRU            1.000E+00        0.700     0.010      55.511    55.000
 6 STEEL700ICRU          8.060E+00        0.700     0.010      55.511    55.000
 7 MYLAR700ICRU          1.380E+00        0.700     0.010      55.511    55.000
********************************************************************************
                          SOURCE PARAMETERS

                  INITIAL PARTICLES are Electrons
                  PARALLEL BEAM ON FRONT FACE at Z=   0.0000 cm
                  Beam radius=   0.4000 cm
               X,Y,Z DIRECTION COSINES = (   0.00000   0.00000   1.00000)

                  KINETIC ENERGY OF SOURCE =    15.000 MeV
```

Figure D. 1: Summary of material used for linac head modelling.

```
================================================================================

                  Electron/Photon transport parameter

================================================================================

 Photon cross sections                                  xcom
 Compton cross sections                                 default
 Photon transport cutoff(MeV)                               0.1000E-01
 Pair angular sampling                                   SIM
 Pair cross sections                                     BH
 Triplet production                                      Off
 Bound Compton scattering                                NOREJ
 Radiative Compton corrections                           Off
 Rayleigh scattering                                     ON
 Atomic relaxations                                      EADL
 Photoelectron angular sampling                          ON

 Electron transport cutoff(MeV)                           0.7000
 Bremsstrahlung cross sections                          BH
 Bremsstrahlung angular sampling                         KM
 Spin effects                                            On
 Electron Impact Ionization                              Off
 Maxium electron step in cm (SMAX)                            5.000
 Maximum fractional energy loss/step (ESTEPE)            0.2500
 Maximum 1st elastic moment/step (XIMAX)                 0.5000
 Boundary crossing algorithm                             EXACT
 Skin-depth for boundary crossing (MFP)                  3.000
 Electron-step algorithm                                 PRESTA-II
```

Figure D. 2: Electron/photon transport parameter

-

REGION and RANGE REJECTION SUMMARY:
****

Total number of regions, including region 1 which surrounds the geometry: 31

Region abs	Region local	CM #	IDENTIF	Dose ZONE (0=no)	IR_ TO_ BIT	Medium (No.&Name)	ECUTRR (MeV)	res_rnge (cm)	ESAVE (MeV)	type
1	1	0	exterior	0	0	0 Vacuum				
2	1	1	TARGET	0	23	2 W700ICRU	0.700	0.000	2.000	DNEAR
3	2	1	TARGET	0	23	3 CU700ICRU	0.700	0.000	2.000	DNEAR
4	1	2	PRICOL	0	23	1 AIR700ICR	0.700	0.000	2.000	DNEAR
5	2	2	PRICOL	0	23	2 W700ICRU	0.700	0.000	2.000	DNEAR
6	3	2	PRICOL	0	23	1 AIR700ICR	0.700	0.000	2.000	DNEAR
7	1	3	FILTERS	0	23	2 W700ICRU	0.700	0.000	2.000	DNEAR
8	2	3	FILTERS	0	23	1 AIR700ICR	0.700	0.000	2.000	DNEAR
9	3	3	FILTERS	0	23	2 W700ICRU	0.700	0.000	2.000	DNEAR
10	4	3	FILTERS	0	23	1 AIR700ICR	0.700	0.000	2.000	DNEAR
11	5	3	FILTERS	0	23	2 W700ICRU	0.700	0.000	2.000	DNEAR
12	6	3	FILTERS	0	23	1 AIR700ICR	0.700	0.000	2.000	DNEAR
13	7	3	FILTERS	0	23	1 AIR700ICR	0.700	0.000	2.000	DNEAR
14	1	4	IONCHAMB	0	23	4 KAPTON700	0.700	0.000	2.000	DNEAR
15	2	4	IONCHAMB	0	23	5 H2O700ICR	0.700	0.000	2.000	DNEAR
16	3	4	IONCHAMB	0	23	4 KAPTON700	0.700	0.000	2.000	DNEAR
17	4	4	IONCHAMB	0	23	6 STEEL700I	0.700	0.000	2.000	DNEAR
18	5	4	IONCHAMB	0	23	1 AIR700ICR	0.700	0.000	2.000	DNEAR
19	1	5	MIRROR	0	23	7 MYLAR700I	0.700	0.000	2.000	DNEAR
20	2	5	MIRROR	0	23	1 AIR700ICR	0.700	0.000	2.000	DNEAR
21	3	5	MIRROR	0	23	1 AIR700ICR	0.700	0.000	2.000	DNEAR
22	4	5	MIRROR	0	23	1 AIR700ICR	0.700	0.000	2.000	DNEAR
23	1	6	JAWS	0	23	1 AIR700ICR	0.700	0.000	2.000	DNEAR
24	2	6	JAWS	0	23	2 W700ICRU	0.700	0.000	2.000	DNEAR
25	3	6	JAWS	0	23	2 W700ICRU	0.700	0.000	2.000	DNEAR
26	4	6	JAWS	0	23	1 AIR700ICR	0.700	0.000	2.000	DNEAR
27	5	6	JAWS	0	23	2 W700ICRU	0.700	0.000	2.000	DNEAR
28	6	6	JAWS	0	23	2 W700ICRU	0.700	0.000	2.000	DNEAR
29	1	7	120MLC	0	23	1 AIR700ICR	0.700	0.000	2.000	DNEAR
30	2	7	120MLC	0	23	2 W700ICRU	0.700	0.000	2.000	DNEAR
31	3	7	120MLC	0	23	1 AIR700ICR	0.700	0.000	0.000	DNEAR

Figure D. 3: Rejection region and range summary

```
 Component Module summary:
 *************************

  There are  7 Component Modules.

     COMPONENT MODULE   FIRST      BOUNDARY     DISTANCE FROM     AIR     SCORING
                       REGION   (1=cyl,2=sq) REFERENCE PLANE    GAP     PLANE
  #   TYPE   IDENTIFIERFLAG     (cm)           (cm)       (cm)   (0=none)

  1 SLABS     TARGET       2      2      0.500          0.000     0.000      0
  2 CONS3R    PRICOL       4      1      5.000          0.247     0.353      0
  3 FLATFILT  FILTERS      7      1      2.898          7.530     8.900      0
  4 CHAMBER   IONCHAMB    14      1     12.000         18.182     2.818      0
  5 MIRROR    MIRROR      19      2      2.000         23.020     0.980      0
  6 JAWS      JAWS        23      2     20.000         28.000     0.000      0
  7 VARMLC    120MLC      29      2     20.000         45.750     0.050      1
```

Figure D. 4: Component Module (CM) summary

```
15MV CLINAC IX 10X10

 NRCC CALN: BEAMnrc(EGSnrc)
 ON win6432                                                  17:15:21 Oct 25 2021
 ********************************************************************************
                  EXECUTION INFORMATION AND WARNING MESSAGES
 ********************************************************************************

********* NEW INPUT FILE *********


 *** FINAL RANDOM NUMBER POINTERS:  ixx jxx =   81  17

 FOR THIS RUN:
 ------------
 ELAPSED& CPU TIMEs, RATIO =  329194.6  171308.6s (=  47.59HR)   1.92
 CPUTIME per history =   0.00017 sec. Number of historiesper hour =   21014709.
   On win6432

                 TOTAL # CHARGED PARTICLE STEPS        1.245E+11 +/- 0.0%
        # CHARGED PARTICLE STEPS/INITIAL HISTORY        1.245E+02 +/- 0.0%
 # PRESTA-II STEPS/TOTAL # CHARGED PARTICLE STEPS            0.720 +/- 0.0%

       NO. OF BREMSSTRAHLUNG EVENTS IN THIS RUN:           -1022929579

                  Maximum depth of stack=      11

                  PHASE SPACE FILE OUTPUT
                  ***********************

 FILE  SCORE    TOTAL     TOTAL    MAX. KE OF       MIN. KE OF     # INCIDENT
  #    PLANE  PARTICLES* PHOTONS*   PARTICLES        ELECTRONS   PARTICLES FROM
                                      (MeV)            (MeV)    ORIGINAL SOURCE

   1      1    5881032  5830039      14.9914           0.1892   999999990.000
```

Figure D. 5: Phase space file output

```
                    FLUENCE RESULTS
                    ***************

 CM SCORE POSITION   TOTAL                      ZONE RADII
    PLANE  (cm)    PARTICLES*                    (cm)
  7    1   51.41     5881032    8.9443   12.6491   15.4919   17.8885   20.0000


*Includes all particles of all weights

 Lines with zero results are not printed

SPECTRAL-AVERAGED QUANTITIES FOR FIRST TIME CROSSINGS OF THE SCORING PLANE
                  NORMALIZED per INCIDENT PARTICLE
ZONE        NUMBER            FLUENCE       ENERGY       ANGLE WRT Z-AXIS
                             (/cm**2)        (MeV)           (degrees)
---- ----------------- ----------------- --------------- ----------------
                        SCORING PLANE 1, CM  7:
ELECTRONS
   1  4.231E-05+- 0.49%  1.901E-07+- 0.52%     3.180+- 0.4%    16.929+- 0.4%
   2  1.018E-06+- 3.13%  5.741E-09+- 3.48%     1.699+- 3.1%    39.069+- 1.0%
   3  4.380E-07+- 4.79%  2.684E-09+- 5.06%     1.761+- 4.6%    44.690+- 1.3%
   4  2.030E-07+- 7.02%  1.339E-09+- 7.87%     1.415+- 6.7%    45.845+- 2.3%
   5  1.360E-07+- 8.57%  9.871E-10+- 9.09%     1.354+- 7.4%    51.448+- 2.4%
   6  1.000E-08+-31.62%  4.776E-11+-32.95%     0.544+-31.8%    45.503+-12.3%
  --------------------
 Tot  4.412E-05+- 0.5%
PHOTONS
   1  5.814E-03+- 0.04%  2.327E-05+- 0.04%     3.647+- 0.0%     3.185+- 0.1%
   2  1.061E-05+- 0.97%  5.569E-08+- 1.02%     1.056+- 0.7%    37.536+- 0.2%
   3  3.067E-06+- 1.81%  1.860E-08+- 1.92%     0.888+- 1.3%    46.223+- 0.3%
   4  1.311E-06+- 2.76%  8.589E-09+- 2.84%     0.832+- 1.9%    50.866+- 0.4%
   5  8.600E-07+- 3.41%  6.220E-09+- 3.57%     0.801+- 2.7%    54.561+- 0.5%
   6  1.700E-08+-24.25%  9.172E-11+-25.59%     0.813+-27.1%    53.038+- 5.2%
  --------------------
 Tot  5.830E-03+- 0.0%
POSITRONS
   1  6.469E-06+- 1.24%  2.962E-08+- 1.32%     3.421+- 0.9%    20.256+- 0.9%
   2  2.490E-07+- 6.34%  1.386E-09+- 6.65%     2.289+- 5.3%    39.705+- 1.9%
   3  8.500E-08+-10.85%  5.283E-10+-11.56%     2.490+- 9.0%    44.788+- 3.2%
   4  4.300E-08+-15.25%  3.005E-10+-17.66%     2.192+-13.5%    49.101+- 3.8%
   5  2.600E-08+-19.61%  1.904E-10+-20.73%     2.125+-13.8%    52.939+- 4.2%
   6  3.000E-09+-57.74%  1.679E-11+-57.82%     0.875+-85.2%*    58.522+-81.7%*
  --------------------
 Tot  6.875E-06+- 1.2%

*Covariance not included in uncertainty because no. of particles
 crossing scoring zone <    10

SPECTRAL-AVERAGED QUANTITIES FOR MULTIPLE CROSSINGS OF THE SCORING PLANE
                  NORMALIZED per INCIDENT PARTICLE
ZONE        NUMBER            FLUENCE       ENERGY       ANGLE WRT Z-AXIS
                             (/cm**2)        (MeV)           (degrees)
---- ----------------- ----------------- --------------- ----------------
```

Figure D. 6: Fluence results

Percentage depth dose and profiles simulated using EGSnrc Monte Carlo code

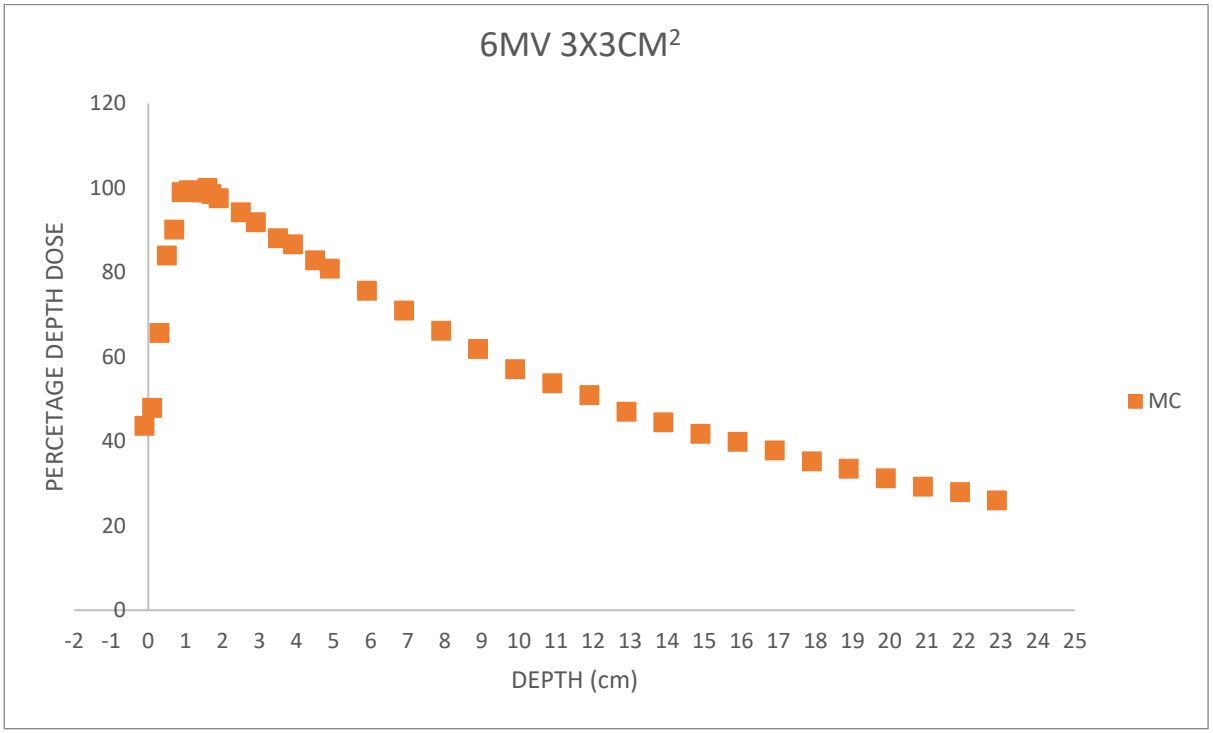

Figure D. 7: 6 MV photon beam percentage depth dose of the 3 x 3 cm^2 field size simulated using EGSnrc MC code.

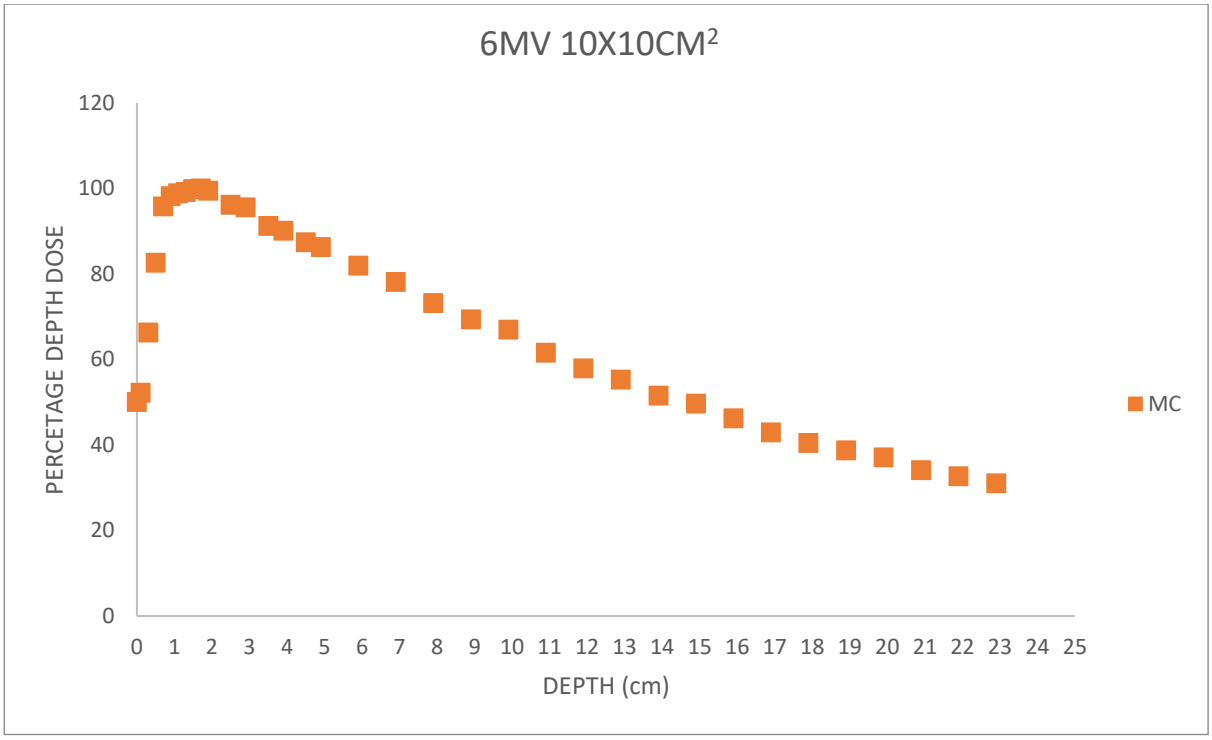

Figure D. 8: 6 MV photon beam percentage depth dose of the 10 x 10 cm^2 field size simulated using EGSnrc MC code.

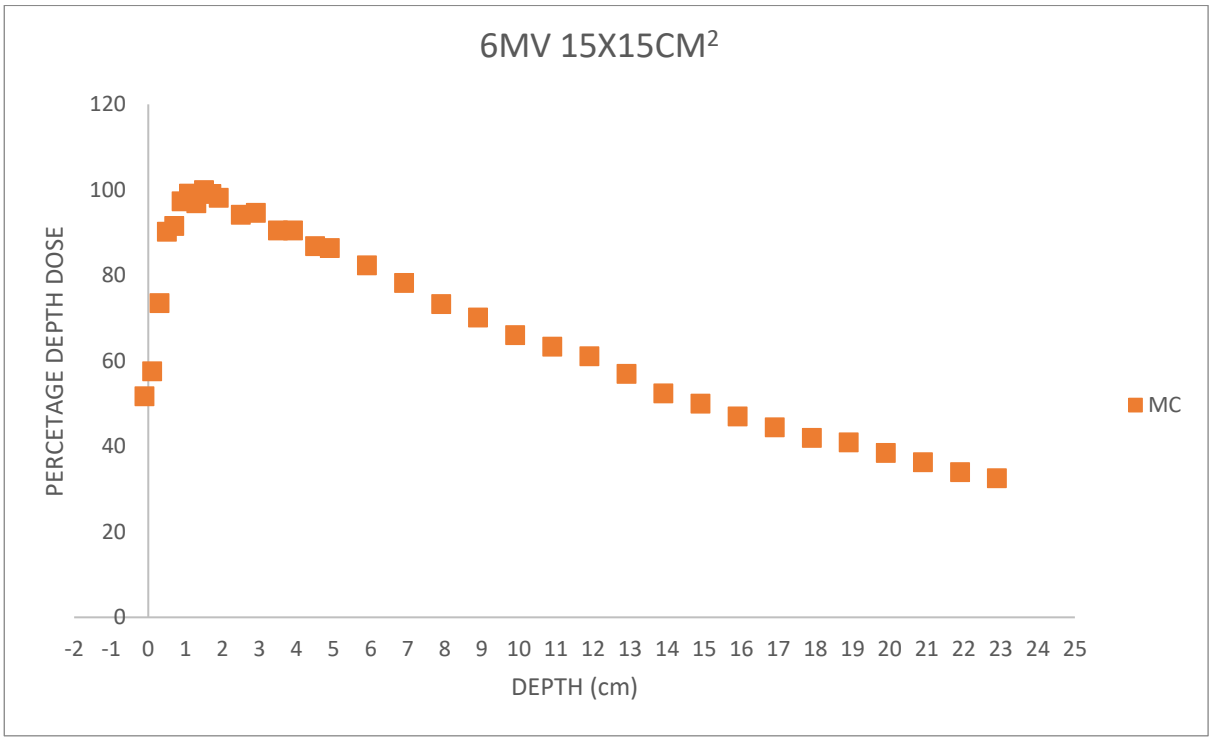

Figure D. 9: 6 MV photon beam percentage depth dose of the 15 x 15cm^2 field size simulated using EGSnrc MC code.

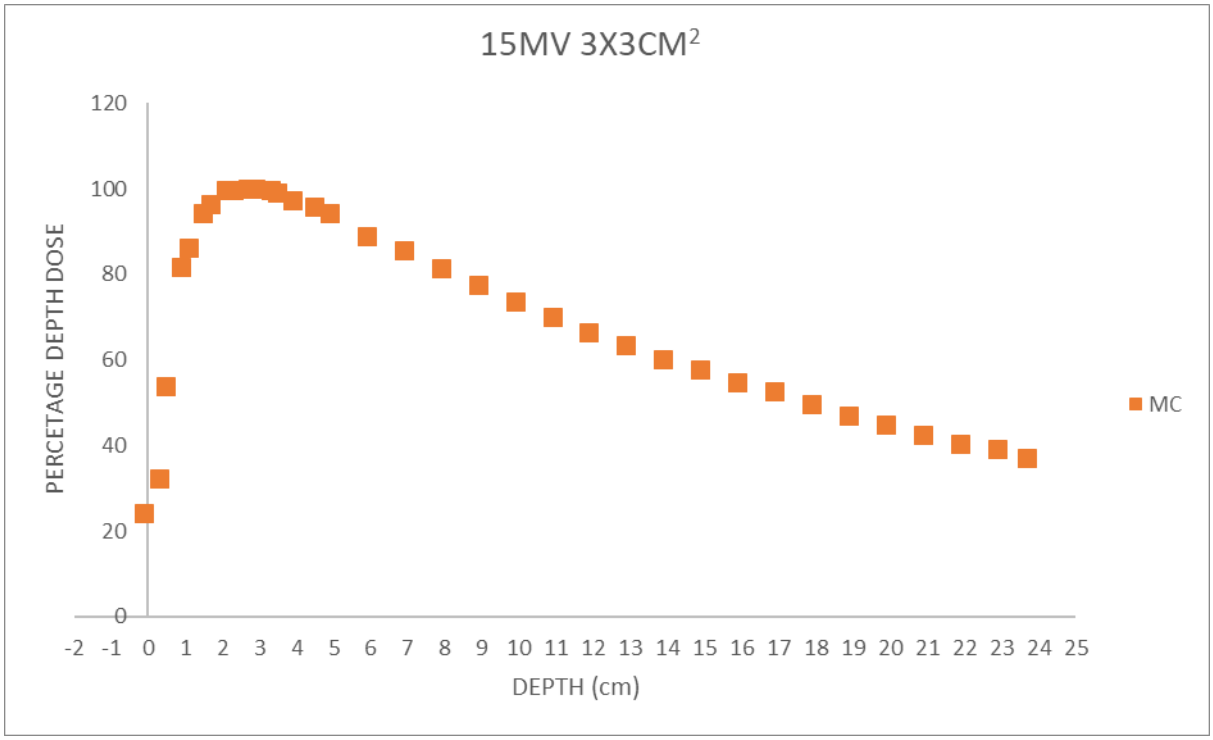

Figure D. 10: 15 MV photon beam percentage depth dose of the 3 x 3 cm^2 field size simulated using EGSnrc MC code.

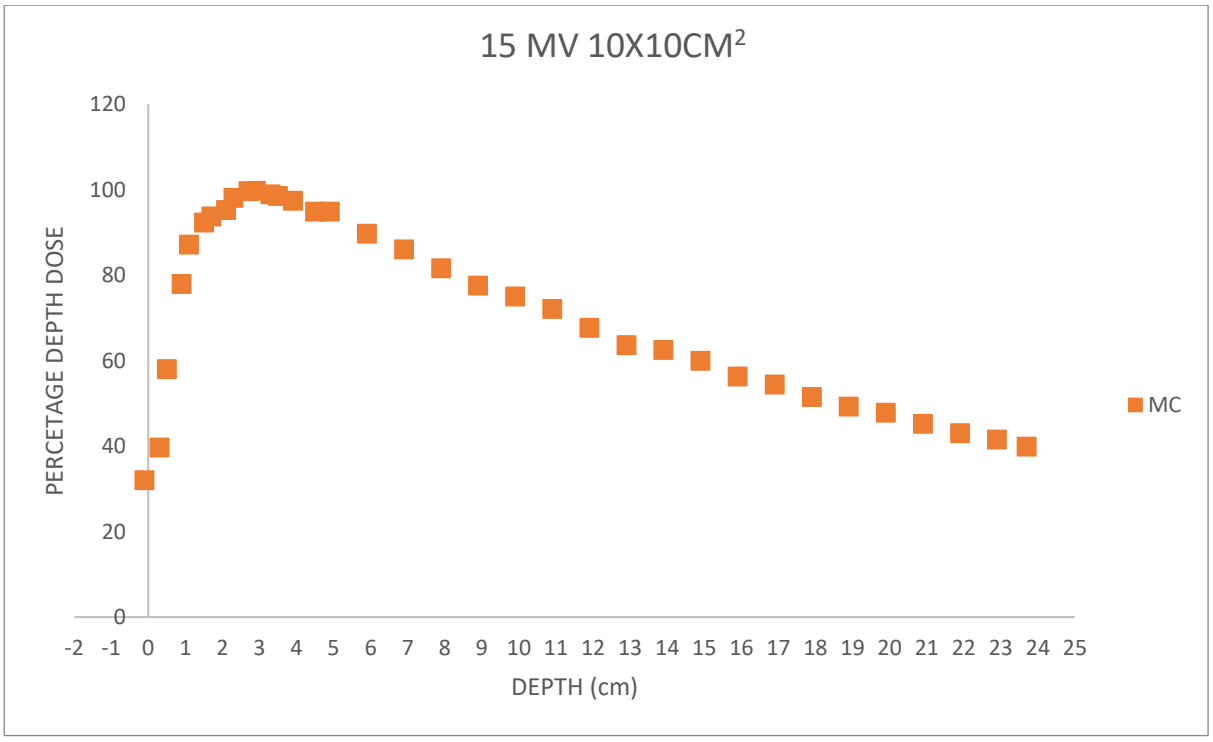

Figure D. 11: 15 MV photon beam percentage depth dose of the 10 x 10 cm^2 field size simulated using EGSnrc MC code.

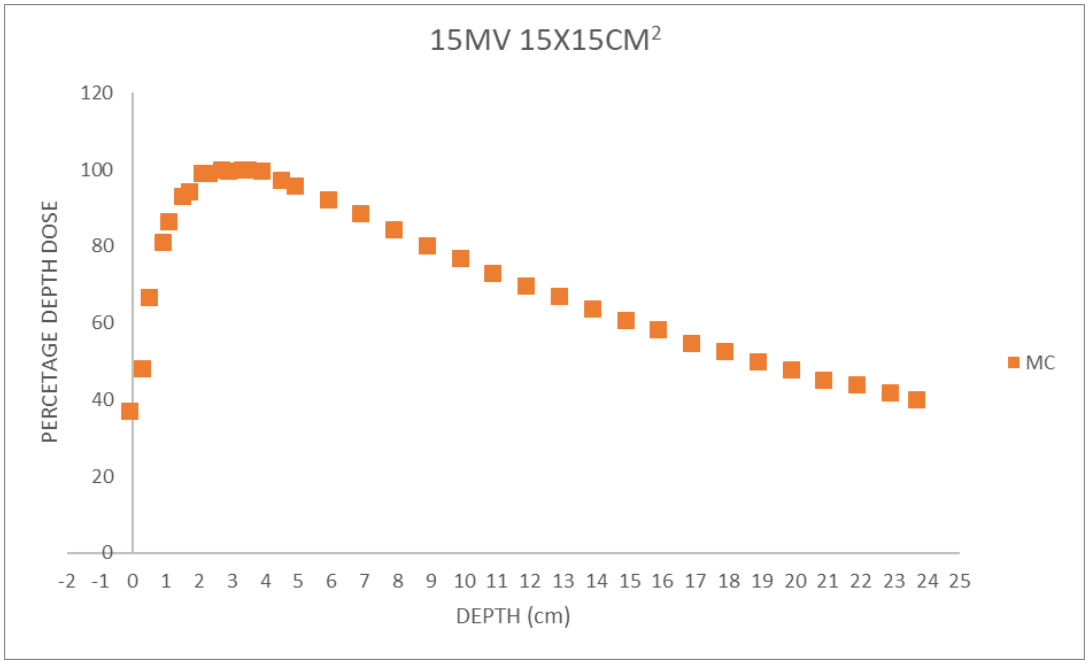

Figure D. 12: 15 MV photon beam percentage depth dose of the 15 x 15 cm^2 field size simulated using EGSnrc MC code.

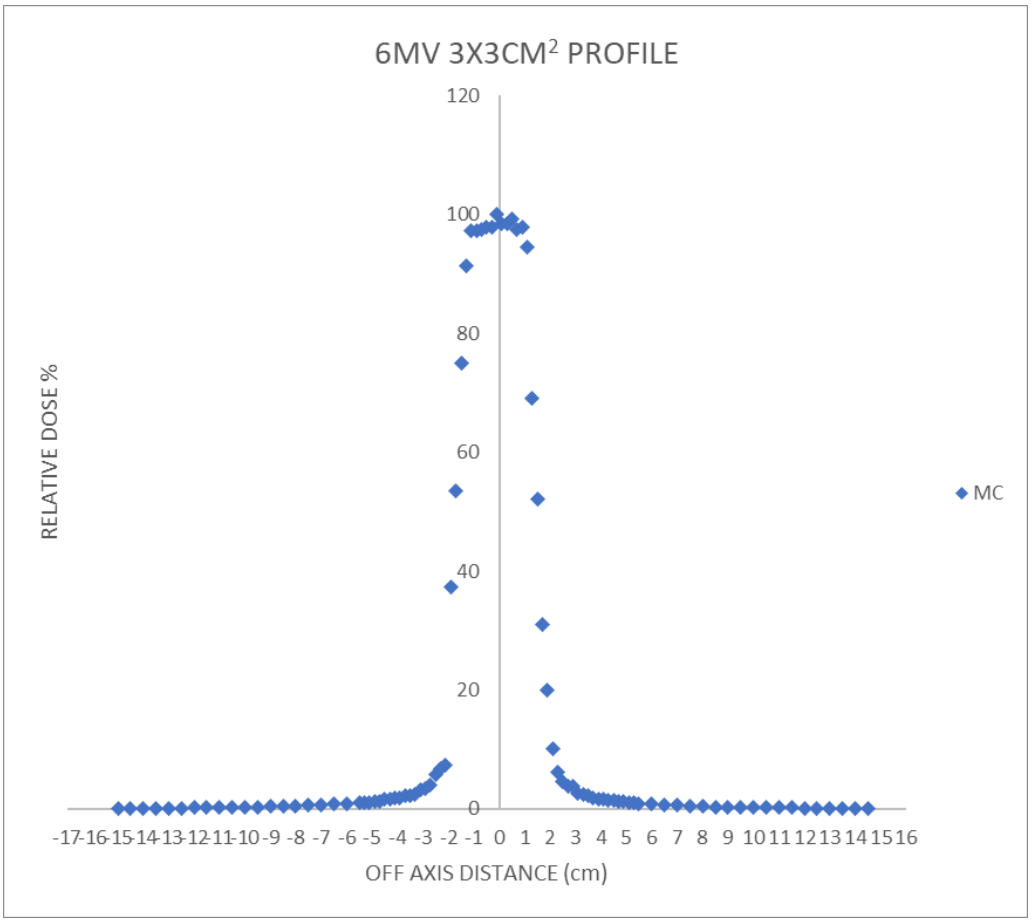

Figure D. 13: 6 MV photon beam profile of the 3 x 3 cm^2 field size simulated using EGSnrc MC code.

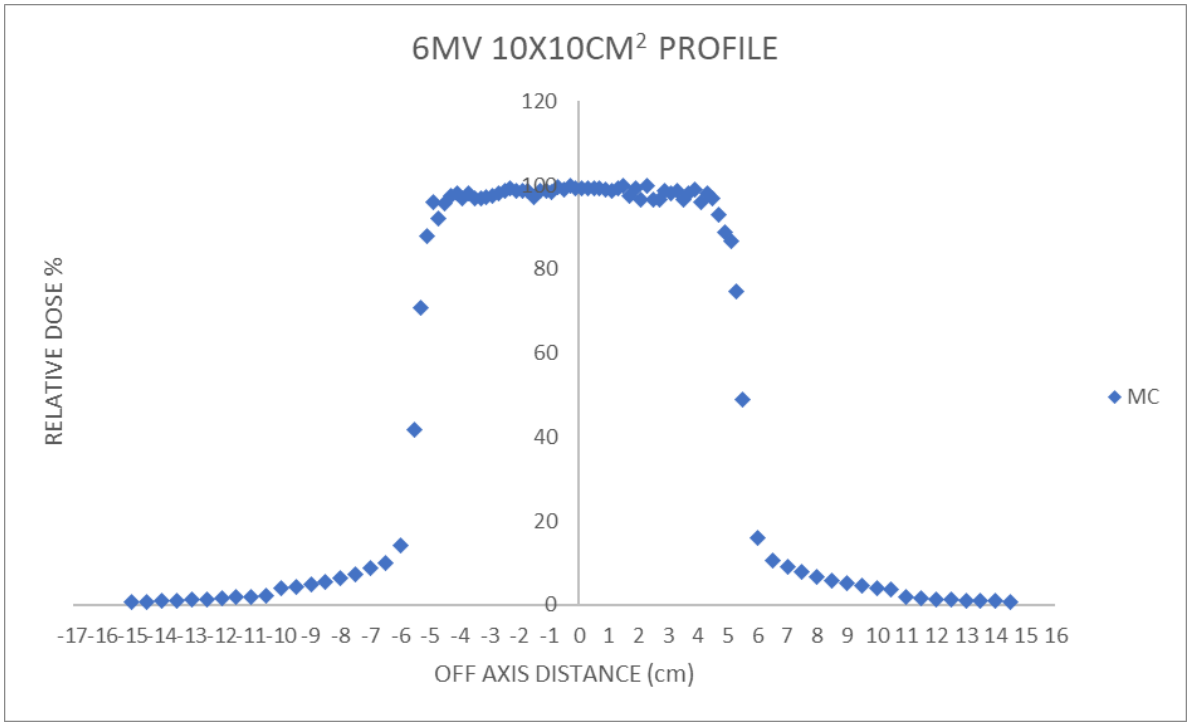

Figure D. 14: 6 MV photon beam profile of the 10 x 10 cm^2 field size simulated using EGSnrc MC code.

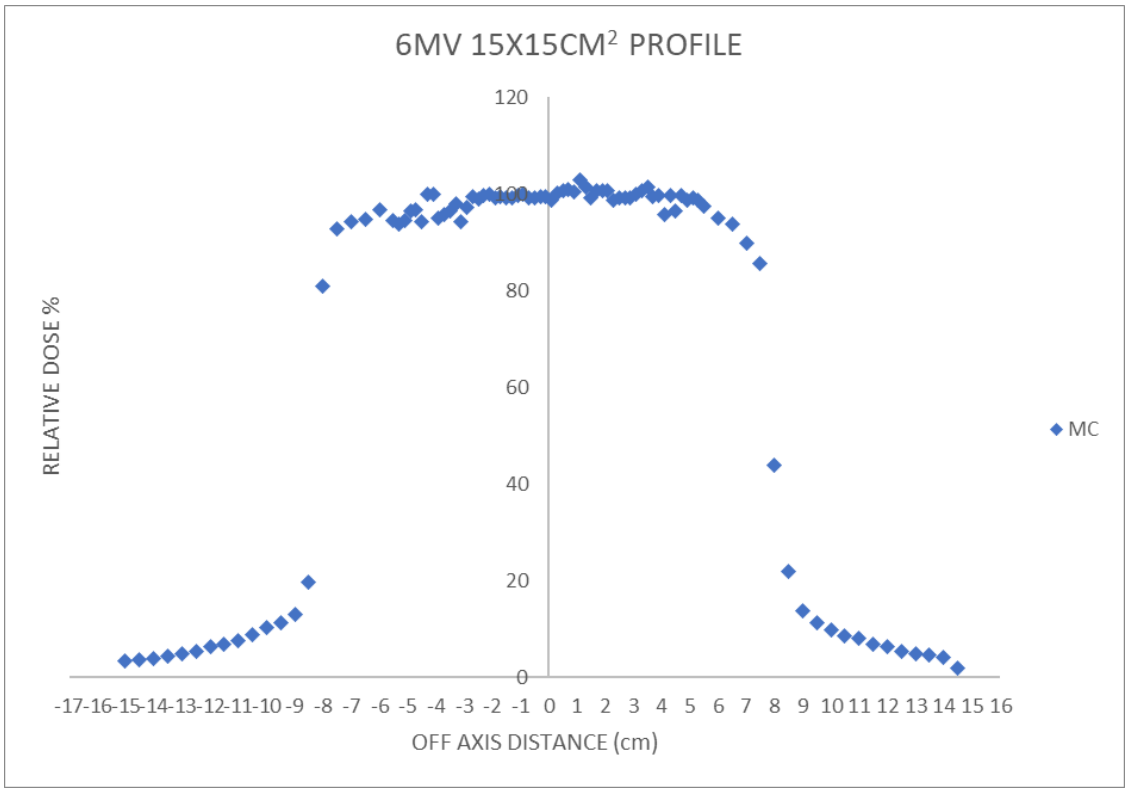

Figure D. 15: 6 MV photon beam profile of the 15 x 15 cm^2 field size simulated using EGSnrc MC code.

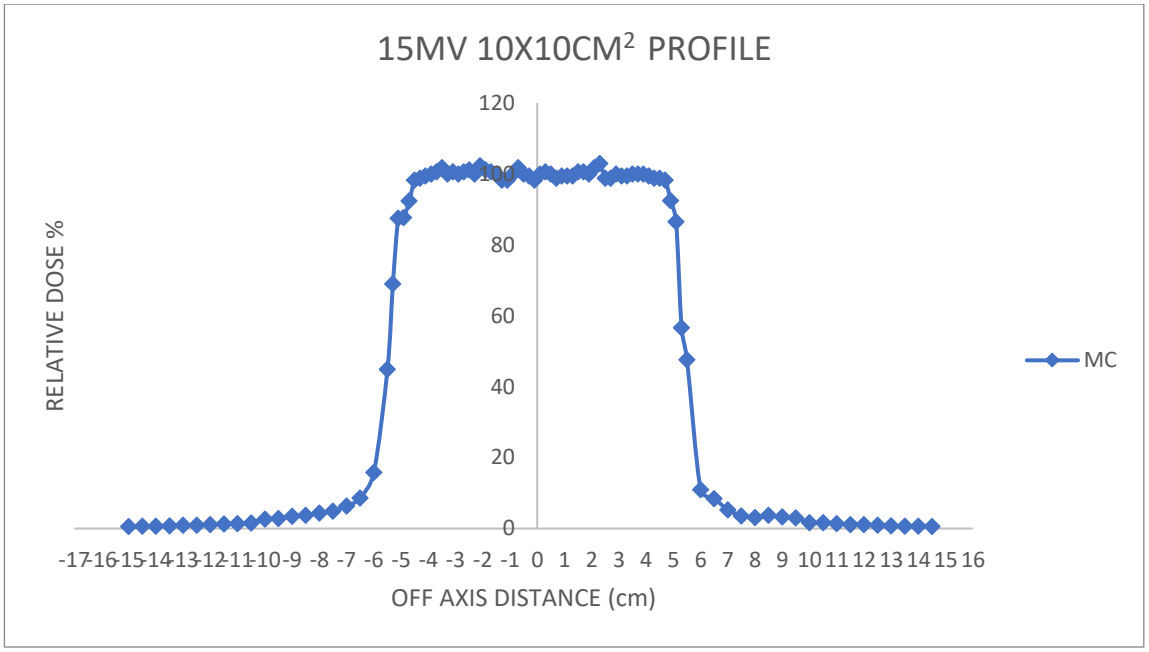

Figure D. 16: 15 MV photon beam profile of the 10 x 10 cm^2 field size simulated using EGSnrc MC code.

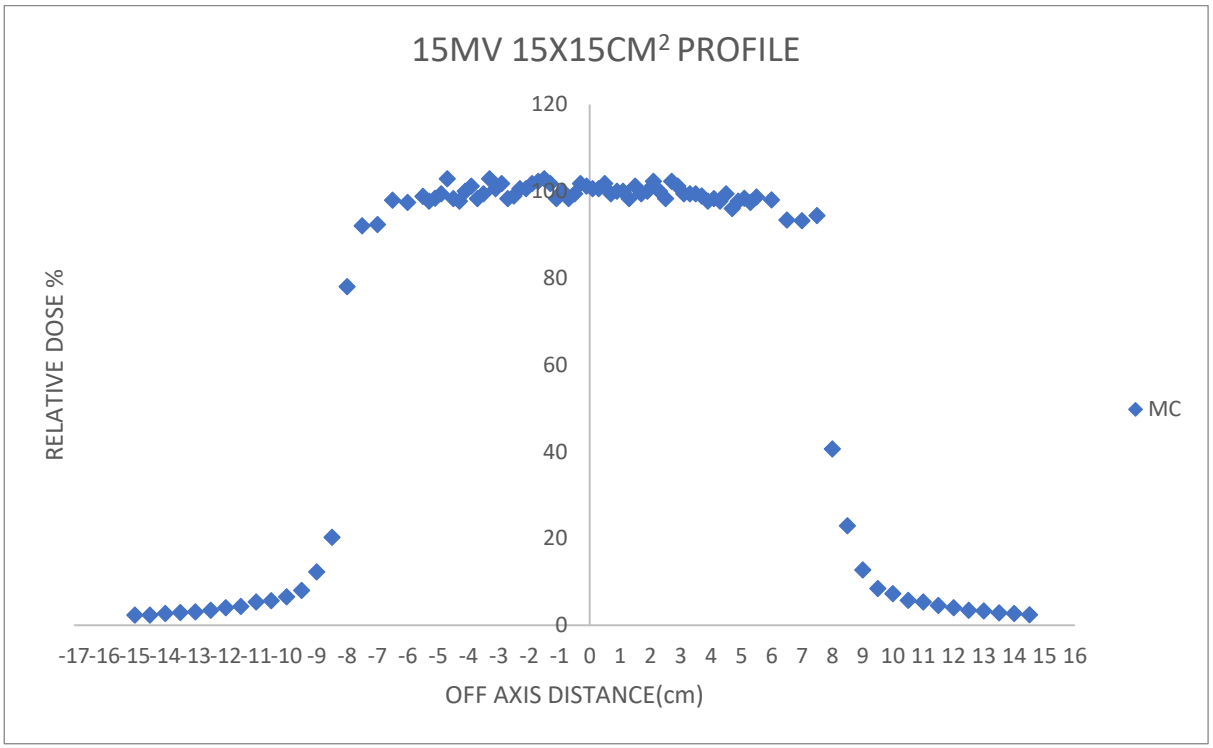

Figure D. 17: 15 MV photon beam profile of the 15 x 15 cm^2 field size simulated using EGSnrc MC code.

(3) file of materials and density data (*. egsphant)

CTPHANTOM.egsphant - Notepad

File Edit Format View Help

```
 4
AIR700ICRU
ICRUTISSUE700ICRU
ICRPBONE700ICRU
TI700ICRU
   1.00000000       1.00000000       1.00000000       1.00000000
   65   34   59
  -15.2832031      -14.7798977      -14.2765923      -13.7732868      -13.2699814      -12.766
-11.2567596       -10.7534542      -10.2501488       -9.74684334      -9.24353790       -8.740232
7.23031616       -6.72701073      -6.22370529       -5.72039986      -5.21709442       -4.7137889
3.20387268       -2.70056725      -2.19726181       -1.69395649      -1.19065118      -0.68734586
0.822570086       1.32587540       1.82918072       2.33248615       2.83579159       3.339097
4.84901333       5.35231876       5.85562420       6.35892963       6.86223507       7.3655405
8.87545681       9.37876225       9.88206768       10.3853731       10.8886786       11.391984
12.9019003       13.4052057       13.9085112       14.4118166       14.9151220       15.418427
16.9283428       17.4316483
   5.22929668       5.73768377       6.24607086       6.75445795       7.26284504       7.7712
9.29639244       9.80477905       10.3131657       10.8215523       11.3299389       11.838325
13.3634853       13.8718719       14.3802586       14.8886452       15.3970318       15.905418
17.4305782       17.9389648       18.4473515       18.9557381       19.4641247       19.972511
21.4976711       22.0060577       22.5144444
  -42.7800102      -42.2766228      -41.7732353      -41.2698479      -40.7664604      -40.263
-38.7529106       -38.2495232      -37.7461357       -37.2427483      -36.7393608       -36.23597
34.7258110       -34.2224236      -33.7190361       -33.2156487      -32.7122612       -32.208873
30.6987057       -30.1953163      -29.6919270       -29.1885376      -28.6851482       -28.181758
26.6715908       -26.1682014      -25.6648121       -25.1614227      -24.6580334       -24.154644
22.6444759       -22.1410866      -21.6376972       -21.1343079      -20.6309185       -20.127529
18.6173611       -18.1139717      -17.6105824       -17.1071930      -16.6038036       -16.100414
14.5902491       -14.0868607      -13.5834723       -13.0800838
```

Figure D. 18: Materials used to create the phantom (*egsphant) using CTCREATE.

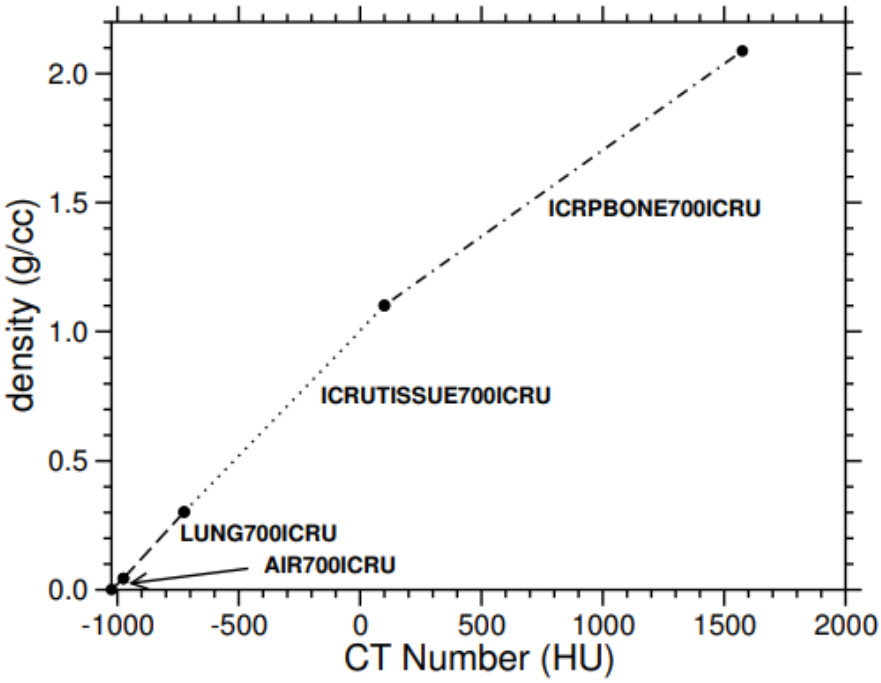

Figure D. 19: The default ramp for converting CT values to material and density in CTCREATE.

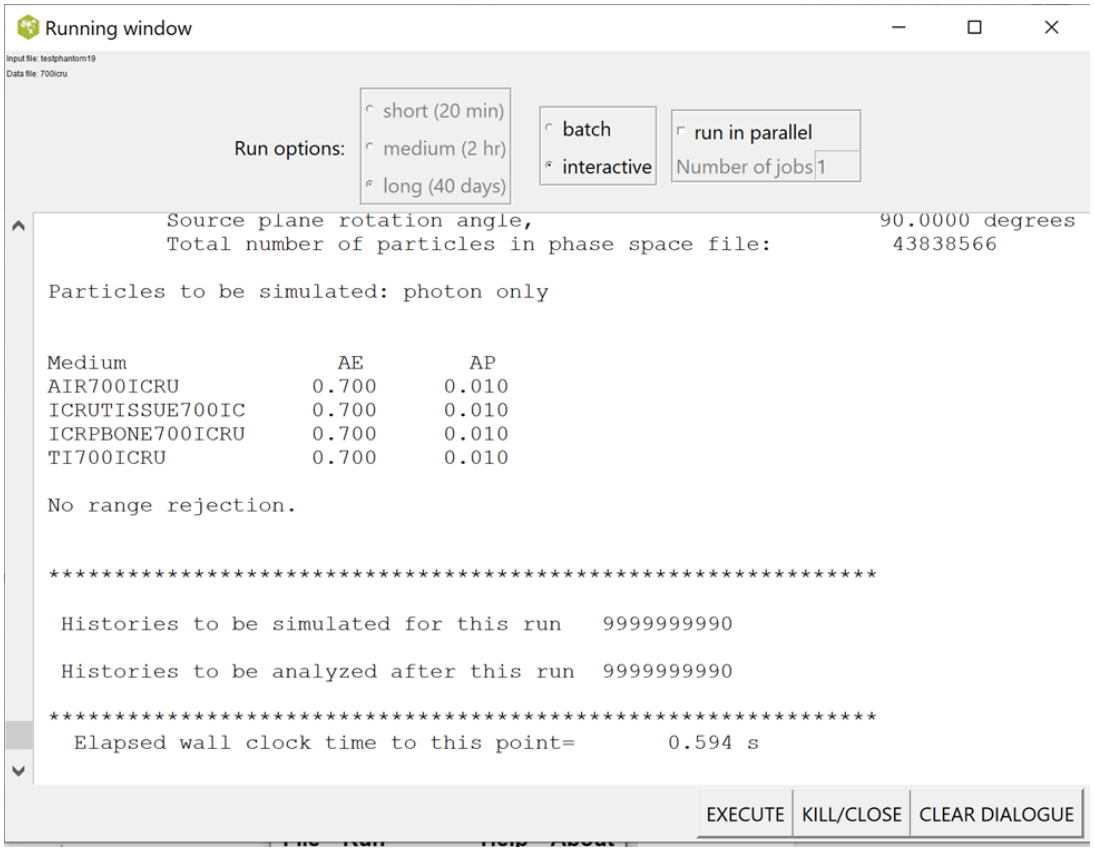

Figure D. 20: DOSXYZ window showing the particle to be simulated in the phantom.

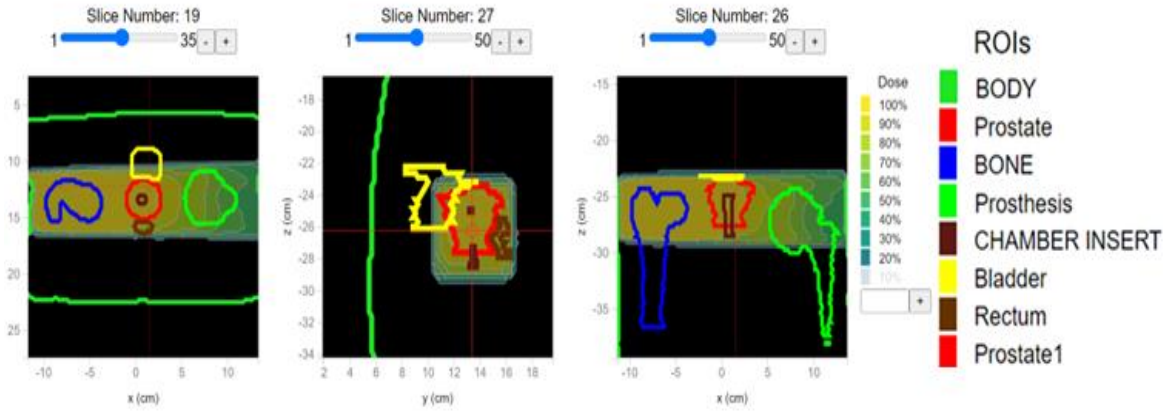

Figure D. 21: 6MV right lateral field MC simulated dose distribution.

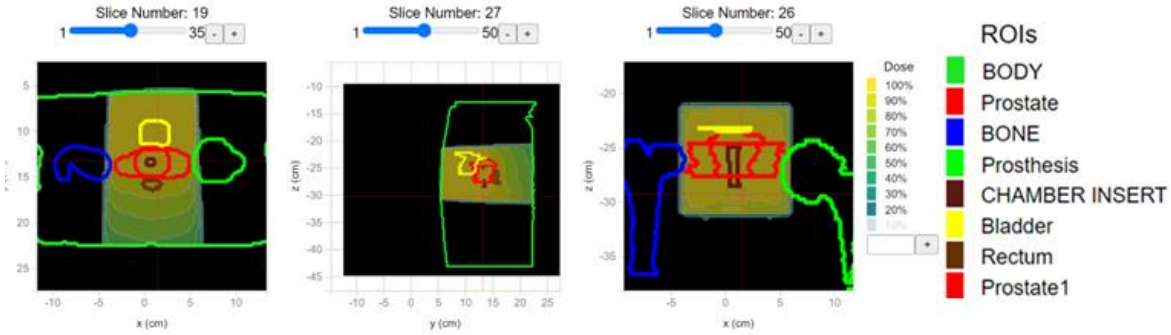

Figure D. 22: 6 MV anterior field MC simulated dose distribution.

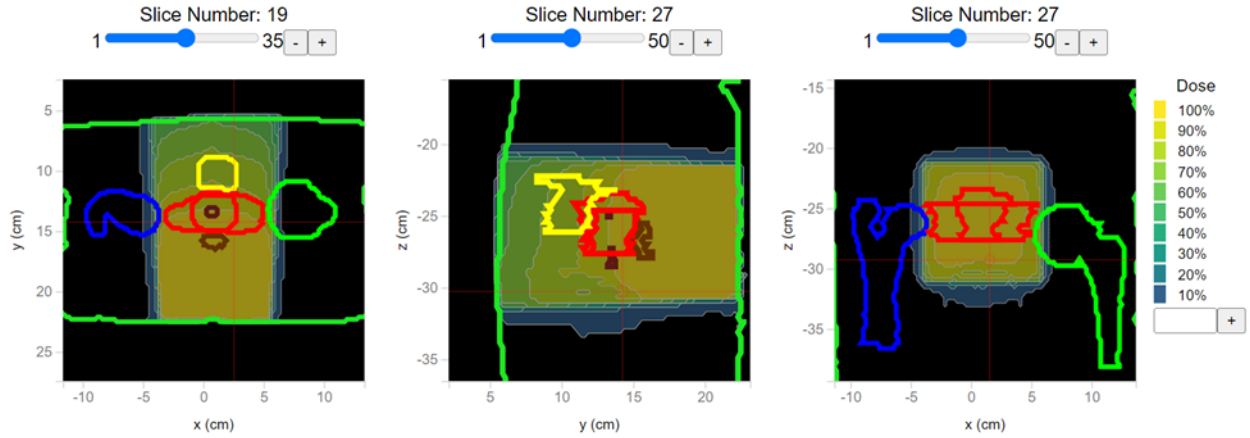

Figure D. 23: 6 MV posterior MC simulated dose distribution.